

Cover Page



Universiteit Leiden



The handle <http://hdl.handle.net/1887/37091> holds various files of this Leiden University dissertation.

Author: Devid, Edwin Johan

Title: Exploring charge transport properties and functionality of molecule-nanoparticle ensembles

Issue Date: 2015-12-17

Exploring charge transport properties and functionality of molecule-nanoparticle ensembles

Proefschrift

ter verkrijging van
de graad van Doctor aan de Universiteit Leiden,
op gezag van Rector Magnificus prof. mr. C. J. J. M. Stolker,
volgens besluit van het College voor Promoties
te verdedigen op donderdag 17 december 2015
klokke 13:45 uur

door

Edwin Johan Devid

geboren te Amsterdam
in 1979

Promotor:	Prof. dr. J. M. van Ruitenbeek	Universiteit Leiden
Co-promotor:	Dr. ir. S. J. van der Molen	Universiteit Leiden
Promotiecommissie:	Prof. dr. B. Doudin	Université de Strasbourg
	Prof. dr. T. E. Keyes	Dublin City University
	Prof. dr. L. D. A. Siebbeles	Technische Universiteit Delft
	Prof. dr. J. Aarts	Universiteit Leiden
	Prof. dr. T. J. Aartsma	Universiteit Leiden
	Dr. S. Bonnet	Universiteit Leiden
	Prof. dr. E. R. Eliel	Universiteit Leiden

Casimir PhD Series, Delft-Leiden 2015-25

ISBN 978-90-8593-231-4

An electronic version of this dissertation is available at

<https://openaccess.Leidenuniv.nl>

Printed by: Proefschriftmaken.nl

Cover: Jonathan Gardenier, Robert Smit en Edwin Devid



Universiteit Leiden

This work is part of the research programme of the Foundation for Fundamental Research on Matter (FOM), which is part of the Netherlands Organisation for Scientific Research (NWO). This research was carried out at Leiden University.

This research has been supported by NanoSci-ERA. A consortium of public or private bodies responsible for financing, managing and stimulating collaborative research programmes in nanoscience in the European Research Area (ERA). The name of this NanoSci-E+ project is: Interfacing single molecules via nanoparticle networks (INTERNET).

Table of contents

Table of abbreviations.....	XII
-----------------------------	-----

Chapter 1. Introduction to molecular charge transport..... 1

1.1	The motivation behind molecular charge transport	2
1.1.1	A short history of molecular charge transport	2
1.1.2	The role of organic molecules and their functionality	5
1.2	Experimental methods to study molecular conduction	7
1.2.1	Single molecular junctions	8
1.2.2	Multi-molecular junctions	10
1.3	Multi-molecular devices based on gold nanoparticles	11
1.4	Spin crossover molecules.....	14
1.4.1	The metal complex	15
1.4.2	Crystal and ligand field theory	16
1.4.3	Spin crossover complexes.....	19
1.4.4	Spin transition in bulk.....	22
1.4.5	Size effects on spin crossover molecules.....	24
1.5	Motivation and outlook of this thesis.....	24
1.6	References.....	26

Chapter 2. Charge transport in molecular systems..... 33

2.1	Charge transport on the macroscopic scale.....	34
2.2	Charge transport at reduced length scales.....	34
2.3	Charge transport through a molecular junction.....	37
2.4	References.....	42

Chapter 3. Molecular devices based on molecule-gold nanoparticle arrays and networks	45
3.1 The synthesis of 2D molecule-metal nanoparticle arrays	46
3.1.1 Part 1: synthesis of gold nanoparticles in aqueous solvent.....	46
3.1.2 Part 2: functionalization of gold nanoparticles by molecules	47
3.1.3 Part 3: self-assembly of 2D alkanethiol-gold nanoparticle array.....	48
3.2 Molecular exchange	51
3.3 Synthesis routes toward spin crossover-gold nanoparticle networks.....	52
3.3.1 Synthesis route 1: molecular exchange.....	52
3.3.2 Synthesis route 2: complexation via a ligand-nanoparticle network ...	53
3.3.3 Synthesis route 3: direct synthesis of Fe(S-BPP) ₂ molecules with gold nanoparticles.....	56
3.4 Charge transport measurements.....	58
3.5 Optical properties of molecule-gold nanoparticle arrays	59
3.5.1 The surface plasmon resonance of a molecular-gold nanoparticle array.....	61
3.5.2 Surface-enhanced Raman scattering	62
3.6 References.....	67
Chapter 4. Enhancing the molecular signature in molecule-nanoparticle networks via inelastic cotunneling	73
4.1 Introduction of molecule-nanoparticle ensembles	74
4.2 Charge transport mechanisms expected.....	76
4.3 Charge transport measurements on nanotrench devices	80
4.4 Charge transport properties of C8 and OPE exchanged gold nanoparticle networks	81
4.5 Conclusions.....	87
4.6 References.....	87

Chapter 5. The influence of molecular mobility on the properties of gold nanoparticle organic ligand networks	91
5.1 Introduction to molecular ligand-nanoparticle ensembles	92
5.2 Capping of gold nanoparticles with S-BPP molecules	93
5.3 The fabrication of 2D Au-NP-S-BPP arrays.....	94
5.4 Imaging of Au-NP-S-BPP arrays and networks	95
5.5 UV-Vis spectroscopy on 2D Au-NP-S-BPP arrays	98
5.6 Room-temperature Raman spectroscopy on 2D Au-NP-S-BPP arrays .	101
5.6.1 Temperature-dependent Raman spectroscopy on 2D Au-NP-S-BPP arrays	104
5.7 Conductance measurements on a multilayered Au-NP-S-BPP network	107
5.8 Conclusions.....	110
5.9 References.....	111
Chapter 6. Spin transition in arrays of gold nanoparticles and spin crossover molecules	117
6.1 Introduction to molecular complex-nanoparticle ensembles	118
6.2 Experimental method of a spin crossover-gold nanoparticle array.....	122
6.3 Temperature-dependent Raman spectroscopy measurements	124
6.4 Magnetization measurements.....	128
6.5 Charge transport experiments	130
6.6 Theoretical charge transport calculations	133
6.7 Discussion.....	136
6.8 Conclusions.....	139
6.9 References.....	140
Appendix A.1	149
Appendix A.2	151
Appendix A.3	152
Appendix A.4	154

Appendix B.1.....	157
Appendix B.2.....	158
Appendix C.1	161
Appendix C.2	162
Appendix C.3	163
Appendix C.4	166
Appendix C.5	168
Appendix C.6	169
Summary	173
Samenvatting	179
List of publications	185
Curriculum Vitae.....	187
Acknowledgements.....	189

Table of abbreviations

AcS-BPP	S-(4-{[2,6-(bipyrazol-1-yl)pyrid-4-yl]ethynyl}phenyl)ethanethioate molecule where the S anchoring group is protected by an acetyl leaving group
Array	2D single layer ensemble
Au	Gold
BPP	2,6-Bi(Pyrazolyl)Pyridine
C8	Octane(mono)thiol
E_C	Charging energy
EDX	Energy-Dispersive X-ray (spectroscopy)
EtOH	Ethanol
$[\text{Fe}(\text{AcS-BPP})_2](\text{ClO}_4)_2$	Fe^{2+} (S-(4-{[2,6-(bipyrazol-1-yl)pyrid-4-yl]ethynyl}phenyl)ethanethioate) ₂ - (ClO ₄) ₂ complex
HAADF-STEM	High Angle Annular Dark Field-Scanning Transmission Electron Microscopy
HAR	High Aspect Ratio
HAuCl ₄	HydroChloroauric acid (also called Gold(III) chloride hydrate)
HS	High-Spin
<i>I-V</i>	Current as function of the Voltage
LS	Low-Spin
MeCN	Acetonitril
Network	A quasi 2D or multiple (i.e. here 3 layers) layer ensemble

NP	Nanoparticle
OPE	Oligo(phenylene ethynylene)
PDMS	Polydimethylsiloxane
RPM	Rotations per minute
<i>R-T</i>	Resistance as function of the Temperature
SAM	Self-Assembled Monolayer
SCO	Spin crossover
SEM	Scanning Electron Microscope
SERS	Surface-enhanced Raman spectroscopy
SPR	Surface Plasmon Resonance
SQUID	Superconducting Quantum Interference Device
ST	Spin transition
3D	Three-dimensional
TEM	Transmission Electron Microscope
2D	Two-dimensional
UV-Vis	Ultraviolet-Visible light spectrum
VRC	Variable Range Cotunneling
VRH	Variable Range Hopping

1



Introduction to molecular charge transport

This chapter contains a brief introduction to the research field of molecular charge transport. First, I deal with its basic driving force and its interesting history. Next, the experimental state of the art is highlighted by introducing the main experimental methods used in present-day research. Then, I will introduce the research in this dissertation, which deals with the question if and how molecular properties can be transferred to or even enhanced in molecular devices. I will pay extra attention to a special type of functional molecules, exhibiting a temperature-dependent spin transition, since it forms a key inspiration for this work. The chapter ends with an outlook on the rest of this thesis. Basic theory on molecular charge transport will be given in Chapter 2.

1.1 The motivation behind molecular charge transport

Research on molecular charge transport is motivated by a simple, but fascinating concept: the idea that a functional device, e.g. a transistor, switch or diode, may be as small as a single molecule connected to electrodes. This concept offers two interconnected advantages. First of all, such devices would be much smaller than present-day silicon components, i.e. around a few nanometers in size (disregarding the electrodes, however). Second, functionalities, such as switchability, rectification, etc., may be pre-programmable in the molecules used. The question if a device incorporating a functional molecule retains the same functionality is generally open. In fact, in many cases, coupling of a molecule to electrodes leads to a dramatic change of properties. This issue has been the subject of considerable scientific efforts and is also touched upon in this dissertation. From a basic research point of view, molecular charge transport has also attracted much attention. This is because small organic molecules are profoundly quantum mechanical in nature, even at elevated temperatures. Hence, the wave nature of the electron as well as its spin degree of freedom should be explicitly considered.

All the ingredients above have motivated scientists from various backgrounds to investigate the properties of molecular devices over the past decades. Chemists, physicists and surface scientists have joined hands, leading to considerable cross-fertilization. Especially with the rise of scanning probe microscopy as well as nanolithography techniques, the field of molecular charge transport (and nanoscience as a whole) seriously took off. During its history that spans around four decades now, it has both seen fast progress and backdrops [1]. For example, few people still believe that molecular electronics will be seriously competitive with silicon electronics. Still, the research has continued to prove fundamentally fascinating, while specific applications, e.g. as sensors, are being explored [2].

1.1.1 A short history of molecular charge transport

The conception of this research field lies between 1950 and 1960, i.e. the time of the invention of the transistor, an era that changed electronics completely. Since 1960, the quest to miniaturize electronic components has continued via a top-down approach (as analyzed by G. E. Moore) [3]. The miniaturization of silicon based electronics was ongoing and successful, but this also brought more complexity and high investment costs. Already then, some people feared that the miniaturization of silicon-based

electronics was bound to arrive at a technological dead end. Hence, the search started toward radically different alternatives to miniaturize electronics.

One way was to miniaturize electronic components via a bottom-up approach. This idea was formulated by A. von Hippel and it was then called molecular engineering [4]. This concept led, at the end of the 1950's, to the name "molecular electronics". This name embodied a new strategy between collaborating research institutes and USA defense-affiliated research branches to fabricate miniaturized electrical components. However, this concept could not compete with the steady miniaturization of the electronic devices from the semiconductor industry. Silicon-based electronic devices evolved further becoming smaller, lighter, consuming less power and emitting less heat [5].

Whereas in the 50's, molecular electronics strived to make microelectronics based on the use of crystalline bulk materials [5], in the 1970's, the perspective shifted to the use of individual molecules as electronic circuits. This was partially inspired by the famous speech by Richard Feynman called: "There's Plenty of Room at the Bottom", delivered in December 1959 [6]. The Swiss chemist H. Kuhn was one of the first scientists to experimentally explore the conductance properties of molecular monolayers. The latter were made by the Langmuir Blodgett method, i.e. via self-assembly of organic material floating on a liquid. B. Mann and H. Kuhn studied the transport of charge through both a "molecular" monolayer and "sandwiched" layers, made of fatty acid salts between metal electrodes [7]. Around the same period, A. Aviram and M. Ratner suggested to synthesize a new type of asymmetric molecular species. Once contacted by electrodes, it would be capable of rectification, thus mimicking the properties of semiconductor diodes in an electrical circuit [8]. Many experiments were conducted to realize this first type of a functional molecular device, but they were largely unsuccessful. Nevertheless, the idea that a molecule could be designed and synthesized with a certain functionality, and that that functionality could subsequently be transferred to a molecular device has remained an essential concept in molecular electronics ever since the Aviram-Ratner paper.

In 1981, IBM invented the first type of experimental platform that was truly capable of visualizing and investigating surfaces on the atomic scale: the scanning tunneling microscope (STM). It also became a key tool to study the charge transport properties of single molecules, as will be detailed below [9, 10]. In the 1990's, another experimental

device, called the mechanically controlled break junction (MCBJ) became available. The MCBJ was first used to study charge transport through metallic atomic-made wires [11], but was subsequently applied to molecular conductance studies as well [12].

At the end of the 90's, more experimental devices and fabrication techniques were introduced, some of which aimed for single molecular junctions, others which focused on probing molecular monolayers. The consequence was that also various companies became active in this field again [1]. The end of the 1990's hence saw a strong momentum, with various exciting results. Unfortunately, a few years later, some of the most spectacular results were heavily debated in literature. For example, HP labs aimed for a voltage-controlled molecular switch based on so-called rotaxanes molecules. These molecules are bistable switches in solution that can be controlled via a redox potential. An architecture of rotaxanes molecules circuits could indeed be made, for which memory/logic functions were demonstrated [13]. However, the interpretation of the achieved results was doubted by some researchers in the molecular charge transport community [14, 15]. The difficulty was that it was not at all clear if the switching effect observed was due to the molecules at all. Other explanations, such as metallic filament formation between the electrodes were (at least) equally probable [15]. This and other controversial situations disappointed scientists involved, and stalled the field for a few years. Fortunately, molecular charge transport as a basic research field picked up momentum again in the 2000's, in a more robust and perhaps also more modest way.

All in all, this brief history points out two of the key questions that will always arise in molecular charge transport: "Are the properties measured due to the contacted molecule?" And if so: "How is the molecule oriented within the device?". Rather fundamentally, these questions are not easy to answer. However, in this last decade, scientists have realized how to come close. Clearly, one wants additional control experiments, e.g. optical spectroscopy, Raman spectroscopy, inelastic electron tunneling spectroscopy (IETS). Furthermore, proper statistics of molecular junction formation and junction properties turn out to be of great importance. Through joint collaboration of researchers from various disciplines, creative methods have been devised that allow the study of the molecular charge transport properties in more robust types of molecular devices. Those molecular devices have the best chance of awaiting an application destiny in the future.

1.1.2 The role of organic molecules and their functionality

Conjugated organic molecules form the backbone of a large part of research on molecular junctions. A conjugated molecule typically contains an alternation of single and double (triple) carbon bonds. This yields an extended π -electron system, with orbitals composed of hybridized atomic p_z states. Conjugated molecules are expected to have relatively low resistance (but still higher than the quantum of resistance $h/2e^2 = 12.9 \text{ k}\Omega$!). Intuitively, this is due to two connected reasons. First, the π -orbitals are delocalized over the entire molecule, facilitating transport over the full entity. Second, the energy gap that separates the highest occupied molecular orbital (HOMO) from the lower unoccupied molecular orbital (LUMO) is lower than for non-conjugated systems, such as alkanes. In general, conjugated molecules will therefore have a larger conductance than non-conjugated molecules. Hence, much fundamental research is being performed on (series) of conjugated molecules. Clearly, this also opens an exciting possibility, i.e. to devise a molecule for which conjugation, and hence conductance, can be turned ‘on’ or ‘off’. As mentioned above, a prime motivation to investigate molecular charge transport has indeed been to study (and utilize) the role of molecular functionality. A molecular species can in principle be “programmed” to perform a certain function in a device. Chemical synthesis offers many ways to design and tailor the properties of organic molecules. For example, certain types of asymmetric molecules may lead to rectification behaviour, once the molecule is contacted (c.f. Aviram and Ratner [8]). Furthermore, a whole library of switchable molecules can be found in chemistry, some sensitive to light, others to temperature or electrochemical potential. The main molecular property that changes upon stimulation may vary. For some, conjugation is broken, others exhibit a length change (due to a cis-trans transformation), while a relatively unexplored subgroup exhibits a change of spin state. The latter type is of special interest for this thesis and will be dealt with in detail below.

As illustrated in the historical overview, a key question must be answered when investigating functional molecules in molecular junctions: “Is the functionality (and connected properties) preserved after a functional molecule is coupled to metal electrodes?” The answer is non-trivial and will depend on the details of the junction, i.e. (i) on the electrode material used, (ii) on the chemical group connecting the molecule to the electrodes and (iii) on the final geometry of the molecule with respect to the electrodes and other molecules [16]. Fundamentally, the molecular orbital structure

will change after connecting to electrodes, via hybridization between molecular orbitals and the metal bands, leading to broadened molecular levels (Lorentzians instead of delta functions, see Chapter 2). This is the case for any molecule, but for functional molecules it is of specific importance. A change in orbital structure may change the switching paths and dynamics completely. Clearly, the exact molecular endgroup that anchors the molecule to a metal surface also plays a key role in defining the exact electronic coupling. A general type of anchoring group used in organic molecules is a thiol (SH) group. The thiol group makes a chemical bond with gold and is the endgroup of choice in this work [1]. Finally, the detailed geometry and environment play a role if the switching process demands some free space available. Switching may be spatially hampered due to neighbouring atoms, molecules or electrodes. Chemists tend to refer to this as ‘steric hindrance’.

To illustrate the above, let us consider a well-known family of switchable molecules, i.e., the diarylethenes. These molecules can be switched between a less conductive (broken conjugated) state and a more conductive (conjugated) state through exposure by different wavelengths of light. In solution, diarylethenes can be converted reversibly [17]. But when these diarylethenes are coupled to gold electrodes through thiol bonding, things change. For example, the molecule shown in Figure 1.1 can only switch in one direction after being contacted: from the ‘on’ state to the ‘off’ state. From that point the functional molecule loses functionality and it becomes passive. The loss of functionality is in this case most likely caused by strong electronic coupling of the diarylethene molecule with the metal. Indeed, by slight changes in the molecular endgroup (meta-coupled phenyls instead of thiophene rings), reversible switching could be recovered in a junction geometry [16]. This illustrates how subtle the issue of retaining molecular functionality can be.

Interestingly, one may also wonder if the presence of electrodes can lead to new functionality. Indeed, this may be the case, as the electrodes define new boundary conditions (i.e. break rotational symmetry that molecules do have in solution).

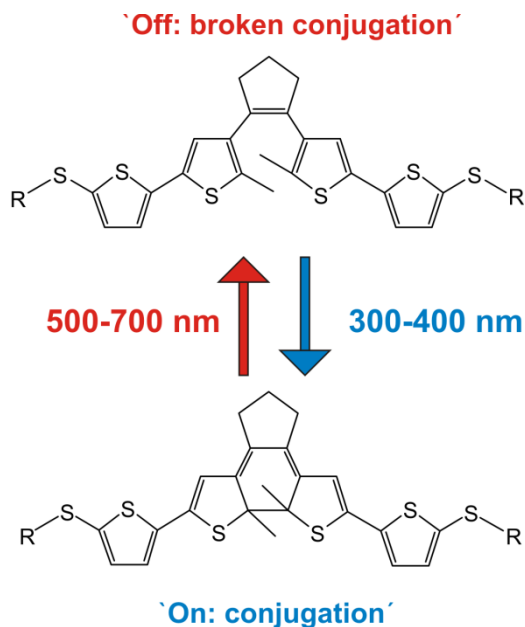


Figure 1.1: Example of a photochromic molecular switch that preserves intrinsic functionality in a solvent environment, but loses reversibility when coupled to metal electrodes.

Hence, the state in which the molecule is oriented parallel to the electrodes may have different properties than the state in which it is perpendicular. If one can switch between both situations, e.g. by a current or voltage, a switchable system is created. This is called extrinsic switching (as opposed to intrinsic switching which is due to the molecular properties themselves), and there are several experimental accounts for the phenomenon by now [16]. Another way in which the electrodes could play a role is in somehow enhancing the switching effect, e.g. by magnifying the conductance change. This thesis will also explore this possibility (see Chapter 4).

1.2 Experimental methods to study molecular conduction

A large set of experimental techniques is available nowadays to study charge transport through a single molecular junction or a multi-molecular junction. We will deal with the main techniques below, before presenting our method of choice that lies in between single molecular junctions and multi-molecular junctions.

1.2.1 Single molecular junctions

STM

Scanning tunneling microscopy (STM) is arguably the most widely used and versatile technique in the research on molecular charge transport. The STM serves a key role in measuring the charge transport properties of single molecular junctions [18, 19, 20] and recently also molecular chain junctions, by applying it unconventionally [21].

A standard STM consists of an atomically sharp metal tip placed above a surface (usually a metal substrate or a metal substrate covered by a very thin insulating layer) at a certain distance, d . During a STM measurement, a bias is applied between the tip and the metal electrode surface. The tip scans the surface of the sample, while its tunneling current is stabilized by a feedback circuit. In this way, STM can reach subatomic resolution. Hence, molecules lying on a surface can be imaged and spectroscopically investigated [1, 22-24]. For a true conductance experiment, however, the STM is used in a different fashion. Basically, the tip is connected to one end of a molecule connected to a surface. Next, the tip is raised (with the feedback mode off) and the conductance is tracked, until the newly formed junction breaks. When done at low temperature, in ultrahigh vacuum (UHV), this yields very good control over particular junctions. In somewhat adapted form, the method is also used at room temperature, to measure junction formation statistics and conductance properties of molecules in solution [25, 26].

The strong points of the STM lie in its versatility to perform both surface scans (and spectroscopy) and transport measurements. A weaker point is that its stability is limited compared to another experimental technique called mechanically controllable break junctions (see below). Also for the STM, which ideally is a single-molecule technique, charge transport measurements of long molecules (like alkanethiol molecules with a length of ~14 carbon atoms) become difficult as these yield very low currents only [27].

Mechanically controllable break junctions (MCBJ)

The term ‘break junction’ refers to an experimental technique in which a junction can be made by breaking one metal wire. When done properly, this results in two nearly symmetrical electrodes. There are two types of break junctions commonly used in the

field of molecular electronics, namely the electromigration break junctions (EBJ) and the mechanically controllable break junctions (MCBJ) [19].

The MCBJ was developed and used by J. Moreland [28] and J. M. van Ruitenbeek [29]. The platform consists of an insulating bendable substrate onto which a metal notched wire (or a lithographically defined metal bridge) is horizontally attached. The insulating substrate will be subjected to a tensile force in the z-direction under nanometer precision through a piezo controlled pushing rod. The counter supports on top of both sides of substrate assure that the sample remains fixed during bending. Upon bending, the substrate will elongate in the middle section of the notched electrodes. This finally causes the metal bridge to break. Once the junction has broken, molecules can be deposited on both fresh nanoscale electrodes. Due to a significant attenuation factor, the gap of the symmetric junction can be controlled below the Angstrom scale [30, 31], until ideally a single molecule can fit. This experimental technique was originally used by J. M. van Ruitenbeek to study atomic contacts and wires. Later, Müller brought the method to Reed's group and together they performed the first MCBJ study of a single molecule, i.e. a 1,4-benzenedithiol [32]. Nowadays, the MCBJ technique, like the STM technique described above, is used by many groups, both in low-temperature UHV experiments and for room-temperature measurements in solution.

The strong point of the MCBJ is that the distance between the metal electrodes can continuously be controlled via the piezo pushing rod. Furthermore, the MCBJ possesses a great stability, especially when working at low temperatures. In addition, with a MCBJ, one is able to repeatedly bend back and forth. This allows one to acquire a large number of measurements on which statistics can be performed [19]. A weaker point of the MCBJ is that one cannot take a topography scan of a single molecule, like in STM [1]. Connected, the exact shape of the metal contacts remains largely unknown.

Electromigration break junctions (EBJ)

A second experimental technique based on break junctions is due to Park *et al.* [33] who devised electromigration break junctions (EBJ). An EBJ is made by passing a large current density through a gold nanowire, defined by electron-beam lithography and shadow evaporation [19]. The electrons will have a net momentum transfer on the gold atoms that cause the latter to migrate to the positive electrode. This

electromigration process is continued until signs of eventual breakage of the gold nanowire becomes visible. Before the wire finally breaks, the current drops drastically and atomic sized contacts may be formed for a rather short time span. If done properly, two clean metal electrode contacts can be formed that are separated by a distance of around 1-2 nm [33-36]. A desired type of molecule can be inserted in this empty nanoscale gap.

A strong point of the experimental technique EBJ is that you can easily make a molecular three-terminal device with it [34, 36], i.e. a device that contains two electrodes contacting the molecule (source and drain) as well as a third, gate electrode. This gate electrode can be used to shift the energy levels of the molecule that is bridging the gap.

A weak point of the EBJ is that the atomic-sized metal contacts, made by electromigration, are hard to close again, unlike in MCBJs. This limits the sheer number of experiments possible, leading to very limited statistics compared to MCBJ and STM methods. Also EBJ is an experimental technique that asks a lot of care and fine-tuning to enable workable EBJ devices. An active feedback system is needed to carefully control the speed of the electromigration procedure [37]. If done incorrectly, metal debris can be formed in between the nearly symmetrically break junction during electromigration. The debris can hinder the insertion of molecules in between the break junction. Moreover, a small metal nanoparticle could have characteristics very similar to single molecules [38, 39].

1.2.2 Multi-molecular junctions

CP-AFM

An experimental technique that bears similarity to STM is conducting probe atomic force microscopy (CP-AFM) [19]. In contrast to STM, however, it is generally used for measurements on molecular monolayers. CP-AFM contains a metal-coated probe that can gently be positioned into contact with the molecules on a conducting surface. By applying a DC bias between the probe and the substrate, the charge transport properties of an ensemble of molecules on the conducting substrate surface can be measured [40-43]. An important difference between CP-AFM and STM is that in the first case, the force and deflection of the probe acting upon the molecules can be measured and controlled. In other words, there is an independent feedback mechanism, disconnected

from the conductance experiments themselves. Another advantage of (CP)-AFM is that the morphology of multi-molecular layers [44] till even polymer structures [45] can be determined while also their conductance can be probed. However, this experimental technique gives a higher uncertainty in the number of molecules measured, because a CP-AFM probe has a larger, often unknown, contact surface compared to an atomically sharpened STM tip. Furthermore, it requires a very sensitive control of the probe loading force [46].

Self-assembled monolayers (LAMJ configuration)

For technological applications, molecular tunnel junctions need to be reliable, reproducible and stable. In 2006, Akkerman *et al.* [47] introduced so-called large area molecular junctions (LAMJ), is also known as the “conductive polymer electrodes” technique [1]. The principle behind LAMJ is to create a self-assembled monolayer (SAM) on gold, onto which a conductive polymer layer is applied, followed by a gold top electrode. The polymer mixture used is poly[3,4-ethylenedioxythiophene] (PEDOT) : poly[4-styrenesulfonic acid] (PSS). It contains large hydrophilic macromolecules that cannot penetrate the hydrophobic densely packed SAM. Thus, the formation of short circuits by metal filaments from the top electrode will be prevented. The advantage of the LAMJ device is that the molecular junction is very robust [1]. The LAMJ device has a stability of at least a year in air, with no degradation of the SAM when sweeping the bias. Also the molecular ensemble of this LAMJ device can be analyzed by optical techniques. Finally, LAMJ devices can be fabricated within diameters up to $\sim 100 \mu\text{m}$ [47]. A weak point of such a LAMJ device, however, is that the shape of the current versus voltage, or $I(V)$, curves is partially determined by the PEDOT:PSS polymer. This makes LAMJ devices less favourable for fundamental research purposes.

1.3 Multi-molecular devices based on gold nanoparticles

An attractive method to study and explore charge transport through (functional) molecules is to make use of hybrid structures in which (gold) nanoparticles are connected by molecular bridges. The method, pioneered by Andres *et al.* [48] and explored by e.g. Schönberger and Jaeger [49-52] can be seen as a bridge between single-molecule and multi-molecular platforms. Its basic philosophy is to overcome the

long-standing problem of size mismatch between the molecules and the macroscopic electrodes by using an intermediate: (gold) nanoparticles ($\sim 10^{-8}$ m in diameter) connect between the nanoscopic (10^{-9} m) dimension of molecules and the macroscopic (10^{-7} to 10^{-3} m) dimensions of the metal electrodes (see Figure 1.2). This is done by connecting bottom-up approaches with top-down technology (lithography of the larger electrodes). Specifically, gold nanoparticles are first synthesized to the desired diameter (5-20 nm, typically). Next, they are covered by an alkanethiol shell, to prevent particle aggregation. Then, they are forced to assemble in a densely packed two-dimensional (2D) structure, on a water surface. The arrays thus formed are stamped on devices with pre-defined electrodes and can be investigated. A crucial step is yet to follow: molecular rods containing two thiol groups can be inserted between neighbouring nanoparticles. This so-called exchange step can take place spontaneously in a solution containing the molecular wires of interest. If a majority of the nanoparticle-molecule-nanoparticle junctions contain dithiolated molecular wires, these molecules will dominate the device's conductance properties.

Using molecule-metal nanoparticle arrays or networks (array will refer to a single layer; network to a few stacked molecule-nanoparticle ensembles) has various advantages. First of all, a large variety of molecular rods, including functional species, can be probed. Second, a conductance experiment will give a spatial average of single nanoparticle-molecule(s)-nanoparticle junctions probed both in series and in parallel. The sheet resistance of an array is ideally $R_{\square} = \frac{R_j}{\sqrt{3}} \approx 0.6R_j$, where R_j is the tunnel resistance of the molecule species in a nanoparticle junction [53]. Hence, results can be compared to time-dependent statistics as obtained in STM and MCBJ experiments. Third, the devices are relatively robust, lasting for between a week and a few months at room temperature. Due to the percolative nature of the devices, they are rather insensitive to defects. Finally, and perhaps most importantly, these networks allow for a range of control experiments. Whereas the signal from a single molecular junction is generally too small to be measurable by standard spectroscopic techniques, this is different for networks combining many junctions. As a result, optical spectroscopy, Raman spectroscopy, and even magnetization measurements come into play. This allows one to correlate (changes of) conductance properties to (changes of) molecular properties, thus relating directly to the key validation questions of the field, mentioned above.

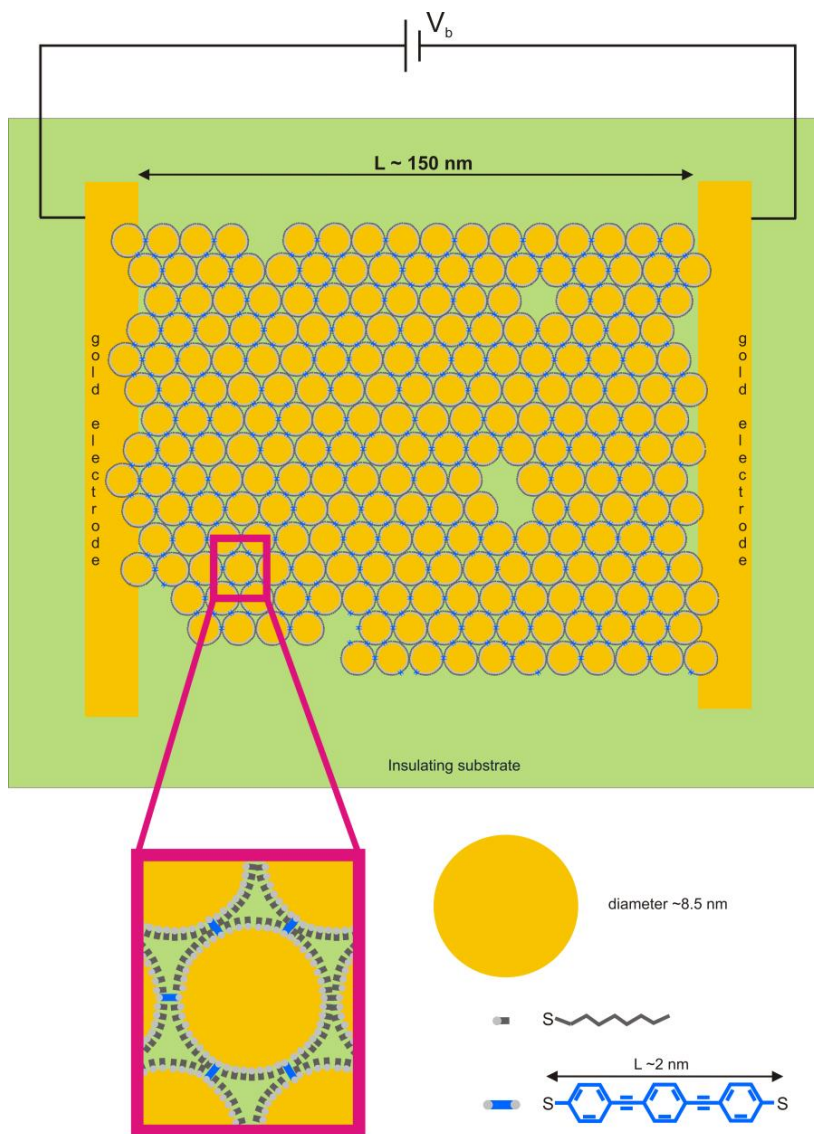


Figure 1.2: Schematic representation of a molecule-gold nanoparticle array deposited on a nanotrench device. The gold nanoparticles are encapsulated by octane(mono)thiol molecules (see gray coloured structure) to allow for self-assembly while avoiding aggregation and to tune the distance between the gold nanoparticles. Via molecular exchange, conjugated molecules (see e.g. the blue coloured bridge structure) can be inserted in between the gold nanoparticle junctions.

Vice versa, the open, 2D structure of molecule-gold nanoparticle arrays also permits molecular junctions to be addressed by external stimuli (i.e., light, pressure, magnetic field, temperature, etc.) [50, 54]. All of this makes the method very attractive to measure and benchmark (functional) molecules, specifically the spin transition molecules discussed below. Therefore, it is a key ingredient in the research presented here.

A weak point of a molecule-gold nanoparticle array connects directly to one of its advantages. At temperatures above ~ 360 K (roughly the experimental flashpoint of liquid octane(mono)thiol), the octanethiol molecules covering the nanoparticles start to decompose or detach. This leads to particle aggregation and eventually to device breakdown. When performing heating-cooling cycles, reversibility should therefore be checked. In Chapter 3, I will elaborate on this method and our work to extend it to three dimensions as well as to use different molecules to initially cover the nanoparticles, beyond alkanethiols. One of the main goals of this work, however, concerns interfacing and studying spin transition molecules in a device geometry. Next, I introduce this fascinating type of system.

1.4 Spin crossover molecules

A spin crossover (SCO) molecule is a molecule that can exhibit two different (total) spin states. Toggling between these configurations is possible via some external stimulus. This may be a temperature variation, irradiation by light or even a local electric field. Spin crossover systems have been synthesized and studied in bulk for over 80 years [55, 56]. Recently however, the research activity in this field has intensified. On the one hand, the prospect of applications has motivated chemists to increase the so-called transition temperature, the temperature at which the molecular system changes spin state, towards room temperature and above. For this, a set of ingeniously designed molecules have been synthesized [57, 58]. In parallel, there has been a trend towards nanoscopic length scales, down to the single molecules. Most of the chemical research is done on bulk powders of SCO molecules, where molecule-molecule interactions play a crucial role. Decreasing from macroscopic dimensions (bulk) down to the nanometer or even single-molecule scale could provide us with new understanding of the fundamentals of the spin transition properties. Devices based on spin transition molecules may find applications in nanoelectronics and spintronics, provided stability is somehow ensured. More generally, SCO molecules may serve as

promising molecular switches [59-62], image display [63], information storage [64, 65] and gas [66, 67] or temperature sensors [68].

However, the switching properties of SCO compounds may strongly differ at the nanoscale, as compared to bulk. In this thesis, specifically in Chapter 6, spin transition molecules will be investigated using nanoparticle networks. This allows us to measure conductance properties versus temperature, while also performing Raman spectroscopy and magnetization measurements. In the rest of this section, however, I will elaborate on the physics and chemistry behind SCO molecules. In general, these consists of a transition metal ion (e.g. Fe^{2+}) surrounded by organic ligands.

1.4.1 The metal complex

To understand what a spin crossover molecule is, we need to briefly review coordination chemistry. A coordination compound is a system in which a central metal ion is attached to a group of surrounding molecules or ions [69]. The organic molecules or ions that surround the central transition metal ion are called ligands. The ligands contain donor atoms that enable the formation of coordination bonds with the central transition metal ion. This means that both electrons involved in bond formation stem from the donor atom involved. Typically, coordination compounds need additional counterions (anions or cations) to acquire electrically neutrality. The term metal complex (or also complex) refers to both neutral coordination compounds and non-neutral coordination compounds.

The coordination number (CN) is the number of ligand donor atoms that surround the central transition metal ion in a complex. Depending on the nature of the central metal ion and its available number of p, d, or f orbitals, the coordination number can vary from 2 (linear), 4 (tetrahedral), 5 (pyramidal), 6 (octahedral) up to 12 (for lanthanides). Here I focus on the octahedral complexes, with CN equal to 6, which are typically found for d metal central ions, the so-called transition metals. For complexes based on transition metals, the distribution of the valence electrons in the available d orbitals is key to understanding their electronic, optical and magnetic behaviour. Different theoretical approaches can be used to understand the emergence of spin state switching.

1.4.2 Crystal and ligand field theory

We first use crystal field theory to explain the properties of a complex further. It is a model to describe how the coordination bonding in complexes arises from electrostatic interactions [70]. Here the coordination bonds are considered to have an “ionic” nature, i.e. there is an electrostatic attraction between the positively charged transition metal ion and the electronegative atoms of the ligands. The properties of a complex are described similarly to the properties of transition metal ions in ionic crystals.

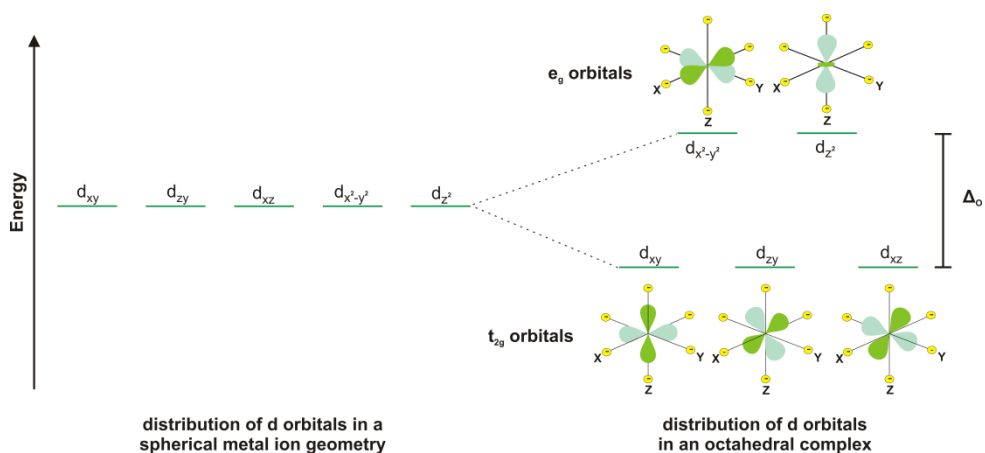


Figure 1.3: Schematic energy level diagram of the five degenerate d orbitals for a free ion (left) and in an octahedral complex (right), where the t_{2g} and e_g orbitals are split by a crystal field splitting energy Δ_o (see paragraph 1.4.2).

To understand crystal field theory of an octahedral complex, let us look at a d orbital energy level diagram (see Figure 1.3). For a metal ion in a spherically symmetric environment (such as in a free ion), there are five degenerate orbitals namely the d_{xy} , d_{xz} , d_{yz} , $d_{x^2-y^2}$ and d_z^2 . Now suppose the ligands are octahedrally closing in on a metal ion. Then the metal ion becomes subject to an electrical field from the charged atomic species on the ligand molecules. This crystal field disrupts the symmetry of a metal ion [71]. The d orbitals are repelled by the orbitals from the ligands and this gives changes in the energies of the five d orbitals. Three of the d orbitals, namely the d_{xy} , d_{xz} and d_{yz} , will adopt spatial orientations in between the charges oriented along the x, y, z axes of the ligands. The energies of these nonbonding d_{xy} , d_{xz} and d_{yz} orbitals (also called the

t_{2g} orbitals) will be lower compared to the other two antibonding d orbitals. These antibonding $d_{x^2-y^2}$ and d_z^2 orbitals (also called the e_g orbitals) will have direct repulsion with the charges of the ligand. The difference in energy between these two sets of d orbitals is called the crystal field splitting energy Δ_O . Depending on the metal ion and ligand species used to form a complex, different splitting energies arise [69, 70].

To find the spin state of a molecular complex, another competing energy scale is important: the mean spin pairing energy P . This is the energy it costs to pair two (interacting) electrons on one of the d orbitals. Now, let us consider a complex with an octahedral iron (Fe^{2+}) complex. Such a system can typically have one of two possible electron distributions of the six 3d valence electrons of the Fe^{2+} ion, corresponding to two different spin states [69, 70].

If $P \gg \Delta_O$, none of the d orbitals will be empty. One of the t_{2g} states will be doubly occupied, whereas the other four will contain one electron. Following the rules of Hund, these electrons will line up their spins. As a result, this complex will have spin quantum number $S = 2$ and it is said to be in a high-spin (HS) state (see Figure 1.4(a)) A high-spin Fe^{2+} complex behaves paramagnetically.

If $P \ll \Delta_O$, the six d-electrons of the Fe^{2+} will occupy the t_{2g} orbitals in three pairs. As a result, this complex has a total spin of $S = 0$. It is said to be in a low-spin (LS) state (see Figure 1.4(b)) and will behave like a diamagnetic complex.

We should note however, that Δ_O does not need to be the same for the molecule in its LS and HS states, somewhat complicating the picture above.

Crystal field theory is a simple and readily visualized ionic model to explain the electronic structure of complexes [70]. But crystal field theory is limited in that it only considers purely ionic bonds. Ligand field theory can be viewed as an extension of crystal field theory, combining concepts of the latter with features from molecular orbital theory. Ligand field theory incorporates the overlap between the ligand orbitals and the d orbitals of the metal ion. Also included is the delocalization of ligand and metal electrons in a complex. Nearly all the results of the crystal field theory are also valid in the ligand field theory [71].

Just like crystal field theory, ligand field theory takes into account the influence of electrostatic forces on the chemical bonding and origin of the orbital splitting of a complex. The presence of overlap will determine the ordering of the orbitals in

complexes and this scheme gives more understanding on Δ_o . To identify overlap, ligand orbitals need to be formulated into symmetrical adapted orbitals. These are then combined with the metal atomic orbitals to form molecular orbitals. Here the valence orbitals of both the ligand and metal ion are used to form symmetry adapted linear combinations (SALC). Based on empirical overlap and energy considerations an estimate can be made about the relative energies of a complex. These estimated energies will need further verification and adaptation before comparison can be made with experimental results [70].

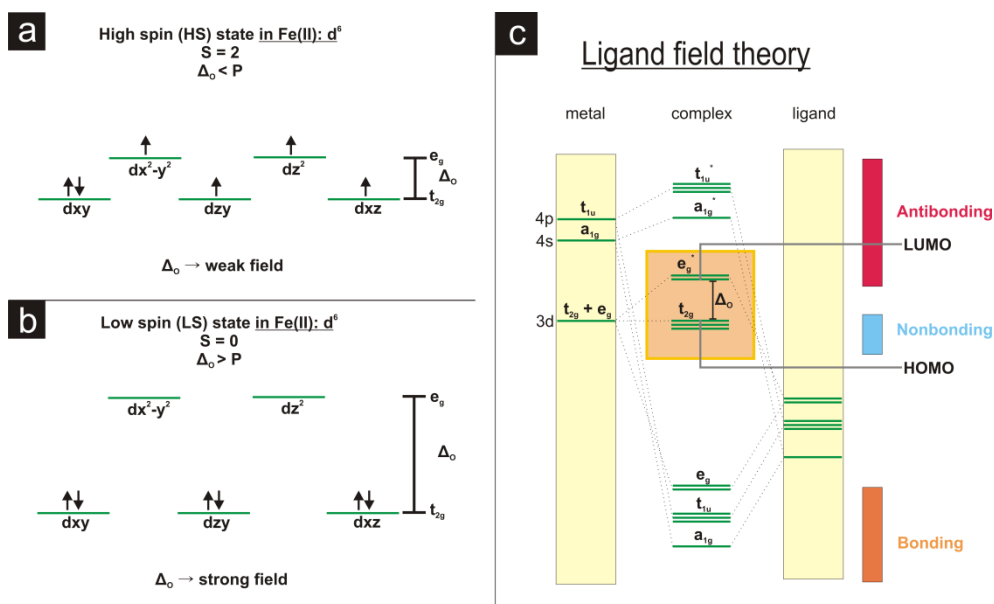


Figure 1.4: (a) Crystal field scheme of a Fe^{2+} complex in a high-spin (HS) configuration, possessing paramagnetic properties. (b) Crystal field scheme of a Fe^{2+} complex in a low-spin (LS) configuration, possessing diamagnetic properties. (c) Molecular orbital scheme of an octahedral complex according to ligand field theory (the * represents here the antibonding character). Ligand field theory allows to identify more accurately the origin and magnitude of the splitting energy Δ_o in a complex (see light orange box) compared to the crystal field theory. The ligand field theory scheme is based on σ bond overlap between the metal ion orbitals and the ligand orbitals.

From ligand field theory one learns that the molecular orbitals involved are partially confined to the metal atom. This is displayed in Figure 1.4(c), via a molecular orbital

energy level diagram. The ground-state electron configuration for a complex can be established through this diagram.

Two matters can be concluded from ligand field theory:

- The six bonding molecular orbitals are supplied by the ligands.
- The remaining n electrons of a d^n complex populate the nonbonding t_{2g} orbitals and the antibonding e_g orbitals. From that point, the crystal field theory approach is then followed.

If a ligand possesses π orbitals that may align with the σ bond along the metal-ligand axis of the complex, then both bonding and antibonding π molecular orbitals can be formed with the metal orbitals. The most crucial part of π bonding related to ligand field theory is that when ligand π orbitals are taken into account, overlap with the nonbonding t_{2g} orbitals can occur. The t_{2g} orbitals of the metal ion will become involved with the bonding of the complex and this will result into changes of the HOMO-LUMO gap [70]. Here, Δ_O can become larger or smaller, depending if the ligand species supplies π accepting orbitals or π donating orbitals, respectively. To inspect the role and influence of the ligand species with respect to Δ_O , a spectrochemical series can be constructed. This empirical ordering of ligands displays how strongly the π bonding will influence the Δ_O of a complex.

To summarize, according to ligand field theory both σ bonds and (possibly) π bonds occur in a complex. The type of ligand species influences, mainly via π bonding, the splitting energy Δ_O of a complex.

1.4.3 Spin crossover complexes

Spin crossover (SCO) molecules [55] (also called spin transition molecules [72]) are a special class of complexes that allow a transition between a low-spin (LS) and high-spin (HS) state. Typically, spin transition molecules will have $\Delta_O \approx P$, i.e. a spin transition can be described as a compromise between the correlative interactions (Hund's principle, energy scale P) and the ligand field energy scale [71]. The crossover is reached via a temperature increase (entropy driven) or by e.g. illumination.

For many decades, the iron (Fe^{2+}) ion has been the most studied metal ion in SCO bulk compounds [55, 58, 72, 73]. Also this thesis will focus on a SCO compound that contains an Fe^{2+} ion. Despite this long history, the synthesis of a Fe^{2+} SCO complex

that features a spin transition around room temperature is still both a science and an art [58].

In 2008, the research group of Mario Ruben developed a SCO molecule [72] by chemically tailoring a $[\text{Fe}(\text{AcS-BPP})_2](\text{ClO}_4)_2$ complex (where AcS-BPP denotes S-(4-{[2,6-(bipyrazol-1-yl)pyrid-4-yl]ethynyl}phenyl)ethanethioate). This metal complex is based on an iron (II) ion and two organic ligands (i.e. S-(4-{[2,6-(bipyrazol-1-yl)pyrid-4-yl]ethynyl}phenyl)ethanethioate). In Figure 1.5, the bulk powder form of this SCO complex is shown, denoted by the abbreviated formula $[\text{Fe}(\text{AcS-BPP})_2](\text{ClO}_4)_2$.

Note that the bulk $[\text{Fe}(\text{AcS-BPP})_2](\text{ClO}_4)_2$ complex contains protecting thioacetate groups to prevent oligomerization and polymerization of the bis-thiol anchoring groups on the bulk $[\text{Fe}(\text{AcS-BPP})_2](\text{ClO}_4)_2$ complex in a solution and allow access to form Au-S bonding between the gold nanoparticle and the complex [74]. After exposure to Au the bulk SCO molecule is deprotected and the composition of the SCO molecule becomes a $\text{Fe}^{2+}(\text{bis}(\text{pyrazol-1-yl})\text{pyridine})_2$ (i.e. $\text{Fe}(\text{S-BPP})_2$) complex. This $[\text{Fe}(\text{AcS-BPP})_2](\text{ClO}_4)_2$ complex can perform a spin transition via external stimuli such as temperature (T), light (λ), pressure (p) and magnetic field (H) [57, 72, 75]. In Figure 1.5 bottom, a magnetic susceptibility measurement of the bulk $[\text{Fe}(\text{AcS-BPP})_2](\text{ClO}_4)_2$ SCO compound is shown. This plot shows a rather abrupt spin transition, from a LS state at low temperatures to a HS state at high temperatures. Furthermore, it shows that the spin transition is reversible with limited thermal hysteresis. One can define $T_{1/2}$, i.e. the temperature where there is a 1:1 ratio of LS and HS molecules, when heated ($\uparrow T_{1/2}$) and cooled ($\downarrow T_{1/2}$). Both are close to room temperature for the $[\text{Fe}(\text{AcS-BPP})_2](\text{ClO}_4)_2$ complex in bulk, as $\downarrow T_{1/2} = 286$ K and $\uparrow T_{1/2} = 290$ K. During spin transition, a SCO molecule will undergo both an electronic change and a mechanical change. When going from the LS state to the HS state, the Fe-N bonds elongate a little and increase the molecular volume of the complex core. Hence, the total length of the $[\text{Fe}(\text{AcS-BPP})_2](\text{ClO}_4)_2$ SCO molecule can change slightly during a spin transition, as illustrated in Figure 1.5. Interestingly, hysteresis is very common in bulk SCO compounds. Moreover, it is seen as an important feature towards applications. Hysteresis is related to cooperativity, i.e. the ability to propagate the spin transition to neighbouring SCO molecules in a bulk SCO compound (i.e. solid crystal lattice). Via short- and long-range interactions a spin transition is elastically communicated to each SCO molecule (i.e. their metal core centres [76, 77]).

Fe(AcS-BPP)₂(ClO₄)₂ SCO complex

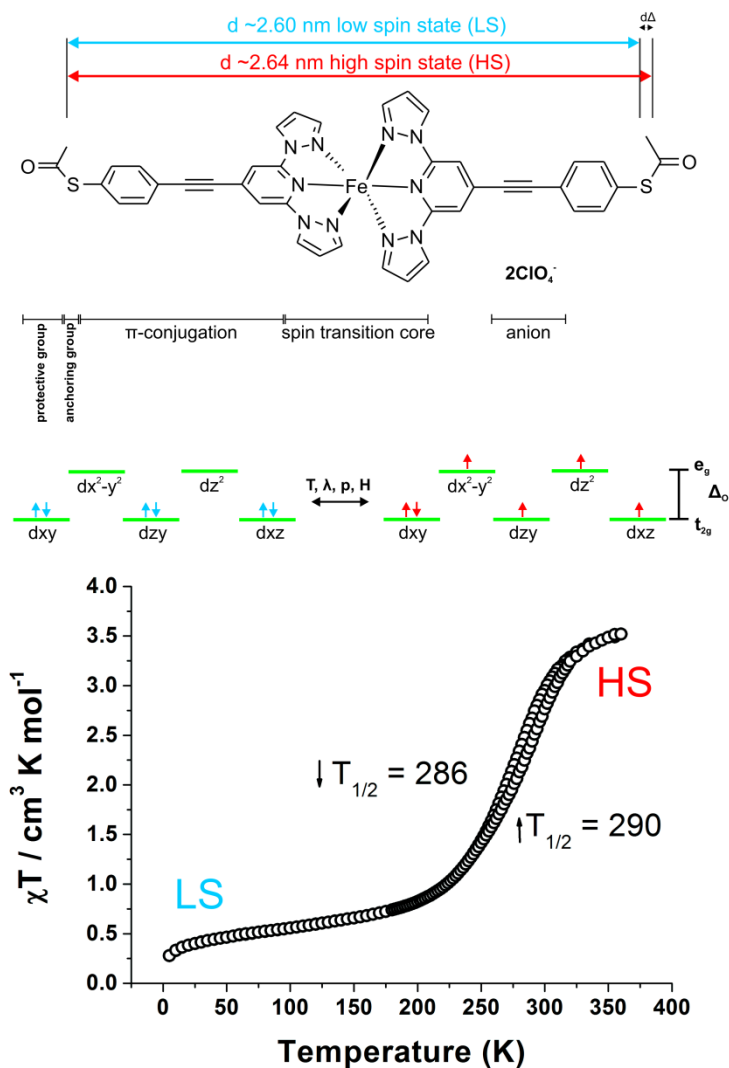


Figure 1.5: Room-temperature spin crossover $[\text{Fe}(\text{AcS-BPP})_2](\text{ClO}_4)_2$ complex. Top Figure shows the SCO molecular structure and its components. Except the electronic change also the molecular length (i.e. the spin transition core) of this complex changes very slightly during spin transition. Middle Figure shows a scheme of how the complex undergoes a spin transition. Bottom Figure shows a magnetic susceptibility plot of the bulk $[\text{Fe}(\text{AcS-BPP})_2](\text{ClO}_4)_2$ compound, indicating a reversible and stable spin transition with small thermal hysteresis, around the average transition temperature $T_{1/2} \approx 288 \text{ K}$.

A bulk SCO compound with low cooperativity, exhibits a gradual spin transition process. For a bulk SCO compound with high cooperativity, the spin transition can be more abrupt, i.e. take place within a very narrow range of temperature (~ 5 K), and thermal hysteresis can occur [55]. More generally, the transition between the LS and HS states can be abrupt, gradual, with or without hysteresis, follow a two-step transition or be incomplete [55]. In the next paragraph, we briefly go into the thermodynamics of the spin transition in bulk compound.

1.4.4 Spin transition in bulk

A spin transition can be modelled by a $x_{HS} = f(T)$ curve, where x_{HS} represents the molar fraction of HS molecular species [78]. For bulk SCO compounds this characteristic curve can be determined from magnetic measurements as function of temperature (i.e. $\chi T \propto f(T)$ plot, see Figure 1.5).

The stability of the two spin states (LS \leftrightarrow HS), is determined by the difference in Gibbs free energy (at constant pressure):

$$\Delta G = \Delta H - T\Delta S. \quad (1.1)$$

Here $\Delta G = G_{HS} - G_{LS}$. $\Delta H = H_{HS} - H_{LS}$ and $\Delta S = S_{HS} - S_{LS}$ denote the difference in enthalpy and entropy, respectively, for an assembly made of N molecules. At the temperature $T_{1/2}$ there is as much LS as HS present (disregarding hysteresis for now) so $\Delta G = 0$ and hence [78, 79]:

$$T_{1/2} = \frac{\Delta H}{\Delta S}. \quad (1.2)$$

The entropic term ΔS may be written as the sum of electronic ΔS_{el} and the vibrational ΔS_{vib} contributions:

$$\Delta S = \Delta S_{el} + S_{vib}, \quad (1.3)$$

where ΔS_{el} is related to the ratio of the electronic degeneracies g_{HS}/g_{LS} between the HS and LS states according to:

$$\Delta S_{el} = Nk_B \ln \left(\frac{g_{HS}}{g_{LS}} \right) [78]. \quad (1.4)$$

As for ΔS_{vib} , this is also positive and the vibrational disorder is more pronounced in the HS state, due to the longer metal-ligand bond lengths. In fact, ΔH and ΔS are both positive to have a finite and positive $T_{1/2}$.

A thermodynamic description of a spin transition is illustrated in Figure 1.6. At low temperatures T , the enthalpy term dominates and hence the LS state is the stable spin state species at 0 K. At the transition point, we have $G_{HS} = G_{LS}$ or $\Delta G = 0$ [78]. At high temperatures, above $T_{1/2}$, the entropic term will dominate, as shown in Figure 1.6(c). The HS state is the most stable spin state at elevated temperatures.

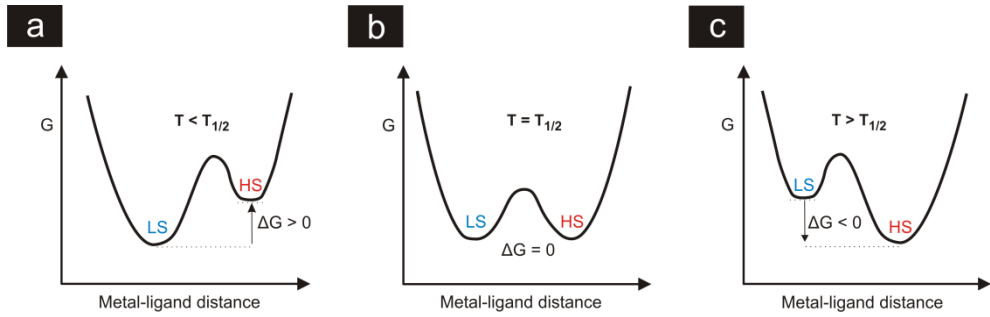


Figure 1.6. Schematic thermodynamic plots (Gibbs free energy (G) as a function of the metal-ligand distance) for a SCO bulk compound. The system changes from the LS (a) to the HS state or phase (c), as a function of temperature. At the spin transition temperature, $G_{HS} = G_{LS}$ (see (b)).

Even if there is no cooperativity, i.e. no direct intermolecular interaction in the SCO compound, one still needs to incorporate a mixing entropy term in the Gibbs free energy [78]. This mixing entropy S_{mix} represents the many ways to distribute $(x_{HS})N$ high-spin molecules and $(1-x_{HS})N$ low-spin molecules within the assembly of N molecules. It can be written as:

$$S_{mix} = -R[x_{HS} \ln(x_{HS}) + (1 - x_{HS}) \ln(1 - x_{HS})], \quad (1.5)$$

where R_B is the gas constant. Clearly, S_{mix} is maximum for $x_{HS} = 0.5$ and vanishes for $x_{HS} = 0$ and 1. The Gibbs free energy is then expressed as:

$$G = x_{HS}G_{HS} + (1 - x_{HS})G_{LS} - TS_{mix}. \quad (1.6)$$

The partial derivative of G with respect to x_{HS} gives:

$$\frac{\partial G}{\partial x} = \Delta G + RT \ln \left(\frac{x_{HS}}{1-x_{HS}} \right), \quad (1.7)$$

At any temperature and pressure, the equilibrium condition for the spin transition is defined by $\left(\frac{\partial G}{\partial x}\right)_{T,p} = 0$. Hence, we have

$$\ln \left(\frac{1-x_{HS}}{x_{HS}} \right) = \frac{\Delta G}{RT} = \frac{\Delta H}{RT} - \frac{\Delta S}{R}. \quad (1.8)$$

From which we obtain, incorporating equation 1.2:

$$x_{HS} = \frac{1}{1 + \exp \left[\frac{\Delta H}{R} \left(\frac{1}{T} - \frac{1}{T_{1/2}} \right) \right]}. \quad (1.9)$$

Equation 1.9 represents the basic macroscopic spin transition behaviour, i.e. $x_{HS} = f(T)$, of a SCO bulk compound without cooperativity. This simple theory is due to Slichter and Drickamer [80]. Note that within this model, the spin transition is never complete, even for $T \rightarrow \infty$.

1.4.5 Size effects on spin crossover molecules

It is largely an open question how the spin transition properties change when the size of a bulk SCO compound is reduced toward the nanoscale or even to single molecules. Recent studies have shown that the spin transition becomes smoother [81, 82]. Also the transition temperature can shift to lower values and hysteresis can become smaller or even vanish upon reducing the size of the SCO [81-84]. In general a decrease of the cooperativity should indeed be expected. Also the influence of a different physical-chemical environment around the nanoscale SCO needs to be considered [84]. SCO molecules are known to be sensitive to environmental conditions, such as packing, chemical and electrostatic conditions, the presence of solvent molecules, etc. [57, 75, 85-89]. Hence, for SCO complexes on the nanoscale, e.g. in molecular devices, the (research) question should be asked whether the spin transition remains and if so, if its properties change.

1.5 Motivation and outlook of this thesis

The research presented in this thesis has been performed within an European research project called INTERNET (i.e. INTERfacing single molecules via nanoparticle NETworks), funded by European Research Agency (ERA) via the NanoSci-E+ scheme.

Initially the project started with four research groups. Apart from our group at Leiden University, these were led by Bernard Doudin (Institut de Physique et Chimie des Matériaux de Strasbourg), Mario Ruben (Karlsruhe Institute of Technology) and Stefano Sanvito (Trinity College Dublin). Along the way, constructive partnerships with other research groups were formed as well, most notably with Tia Keyes (Dublin City University) and Christian Kübel (Karlsruhe Institute of Technology). The main objective of project INTERNET has been to realize and study the properties of a reliable molecular interface, specifically with the aim of investigating functional molecules. This dissertation reflects the research at Leiden and the measurements done in direct collaboration. For these, I travelled to Strasbourg, Karlsruhe and Dublin on many occasions.

Let me end this paragraph with a brief overview of the rest of this thesis.

In Chapter 2, a theoretical introduction is given in charge transport at the nanoscale and specifically in molecular junctions.

In Chapter 3, a closer look is taken at the experimental methods behind the self-assembly of molecule-gold nanoparticle arrays and networks. Furthermore several synthesis routes are explored to make new types of molecule-gold nanoparticle arrays. Besides introducing conductance experiments on these molecular devices, this chapter also describes several optical analysis methods, which can be used as control experiments. The possibility to combine several measurement techniques on one sample structure is a clear advantage of the approach taken.

In Chapter 4, the charge transport properties of gold nanoparticle networks functionalized by benchmark molecules (octanethiol molecules and conjugated dithiols) are investigated. At low temperatures, the gold nanoparticles in a molecule-gold nanoparticle network start to play their own role, displaying properties such as Coulomb blockade [90]. Charge transport becomes dominated by multiple inelastic cotunneling. By changing the molecular species in a molecule-gold nanoparticle network we study in which way the molecules themselves influence charge transport in this regime. Our work on passive molecules turns out to have an interesting consequence for molecular switches: the ratio of the on-state and off-state conductance values may be ‘artificially’ enhanced in a nanoparticle network [54].

In Chapter 5 we demonstrate the synthesis of a new type of molecule-gold nanoparticle array, where the gold nanoparticles are functionalized by S-BPP molecular species (the

half-molecules in Figure 1.5). We study the properties of these arrays, comparing them to alkanethiol-gold nanoparticle arrays.

Finally, in Chapter 6 we scrutinize the properties of $\text{Fe}(\text{S-BPP})_2$ SCO molecules in molecule-gold nanoparticle networks. We investigate if the spin functionality is preserved in such a structure and if so, how spin switching influences the conductance properties of such molecular devices.

1.6 References

1. J. C. Cuevas and E. Scheer, *Molecular Electronics: An Introduction to Theory and Experiment*, World Scientific, Singapore, **2010**.
2. S. J. van der Molen, R. Naaman, E. Scheer, J. B. Neaton, A. Nitzan, D. Natelson, N. J. Tao, H. S. J. van der Zant, M. Mayor, M. Ruben, M. Reed and M. Calame, Visions for a Molecular Future, *Nature nanotechnology*, **8**, (2013), 385-389.
3. G. E. Moore, Cramming More Components onto Integrated Circuits, *Electronics*, **38**, (1965), 114-117.
4. A. R. von Hippel, Molecular Engineering, *Science*, **123**, (1956), 315-317.
5. H. Choi and C. C. M. Mody, The Long History of Molecular Electronics: Microelectronics Origins of Nanotechnology, *Social Studies of Science*, **39**, (2009), 11-50.
6. R. P. Feynman, There's Plenty of Room at the Bottom, *Engineering and science*, **23**, (1960), 22-36.
7. B. Mann and H. Kuhn, Tunneling Through Fatty Acid Salt Monolayers, *J. Appl. Phys.* **42**, (1971), 4398-4405.
8. A. Aviram and M. Ratner, Molecular rectifiers, *Chem. Phys. Lett.*, **29**, 1974, 277-283.
9. G. Binnig, H. Rohrer, Ch. Gerber and E. Weibel, Vacuum Tunneling, *Physica B*, **109-110**, (1982), 2075-2077.
10. G. Binnig, H. Rohrer, Ch. Gerber and E. Weibel, Surface Studies by Scanning Tunneling Microscopy, *Phys. Rev. Lett.*, **49**, (1982), 57-61.
11. N. Agrait, A. L. Yeyati and J. M. van Ruitenbeek, Quantum properties of atomic-sized conductors, *Phys. Rep.*, **377**, (2003), 81-279.
12. M. A. Reed, C. Zhou, C. J. Muller, T. P. Burgin and J. M. Tour, Conductance of a Molecular Junction, *Science*, **278**, (1997), 252-254.
13. Y. Chen, G.-Y. Jung, D. A. A. Ohlberg, X. Li, D. R. Stewart, J. O. Jeppesen, K. A. Nielsen, J. F. Stoddart and R. S. Williams, Nanoscale Molecular-switch Crossbar Circuits, *Nanotechnology*, **14**, (2003), 462468.
14. J. R. Heath et al., E. A. Chandross and P. S. Weiss, More on Molecular Electronics, *Science*, **303**, (2004), 1136-1137.
15. R. F. Service, Next-generation Technology Hits an Early Midlife Crisis, *Science*, **302**, (2003), 556-559.

-
16. S. J. van der Molen and P. Liljeroth, Charge Transport Through Molecular Switches, *J. Phys.: Condens. Matter*, **22**, (2010), 133001(1-30).
 17. D. Dulić, S. J. van der Molen, T. Kudernac, H. T. Jonkman, J. J. D. de Jong, T. N. Bowden, J. van Esch, B. L. Feringa and B. J. van Wees, One-way Opto-electronic Switching of Photochromic Molecules on gold, *Phys. Rev. Lett.*, **91**, (2003), 207402(1-4).
 18. T. Miyamachi, M. Gruber, V. Davesne, M. Bowen, S. Boukari, L. Joly, F. Scheurer, G. Rogez, T. K. Yamada, P. Ohresser, E. Beaurepaire and W. Wulfhekel, Robust Spin Crossover and Memristance Across a Single Molecule, *Nat. Commun.*, **3**, (2012), 1-6.
 19. H. Song, M. A. Reed and T. Lee, Single Molecule Electronic Devices, *Adv. Mater.*, **23**, (2011), 1583-1608.
 20. R. Temirov, A. Lassise, F. B. Anders and F. S. Tautz, Kondo Effect by Controlled Cleavage of a Single-molecule Contact, *Nanotechnology*, **19**, (2008), 065401 (1-13).
 21. L. Lafferentz, F. Ample, H. Yu, S. Hecht, C. Joachim and L. Grill, Conductance of a Single Conjugated Polymer as a Continuous Function of its Length, *Science*, **323**, (2009), 1193-1197.
 22. M. F. Crommie, C. P. Lutz and D. M. Eigler, Imaging Standing Waves in a Two-dimensional Electron Gas, *Nature*, **363**, (1993), 524-527.
 23. J. Repp, G. Meyer, S. M. Stojkovic, A. Gourdon and C. Joachim, Molecules on Insulating Films: Scanning-tunneling Microscopy Imaging of Individual Molecular Orbitals, *Phys. Rev. Lett.*, **94**, (2005), 026803(1-4).
 24. H. C. Manoharan, C. P. Lutz and D. M. Eigler, Quantum Mirages Formed by Coherent Projection of Electronic Structure, *Nature*, **403**, (2000), 512-515.
 25. N. J. Tao, Electron Transport in Molecular Junctions, *Nature Nanotech.*, **1**, (2006), 173-181.
 26. L. Venkataraman, J. E. Klare, I. W. Tam, C. Nuckolls, M. S. Hybertsen and M. L. Steigerwald, Single-molecule Circuits with Well-defined Molecular Conductance, *Nano Letters*, **6**, (2006), 458-462.
 27. R. L. McCarley, D. J. Dunaway and R. J. Willicut, Mobility of the Alkanethiol-Gold (111) Interface Studied by Scanning Probe Microscopy, *Langmuir*, **9**, (1993), 2775-2777.
 28. J. Moreland and J. W. Ekin, Electron Tunneling Experiments Using NbSn "Break" Junctions, *J. Appl. Phys.*, **58**, (1985), 3888-3895.
 29. C. J. Muller, J. M. van Ruitenbeek and L. J. de Jongh, Conductance and Supercurrent Discontinuities in Atomic Scale Metallic Constrictions of Variable Width., *Phys. Rev. Lett.*, **69**, (1992), 140-143.
 30. N. Agrait, A. Levy Yeyati and J. M. van Ruitenbeek, Quantum Properties of Atomic-sized Conductors., *Physics Reports*, **377**, (2003), 81-279.
 31. S. A. G. Vrouwe, E. van der Giessen, S. J. van der Molen, D. Dulić and B. J. van Wees, Mechanics of Lithographically Defined Break Junctions, *Phys. Rev. B*, **71**, (2005), 035313(1-7).
 32. M. A. Reed, C. Zhou, C. J. Muller, T. P. Burgin and J. M. Tour, Conductance of a Molecular Junction, *Science*, **278**, (1997), 252-254.

33. H. Park, A. K. L. Lim, A. P. Alivisatos, J. Park and P. L. McEuen, Fabrication of Metallic Electrodes with Nanometer Separation by Electromigration, *Appl. Phys. Lett.*, **75**, (1999), 301-303.
34. J. Park, A. N. Pasupathy, J. I. Goldsmith, C. Chang, Y. Yaish, J. R. Petta, M. Rinkoski, J. P. Sethna, H. D. Abruña, P. L. McEuen and D. C. Ralph, Coulomb Blockade and the Kondo Effect in Single-atom Transistors, *Nature*, **417**, (2002), 722-725.
35. Y. Selzer, L. Cai, M. A. Cabassi, Y. Yao, J. M. Tour, T. S. Mayer and D. L. Allara, Effect of Local Environment on Molecular Conduction: Isolated Molecule versus Self-assembled Monolayer, *Nano Lett.*, **5**, (2005), 61-65.
36. W. J. Liang, M. P. Shores, M. Bockrath, J. R. Long and H. Park, Kondo Resonance in a Single-molecule Transistor, *Nature*, **417**, (2002), 725-729.
37. M. L. Trouwborst, S. J. van der Molen and B. J. van Wees, The Role of Joule Heating in the Formation of Nanogaps by Electromigration, *J. Appl. Phys.*, **99**, (2006), 114316(1-7).
38. H. B. Heersche, Z. de Groot, J. A. Folk, L. P. Kouwenhoven, H. S. J. van der Zant, A. A. Houck, J. Labaziewicz and I. L. Chuang, Kondo Effect in the Presence of Magnetic Impurities, *Phys. Rev. Lett.*, **96**, (2006), 017205(1-4).
39. A. A. Houck, J. Labaziewicz, E. K. Chan, J. A. Folk and I. L. Chuang, Kondo Effect in Electromigrated Gold Break Junctions, *Nano Lett.*, **5**, (2005), 1685-1688.
40. D. J. Wold and C. D. Frisbie, Formation of Metal-Molecule-Metal Tunnel Junctions: Microcontacts to Alkanethiol Monolayers with a Conducting AFM Tip, *J. Am. Chem. Soc.*, **122**, (2000), 2970-2971.
41. D. J. Wold and C. D. Frisbie, Fabrication and Characterization of Metal-Molecule-Metal Junctions by Conducting Probe Atomic Force Microscopy, *J. Am. Chem. Soc.*, **123**, (2001), 5549-5556.
42. J. M. Beebe, V. B. Engelkes, L. L. Miller and C. D. Frisbie, Contact Resistance in Metal-Molecule-Metal Junctions based on aliphatic SAMs: Effects of Surface Linker and Metal Work Function, *J. Am. Chem. Soc.*, **124**, (2002), 11268-11269.
43. G. Wang, T. W. Kim, G. Jo and T. Lee, Enhancement of Field Emission Transport by Molecular Tilt Configuration in Metal-Molecule-Metal Junctions, *J. Am. Chem. Soc.*, **131**, (2009), 5980-5985.
44. C. M. Guédon, H. Valkenier, T. Markussen, K. S. Thygesen, J. C. Hummelen, and S. J. van der Molen, Observation of Quantum Interference in Molecular Charge Transport, *Nature Nanotechnology*, **7**, (2012), 305-309.
45. D. B. Mitzi, L. L. Kosbar, C. E. Murray, M. Copel and A. Afzali, High-mobility Ultrathin Semiconducting Films prepared by Spin Coating, *Nature*, **428**, (2004), 299-303.
46. K.-A. Son, H. I. Kim and J. E. Houston, Role of Stress on Charge Transfer through Self-assembled Alkanethiol Monolayers on Au, *Phys. Rev. Lett.*, **86**, (2001), 5357-5360.
47. H. B. Akkerman, P. W. M. Blom, D. M. de Leeuw and B. de Boer, Towards Molecular Electronics with Large-area Molecular Junctions, *Nature*, **441**, (2006), 69-72.
48. R. P. Andres, J. D. Bielefeld, J. I. Henderson, D. B. Janes, V. R. Kolagunta, C. P. Kubiak, W. J. Mahoney and R. G. Osifchin, Self-assembly of a Two-dimensional

-
- Superlattice of Molecularly Linked Metal Clusters, *Science*, **273**, (1996), 1690-1693.
49. J. Liao, L. Bernard, M. Langer, C. Schöenberger and M. Calame, Reversible Formation of Molecular Junctions in 2D Nanoparticle Arrays, *Adv. Mater.*, **18**, (2006), 2444-2447.
50. L. Bernard, Y. Kamdzhilov, M. Calame, S. J. van der Molen, J. Liao and C. Schöenberger, Spectroscopy of Molecular Junction Obtained by Place Exchange in 2D Nanoparticle Arrays, *J. Phys. Chem. C*, **111**, (2007), 18445-18450.
51. X. M. Lin, H. M. Jaeger, C. M. Sorensen and K. J. Klabunde, Formation of Long-range-Ordered Nanocrystal Superlattices on Silicon Nitride Substrates, *J. Phys. Chem. B*, **105**, (2001), 3353-3357.
52. T. P. Bigioni, X. M. Lin, T. T. Nguyen, E. I. Corwin, T. A. Witten and H. M. Jaeger, Kinetically Driven Self Assembly of Highly Ordered Nanoparticle Monolayers, *Nature Materials*, **5**, (2006), 265-270.
53. C. M. Guédon, J. Zonneveld, H. Valkenier, J. C. Hummelen, S. J. van der Molen, Controlling the Interparticle Distance in a 2D Molecule-nanoparticle Network, *Nanotechnology*, **22**, (2011), 125205(1-5).
54. S. J. van der Molen, J. Liao, T. Kudernac, J. S. Agustsson, L. Bernard, M. Calame, B. J. van Wees, B. L. Feringa and C. Schöenberger, Light-controlled Conductance Switching of Ordered Metal-Molecule-Metal Devices, *Nano Letters*, **9**, (2009), 76-80.
55. P. Gütllich, Y. Garcia and H. A. Goodwin, Spin Crossover Phenomena in Fe(II) Complexes, *Chem. Soc. Rev.*, **29**, (2000), 419-427.
56. P. Gütllich and A. Hauser, Thermal and Light-induced Spin Crossover in Iron(II) Complexes, *Coord. Chem. Rev.*, **97**, (1990), 1-22.
57. M. Cavallini, I. Bergenti, S. Milita, J. C. Kengne, D. Gentili, G. Ruani, I. Šalitroš, V. Meded and M. Ruben, Thin Deposits and Patterning of Room-Temperature-Switchable One-dimensional Spin-crossover Compounds, *Langmuir*, **27**, (2011), 4076-4081.
58. Z. Arcis-Castillo, S. Zheng, M. A. Siegler, O. Roubeau, S. Bedoui and S. Bonnet, Tuning the Transition Temperature and Cooperativity of Bapbpy-based Mononuclear Spin-crossover Compounds: Interplay between Molecular and Crystal Engineering, *Chem. Eur. J.*, **17**, (2011), 14826-14836.
59. O. Kahn and C. Jay Martinez, Spin-transition Polymers: From Molecular Materials Toward Memory Devices, *Science*, **279**, (1998), 44-48.
60. J.-F. Létard, P. Guionneau and L. Goux-Capes, Towards Spin Crossover Applications, *Top. Curr. Chem.*, **235**, (2004), 221-249.
61. A. Bousseksou, G. Molnár and G. Matouzenko, Switching of Molecular Spin States in Inorganic Complexes by Temperature, Pressure, Magnetic Field and Light: Towards Molecular Devices, *Eur. J. Inorg. Chem.*, **2004**, (2004), 4353-4369.
62. P. Gamez, J. S. Costa, M. Quesada and G. Aromí, Iron Spin-crossover Compounds: From Fundamental Studies to Practical Applications, *Dalton Trans.*, **38**, (2009), 7845-7853.
63. J.-F. Létard, N. Daro and S. Auffret in *Spin Transition Materials*, patent US 2010/0178511, **2010**.

64. M. Cavallini, I. Bergenti, S. Milita, G. Ruani, I. Šalitraš, Z. R. Qu, R. Chandrasekar and M. Ruben, Micro- and Nanopatterning of Spin-transition Compounds into Logical Structures, *Angew. Chem.*, **120**, (2008), 8724-8728.
65. M. S. Alam, M. Stocker, K. Gieb, P. Müller, M. Haryono, K. Student and A. Grohmann, Spin-state Patterns in Surface-grafted Beads of Iron(II) Complexes, *Angew. Chem. Int. Ed.*, **49**, (2010), 1159-1163.
66. M. Ohba, K. Yoneda, G. Agustí, M. C. Muñoz, A. B. Gaspar, J. A. Real, M. Yamasaki, H. Ando, Y. Nakao, S. Sakaki and S. Kitagawa, Bidirectional Chemo-switching of Spin State in a Microporous Framework, *Angew. Chem.*, **121**, (2009), 4861-4865.
67. P. D. Southon, L. Liu, E. A. Fellows, D. J. Price, G. J. Halder, K. W. Chapman, B. Moubaraki, K. S. Murray, J. F. Létard and C. J. Kepert, Dynamic Interplay between Spin-crossover and Host-guest Function in a Nanoporous Metal-organic Framework Material, *J. Am. Chem. Soc.*, **131**, (2009), 10998-11009.
68. L. Salmon, G. Molnár, D. Zitouni, C. Quintero, C. Bergaud, J. C. Micheau and A. Bousseksou, A Novel Approach for Fluorescent Thermometry and Thermal Imaging Purposes Using Spin Crossover Nanoparticles, *J. Mater. Chem.*, **20**, (2010), 5499-5503.
69. J. McMurry and R. C. Fay, *Chemistry*, Prentice Hall, New Jersey, **2001**.
70. D. F. Shiver and P. W. Atkins, *Inorganic chemistry*, Oxford university press, Oxford, **1999**.
71. C. J. Ballhausen, *Introduction to ligand field theory*, McGraw-Hill, New York, **1962**.
72. R. Chandrasekar, F. Schramm, O. Fuhr and M. Ruben, An Iron(II) Spin-transition Compound with Thiol Anchoring Groups, *Eur. J. Inorg. Chem.*, **17**, (2008), 2649-2653.
73. S. Brooker and J. A. Kitchen, Nano-magnetic Materials: Spin Crossover Compounds vs. Single Molecule Magnets vs. Single Chain Magnets, *Dalton Trans.*, **36**, (2009), 7331-7340.
74. H. Valkenier, E. H. Huisman, P. A. van Hal, D. M. de Leeuw, R. C. Chiechi and J. C. Hummelen, Formation of High-quality Self-assembled Monolayers of Conjugated Dithiols on Gold: Base Matters, *J. Am. Chem. Soc.*, **133**, (2011), 4930-4939.
75. I. Šalitraš, O. Fuhr, A. Eichhöfer, R. Kruk, J. Pavlik, L. Dlháň, R. Boča and M. Ruben, The Interplay of Iron(II) Spin Transition and Polymorphism, *Dalton Trans.*, **41**, (2012), 5163-5171.
76. H. Spiering, T. Kohlhaas, H. Romstedt, A. Hauser, C. Bruns-Yilmaz, J. Kusz and P. Gütllich, Correlations of the Distribution of Spin States in Spin Crossover Compounds, *Coord. Chem. Rev.*, **192**, (1999), 629-647.
77. J. A. Real, A. B. Gaspar and M. C. Munoz, Thermal, Pressure and Light Switchable Spin-crossover Materials, *Dalton Trans.*, (2005), 2062-2079.
78. O. Kahn, *Molecular Magnetism*, VCH: New York, **1993**.
79. A. Bousseksou, J. J. McGarvey, F. Varret, J. A. Real, J.-P. Tuchagues, A. C. Dennis and M. L. Boillot, Raman Spectroscopy of the High- and Low-spin States of the Spin Crossover Complex Fe(phen)₂(NCS)₂: An Initial Approach to Estimation of Vibrational Contributions to the Associated Entropy Change, *Chemical Physics Letters*, **318**, (2000), 409-416.

-
80. C. P. Slichter and H. G. Drickamer, Pressure-induced Electronic Changes in Compounds of Iron, *J. Chem. Phys.*, **56**, (1972), 2142-2160.
81. M. Mikolasek, G. Félix, W. Nicolazzi, G. Molár, L. Salmon and A. Bousseksou, Finite Size Effects in Molecular Spin Crossover Materials, *New J. Chem.*, **38**, (2014), 1834-1839.
82. J. Larionova, L. Salmon, Y. Guari, A. Tokarev, K. Molvinger, G. Molár and A. Bousseksou, Towards the Ultimate Size Limit of the Memory Effect in Spin-crossover Solids, *Angew. Chem. Int. Ed.*, **47**, (2008), 8236-8240.
83. F. Volatron, L. Catala, E. Riviere, A. Gloter, O. Stephan and T. Mallah, Spin-crossover Coordination Nanoparticles, *Inorg. Chem.*, **47**, (2008), 6584-6586.
84. A. Bousseksou, G. Molnar, L. Salmon and W. Nicolazzi, Molecular Spin Crossover Phenomenon: Recent Achievements and Prospects, *Chem. Soc. Rev.*, **40**, (2011), 3313-3335.
85. S. Sanvito, Molecular Spintronics, *Chem. Soc. Rev.*, **40**, (2011), 3336-3355.
86. J. Olguin and S. Brooker, Spin Crossover Active Iron(II) Complexes of Selected Pyrazole-Pyridine Pyrazine Ligands, *Coordination Chemistry Reviews*, **255**, (2011), 203-240.
87. M. G. Cowan, J. Olguín, S. Narayanaswamy, J. L. Tallon and S. Brooker, Reversible Switching of a Cobalt Complex by Thermal, Pressure and Electrochemical Stimuli: Abrupt, Complete, Hysteretic Spin Crossover, *J. Am. Chem. Soc.*, **134**, (2012), 2892-2894.
88. M. Yamada, H. Hagiwara, H. Torigoe, N. Matsumoto, M. Kojima, F. Dahan, J.-P. Tuchagues, N. Re, and S. Iijima, A Variety of Spin-crossover Behaviours Depending on the Counter Anion: Two-dimensional Complexes Constructed by NH...Cl Hydrogen Bonds, $[\text{Fe}^{\text{II}}\text{H}_3\text{L}^{\text{Me}}]\text{Cl}\cdot\text{X}$ ($\text{X} = \text{PF}_6^-$, AsF_6^- , SbF_6^- , CF_3SO_3^- ; $\text{H}^3\text{L}^{\text{Me}} = \text{Tris}[2-[(2\text{-methylimidazol-4-yl)methylidene}]\text{amino}]\text{ethyl}]\text{amine}$), *Chem. Eur. J.*, **12**, (2006), 4536-4549.
89. I. Šalitroš, N. T. Madhu, R. Boča, J. Pavlik and M. Ruben, Room-temperature Spin-transition Iron Compounds, *Monatsh. Chem.*, **140**, (2009), 695-733.
90. M. A. Mangold, M. Calame, M. Mayor and A. W. Holleitner, Negative Differential Photoconductance in Gold Nanoparticle Arrays in the Coulomb Blockade Regime, *ACS Nano*, **6**, (2012), 4181-4189.

2

Charge transport in molecular systems

In this Chapter, a basic description of the conductance properties of molecular junctions is given. First, I briefly introduce charge transport at low length scales, leading to the concept that conductance can be described in terms of electron wave transmission. Next, the transmission function $T(E)$ of a molecular junction and its relation to the molecular orbital structure is discussed, specifically for spin transition compounds.

2.1 Charge transport on the macroscopic scale

To appreciate molecular charge transport as a quantum phenomenon, let us start on the macroscopic scale. The classical Ohm's Law states that the current I , running through a macroscopic conductor, is linearly related to the applied voltage bias V via $I = V/R$. The proportionality constant between the two is the resistance R . This simple law holds for metal wires within the classical Drude picture. Here, the charge carriers (electrons) are seen as small diffusing particles scattering off defects and phonons in an atomic lattice. This gives rise to a mean free path, l_e and a finite conductance $G = 1/R$. The question naturally arises what happens to the conductance if the conducting wire is reduced to length scales shorter than the mean free path.

2.2 Charge transport at reduced length scales

Let us next consider a junction for which the mean free path exceeds the length of the 'wire' L . Moreover, we will consider that $L < l_e, l_\phi$, where l_ϕ is the phase coherence length. In that case, the wavelike properties (phase) of the electrons become relevant and the conductance needs to be described from a quantum mechanics perspective. The 'wire' in this case could be a single gold atom (diameter $\sim 2.5 \text{ \AA}$) or a molecule (typically a few nanometers in length) contacted by two electrodes. However, it may also be a narrow constriction (quantum point contact) defined in a two-dimensional electron gas [1, 2].

If there is virtually no scattering within the wire, the conductance will only be limited by the constriction itself. Sharvin [3, 4] approximated this problem in a semi-classical way, assuming $\lambda_F \ll L \ll l_e, l_\phi$, where λ_F is the Fermi wavelength. This case is comparable to that of a diluted gas flowing through an opening of radius r under a slight pressure difference between the chambers left and right of the constriction. When the potential difference is eV , the electrons will change their velocity by $\Delta v = \pm eV/p_F$ when passing the opening. (Here $p_F = \hbar k_F = h/\lambda_F$ is the Fermi momentum, h is Planck's constant and $\hbar = h/2\pi$). Now, the net current will be $I = ne\Delta v S$, where $S = \pi r^2$ is the area of the orifice. Taking into account Fermi-Dirac statistics for the electron density n , the conductance for a circular ballistic point contact becomes:

$$G \approx \frac{2e^2}{h} \left(\frac{\pi r}{\lambda_F} \right)^2 = \frac{2e^2}{h} \left(\frac{k_F r}{2} \right)^2. \quad (2.1)$$

Note that the conductance found is independent of the length of the wire, as expected for ballistic transport. It is only determined by the electron density (via p_F) and the orifice's radius r . Interestingly, the constant $G_0 = 2e^2/h = (12.9 \text{ k}\Omega)^{-1}$ emerged in this equation. Often denoted the quantum of conductance, it will generally appear in equations describing quantum charge transport.

The Sharvin approach is semi-classical and will break down as the width of the constriction approaches the electron wavelength. To describe charge transport in a fully quantum mechanical way, we follow R. Landauer [5]. He was the first to realize that electrical conductance can be described in terms of transmission and reflection probabilities of electron waves. To appreciate this, let us again assume a constriction in a metal conductor (with length L and width W), contacted by two electrodes (see Figure 2.1(a)). The lateral confinement, will only allow for a discrete number of transverse states with energy below the Fermi level of the conduction electrons in the leads. Intuitively these eigenstates or modes can be seen as those for which a transverse standing wave is formed, i.e. they have $i\lambda/2 = W$, where i is an integer and λ is the electron wavelength. Landauer realized that each of these states gives rise to a so-called conductance channel. Incoming electrons coupling into a state i will hence be transmitted with a certain probability T_i . The maximum transmission equals 1 (no reflection), which gives rise to a conductance of exactly $G_0 = 2e^2/h$ (assuming spin degeneracy).

More generally, the conductance is obtained by summing up the transmission values connected to all N conductance channels in the scatterer, i.e.

$$G = \frac{2e^2}{h} \sum_{i=1}^N T_i, \quad (2.2)$$

where $0 \leq T_i \leq 1$ denote the transmission values of each of the N channels.

Interestingly, this formula also holds if an elastic scatterer is present in the constriction (see Figure 2.1(b)). In that case, a scattering matrix is used to connect outgoing states and ingoing states phase coherently [4, 6]. This matrix can hence be written in this form:

$$\hat{S} = \begin{pmatrix} r & t' \\ t & r' \end{pmatrix}, \quad (2.3)$$

where t and t' represent the transmission amplitudes to the right and left electrodes respectively. Similarly, r and r' represent the reflection amplitudes toward the left and

right electrodes respectively. As a result of conservation of current, $tt^\dagger + rr^\dagger = t^\dagger t + r^\dagger r$. Now, the eigenvalues of tt^\dagger correspond to the transmission probabilities T_i in equation 2.2.

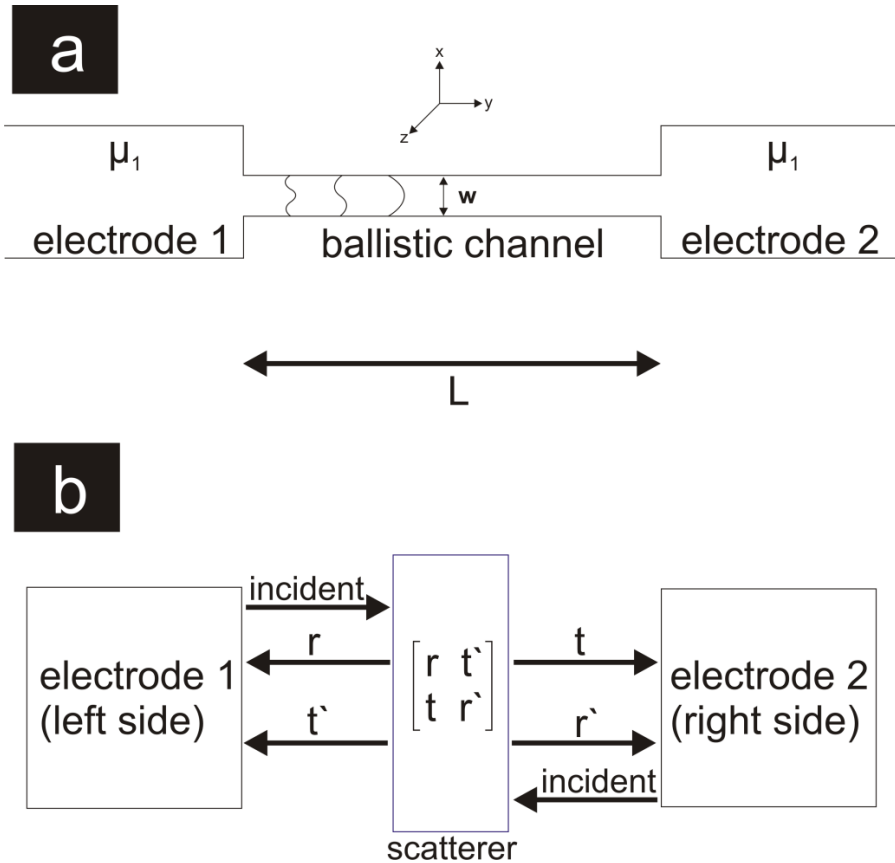


Figure 2.1: (a) Schematic representation of a ballistic channel of length L , width W and height H . The electrons travel through this narrowing channel while they are confined in the y - and z - directions. Here, only transversal wavelengths are allowed with $\lambda_x = 2W/i$ and $\lambda_z = 2H/j$ (here i, j are integers). The channel separates the two electrodes with electrochemical potentials μ_1 and μ_2 . (b) Schematic representation of the transmission formalism, where the channel is assumed to be connected to the electrodes. Here, the channel can be viewed as a quantum wire with multiple subbands. The one-channel scatterer can be defined by a S-matrix that relates the incoming and outgoing amplitudes. The presence of a scatterer in one transverse channel gives rise to transmission and reflection eigenstates.

Experimentally, conductance quantization was discovered using constrictions in two-dimensional electron gases. As the constriction was gradually closed (using negatively polarized side gates), the number of transmission channels decreased discretely and hence the conductance went down stepwise. Such experiments formed the first clear proof of the Landauer formula in equation 2.2 [1, 2, 7].

2.3 Charge transport through a molecular junction

After reviewing the charge transport properties of a nanoscopic metal conductor, let us focus on charge transport through a molecular junction. Here, two metal electrodes called the source and the drain (also called contacts or reservoirs) are connected by a molecule with a specific length L . Charge transport through such a device is dominated by the molecular energy levels, by their coupling to the reservoirs and, in some regime, by the charging energy E_C of the molecule (if coupling is weak). In general, the energy level separation for organic molecules is much larger than the thermal energy $k_B T$, even at room temperature, emphasizing the need to describe molecular charge transport as a form of quantum transport.

For a free molecule, the energy level (eigenvalues connected to the molecular orbitals) are discrete and well-defined. This can be understood within the Heisenberg uncertainty relations. Electrons have no way to hop off the molecule, i.e. the residence time τ is very high, and as a result the uncertainty in the energy of a level is very small. This changes once a molecule is coupled to electrodes. In that case, electrons can coherently move in and out of the molecule, decreasing τ and hence leading to a significant uncertainty of the energy level value. This is referred to as level broadening. Note that this is the case even with no bias present ($V_b = 0$). Level broadening plays an important role in charge transport, as we shall see below. Note that in a more chemical picture, level broadening can be understood in terms of hybridization between a molecular level and the bands in the metal electrodes.

To describe transport, we next need the electron distribution in the electrodes. It is given by the Fermi-Dirac function:

$$f_0(E - \mu) = \frac{1}{1 + e^{\frac{E - \mu}{k_B T}}}, \quad (2.4)$$

where μ denotes the electrochemical potential at an electrode. At 0 K, the states below μ are occupied, so $f_0 = 1$, whereas bands with energy above μ are empty, i.e. the

distribution is a step function. But at room temperature ($k_B T \approx 25$ meV) the distribution is smeared out around μ and $0 \leq f_0 \leq 1$ [8, 9].

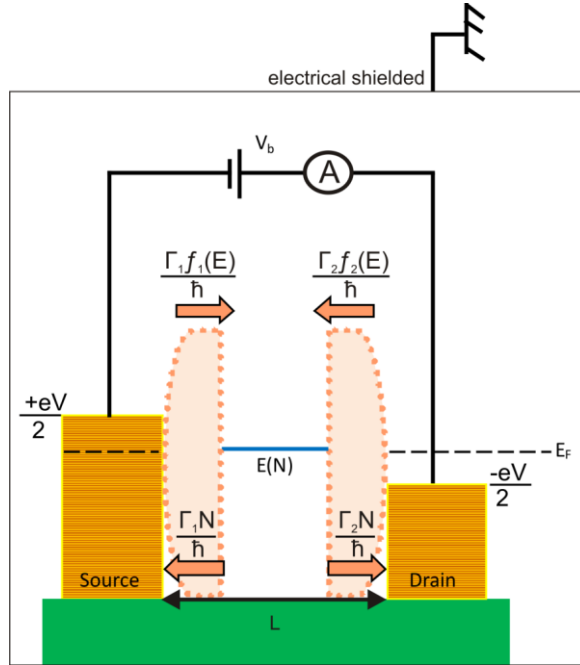


Figure 2.2: Scheme of the transfer of electrons through a molecular junction connected to the source and the drain. The molecular junction considered has a sharp energy level and symmetric coupling to the leads. The orange arrows display the net flux of electrons in and out of a one-level molecular channel.

By applying a bias V_b between the source and drain metal electrodes, the electrochemical potentials, μ_1 and μ_2 respectively, will differ by:

$$\mu_1 - \mu_2 = eV_b. \quad (2.5)$$

Now, there can be a net electron flow towards the anode. However, electrons can only flow from an occupied energy level in one electrode to an unoccupied state in the other contact, via a broadened molecular level. If coupling to the electrodes is relatively strong, electron waves will be delocalized over the junction and charge transport can be considered coherent. In the case that the metal Fermi levels line up with a molecular

level, one speaks of resonant charge transport. In that regime, transmission can be near unity. More generally, however, transport is via the tails of the broadened molecular energy levels. This is referred to as off-resonant transport. Clearly, this calls for an extension of Landauer's formula in order to include a continuous energy dependence of the transmission.

To do so, let us consider level broadening in more detail. Following Figure 2.2, we denote Γ_1/\hbar and Γ_2/\hbar as the rate constants from which an electron on energy level $E(N)$ will move in and out of the source and the drain electrodes respectively. Hence, $\Gamma_{1,2}$ has the dimension of energy. Broadening gives rise to a Lorentzian density of states (DOS) for a level at energy ε [9]

$$D_\varepsilon(E) = \frac{\Gamma/2\pi}{(E-\varepsilon)^2 + (\Gamma/2)^2}. \quad (2.6)$$

Here, $\Gamma = \Gamma_1 + \Gamma_2$, i.e. the level broadening is due to coupling to both electrodes (see Figure 2.3). Now, the current flowing through the junction is given by integrating over all possible electron energies, incorporating the DOS and the coupling factors, i.e.:

$$I = \frac{2e}{\hbar} \int_{-\infty}^{+\infty} D_\varepsilon(E) \frac{\Gamma_1\Gamma_2}{\Gamma} [f_1(E) - f_2(E)] dE. \quad (2.7)$$

This incorporates a spin degeneracy in the energy levels, giving rise to the prefactor 2. At 0 K, then $f_1(E) - f_2(E) = 1$ for $\mu_1 > E > \mu_2$, which gives:

$$I_{max} = \frac{2e}{\hbar} \frac{\Gamma_1\Gamma_2}{\Gamma} \int_{\mu_2}^{\mu_1} D_\varepsilon(E) dE, \quad (2.8)$$

where again $\mu_1 - \mu_2 = eV_b$.

For resonant tunneling, the energy level ε will be between μ_1 and μ_2 , even at low-bias. Hence, a maximum conductance will be obtained for symmetric coupling (i.e. $\Gamma_1 = \Gamma_2$):

$$G \equiv \frac{I}{V_b} = \frac{2e^2}{h} \frac{4\Gamma_1\Gamma_2}{(\Gamma_1+\Gamma_2)^2} = \frac{2e^2}{h} = G_0. \quad (2.9)$$

Having noted that the maximum conductance value for a molecular junction is the quantum of conductance, we can extend to the general case. Let us therefore define a so-called transmission function $T(E)$, related to the DOS via $D_\varepsilon(E) \frac{\Gamma_1\Gamma_2}{\Gamma_1+\Gamma_2} = \frac{1}{2\pi} \bar{T}(E)$, (at steady state conditions). With this identification, we find the so-called extended or energy-dependent Landauer formula. It describes transport in terms of transmission, summing over all possible electron energies:

$$I = \frac{2e}{h} \int_{-\infty}^{+\infty} \bar{T}(E) [f_1(E) - f_2(E)] dE. \quad (2.10)$$

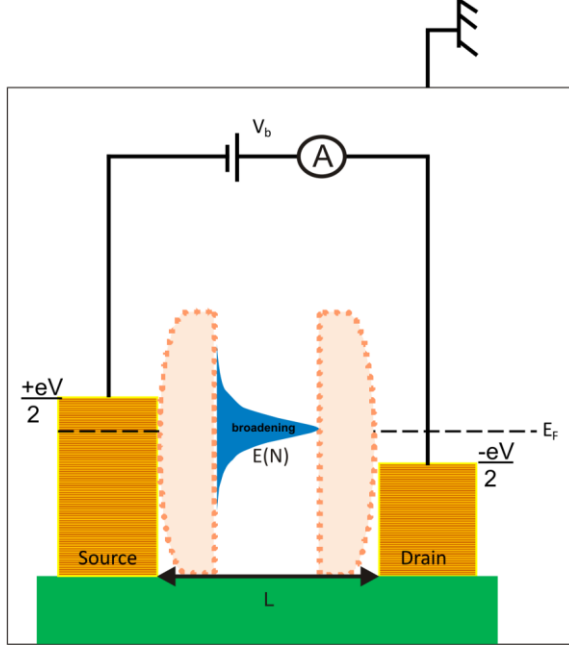


Figure 2.3: Schematic level diagram for a molecule coupled to two electrodes. In this case, the molecular level depicted is close to the electrodes' Fermi level. It broadens to a Lorentzian due to the electronic coupling to the leads. When a voltage bias V is applied, transport is described by the energy-dependent Landauer formula (see equation 2.10). In the case displayed, we have near-resonant transport.

In words, the transmission function denotes the probability [10] of electrons with a certain energy E to be transmitted through a molecular junction.

Finally, we consider the value of the potential on the molecule itself. This is determined by capacitive coupling and is given by [9]:

$$U_C = \frac{C_D}{C_E} (-eV_b), \quad (2.11)$$

assuming there is no further potential drop within the molecule. Here C_E is the total capacitance, the sum of the capacitance to the source and the drain ($C_E = C_S + C_D$). If electrostatic coupling is symmetric, the voltage drop from the left electrode to the

molecule will equal the voltage drop from the molecule to the right electrode. In that case, the electrostatic coupling parameter η has a value $\eta = 1/2$, while in general $0 \leq \eta \leq 1$. Asymmetric electrostatic coupling will generally lead to asymmetric $I(V)$ -curves, unless the transmission function is perfectly symmetric around the electrodes Fermi level. Note that electrostatic coupling should not be confused with electronic (overlap) coupling, as denoted by $\Gamma_{1,2}$. There is at best a qualitative relationship.

The transmission function can be calculated by various means, ranging from a simple tight binding approach to methods based on Density Function Theory (DFT) and non-equilibrium Green's function techniques (NEGF).

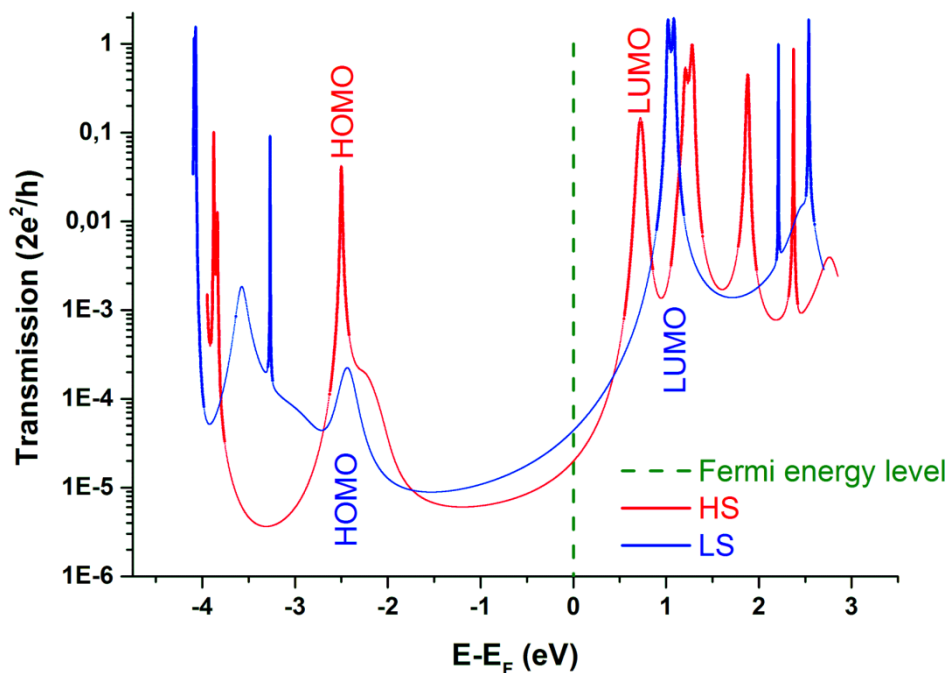


Figure 2.4: Transmission plot of a single spin crossover $\text{Fe}(\text{S-BPP})_2$ molecule coupled to gold leads [11]. The low-spin (LS) and high-spin (HS) transmission of this SCO is simulated by NEGF using B3LYP as XC-functional (calculation by Dr. V. Meded; see Chapter 6 for details).

Figure 2.4 shows the transmission function of both the low-spin and high-spin varieties of the spin crossover molecule introduced in Chapter 1 (see Figure 1.5). Note that the Fermi level of the electrodes is defined to be at 0 eV. Unfortunately, it is difficult to

independently determine the precise position of E_F for a molecular junction. The peaked nature of $T(E)$ is clearly related to the molecular energy levels. Below 0 eV, the highest occupied molecular orbital (HOMO) is marked by the first transmission peak. Above 0 eV, the first peak represents the lowest unoccupied molecular orbital (LUMO) in this nanoscale device. From the figure, it is clear that broadening varies per level. It depends on the exact electronic overlap that a particular molecular orbital has with the electrodes. Moreover, it also depends on the molecule's spin configuration. For example, the LUMO of the low-spin state is more broadened than the LUMO of the high-spin molecule. In fact, this difference in broadening is one of the reasons that theoretical predictions on how the conductance of SCO molecules should change during spin transition vary. In practice, two effects compete. On the one hand, the energy gap between the frontier orbitals (HOMO-LUMO gap) tends to decrease upon a LS to HS transition, as seen in Figure 2.4. This is intuitively expected to increase conductance, as the distance from Fermi level to the nearest level will generally decrease as well. On the other hand, the electronic coupling between the ligands at both sides of the Fe^{2+} ion decreases when going from the LS to HS state. In first approximation, the related decrease in wave function overlap should lead to a reduced transmission peak width and hence reduced conductance, as also seen in the figure. In the case of Figure 2.4, the overall effect is that the conductance is predicted to decrease for a LS to HS transition. In general, however, it is not *a priori* obvious if one should expect a conductance increase or decrease upon spin transition for a particular type of molecules. This in itself emphasizes the need for experimental data, as discussed in Chapter 6.

2.4 References

1. B. J. van Wees, H. van Houten, C. W. J. Beenakker, J. G. Williamson, L. P. Kouwenhoven, D. van der Marel and C. T. Foxon, Quantum Conductance of Point Contacts in a Two-dimensional Electron Gas, *Physical Review Letters*, **60**, (1988), 848-850.
2. D. A. Wharam, T. J. Thornton, R. Newbury, M. Pepper, H. Ahmed, J. E. F. Frost, D. G. Hasko, D. C. Peacock, D. A. Ritchie and G. A. C. Jones, One-dimensional Transport and the Quantisation of the Ballistic Resistance, *J. Phys. C: Solid State Phys.*, **21**, (1988), L209-L214.
3. Y. V. Sharvin, A Possible Method for Studying Fermi Surfaces, *Sov. Phys. -JETP*, **21**, (1965), 655-656.

-
4. J. C. Cuevas and E. Scheer, *Molecular Electronics: An Introduction to Theory and Experiment*, World Scientific, Singapore, **2010**.
 5. R. Landauer, Spatial Variation of Currents and Fields due to Localized Scatterers in Metal Conduction, *IBM J. Res. Dev.*, **1**, (1957), 223-231.
 6. M. Buttiker, Scattering Theory of Current and Intensity Noise Correlations in Conductors and Wave Guides, *Phys. Rev. B*, **46**, (1992), 12485-12507.
 7. N. Agraït, A. L. Yeyati and J. M. van Ruitenbeek, Quantum Properties of Atomic-sized Conductors, *Physics Report*, **377**, (2003), 81-279.
 8. J. M. Thijssen and H. S. J. van der Zant, Charge Transport and Single-electron Effects, *Phys. stat. sol. (b)*, **245**, (2008), 1-16.
 9. S. Datta, *Quantum Transport: Atom to transistor*, Cambridge University Press, New York, **2005**.
 10. C. Durkan, *Current at the Nanoscale: An Introduction to Nanoelectronics*, Imperial college Press, Londen, **2007**.
 11. E. J. Devid, P. N. Martinho, M. V. Kamalakar, I. Šalitroš, Ú. Prendergast, J.-F. Dayen, V. Meded, T. Lemma, R. González-Prieto, F. Evers, T. E. Keyes, M. Ruben, B. Doudin and S. J. van der Molen, Spin Transition in Arrays of Gold Nanoparticles and Spin Crossover Molecules, *ACS Nano*, **9**, (2015), 4496-4507.

3



Molecular devices based on molecule-gold nanoparticle arrays and networks

Here, I describe how molecule-gold nanoparticle arrays and networks are synthesized and characterized. Specifically, I present several synthesis routes to create gold nanoparticle arrays and networks functionalized with spin crossover molecules. Furthermore, the prime measurement techniques and setups are introduced here. These include basic charge transport measurements as well as optical analysis methods (UV-Vis spectroscopy and Raman spectroscopy). The latter provide information about the presence and properties of the molecules of choice in the network devices.

3.1 The synthesis of 2D molecule-metal nanoparticle arrays

Molecule-gold nanoparticle arrays and networks offer a variety of possibilities. By interfacing chemically tailored molecules [1] in between the metal nanoparticles, their physical properties [2, 3, 4] can in principle be tuned, e.g. to incorporate switchability. To synthesize molecule-gold nanoparticle arrays I have used a method adapted from L. Bernard *et al.* [5]. Basically, I synthesize a 2D molecule-metal nanoparticle array in a three-stage process. The first part is the synthesis of monodisperse gold nanoparticles in an aqueous solvent. The second part is the use of solvent exchange to change the polarity of the colloidal dispersion and to functionalize the gold nanoparticles by organic molecules. The third part incorporates another step of solvent exchange, to obtain apolar colloidal dispersions. Such a dispersion can then be used, by Langmuir methods [2], to have a 2D molecule-metal nanoparticle array self-assembled.

After obtaining a 2D molecule-metal nanoparticle array through self-assembly, several methods can be used to electrically contact the array. In addition, molecular exchange [6] (also called ligand substitution reactions [7, 8, 9]) can subsequently be performed.

3.1.1 Part 1: synthesis of gold nanoparticles in aqueous solvent

The method of preparing gold nanoparticles in an aqueous solvent (one-phase synthesis) was devised by J. Turkevich *et al.* [10]. A sodium citrate solution was used as a reducing agent to produce gold nanoparticles from a HAuCl_4 hydrate solution under boiling temperatures. This method was optimized by J. Slot *et al.* [11] and G. Tsutsui *et al.* [12] to synthesize [2] gold nanoparticles of ~5 nm or larger (in diameter) in a charge stabilized dispersion. In this optimized synthesis method, the reduction of gold is performed via a mixture of trisodium citrate and tannic acid. Here the tannic acid has a fast reductive and protective (stabilizing) effect during the synthesis [13, 14]. The particle size of the gold nanoparticles is further influenced by tannic acid through the number of nucleation sites formed during the reduction of chloroauric acid in ultra pure water. The trisodium citrate is a slow reducing reactant. It reduces the formed amount of gold nuclei further near boiling temperatures to allow the growth of the gold nanoparticles. In this part and following parts of the synthesis only ultrapure water (type 1 water, 18.2 M Ω cm, also referred to as Millipore water) is to be used.

The synthesis begins by preparing a 20 mL aqueous solution that contains 4 mL 1% (w/v) trisodium citrate and 0.08 mL 1% tannic acid. The second aqueous solution

contains 1 mL 1%(w/v) chloroauric acid in 80 mL ultrapure water. Both solutions are heated up to 60 °C for 2 minutes. Then the reducing solution is quickly added to the gold ion solution. The reactant mixture is heated up to 100 °C and a condenser is connected to the reactor to allow reflux of the water. Boiling is done for at least 10 minutes to make sure that the reaction is complete. Then the colloidal dispersion can be cooled down toward room temperatures. After the synthesis, the colloidal dispersion is stored in a fridge (~7 °C) for months. A ruby red charge-stabilized colloidal dispersion (~100 mL) of spherical gold nanoparticles (~ 10^{12} particles/mL) is obtained in water. Here the gold nanoparticles are stabilized by the tannic acid and aggregation is prevented among the charge-stabilized gold nanoparticles [14]. The diameter size of a gold nanoparticle is chosen to be near ~10 nm, to balance the effects of the charging energy E_C on the gold nanoparticles and to optimize the self-assembly of the gold nanoparticles into an array. The properties of a nanoparticle array will depend on the type of self-assembly method used [15, 16].

3.1.2 Part 2: functionalization of gold nanoparticles by molecules

In the second part of the synthesis of molecule-gold nanoparticle arrays, the gold nanoparticles (NP) will trade in its previous electrostatic stabilization by a steric stabilization. This is done by changing the polarity of the solvent in the gold nanoparticle dispersion via a solvent exchange. Next, thiolated molecules can be used as a capping ligand for the nanoparticles, to allow stabilization of the nanoparticle ensemble via steric hindrance.

The procedure starts as follows. First, centrifugation is performed on a desired volume of aqueous gold nanoparticle dispersion. After 15000 RPM (rotations per minute) cooled (10 °C) centrifugation for 1 hour the gold nanoparticles have settled down. The supernatant (water) is removed and ethanol is added to redisperse the settled down gold nanoparticles. The dispersion is sonicated to yield a stable redispersion. The next step is to prepare a solution of alkane(mono)thiol molecules in (N_2 washed) ethanol with an (excess) concentration of 0.14 mol/L [16, 17]. This is done in a glovebox in a N_2 atmosphere. Octane(mono)thiol (C8) molecules (molecule length ~1.3 nm [5]) are used most, to later define stable gold nanoparticle-molecule(s)-gold nanoparticle junctions with a junction length of around 2 nm [2, 6, 18, 19]. The alkanethiol solution is added quickly to the redispersed gold nanoparticle dispersion. The mixed octanethiol-gold nanoparticle dispersion in a glass bottle (sealed with a screwable lid) is again sonicated

in a water bath for more than five minutes to further stimulate the capping of the gold nanoparticle surfaces by octanethiol molecules. In time the functionalized gold nanoparticles will aggregate and start to settle down. The sedimentation of the functionalized gold nanoparticles can be accelerated by cooling the dispersion via a refrigerator. After at least two days all the functionalized gold nanoparticles have settled down and a dark blue sediment lies on the bottom of the bottle [20].

3.1.3 Part 3: self-assembly of 2D alkanethiol-gold nanoparticle array

In the third and final part, the supernatant (ethanol) is first removed from the functionalized gold nanoparticles settled down on the bottom of the bottle. Then the particles are redispersed in chloroform (CHCl_3) [20]. This dispersion displays a ruby-red colour again and is ready for self-assembly of C8-gold nanoparticle arrays. The self-assembly of a 2D array (see Figure 3.1) is based on an adapted Langmuir-Schaefer (L-S) technique [20, 21, 22]. A chosen μL volume of a C8-gold nanoparticles dispersion is added on the water layer in a teflon hole. If done properly, a well-ordered C8-gold nanoparticle array self-assembles on the water surface. To create large arrays a low particle concentration (between 0.06 and 0.3 mg/mL) is used [20, 23, 24].

By using a microcontact printing method (see Figure 3.2) an array can be transferred to the desired substrate [2, 20, 22]. This works well when both the array and substrate surface are hydrophobic. Hydrophilic surfaces tend to give rise to buckling or tearing of the array during microcontact printing [21]. Working with patterned PDMS stamps gives the possibility to imprint desired patterns and lines of C8-gold nanoparticle arrays on various substrates (i.e. glass, quartz, etc.). Furthermore, multilayered networks can be produced. This is done by transferring and imprinting 2D self-assembled arrays multiple times on the same substrate surface [21]. Finally, the gold nanoparticle arrays on a substrate are dried with N_2 gas and stored in a dark and sealed environment.

After the C8-gold nanoparticle array is printed on a substrate, scanning electron microscopy (SEM) is used to check both the gold nanoparticles and the C8-gold nanoparticle array. Figure 3.3 shows that the method used is feasible to make long-range-order C8-gold nanoparticle arrays on a flat SiO_2 -Si substrate. Small areas (sizes ~ 150 nm) show well-ordered arrays with local defects.

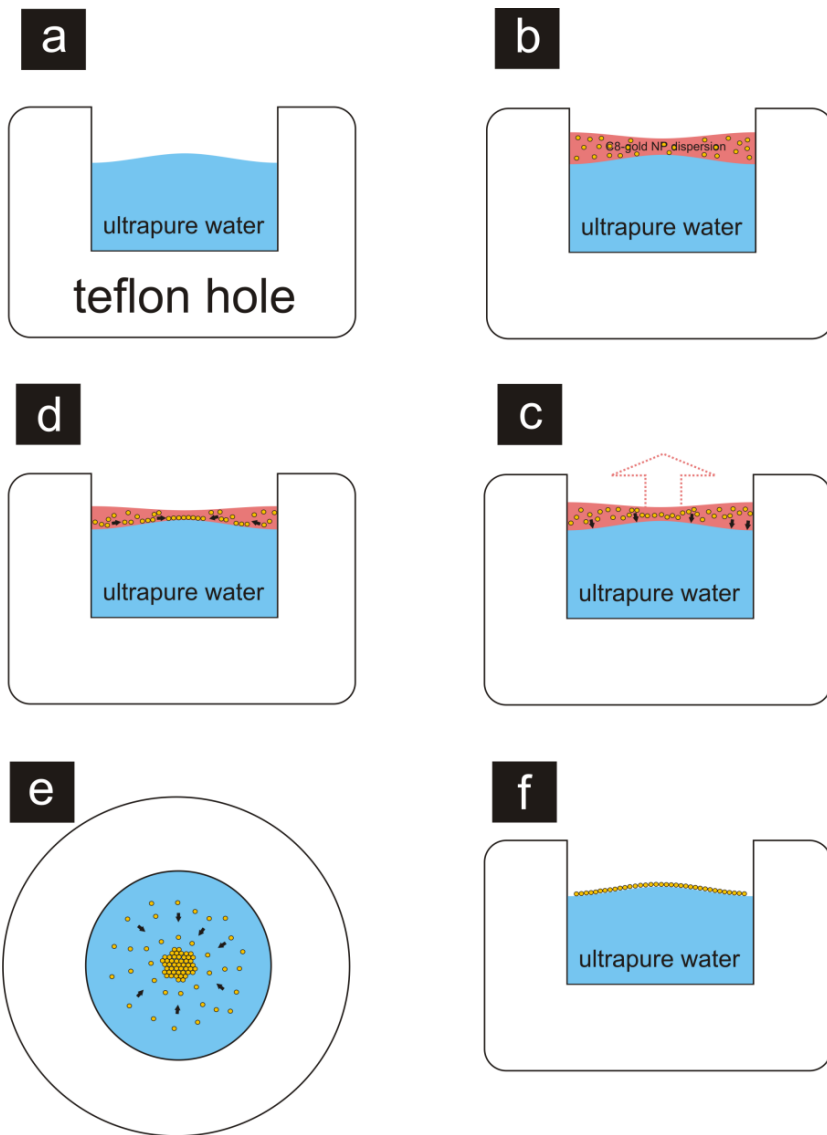


Figure 3.1: Schematics of the self-assembly of C8-gold nanoparticle (NP) array on an air-water interface. (a) A teflon model containing a hole in the middle filled with 300 μL ultrapure water containing a slight upward convex surface. (b) 30 μL C8-gold nanoparticle dispersion is added on the water to form a liquid lens surface. (c) The chloroform solvent is evaporating thereby concentrating the C8-gold nanoparticles. (d) The C8-gold nanoparticles go toward the air-water interface and form an initial self-assembled C8-gold nanoparticle array. (e) See schematic (d) from the top view perspective. (f) The self-assembly is complete and a 2D C8-gold nanoparticle array is formed floating on the water layer.

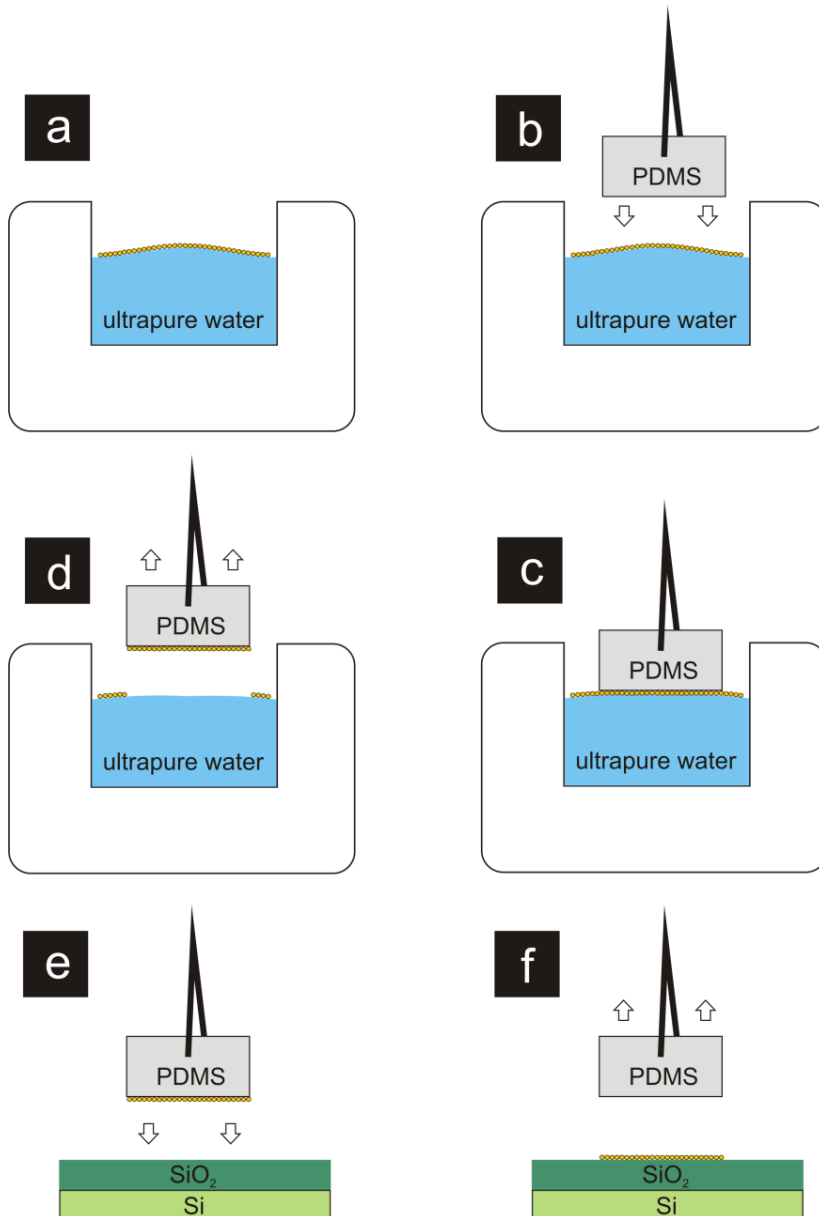


Figure 3.2: Schematics of microcontact printing of a self-assembled C8-gold nanoparticle (NP) array on an insulating SiO₂-silicon substrate. (a) The array on the water surface. (b) A PDMS stamp is picked up by tweezers to perform microcontact printing. (c) The stamp is put on top of the self-assembled array. (d) The stamp, containing the C8-gold nanoparticle array, is lifted up and dried with N₂. (e) The array is gently microcontact printed on the SiO₂-Si substrate (insulating SiO₂ layer ~200 nm thick). (f) The PDMS stamp is gently lifted up and the imprinted 2D array is inspected.

On larger length scales, however, boundaries between 2D grains can be observed.

The 2D alkanethiol-gold nanoparticle array opens several possibilities concerning tunability. By using different types of alkanethiol molecules one can tune the interparticle distance between the nanoparticles.

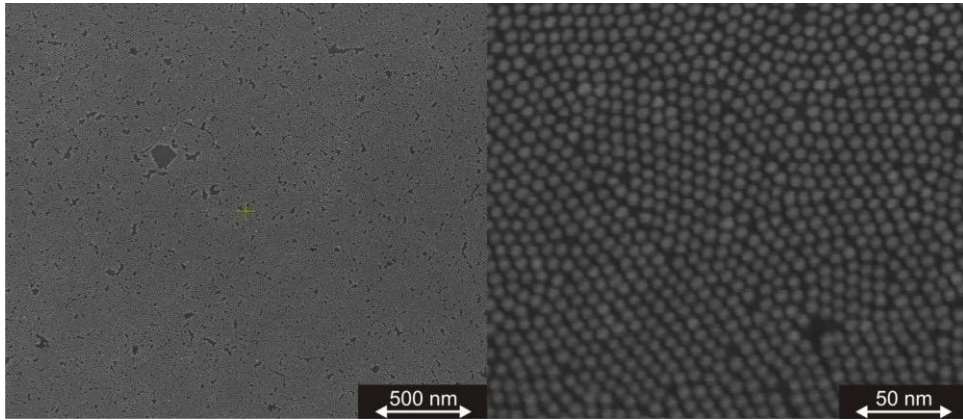
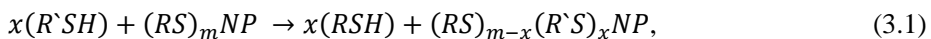


Figure 3.3: SEM images of a 2D C8-gold nanoparticle array that has been microcontact printed on SiO₂-Si substrate. The right image shows a zoom of the left image.

3.2 Molecular exchange

Molecular exchange (also called place-exchange [25] or ligand exchange [2]) is an alternative method to modify the functionalization of a gold nanoparticle surface. Molecular exchange involves the diffusion and chemical substitution of other species into capped-gold nanoparticle ensembles. Once molecular bridges are formed between the gold nanoparticle junctions the conductance properties of dithiol molecules can be studied.

The associative mechanism of molecular exchange is based on the following substitution reaction:



where x and m represent the number of incoming and outgoing molecular species respectively and NP denotes a nanoparticle [8]. The rate of exchange depends on the concentration of both the incoming (R'-SH) and outgoing (R-SH) molecular species.

Furthermore, it is higher if the outgoing molecular species (i.e. alkanethiols) have shorter lengths. The exchange dynamics also depend on the temperature and the pH of the solvent used during the molecular exchange [26, 27, 28]. The exchange of molecular species can be confirmed via various analysis methods [6, 29, 30], including conductance measurements, as discussed below.

To illustrate this, we describe molecular exchange on octanethiol (C8)-gold nanoparticle networks. The molecular species to be inserted is Oligo(phenylene ethynylene)-dithiol (i.e. OPE), a benchmark molecular bridge. First, octanethiol networks are stamped onto a substrate (typically a nanotrench device, see paragraph 3.4 and a transparent substrate, see paragraph 3.5). After a series of conductance and optical measurements on the virgin samples, molecular exchange is carried out. For this, we use an OPE concentration of 0,5 mM in a 5:1 solution of pure tetrahydrofuran (THF) versus pure triethylamine (Et_3N). Here Et_3N is used as a deprotection agent to remove the protective acetate groups from OPE [31]. The molecular device is placed upside down (the C8-gold nanoparticle network is in contact with the OPE solution) while not touching the bottom of the glass jar. The molecular exchange is done in 24 hours. After 24 hours the exchanged molecular devices are extensively washed and rinsed with pure THF. The molecular devices are dried in a nitrogen atmosphere (i.e. in a glove box). Later they are further dried using nitrogen gas. With this, they are ready for another series of measurements, ranging from charge transport experiments to optical experiments.

3.3 Synthesis routes toward spin crossover-gold nanoparticle networks

One of the main goals of this thesis is to investigate the (charge transport) properties of spin transition molecules in a device structure, as introduced in Chapter 1. In this paragraph, I introduce three synthesis routes to prepare a spin crossover-gold nanoparticle network. Below, I describe all routes and discuss their possibilities and limitations.

3.3.1 Synthesis route 1: molecular exchange

The first synthesis route can be described as an indirect approach to make a spin crossover-gold nanoparticle array. Here, an alkanethiol-gold nanoparticle array is first

constructed (see section 3.1). Then this array is functionalized by spin crossover molecules through a molecular exchange process (see paragraph 3.2).

Octanethiol (C8) molecules are chosen to be used as spacer molecules in an alkanethiol-gold nanoparticle type of array. The interparticle distance in such an array is compatible with the length of a $\text{Fe}(\text{S-BPP})_2$ molecule. The key step is then to design a process that is feasible for exchanging $\text{Fe}(\text{S-BPP})_2$ molecules into a C8-gold nanoparticle ensemble. During molecular exchange of $\text{Fe}(\text{S-BPP})_2$ molecules, no deprotection reagents can be used, in contrast to the case of OPE, because experiments have shown that deprotective reagents have detrimental effects and leads to breakdown of the $\text{Fe}(\text{S-BPP})_2$ complex molecule. The solvent acetonitril (MeCN) (pure 99,9%) turns out to be the best candidate to dissolve the $\text{Fe}(\text{S-BPP})_2$ molecules, while not detrimentally affecting the C8-gold nanoparticle ensemble on the nanotrench device.

Molecular exchange was carried out with a $\text{Fe}(\text{S-BPP})_2$ concentration of 0,5 mM, dissolved in MeCN. The molecular device, containing a C8-gold nanoparticle network, is placed upside down in the $\text{Fe}(\text{S-BPP})_2$ solution. The molecular exchange was done in 4 days (i.e. to allow the $\text{Fe}(\text{S-BPP})_2$ molecule to lose its protective acetate groups from the sulphur anchor groups in MeCN when contacting the gold surface [31]). After this step, the network is extensively washed and rinsed with pure MeCN. These molecular devices are dried in the glove box with the use of pure nitrogen gas. In Chapter 6 we further elaborate on the properties of such networks.

3.3.2 Synthesis route 2: complexation via a ligand-nanoparticle network

In this second synthesis route I first synthesize a ligand-gold nanoparticle ensemble. Here, the ligand is S-(4-{[2,6-(bipyrazol-1-yl)pyrid-4-yl]ethynyl}phenyl)ethanethioate, hereafter called AcS-BPP. If we compare to the spin transition molecule of interest (see Figure 1.5, in Chapter 1), we see that the latter basically consist of two AcS-BPP that are connected via a Fe^{2+} ion. The strategy chosen here is based on this observation. First, we make networks capped with the ligands. Then, we insert Fe^{2+} ions. This may lead to local formation of spin transition bridges between neighbouring nanoparticles, the Fe^{2+} working as a ‘glue’ for nearby ligands. Note that in this route, no alkanethiols are used. This type of strategy has been performed earlier to cap terpy-functionalized phospholipid on lecithin vesicles and to connect them via iron(II)-directed complexation [32].

To directly functionalize the gold nanoparticles with S-BPP molecules, we heat up a solution of 14.5 mg of AcS-BPP molecules in 2 mL pure (absolute) ethanol (EtOH) to 70 °C. The next step is to add the hot AcS-BPP ethanolic solution quickly into a warm (heated around 50 °C) gold nanoparticle ethanolic dispersion. The functionalized S-BPP-gold nanoparticles will settle down by gravity during three days and they are saved in a cold, dark storage environment. To obtain self-assembled S-BPP-gold nanoparticle arrays on substrates, a procedure similar to the one in paragraph 3.1.3 is used (array formation on a water surface; stamping). In Chapter 5 we elaborate on the properties of S-BPP-gold nanoparticle arrays without Fe²⁺ ions.

Based on this concept two routines have been tested to learn if Fe²⁺ complexation in a S-BPP-gold nanoparticle array is actually possible.

The first is to perform the self-assembly of a S-BPP-gold nanoparticle array in a diluted Fe²⁺ solution, instead of in pure Millipore water. The idea is that during self-assembly of the S-BPP-gold nanoparticles, the Fe²⁺ ions can be ‘grabbed’ by the nitrogen atoms of a S-BPP molecule. Another S-BPP-gold nanoparticle may contact the Fe(S-BPP)-gold nanoparticle, resulting in direct complexation. Unfortunately, this routine turned out to be complicated. A main point of concern is that the self-assembly process of S-BPP-gold nanoparticles is disrupted when Fe²⁺ ion concentrations are used above 3.5 mM. It seems that above a certain Fe²⁺ ion concentration threshold the S-BPP molecules become saturated with Fe²⁺ ions. Thereby the polarity of the capping S-BPP molecules can be changed and this will hamper the self-assembly process of the S-BPP-gold nanoparticles into an array. Another observation is that the type of solvent used during this assembly step influences the structuring of a S-BPP-gold nanoparticle ensemble. I have experimented with hot ethanol and acetonitril solvents. When synthesizing the S-BPP-gold nanoparticles in acetonitril solvents, the self-assembly process gives an ensemble that appears strongly three dimensional (3D), as seen in Figure 3.4. Importantly, Figure 3.4 shows that the gold nanoparticles are not aggregated. Figure 3.5 shows an ensemble obtained using hot ethanol solvent.

Unfortunately, several areas on top of the ensemble appear to be covered by a darkish layer (see right dark area on the left zoomed out SEM image of Figure 3.5). This is presumably a layer of cross-linked S-BPP molecules that is possibly mediated by Fe²⁺ ions. Figure 3.5 (the right zoomed in SEM image) displays a close packed gold nanoparticle structure. Apparently the type of solvent can affect the linking between

the S-BPP molecules (via the Fe^{2+} ions) during the self-assembly of the capped gold nanoparticles.

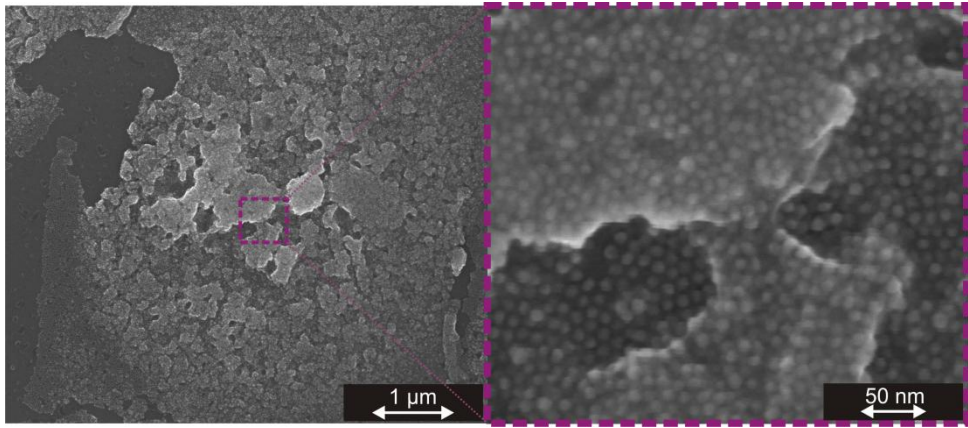


Figure 3.4: (left image) SEM image of S-BPP-gold nanoparticle ensemble (prepared via MeCN solvent and self-assembled with the presence of Fe^{2+} ions (i.e. 0.1 mM solution of Iron(II) perchlorate hydrate in Millipore water)). (right image) A zoom in on the 3D gold nanoparticle ensemble structuring, composed of several layers of non-aggregated gold nanoparticles. This ensemble is microcontact printed on (oxidized) silicon substrate.

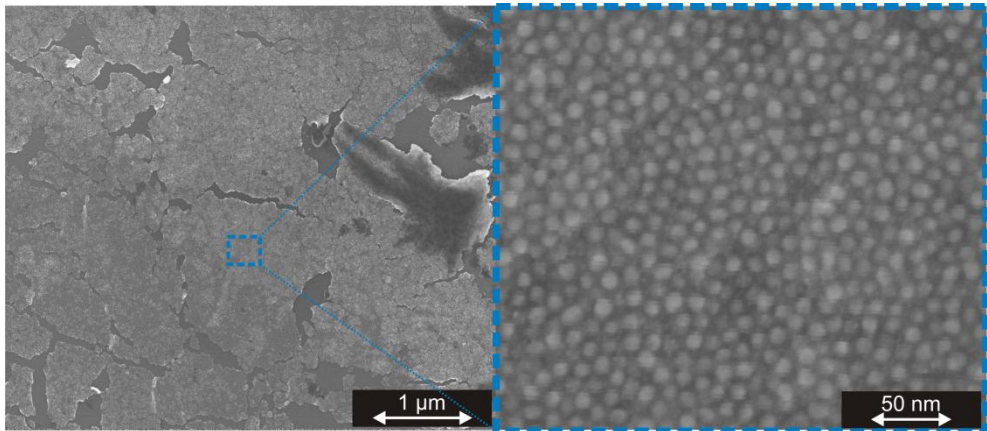


Figure 3.5: (left image) SEM image of S-BPP-gold nanoparticle ensemble (prepared via ethanol solvent and self-assembled with the presence of Fe^{2+} ions (i.e. 0.1 mM solution of Iron(II) perchlorate hydrate in Millipore water)). (right image) A zoom in on the hard, brittle ensemble of close packed non-aggregate S-BPP-gold nanoparticles. This ensemble is microcontact printed on (oxidized) silicon substrate.

The second routine is to perform Fe^{2+} ion exchange of a S-BPP-gold nanoparticle array already microcontact printed on a substrate. Here, a S-BPP-gold nanoparticle array is self-assembled on a Millipore water layer. This array is then microcontact printed on a substrate. The final step is to exchange Fe^{2+} ions into the S-BPP-gold nanoparticle array. This is carried out by using a 0.5 mM concentration of Iron(II) perchlorate hydrate in a (weak) polar solvent (i.e. ethanol or acetonitril). The exchange is done in 4 days. The array obtained is then washed and rinsed with the same type of pure solvent and dried in a glove box with nitrogen gas.

Unfortunately, room-temperature conductance experiments on arrays obtained via both routines above indicate very large resistances (above 100 GOhm). This has hampered the use of these samples.

3.3.3 Synthesis route 3: direct synthesis of $\text{Fe}(\text{S-BPP})_2$ molecules with gold nanoparticles

Finally, I elaborate on a third synthesis route to obtain a $\text{Fe}(\text{S-BPP})_2$ -gold nanoparticle array. Here, full $\text{Fe}(\text{S-BPP})_2$ molecules are used to bridge directly between gold nanoparticles. Neither alkanethiols nor S-BPP molecules are used in this procedure.

In short, a $\text{Fe}(\text{S-BPP})_2$ solution with a concentration of 1 mM to 1.3 mM is prepared in pure methanol (MeOH). The temperature of the $\text{Fe}(\text{S-BPP})_2$ solution in methanol can be elevated toward 40 °C till 50 °C to accelerate dissolving of the $\text{Fe}(\text{S-BPP})_2$ molecules and to deprotect the thiol anchoring groups of the molecules. Also the gold nanoparticles are dispersed in a methanol solvent. Functionalization of the gold nanoparticles starts when the $\text{Fe}(\text{S-BPP})_2$ solution is added to the gold nanoparticle dispersion. The functionalized $\text{Fe}(\text{S-BPP})_2$ -gold nanoparticles will settle down and the dispersion is saved in a cold, dark storage environment. After three days all the $\text{Fe}(\text{S-BPP})_2$ -gold nanoparticles have settled down. The synthesis of self-assembled $\text{Fe}(\text{S-BPP})_2$ -gold nanoparticle arrays can be continued in a way similar described in paragraph 3.1.3.

A limitation of these self-assembled $\text{Fe}(\text{S-BPP})_2$ -gold nanoparticle arrays (self-assembled on a water layer) is that microcontact printing via PDMS stamps fails. I suspect that this $\text{Fe}(\text{S-BPP})_2$ -gold nanoparticle array is more polar compared to other types of apolar molecule-gold nanoparticle arrays. The polarity of the $\text{Fe}(\text{S-BPP})_2$

molecules appears to detrimentally affect the attachment of the $\text{Fe}(\text{S-BPP})_2$ -gold nanoparticle array on a PDMS stamp.

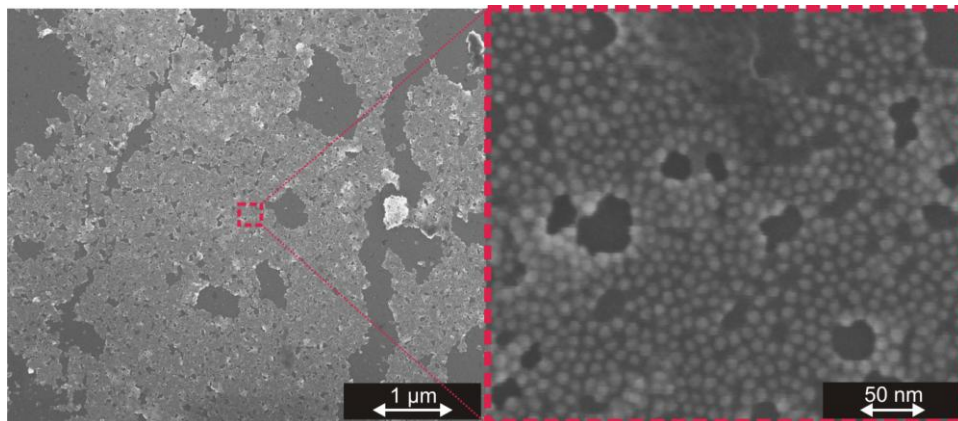


Figure 3.6: (left image) SEM image of $\text{Fe}(\text{S-BPP})_2$ -gold nanoparticle array (prepared via methanol solvent). (right image) A zoom in on the fragmented non-aggregate gold nanoparticles separated by only $\text{Fe}(\text{S-BPP})_2$ molecules.

Alternative techniques (like Langmuir Blodgett (i.e. dipping) etc.) are required to transfer a $\text{Fe}(\text{S-BPP})_2$ -gold nanoparticle array to a substrate. But these techniques can give rise to more fragmented array structures. Figure 3.6 shows the best attempt to partially transfer a $\text{Fe}(\text{S-BPP})_2$ -gold nanoparticle array to the (oxidized) silicon substrate via microcontact printing. Still this array is too fragmented to perform conductive measurements on it at room temperatures. A possible solution to obtain a better structured $\text{Fe}(\text{S-BPP})_2$ -gold nanoparticle array on a substrate is done via dropwise self-assemble techniques.

During this dropwise technique, first 20 μL Millipore water is pipetted on the surface of the (oxidized) silicon substrate. The next step is to pipette a 10 μL $\text{Fe}(\text{S-BPP})_2$ -gold nanoparticle dispersion (in CHCl_3 solvent) into the middle of the convex water drop. If done properly, the drop of $\text{Fe}(\text{S-BPP})_2$ -gold nanoparticles will go through the convex water drop. The $\text{Fe}(\text{S-BPP})_2$ -gold nanoparticle dispersion is then trapped in between the silicon substrate and the polar water drop above it. The CHCl_3 solvent will evaporate from the $\text{Fe}(\text{S-BPP})_2$ -gold nanoparticle dispersion and the $\text{Fe}(\text{S-BPP})_2$ -gold nanoparticles arrange themselves orderly in between the substrate-water interface. Once

the water is evaporated, a $\text{Fe}(\text{S-BPP})_2$ -gold nanoparticle array is deposited on the substrate. However, this combined self-assembly and deposition technique needs further optimization before room-temperature conductive measurements can be performed on these dropwise $\text{Fe}(\text{S-BPP})_2$ -gold nanoparticle arrays.

For this reason, the samples used in Chapter 6 are based on the ‘traditional’ exchange method (i.e. synthesis route 1, see paragraph 3.3.1).

3.4 Charge transport measurements

To study their charge transport properties, devices are required that provide reliable electrical contacts with the arrays. We achieve this via high-aspect-ratio (HAR) nanotrench structures. These devices are made via a combination of optical lithography and electron beam lithography. As shown in Figure 3.7 they consist of two wide electrodes separated by a tuneable gap of 50-200 nanometer. The gap size between the electrodes of these devices can be controlled over a wide size range. The individual electrodes consist of an adhesion layer of around 3 nm thick Ti covered by a 47 nm thick layer of gold [33].

Room-temperature charge transport measurements are performed in a dedicated probe station within a Faraday cage. The resistances typically being high, we use a voltage source and measure the current in the circuit. Charge transport measurements are controlled via a Labview program and a National Instrument data acquisition DAQ-mx card (see Figure 3.8(a)). The current is converted via a low noise current-voltage convertor-amplifier with variable-gain of 10^3 to 10^{11} V/A (Femto DLPCA-200).

To demonstrate the effect of molecular exchange, we refer to Figure 3.9. It shows current-voltage (I - V) measurements on a molecule-gold nanoparticle network printed on a HAR nanotrench device at room temperature. The blue line shows data for a virgin octanethiol (C8)-based network. In red (see Figure 3.9), we show results for the same sample after molecular exchange with conjugated OPE molecules. A clear increase in the conductance is observed (the exact ratio fluctuates [5, 34]). Interestingly, a back-exchange process, in which octanethiol molecules are re-inserted (see Figure 3.9, in green), is possible as well.

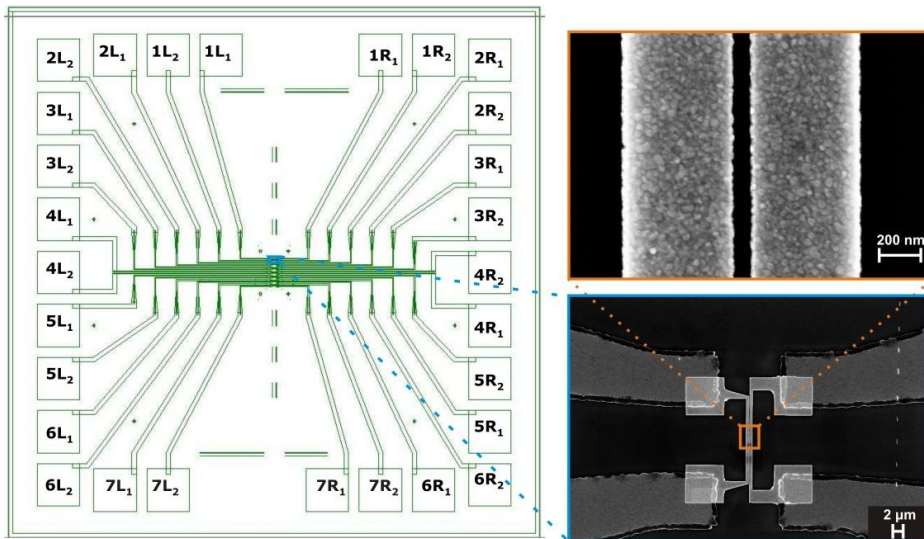


Figure 3.7: High-aspect-ratio nanotrench device onto which a molecule-gold nanoparticle array can be microcontact printed (in total 7 nanotrenches on one device). The gap between the gold electrodes can be 50-200 nm and the width of the electrodes can be as much as 10 μm .

After room-temperature characterization, charge transport measurements can be performed in the temperature range 1.5-325 K. This is done in a helium-based cryostat with a variable temperature insert (VTI) in Strasbourg. The devices are placed on a chip carrier, connected to a sample stick and then the whole dipstick is inserted in the cryostat (see Figure 3.8(b)). The DC electrical properties of the sample are measured using a semiconductor parameter analyzer (Agilent E5270B).

3.5 Optical properties of molecule-gold nanoparticle arrays

Exposing a 2D molecular-gold nanoparticle array to light, analytical information can be obtained about the properties of both the gold nanoparticles and the molecular species. Two types of optical techniques have been used here, namely ultraviolet (UV)-visible (Vis) spectroscopy and Raman spectroscopy. The first is used to analyze shifts in the surface plasmon absorbance of the nanoparticles. The second reveals information on (shifts of) vibrations of molecules in the molecule-gold nanoparticle ensemble.

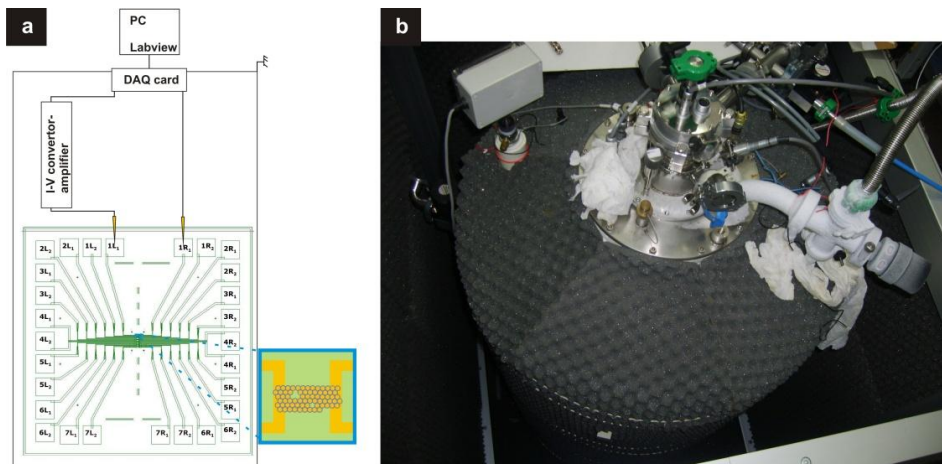


Figure 3.8: Setup used for measuring the electrical properties of molecular-gold nanoparticle ensemble devices. (a) Scheme of two-probe electrical measurement circuit used in Leiden for room-temperature measurements. (b) An image of the cryostat in Strasbourg (temperature range 1.5-325 K).

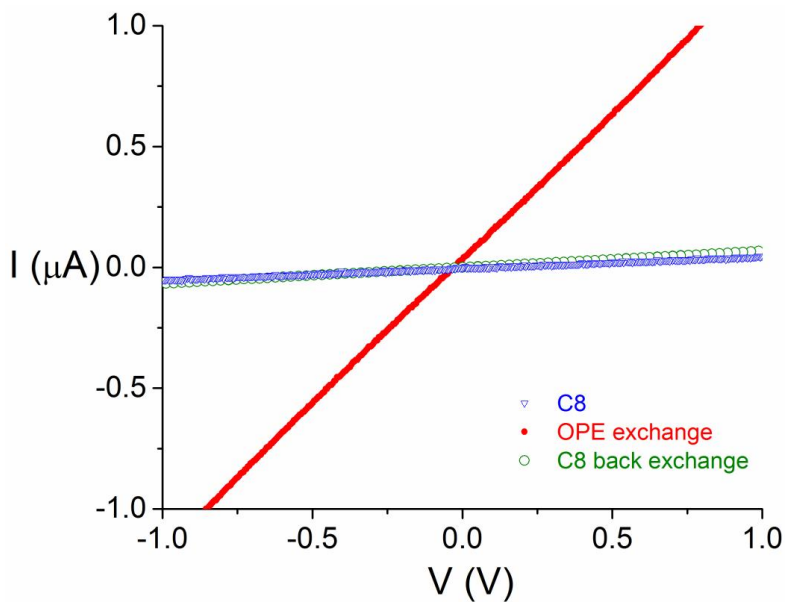


Figure 3.9: Room-temperature current-voltage (I - V) measurements on a C8-gold nanoparticle network (blue curve, $R \approx 21 \text{ M}\Omega$). This network can then later be exchanged with (OPE) molecules (red curve, $R \approx 0.8 \text{ M}\Omega$). Also on this same network, one can perform a back exchange with C8 molecules (green curve, $R \approx 15 \text{ M}\Omega$).

3.5.1 The surface plasmon resonance of a molecular-gold nanoparticle array

With UV-Vis spectroscopy, we can characterize the surface plasmon resonance (SPR) of gold nanoparticles, either in solution or in an array. This resonance comes about because the electric-field component of the incoming light wave induces a polarization of the free conduction electrons at the particle surface (see Figure 3.10(a)) [4]. As the positive charges on the surface of a gold nanoparticle can be assumed static, a net charge difference occurs due to the electron cloud displacement. This will give rise to a restoring force, finally resulting in a dipolar oscillation of the electron cloud. For gold nanoparticles, this resonance is typically observed in the visible regime. However, the exact resonance wavelength depends sensitively on the surroundings of the individual nanoparticle, specifically on the molecular capping layer and the packing of the gold nanoparticles in the array (see Figure 3.10(c)). This makes UV-Vis spectroscopy a good probe to check if a molecular exchange procedure has been successful [3].

To describe the interaction of light with metal nanoparticles, scattering theory was developed by Gustav Mie [35]. This theory describes the absorption and scattering of spherical particles based on the Maxwell equations. The main assumption of Mie theory is that both the surrounding molecular medium and gold nanoparticle are homogeneous and describable according to their bulk optical dielectric functions [4]. The optical absorption cross-section σ of the nanoparticles is calculated via equation 3.2:

$$\sigma = 12\pi \frac{\omega}{c} \varepsilon_m^{3/2} R^3 \frac{\varepsilon_2(\omega)}{[\varepsilon_1(\omega) + 2\varepsilon_m]^2 + [\varepsilon_2(\omega)]^2}. \quad (3.2)$$

Where ε_m is the permittivity of the surrounding medium (i.e. the real part) and $\varepsilon(\omega) = \varepsilon_1(\omega) + i\varepsilon_2(\omega)$ is the complex dielectric function of the cluster (i.e. the complex part) [5]. Note that equation 3.2 yields the resonance condition $\varepsilon_1(\omega) + 2\varepsilon_m = 0$, from which the resonance frequency (or frequencies) may be deduced.

The Mie theory is adequate in explaining the coupling of isolated spherical particles in an external field in the quasi-static regime (i.e. $\lambda \gg 2r$, where r is the radius of the gold particle). However, Mie theory starts to break down when interactions between neighbouring gold nanoparticles are to be considered [3, 36]. This occurs approximately when $D \leq 5r$, where D represents the center-to-center distance between

the particles [4]. Coupling of the modes results in a red shift and broadening of the resonance. In this case, Maxwell-Garnett theory offers a more adequate description. This theory is used in Chapter 5.

Figure 3.10(b) displays the schematic experimental setup used for SPR measurements. A deuterium-halogen light source (for UV or Visible light respectively) illuminates a molecular-gold nanoparticle array, microcontact printed on a glass or quartz substrate, via an optical fiber. Via another fiber, the transmitted light is coupled into a spectrograph with a detector that can be cooled (to reduce thermal noise). Read-out is done by a pc. All the SPR measurements are performed in air at room temperature.

3.5.2 Surface-enhanced Raman scattering

Raman spectroscopy is a versatile analytical method for vibrational spectroscopy that allows one to analyze the chemical and structural composition of gases, liquids or solids [37, 38]. Unlike conventional infrared vibrational spectroscopy, Raman is a scattering method. The dominant form of optical scattering is Rayleigh scattering, where incident photons are elastically scattered from a molecule. Raman scattering is the inelastic scattering of photons by a molecule. The difference in frequency (i.e. wavelength) between the incident and scattered photons corresponds to vibrational quanta [39]. In accordance with the Raman selection rules (i.e. symmetry relates to Raman activity), the intensity of the Raman scattering is proportional to the magnitude of the change in molecular polarizability. So aromatic organic molecules will typically exhibit a more intense Raman scattering compared to aliphatic molecules [40].

For the Raman line intensity, one has

$$I_r \propto \nu^4 \sigma I \exp\left(\frac{-E_i}{kT}\right) c. \quad (3.3)$$

Here I and ν represent the intensity and frequency respectively of the incident radiation. Furthermore, σ represents the Raman cross-section; $e^{-E_i/kT}$ is the Boltzmann factor for state i and c is the concentration of molecules [38]. The main limitation of Raman scattering is its sensitivity, that is low due to the low cross-section ($\sim 10^{-31}$ - 10^{-26} cm²) of a molecule [38, 41]. Especially when the molecular adsorbate concentration in the sample is also low.

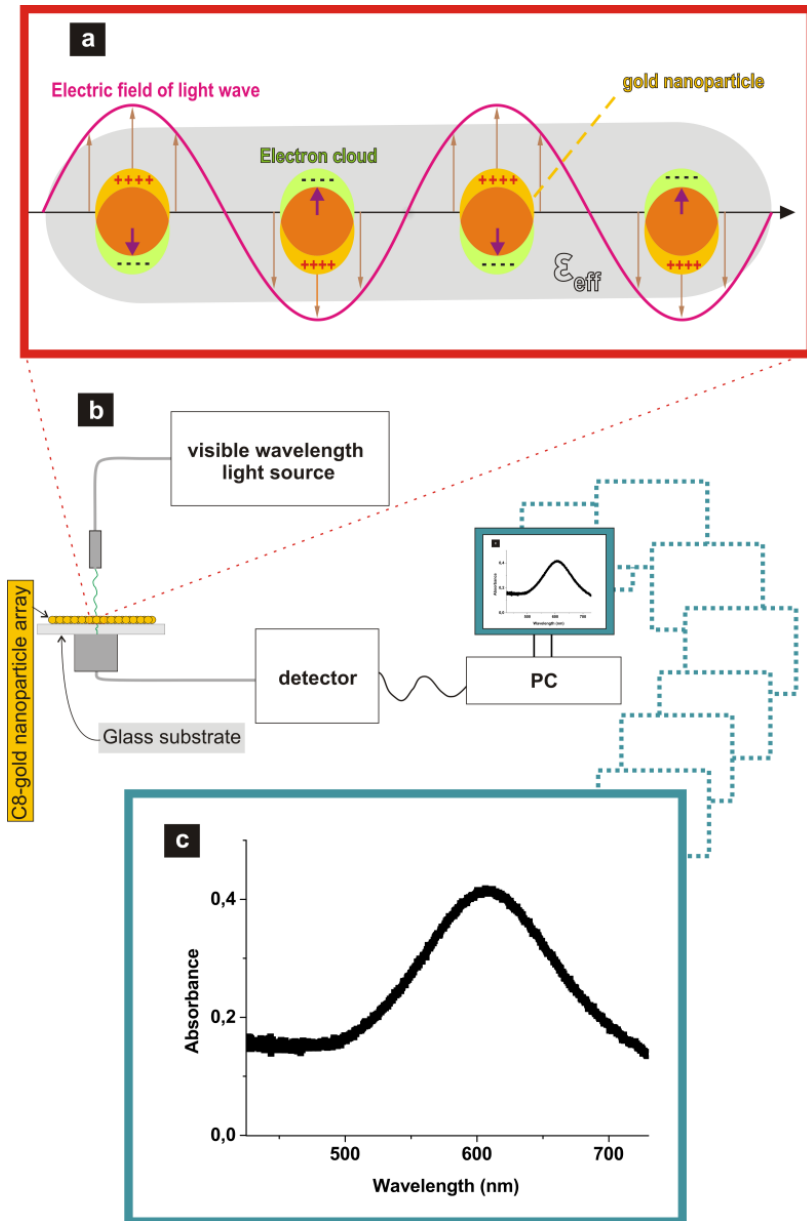


Figure 3.10: (a) Surface plasmon excitation of a gold nanoparticle (in the quasistatic regime) in a dielectric with permittivity ϵ_{eff} . (b) Scheme of the experimental setup to perform optical SPR measurements on molecular-gold nanoparticle arrays. (c) UV-Vis spectra of a microcontact printed C8-gold nanoparticle array on a glass substrate. The SPR peak is found around 608 nm.

In the 1970s, surface-enhanced Raman scattering (SERS) [4, 37, 38, 41-45] spectroscopy was introduced. With signal enhancements of several orders of magnitude, it allows for the analysis of samples containing minimal concentrations of molecular adsorbates on a nanostructured (noble) metal surface. The enhancement originates from both an electromagnetic (EM) effect and a chemical (CE) effect. The EM contribution stems from the increase in local electromagnetic fields due to resonant excitation of plasma oscillations (i.e. plasmon) in metal nanoparticles [40]. The CE contribution is related to the electronic properties of the molecules adsorbed on metal nanograins or particles. The presence of a metal nanoparticle may change the polarizability of the adsorbed molecules and this gives an increase in the Raman scattering efficiency [37].

The power of the SERS signal of molecules adsorbed onto metal nanoparticles (either in suspension or on a surface) is given by:

$$P_{SERS} = NI_L |A(v_L)|^2 |A(v_S)|^2 \sigma_{ads}^R \quad (3.4)$$

Where I_L represents the intensity of the laser, N is the amount of molecules, σ_{ads}^R is the effective Raman cross-section of the adsorbed molecular species [37]. The enhancement factors $|A(v_L)|^2$ and $|A(v_S)|^2$ represent the increase of the laser excitation and scattered fields respectively. Thus, EM enhancement involves the increase of both incident and Raman-scattered fields. At resonance, the laser beam excites the surface plasmons of a rough or curved noble metal surface. Due to the collective oscillations of conduction electrons a dipolar field (i.e. E_{SP}) will be emitted. At the surface of a gold nanoparticle, this induced dipolar field is related to the incoming laser field according equation 3.5:

$$E_{SP} = \left(\frac{\varepsilon - \varepsilon_0}{\varepsilon + 2\varepsilon_0} \right) E_{laser} \left(\frac{r}{r+d} \right)^3 \quad (3.5)$$

Where ε is the dielectric constant of the metal and ε_0 is the dielectric constant of the external molecular medium. The interaction between the incoming electric field and the dipolar field will lead to a redistribution of electric field intensities in a region (i.e. a hot spot) near the gold nanoparticle. The magnitude of E_{SP} is further influenced by the decay distance around a spherical gold nanoparticle, where d is the distance of a single molecule separated from the surface of the gold nanoparticle (r is the particle radius again). The enhanced local field felt by the molecules, E_m , is the sum of the electric field magnitudes, i.e. $E_{SP} + E_{laser}$. The field enhancement $A(v)$ felt by the molecular adsorbate is then determined by the ratio of field amplitudes E_m/E_{laser} .

The amplitude of the SERS scattered field will be given by $E_{SERS} \propto |A(v_L)| |A(v_S)| E_{laser}$. The SERS (EM) enhancement factor $G_{SERS}^{EM} = |A(v_L)|^2 |A(v_S)|^2$ becomes particularly strong when the real part of the ϵ is equal to $-2\epsilon_0$ in equation 3.5. This is exactly the resonance condition for surface plasmons (cf. equation 3.2). In that case, small increases in the local field will produce large enhancements in the overall Raman scattering that approximately scales as E^4 [4, 37, 42, 43]. Any molecular adsorbate in proximity (i.e. a few nm) of the gold nanoparticle surface will feel an enhanced excitation intensity.

The second mechanism, namely CE enhancement, involves the electronic interaction between molecular adsorbate and the gold nanoparticle surface. CE enhancement relates to a mechanism called resonance Raman scattering. This describes how resonant intermediate states are created from new electronic states via charge transfer excitations between adsorbate and surface [42, 46]. These charge transfer excitations (i.e. either from the metal to the molecule or vice versa) can occur at about half the energy of the intrinsic intramolecular excitations of the molecular adsorbate [46]. The excited electrons can go from the filled molecular adsorbate orbitals to unfilled metal orbitals that lie above the Fermi level (i.e. molecule-metal charge transfer). Or the metal electrons can be excited to an empty lowest molecular adsorbate orbital (i.e. a metal-molecule charge transfer). These intermediate resonances cost less energy compared with intrinsic intramolecular excitations of the molecular adsorbate. Also the charge transfer processes may change the polarizability of the molecule and this will result in a change of the Raman scattering cross-section [47]. For example the polarizability of a ligand will change when it becomes coordinatively bonded to a metal transition.

Present-day SERS is a robust and effective analytical tool capable of combining and providing chemical information with single molecule sensitivity [4, 38-40]. Specifically, this thesis shows its great value for investigating molecule-nanoparticle networks.

Raman spectroscopy on molecular-gold nanoparticle arrays was carried out using a Horiba Jobin-Yvon LabRAM HR instrument with an Olympus confocal microscope (see Figure 3.11). The molecular-gold nanoparticle array was excited with a 632.8 nm HeNe laser or a 784.5 nm diode laser.

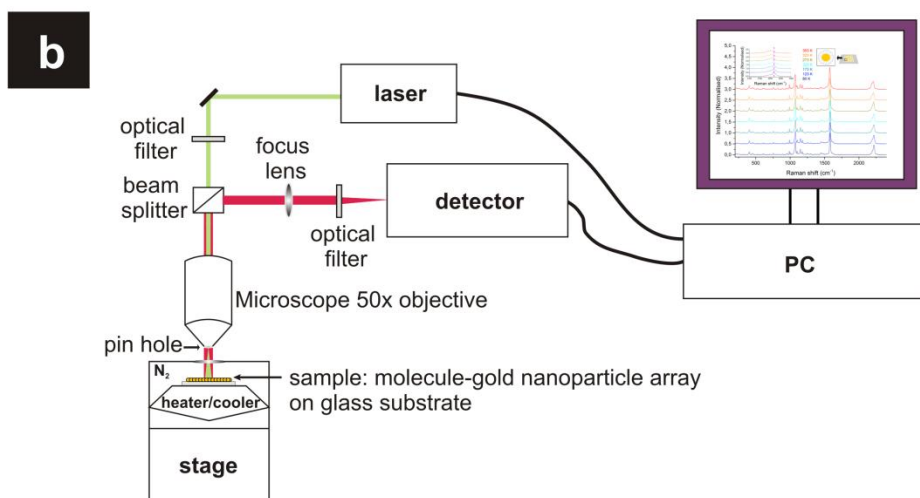


Figure 3.11: (a) An image of the Raman spectroscopy apparatus in Dublin. (b) A schematic of the Raman system in (a) used to perform variable temperature SERS measurements on a molecule-gold nanoparticle array.

An appropriate edge filter was put in the spectrometer depending on the excitation source. The laser was focused on a spot of approximately $3\ \mu\text{m}$ with a 50x objective. A $300\ \mu\text{m}$ confocal pinhole and a 600 lines per mm diffraction grating were employed, providing data at approximately $1\ \text{cm}^{-1}$ resolution. The x-axis was calibrated versus the Rayleigh line ($0\ \text{cm}^{-1}$) and the phonon mode from silicon wafer ($520\ \text{cm}^{-1}$). Spectra were collected on a cooled 2D Andor CCD detector.

Temperature-dependent Raman measurements were performed on molecular-gold nanoparticle arrays from 77 K to 353 K in a nitrogen atmosphere. This was achieved by placing the molecular-gold nanoparticle array into a Linkam Scientific THMS600 temperature stage, which was cooled with liquid nitrogen. The desired temperature was set on the control unit and the sample was allowed to equilibrate for 30 minutes before measurement. An exposure time of 8 seconds was used with 5 accumulations for each spectrum. Three spectra were collected at each temperature and at different positions on the sample. The baseline of each spectrum was corrected using a polynomial fit with the Lab Spec software, before spectra were normalized to a temperature-independent peak. The three spectra for each temperature were then averaged.

Note: Dr. Ú. Prendergast performed the Raman spectroscopy experiments, while Professor Dr. T. E. Keyes did the SERS analyses of the samples (both are at DCU, Dublin). The samples discussed in this thesis were all made in Leiden.

3.6 References

1. J. C. Cuevas and E. Scheer, *Molecular Electronics: An Introduction to Theory and Experiment*, World Scientific, Singapore, **2010**.
2. A. Zabet-Khosousi and A.-A. Dhiran, Charge Transport in Nanoparticle Assemblies, *Chem. Rev.*, **108**, (2008), 4072-4124.
3. A. N. Shipway, E. Katz, and I. Willner, Nanoparticle Arrays on Surfaces for Electronic, Optical, and Sensor Applications, *Chemphyschem*, **1**, (2000), 18-52.
4. S. K. Ghosh and T. Pal, Interparticle Coupling Effect on the Surface Plasmon Resonance of Gold Nanoparticles: From Theory to Applications, *Chem. Rev.*, **107**, (2007), 4797-4862.
5. L. Bernard, *Expanding the Horizon of Molecular Electronics via Nanoparticle Assemblies*. Ph. D. Thesis, University of Basel, Switzerland, **2006**.
6. J. Liao, L. Bernard, M. Langer, C. Schönenberger and M. Calame, Reversible Formation of Molecular Junctions in 2D Nanoparticle Arrays, *Adv. Mater.*, **18**, (2006), 2444-2447.
7. M. J. Hostetler, S. J. Green, J. J. Stokes and R. W. Murray, Monolayers in Three Dimensions: Synthesis and Electrochemistry of ω -Functionalized Alkanethiolate-Stabilized Gold Cluster Compounds, *J. Am. Chem. Soc.*, **118**, (1996), 4212-4213.
8. M. J. Hostetler, A. C. Templeton and R. W. Murray, Dynamics of Place-exchange Reactions on Monolayer-protected Gold Cluster Molecules, *Langmuir*, **15**, (1999), 3782-3789.
9. C. B. Murray, C. R. Kagan and M. G. Bawendi, Synthesis and Characterization of Monodisperse Nanocrystals and Close-packed Nanocrystal Assemblies, *Annu. Rev. Mater. Sci.*, **30**, (2000), 545-610.

10. J. Turkevich, P. C. Stevenson and J. Hillier, A Study of the Nucleation and Growth Processes in the Synthesis of Colloidal Gold, *Discuss. Faraday Soc.*, **11**, (1951), 55-75.
11. J. Slot and H. Geuze, A New Method for Preparing Gold Probes for Multiple Labeling Cytochemistry, *Eur. J. Cell. Biol.*, **38**, (1985), 87-93.
12. G. Tsutsui, S. J. Huang, H. Sakaue, S. Shingubara and T. Takahagi, Well-Size-Controlled Colloidal Gold Nanoparticles Dispersed in Organic Solvents, *J. Appl. Phys.*, **40**, (2001), 346-349.
13. H. Mühlpfordt, The Preparation of Colloidal Gold Particles Using Tannic Acid as an Additional Reducing Agent, *Experientia*, **38**, (1982), 1127-1128.
14. S. K. Sivaraman, S. Kumar and V. Santhanam, Room-temperature Synthesis of Gold Nanoparticles - Size-control by Slow Addition, *Gold Bulletin*, **43**, (2010), 275-286.
15. S. Datta, D. B. Janes, R. P. Andres, C. P. Kubiak and R. G. Reifengerger, Molecular Ribbons, *Semicond. Sci. Technol.*, **13**, (1998), 1347-1353.
16. X. M. Lin, H. M. Jaeger, C. M. Sorensen and K. J. Klabunde, Formation of Long-Range-Ordered Nanocrystal Superlattices on Silicon Nitride Substrates, *J. Phys. Chem. B*, **105**, (2001), 3353-3357.
17. H. B. Akkerman and B. de Boer, Electrical Conduction Through Single Molecules and Self-assembled Monolayers, *J. Phys.: Condens. Matter*, **20**, (2008), 013001(1-20).
18. L. Bernard, Y. Kamdzhilov, M. Calame, S. J. van der Molen, J. Liao and C. Schönenberger, Spectroscopy of Molecular Junction Obtained by Place Exchange in 2D Nanoparticle Arrays, *J. Phys. Chem. C*, **111**, (2007), 18445-18450.
19. C. M. Guédon, J. Zonneveld, H. Valkenier, J. C. Hummelen and S. J. van der Molen, Controlling the Interparticle Distance in a 2D Molecule-nanoparticle Network, *Nanotechnology*, **22**, (2011), 125205(1-5).
20. S. Huang, G. Tsutsui, H. Sakaue, S. Shingubara and T. Takahagi, Experimental Conditions for a Highly Ordered Monolayer of Gold Nanoparticles Fabricated by the Langmuir-Blodgett Method, *J. Vac. Sci. Technol. B*, **19**, (2001), 2045-2049.
21. V. Santhanam, J. Liu, R. Agarwal and R. P. Andres, Self-assembly of Uniform Monolayer Arrays of Nanoparticles, *Langmuir*, **19**, (2003), 7881-7887.
22. V. Santhanam and R. P. Andres, Microcontact Printing of Uniform Nanoparticle Arrays, *Nano Letters*, **4**, (2004), 41-44.
23. S. Huang, K. Minami, H. Sakaue, S. Shingubara and T. Takahagi, Effects of the Surface Pressure on the Formation of Langmuir-Blodgett Monolayer of Nanoparticles, *Langmuir*, **20**, (2004), 2274-2276.
24. S. Chen, Langmuir-Blodgett Fabrication of Two-dimensional Robust Cross-linked Nanoparticle Assemblies, *Langmuir*, **17**, (2001), 2878-2884.
25. J. Liao, M. A. Mangold, S. Grunder, M. Mayor, C. Schönenberger and M. Calame, Interlinking Au Nanoparticles in 2D Arrays via Conjugated Dithiolated Molecules, *New Journal of Physics*, **10**, (2008), 065019(1-7).
26. Y. Song and R.W. Murray, Dynamics and Extent of Ligand Exchange Depend on Electrical Charge of Metal Nanoparticles, *J. Am. Chem. Soc.*, **124**, (2002), 7096-7102.

-
27. R. L. Donkers, Y. Song and R. W. Murray, Substituent Effects on the Exchange Dynamics of Ligands on 1.6 nm Diameter Gold Nanoparticles, *Langmuir*, **20**, (2004), 4703-4707.
 28. R. Hong, J. M. Fernandez, H. Nakade, R. Arvizo, T. Emrick and V. M. Rotello, In Situ Observation of Place Exchange Reactions of Gold Nanoparticles. Correlation of Monolayer Structure and Stability, *Chem. Comm.*, **22**, (2006), 2347-2349.
 29. F. L. Leibowitz, W. Zheng, M. M. Maye and C.-J. Zhong, Structures and Properties of Nanoparticle Thin Films Formed via a One-step Exchange-Cross-Linking-Precipitation Route, *Anal. Chem.*, **71**, (1999), 5076-5083.
 30. A. C. Templeton, W. P. Wuelfing and R. W. Murray, Monolayer-protected Cluster Molecules, *Acc. Chem. Res.*, **33**, (2000), 27-36.
 31. H. Valkenier, E. H. Huisman, P. A. van Hal, D. M. de Leeuw, R. C. Chiechi and J. C. Hummelen, Formation of High-quality Self-assembled Monolayers of Conjugated Dithiols on Gold: Base Matters, *J. Am. Chem. Soc.*, **133**, (2011), 4930-4939.
 32. E. C. Constable, W. Meier, C. Nardin and S. Mundwiler, Reversible Metal-directed Assembly of Clusters of Vesicles, *Chem. Commun.*, (1999), 1483-1484.
 33. J.-F. Dayen, V. Faramarzi, M. Pauly, N. T. Kemp, M. Barbero, B. P. Pichon, H. Majjad, S. Begin-Colin and B. Doudin, Nanotrench for Nano and Microparticle Electrical Interconnects, *Nanotechnology*, **21**, (2010), 335303(1-7).
 34. C. M. Guédon, *Molecular Charge Transport: Relating Orbital Structures to the Conductance Properties*. Ph. D. Thesis, Leiden University, The Netherlands, **2012**.
 35. G. Mie, Beiträge Zur Optik Trüber Medien, Speziell Kolloidaler Metallösungen, *Ann. Phys.*, **25**, (1908), 377-445.
 36. J. Wang, W. M. Lau and Q. Li, Effects of Particle Size and Spacing on the Optical Properties of Gold Nanocrystals in Alumina, *Journal of Applied Physics*, **97**, (2005), 114303(1-8).
 37. K. Kneipp, Surface-enhanced Raman Scattering, *Physics Today*, **60**, (2007), 40-46.
 38. U. K. Sur, Surface-enhanced Raman Spectroscopy Recent Advancement of Raman Spectroscopy, *Resonance*, **15**, (2010), 154-164.
 39. P. L. Stiles, J. A. Dieringer, N. C. Shah and R. P. van Duyne, Surface-enhanced Raman Spectroscopy, *Annu. Rev. Anal. Chem.*, **1**, (2008), 601-626.
 40. C. L. Haynes, A. D. McFarland and R. P. van Duyne, Surface-enhanced Raman Spectroscopy, *Analytical Chemistry*, **77**, (2005), 338A-346A.
 41. J. Popp and T. Mayerhöfer, Surface-enhanced Raman Spectroscopy, *Anal. Bioanal. Chem.*, **394**, (2009), 1717-1718.
 42. A. Campion and P. Kambhampati, Surface-enhanced Raman Scattering, *Chemical Society Reviews*, **27**, (1998), 241-250.
 43. M. Moskovits, Surface-enhanced Raman Spectroscopy: a Brief Retrospective, *J. Raman Spectrosc.*, **36**, (2005), 485-496.
 44. D. L. Jeanmaire and R. P. van Duyne, Surface Raman Spectroelectrochemistry Part I. Heterocyclic, Aromatic, and Aliphatic Amines Adsorbed on the Anodized Silver Electrode, *J. Electroanal. Chem.* **84**, (1977), 1-20.
 45. M. G. Albrecht and J. A. Creighton, Anomalously Intense Raman Spectra of Pyridine at a Silver Electrode, *J. Am. Chem. Soc.*, **99**, (1977), 5215-5217.

46. A. Campion, J. E. Ivanecky III, C. M. Child, and M. Foster, On the Mechanism of Chemical Enhancement in Surface-enhanced Raman Scattering, *J. Am. Chem. Soc.*, **117**, (1995), 11807-11808.
47. S. Schlücker, Surface-enhanced Raman Spectroscopy: Concepts and Chemical Applications, *Angew. Chem. Int. Ed.*, **53**, (2014), 2-42.

4



Enhancing the molecular signature in molecule-nanoparticle networks via inelastic cotunneling

Here, we investigate charge transport in networks of nanoparticles linked by molecular spacers, as a function of temperature. Specifically, we compare octanethiol-based structures with networks containing dithiolated OPE3. Around room temperature, the resistance ratio of these two types of devices is around 50. However, at lower temperatures, this ratio increases dramatically, to 10^5 . We demonstrate that this is a result of crossing from the sequential tunneling regime to the inelastic cotunneling regime. The consequence is that the intrinsic molecular properties can be amplified through nanoscale engineering.

This chapter is based on the article published in *Adv. Mater.*, **25**, (2013), 400-404.

Enhancing the Molecular Signature in Molecule-Nanoparticle Networks via Inelastic Cotunneling.
J.-F. Dayen, E. J. Devid, M. V. Kamalakar, D. Golubev, C. M. Guédon, V. Faramarzi, B. Doudin and S. J. van der Molen.

4.1 Introduction of molecule-nanoparticle ensembles

In the field of molecular charge transport, several techniques have been developed to probe molecular conductance properties, ranging from mechanically controllable break junctions to large-area molecular junctions [1]. Two-dimensional (2D) molecule-nanoparticle ensembles have proven to combine several advantageous properties [2-4]. In these structures the gold nanoparticles are ordered in a triangular 2D-network and bridged by a molecular species of choice. In such networks the sheet resistance R is a direct measure of the (spatially averaged) conductance value of a nanoparticle-molecule-nanoparticle junction, R_T . This provides direct macroscopic access to the charge transport through molecules. Furthermore, these networks are defect-tolerant, resulting in device robustness, in particular when compared to most molecular devices. Finally, the molecules within the network are easily probed or addressed by an external stimulus, such as light. The latter provides the unique possibility to investigate the properties of these molecules that may possess a passive or active functionality. A nice example of active functional molecules are switchable light-sensitive molecules. These molecules have demonstrated their reversible photochromic switching for several types of diarylethene derivatives inserted within molecular-nanoparticle arrays [5-7]. Opto-electronic devices based on functional nano-sized elements have become possible.

The critical question remains if such devices can reach high on-off ratios (on-state conductance divided by off-state conductance), i.e. ratios of several orders of magnitude. Here, we investigate a principle path towards enhancing this ratio artificially, by making use of the electrostatic properties of the nanoparticles advantageously. Below, we present the concept in a nut shell.

From a simple perspective, molecule-nanoparticle ensembles can be described as granular systems containing metal particles, where these particles are embedded in an insulating molecular matrix [8]. However, molecule-nanoparticle ensembles will display an intricate combination of the properties of both ingredients: the molecules and the metal nanoparticles. The effect of the metal nanoparticles in a molecule-nanoparticle ensemble is the following. The smaller these nanoparticles get, the stronger the effect of local electron-electron repulsion will be. If the thermal energy is lower than the typical energy needed to move an electron to a neighbouring nanoparticle (the charging energy, E_C), the nanoparticles cannot be treated as ideal

metallic shorts any longer, and the Coulomb energy barrier suppresses transport (see Figure 4.1(a)). This is called Coulomb blockade [9]. Still, some current can flow, and at lower temperatures this happens via a process called multiple inelastic cotunneling (see below for more details). This process, illustrated in Figure 4.1(b), involves coordinated charge transfer of several charges through typically j junctions (where j can be 2, 3, 4, ...) [8, 10-13]. As a result, the conductance of a network device will be related to the product of the transfer probabilities of each junction involved. In other words, the network's resistance will approximately scale with $(R_T)^j$, where R_T denotes the resistance of a single (molecular) junction. This differs significantly from the linear scaling of network resistance with R_T , which is expected when Coulomb blockade does not occur (see Chapter 3). The above has a remarkable consequence for networks containing switchable molecules. In the multiple cotunneling regime, the on-off ratio P of such devices will scale as $P = \frac{R_{device}^{OFF}}{R_{device}^{ON}} = \left(\frac{R_{mol}^{OFF}}{R_{mol}^{ON}} \right)^j$. Thus, the on-off ratio of the device is enhanced by a power $j > 1$ as compared to the on-off ratio of a single molecular junction.

Here, we present a proof-of-principle experiment of this 'enhancement' via inelastic multiple cotunneling. To do so, we use the methodology of molecular exchange in 2D nanoparticle networks. We compare two types of *passive* networks: one with a higher resistance (based on octanethiols, comparable to an 'off-state') and one with a lower resistance (the same networks, but after an OPE3-dithiol exchange step, representing the "on-state"). The procedure behind molecular exchange is explained in paragraph 3.2 and also in past reports [3, 4, 6].

Systematic temperature-dependent transport measurements on so-called nanotrench devices (see below and see paragraph 3.4) will be presented to provide a more complete insight into the regimes of conduction. Interestingly, the work described here also sheds new light on a set of recent experiments which have shown different current-voltage dependencies [14-16]. We demonstrate that these dependencies are signatures of cotunneling processes in different regimes. Indeed, the unique possibility to modify the interparticle tunneling probability via molecular exchange, allows us to provide a unified picture of conduction in ordered 2D networks. Let us first gain further insight in the regimes expected.

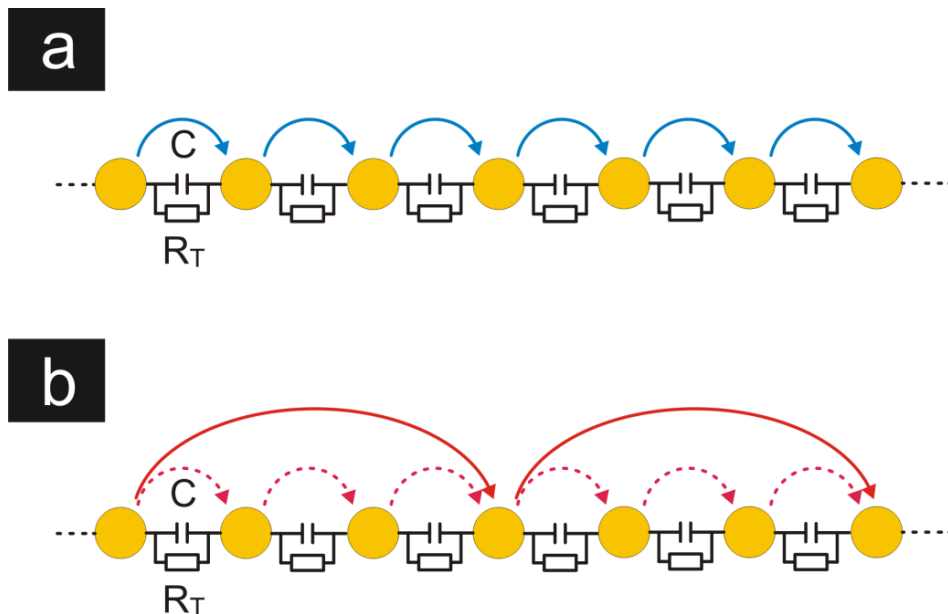


Figure 4.1: Simplified diagrams of the nanoparticle circuit, with Au clusters (yellow circles), having charging energy E_C , separated by molecular spacers of resistance R_T . (a) The sequential tunneling diagram shows tunneling between neighbours as the origin of conduction (represented by small blue solid arrows). (b) The cotunneling regime diagram illustrates how charge transfer takes place through a succession of jumps (large red solid arrows) involving cooperative tunneling of j electrons (small red dashed arrows) through $j + 1$ nanoparticles.

4.2 Charge transport mechanisms expected

Several regimes of charge transport are accessible for molecule-nanoparticle ensembles. The manifestation of these will depend on detailed characteristics, such as the molecular species used, the nanoparticle properties and the structuring of the ensemble itself [17].

Let us first consider elevated temperatures, i.e. $k_B T \gg E_C$; the regime where the nanoparticles behave as simple metal electrodes. Transport is then dominated by sequential (off-resonant) tunneling from one gold particle to another via the molecule(s) in between them. Hence, the conductance of a network is directly proportional to the conductance of the molecular intermediates (see Chapter 1 and 3). At lower temperatures, i.e. $k_B T \leq E_C$, however, transport is strongly affected by Coulomb

interaction between the electrons. If an electron tunnels from one nanoparticle to a neighbouring one, both of them become electrically charged, i.e., one with a hole, one with an electron. The electrostatic energy associated with this charge configuration for a nanoparticle, the charging energy E_C , plays a central role in theory as it raises a barrier for transport. This energy can be written as $E_C = \frac{e^2}{2C}$, where e is the electron charge and C is the total capacitance associated with a nanoparticle in a network. The latter depends on the number of nanoparticles surrounding a single nanoparticle with self-capacitance C_s . Specifically, we have $C = C_s + \sum C_i$, where, C_i is the capacitance with respect to each of the neighbouring particles. Charging effects can dramatically suppress electron transport. For a nanoparticle network exhibiting Coulomb blockade, the conductance properties can be described by the (semi-classical) ‘orthodox theory’, assuming the metal nanoparticles in alkanethiol-metal nanoparticle ensembles have periodic ordering [18-20]. In this regime, the sequential contribution to the conductance becomes exponentially suppressed via an Arrhenius relation:

$$G \propto e^{-E_C/k_B T}, \quad (4.1)$$

where higher order processes are ignored. Interestingly, however, in weakly coupled gold nanoparticle assemblies, the conductance values start to deviate from orthodox theory at lower temperatures [14, 16, 18, 21]. In fact, (multiple) inelastic cotunneling becomes important. In this regime, a set of virtual states allow for cooperative electron transfer over length scales beyond one particle-particle distance, leaving a hole behind (see Figure 4.1(b)) [14].

Unfortunately, a quantitative analysis of multiple inelastic cotunneling transport in granular metals is very difficult, because of the complexity of the exact analytical expressions for the current. In order to overcome this problem, Belobodorov *et al.* [14] have proposed an approximate formula which captures the basic physics. For an ideal system with identical tunnel (or in our case: molecular) resistances and equal charging energy for all nanoparticles, a model reminiscent to variable range hopping, referred to as variable range cotunneling (VRC), yields a current I versus voltage V relation given by [14]:

$$I \propto V_{jct} \sum_j \left(\frac{\hbar}{e^2 R_T} \right)^j \left(\frac{k_B^2 T^2 + e^2 V_{jct}^2}{E_C^2} \right)^{j-1} \exp \left(- \frac{E_C - jeV_{jct}}{k_B T} \right). \quad (4.2)$$

The current in this model is given by a Taylor series in the small parameter h/e^2R_T . Here T is the temperature, k_B Boltzmann's constant, and $V_{jet} = V/N$ is the voltage drop over a single tunnel junction connecting two neighbour nanoparticles (with N the total number of tunnel barriers along the array). The summation in equation 4.2 runs over the number of junctions j involved in the cotunneling events.

To appreciate equation 4.2, we first note that the contribution of cotunneling through j junctions is proportional to $(h/e^2R_T)^j$ and hence decreases strongly with increasing j . Still, at lower temperatures, multiple cotunneling may become the dominant process. This is due to a counterbalancing effect, which is related to the Boltzmann term in equation 4.2. In fact, the electrostatic potential barrier associated with the process decreases with increasing j . The reason for this is that an electron and a hole created in the array after a cotunneling event are separated by j junctions. In the experimentally relevant case of weak screening, one can roughly estimate the interaction energy between them as $U \sim e^2/\epsilon L$, where L is the distance between the nanoparticles hosting the electron and the hole. Since $L = jr$ in closely packed array of particles, with r the average center-to-center distance between two nanoparticles, this energy U may be transformed to a form that explicitly reveals the reduction of the potential barrier: $U \approx E_C / j$.

All in all, the competition between the decreasing factor $(h/e^2R_T)^j$ and increasing activation exponent $e^{(-U/k_B T)}$ with j , determines the optimal number of junctions, $j_{opt} \equiv N_{cot}$, through which cotunneling occurs. At low temperatures, N_{cot} may reach 5 or even more. To illustrate this, Figure 4.2 shows an example calculation of the current's dependence on temperature and j via cotunneling, according to equation 4.2.

Figure 4.2(a) displays how the partial current, associated with each (co)tunnel process involving j junctions, increases with temperature. (Note that the total current versus temperature is given by the sum of these curves, for all j .) Clearly, the current due to sequential tunneling ($j = 1$) dominates at higher temperatures. However, as T decreases, a transition occurs to multiple cotunneling. First, the current due to $j = 2$ dominates, so here $N_{cot} = j_{opt} = 2$. At even lower T , higher values of N_{cot} can be found. Figure 4.2(b) displays the same data set in a different plot, showing partial current values for a series of temperatures versus j . Here, the competition between the cotunneling probability factor $(h/e^2R_T)^j$ and the activation term $e^{(-E_C/jk_B T)}$ is visualized more clearly.

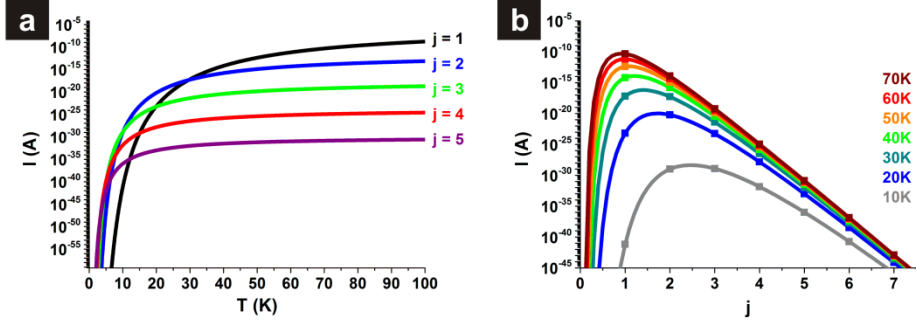


Figure 4.2: (a) Calculation of the partial current for each of the (multiple co-)tunneling processes, involving j junctions, as a function of temperature. (b) Partial current versus j at various temperatures. Both (a) and (b) are calculated from equation 4.2, using $R_T = 1 \text{ M}\Omega$, $V_{jct} = 0.5 \text{ mV}$, $E_C = 0.072 \text{ eV}$.

Again, we see that at lower temperatures the optimal $j_{opt} = N_{cot}$ shifts to values greater than 1. In Appendix A.1, we derive the approximate temperature-dependence of N_{cot} to find:

$$N_{cot} \approx \sqrt{\frac{E_C}{k_B T \ln(e^2 R_T / h)}} \propto 1/\sqrt{T}. \quad (4.3)$$

Finally, we note that the summation in equation 4.2 is restricted by the requirement of a positive potential barrier, $U > 0$. This specifically has consequences for the case of high applied biases. Since the effective voltage drop over the set of j junctions lowers the Boltzmann term, the requirement $U > 0$ restricts the number of junctions to: $j \leq N_{max} \approx \sqrt{E_C / eV_{jct}}$. Formally, higher values of j also contribute to the current, but the corresponding terms do not contain an activation exponent. Since this eliminates the term favouring higher j , the full expression quickly decays with increasing j . Thus these terms can be ignored.

At low temperatures, when the charging energy E_C becomes larger than $k_B T$, equation 4.2 predicts how the current will evolve with voltage-bias. Interestingly, this relation can be approximated by three asymptotic expressions (see Appendix A.1), categorized as cotunneling regimes C1, C2, and C3, for different voltage ranges between neighbouring particles:

$$\text{C1:} \quad I \propto V, \quad \text{for } eV_{jct} \ll k_B T. \quad (4.4)$$

$$\text{C2: } I \propto V^\alpha, \text{ where } \alpha = 2N_{cot} - 1, \text{ for } k_B T < eV_{jct} < k_B T \ln\left(\frac{e^2 R_T}{h}\right). \quad (4.5)$$

$$\text{C3: } I \propto \exp\left[-\sqrt{\frac{V^*}{V}}\right], \quad \text{for } k_B T \ln\left(\frac{e^2}{h} R_T\right) < eV_{jct}. \quad (4.6)$$

In regime C1, i.e. the very low-bias regime, equation 4.2 yields Ohmic behaviour.

In regime C2, the middle part of equation 4.2, which stems directly from cotunneling theory, becomes important. This results in a strong power law dependence of the $I(V)$ curves, with a power that depends on N_{cot} .

Finally, an interesting regime is reached in C3, where the current scales with voltage in an Efros-Shklovskii-like fashion, but with temperature replaced by voltage. In other words, the current depends exponentially on $-\sqrt{V^*/V}$, where V^* is a constant related to E_C and R_T . Interestingly, this relation connects to the temperature-dependence expected for low-bias voltages (within regime C1). In that situation, a true Efros-Shklovskii dependence is anticipated, i.e.

$$G \propto \exp\left[-\sqrt{\frac{T^*}{T}}\right], \quad (4.7)$$

where T^* depends on E_C and R_T and is approximately constant (see Appendix A.1).

For completeness, at very high voltage biases $eV_{jct} \approx E_C$, the system is in the sequential tunneling regime, as first proposed by Ref. [22].

4.3 Charge transport measurements on nanotrench devices

To fully characterize transport mechanisms, temperature and bias voltage are to be varied over a wide range. Anticipating the sample resistance to dramatically increase when lowering the temperature, a device structure (called a nanotrench device, see paragraph 3.4) with a large width-to-length aspect ratio (~ 100) is used. This limits the number of nanoparticles spanning the gap between the electrodes. In this way, our samples, involving a minimum number of charge transfer steps, avoid percolation or distributions of cotunneling domain sizes which often complicate the data interpretation. Furthermore, we make use of the advantageous possibility to modify the inter-particle resistance values in the molecule-gold nanoparticle network by molecular exchange. This gives us an extra tool to assess conduction.

For the nanotrench devices, electron beam lithography is used to pattern Ti (3 nm)/Au (47 nm) electrodes separated by a gap of 100-150 nm length and 10 μm width over silicon oxide substrate. On top of these structures, a two-dimensional network of coated gold nanoparticles (~ 8.5 nm in diameter, covered with octanemonothiols: “C8”) is deposited using a polydimethylsiloxane (PDMS) microcontact printing method, following literature procedures [3, 4, 6, 23, 24]. Unlike stamping large arrays between widely gapped electrode pairs, [3, 4, 6, 7, 25, 26] the process of stamping between narrowly spaced electrodes proved quite challenging and order is only locally conserved. A typical sample can be seen in Figure 4.3.

We first characterized the as-prepared samples, with C8 spacers, at room temperature. Low-temperature electrical measurements were carried out using a semiconductor parameter analyzer suitable for low-signal measurements, with samples inside a He-flow cryostat of 1.5 K base temperature. Figure 4.4(a) shows temperature-dependent I - V curves for a typical C8 sample. After characterization, the C8 samples were transferred to a glove box, where a molecular exchange procedure with conjugated oligo(phenylene ethynylene)-dithiol (OPE) molecular bridges (referred as OPE state) was performed, in an OPE solution in tetrahydrofuran for 24 hours. This resulted in a decrease of the room-temperature resistance of typically two orders of magnitude, in agreement with previous reports [3, 26]. The OPE-samples were then studied as a function of temperature.

We found good reproducibility after temperature sweeps (without hysteresis), confirming the robustness of our samples. We also checked that molecular exchange was reversible, by confirming that the temperature-dependent transport of a C8 back-exchanged sample was similar to the initial C8 sample. Finally, measurements were reproducible from sample to sample, within a scaling factor related to the nanotrench filling after stamping the particles.

4.4 Charge transport properties of C8 and OPE exchanged gold nanoparticle networks

Measurements of I - V curves for various temperatures are presented in Figures 4.4(a) and 4.4(b), for C8 and OPE (i.e. exchanged) samples, respectively. All samples showed a transition from ohmic behaviour at room temperature, to non-linear behaviour below a temperature in the 100 K to 200 K range.

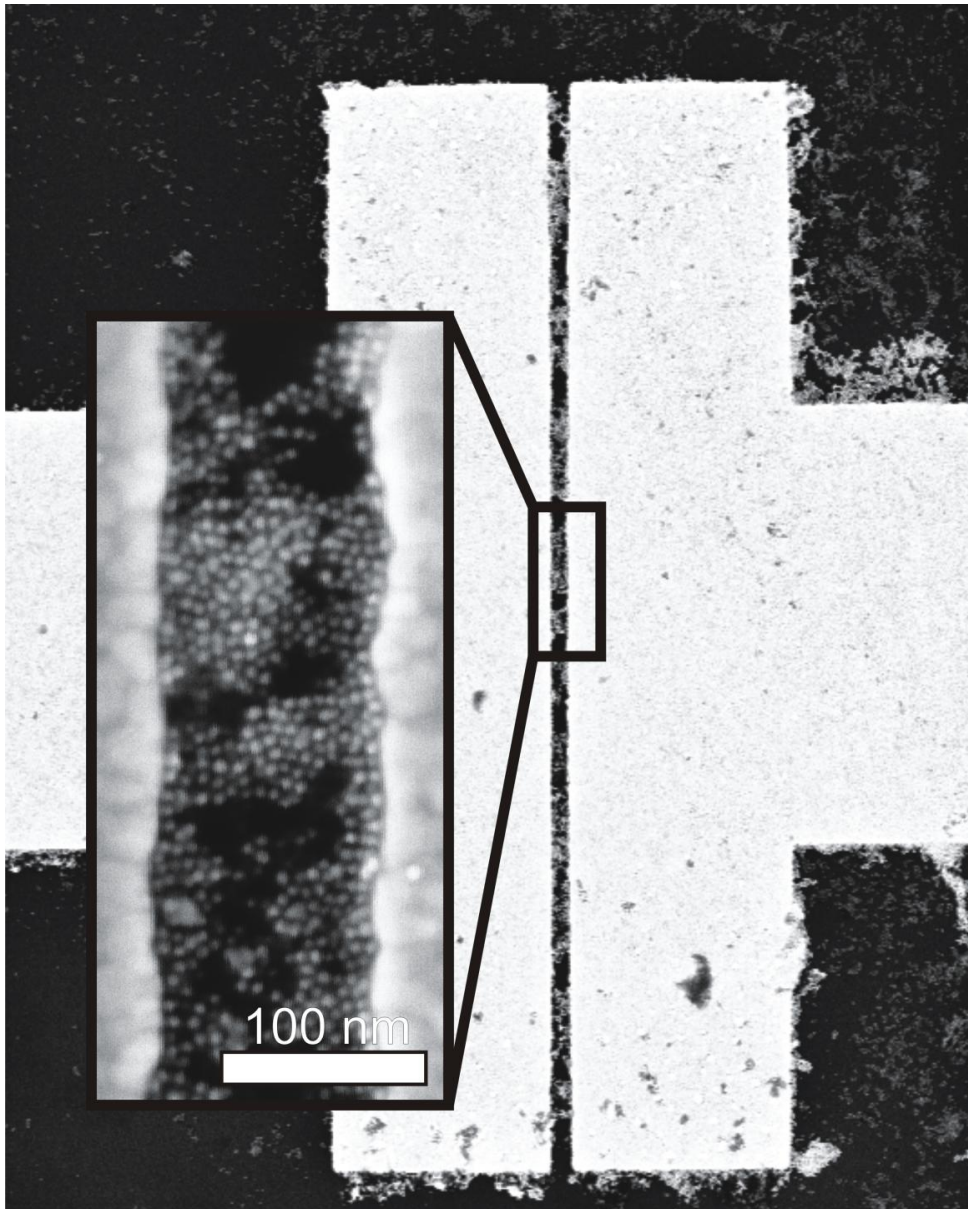


Figure 4.3: Scanning electron microscope image of a 2D nanoparticle network sample with a zoomed inset showing the nanotrench coverage.

In the same temperature range the low-bias resistance also increases significantly (see inset of Figure A-1(a) in Appendix A.2). This is consistent with the charging energy of the nanoparticles estimated from the simplest two concentric shells model,

$$E_C = \frac{e^2}{8\pi\epsilon_0\epsilon_r} \left(\frac{1}{r} - \frac{1}{r+d} \right), \quad (4.8)$$

with ϵ_0 the vacuum permittivity, ϵ_r the relative permittivity of the molecules surrounding the nanoparticles of radius r and separation d . This gives $E_C^{\text{C8}} \approx 17 \text{ meV} \approx 200 \text{ K}$ and $E_C^{\text{OPE}} \approx 14 \text{ meV} \approx 150 \text{ K}$, respectively. The slight change of charging energy when exchanging the molecules, interpreted as a modification of the medium permittivity, is consistent with our findings of the C8 state having a slightly more pronounced non-linear behaviour at low temperatures, which can be interpreted as an increase of the charging energy, not exceeding twice the OPE value.

Power-law behaviour of the I - V curves is illustrated in Figure 4.4(c), where the data for an OPE sample are plotted double-logarithmically. At sufficiently high temperatures, i.e. when the thermal energy overcomes the charging energy E_C , the network exhibits an almost ohmic behaviour, with a macroscopic sheet resistance proportional to R_T . At lower temperatures, but at high-bias voltages, $eV_{jct} \sim E_C$, sequential tunneling through the blockaded islands becomes the dominant process. The corresponding region is indicated as “sequential” (labelled “seq” in Figure 4.4(c)). This regime has been discussed in much detail in literature [17, 22, 27]. At low biases and low temperatures, however, the VRC regime is entered, described by equation 4.2, which is at the heart of this study. Figure 4.4(c) separates the areas where regimes C1, C2 and C3 apply (see equation 4.4 till 4.6 and Appendices A.3 and A.4). Within region C1, linear I - V curves are found (see equation 4.4). In contrast, in the C2 zone indicated, the slope on the double-logarithmic scale reveals power-law behaviour with an exponent that depends on temperature, reaching values of up to 7 (see equation 4.5). Indeed, Tran *et al.* also reported temperature-dependent power law behaviour, characteristic of the regime C2, with similar exponents [14, 15].

On the other hand, Moreira *et al.* recently emphasized the applicability of an Efros-Shklovskii-type relation, comparable to equation 4.6. They explained this behaviour phenomenologically, by assuming that the voltage dependence for cotunneling mirrors the zero-bias temperature dependence [11, 12].

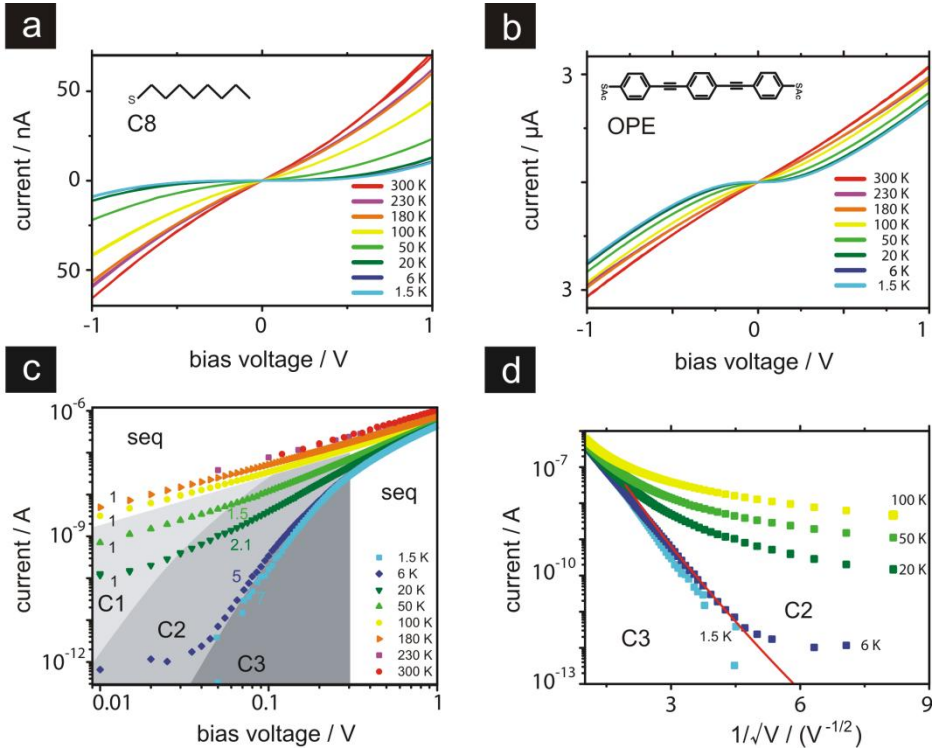


Figure 4.4: I - V curves of a nanoparticle network, in the C8 (Figure 4.4(a)) and OPE (Figure 4.4(b)) states respectively, measured at several temperatures. (c) Log-Log plot of OPE data, illustrating the power law behaviour, $I \propto V^\alpha$, and discriminating the different conductance regimes (data are taken from a second sample). $\alpha = 1$ is expected in the sequential tunneling (labelled “seq”) and thermally activated cotunneling (labelled “C1”) regimes. In regime C2 (multiple inelastic cotunneling), however, the number of cotunneling events, N_{cot} , relates to $\alpha = 2N_{cot} - 1$ (with an exponent between 1.5 and 7, indicated next to the curves). (d) Semilog plot of current versus $1/\sqrt{V}$ for the data set in Figure 4.4(c), illustrating the transition between regime C2 and the Efros-Shklovskii-like behaviour (regime C3), observed at the lowest temperatures. See Appendix A.3 for a similar analysis of the $I(V)$ -curves in panels (a)-(b).

Our experimental results (see Figures 4.4(c) and 4.4(d)), show that the lowest-temperature I - V curves turn out to be at the boundary between the power law form (region C2) and Efros-Shklovskii-type voltage dependence (region C3).

The distinction between the power law behaviour of regime C2 and the Efros-Shklovskii-type behaviour of regime C3, however, is not visible on a log-log plot such as Figure 4.4(c) due to the limited V and I ranges. In order to check the existence of regime C3 at high-bias and low temperature, we replot the data in an Efros-type plot with voltage playing the role of temperature, i.e., we plot the current semi-logarithmically versus $1/\sqrt{V}$. In addition, for full consistency, the transition from C2 to C3 regimes should take place close to the C2-C3 delimitation line predicted by the theory. In Figure 4.4(d) we illustrate that the lowest-temperature curves also satisfy a $I \propto \exp\left(-\sqrt{V^*/V}\right)$ dependence, expected for regime C3 (see equation 4.6). Moreover, as it can be seen in Figure 4.4(c) and 4.4(d), the region at which the transition from C2 to C3 is observed, matches well with the boundary predicted by theory (see also Appendix A.4). In Appendix A.3, we show that the same observations and conclusions hold for the C8 case. Our measurements therefore indicate that the discrepancy between transport regimes reported previously (power law versus Efros-Shklovskii-like) [14-16] can possibly be explained within a model of multiple inelastic cotunneling based on the equation 4.2. The transfer between the various regimes is continuous. This is the first main conclusion of this work.

Interestingly, the cotunneling regime corresponds to a charge transfer probability proportional to $(R_T)^{N_{cot}}$ i.e. the product of the resistances of the N_{cot} junctions involved. This specific property leads to new opportunities for device applications, especially when seeking for increased susceptibilities. Spin-dependent resistance in magnetic systems enhanced by cotunneling is a well-documented example [28], as recently shown in a nanoparticles network [13]. Figure 4.5 provides a more complete insight into the transport properties in regime C2. To show that the deduced N_{cot} values are robust, the temperature-dependent N_{cot} values are plotted as a function of $\sqrt{1/T}$ (see Figure 4.5(a)), as anticipated by equation 4.3. The N_{cot} values are deduced from fitting the I - V curves in the C2 region to the power law $I \propto V^{2N_{cot}-1}$ for several samples, both in the C8 and OPE states (see also Appendices A.3 and A.4). The change of R_T when exchanging the molecules does not significantly alter the number of particles over which coherent cotunneling occurs, here taking place over 1 to 4 particles when cooling down the samples. Having gained confidence that the data of C8 and OPE

relate to similar numbers of cotunneling events, the evolution of the current scales ratio between the two type of molecules when cooling down can be made explicit.

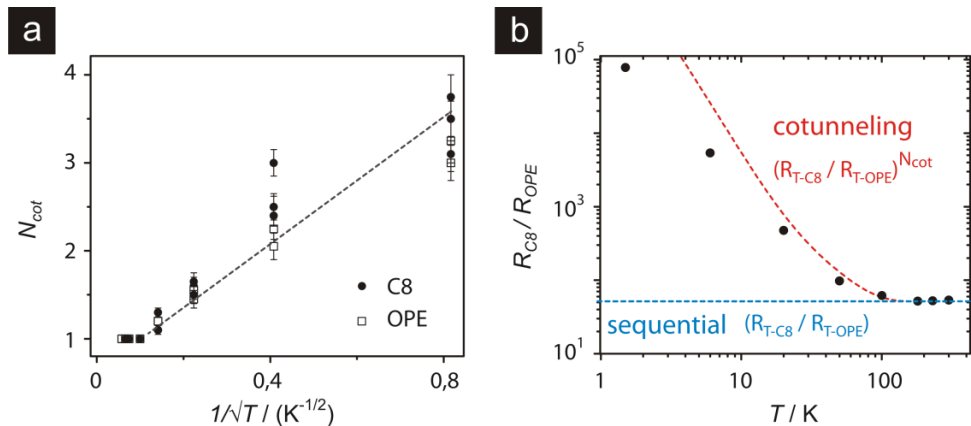


Figure 4.5: (a) The number of junctions N_{cot} involved in a cotunneling event at several temperatures, for several samples in C8 and OPE states. The dotted line is a guide to the eye, following the model of inelastic multiple cotunneling $N_{cot} \approx \sqrt{E_C / k_B T \ln(e^2 R_{jct} / h)}$. (b) The temperature evolution of the resistance ratio R_{C8}/R_{OPE} of the network resistance in the C8 and OPE states. The red dotted line shows the model behaviour, with a transition from classical regime $R_{C8}/R_{OPE} \propto R_{T-C8}/R_{T-OPE}$, to cotunneling regime $R_{C8}/R_{OPE} \propto (R_{T-C8}/R_{T-OPE})^{N_{cot}}$. The blue dotted line shows the expected curve for sequential tunneling only.

The key experimental outcome, demonstrating enhanced susceptibility, is shown in Figure 4.5(b). The ratio R_{C8}/R_{OPE} , i.e. the ratio of the full network resistances before and after molecular exchange, is around 50 at room temperature, and it remains unchanged down to 200 K, i.e. as long as the samples are in the sequential tunneling regime. At lower temperatures, however, the sample enters the cotunneling regime and this ratio increases up to 10^5 , now being governed by $(R_{T-C8}/R_{T-OPE})^3$ to $(R_{T-C8}/R_{T-OPE})^4$ at 1.6 K (cf. Figure 4.5(a)). This spectacular increase of R_{C8}/R_{OPE} ratio matches well with the cotunneling trend expected (see red dotted line in Figure 4.5(b)). These results are hence a direct indication of cotunneling processes taking place in nanoparticles network.

4.5 Conclusions

In conclusion, molecular exchange in metallic nanoparticle-molecule networks is a high-value tool for validating a complete picture of cotunneling. By putting our data in the light of equation 4.2, a simple picture of cotunneling transport signatures related to the probed energy scale allows us to reconcile the different approaches found in the literature. The temperature change of the number N_{cot} of junctions involved in cotunneling confirms the trend $N_{cot} \propto \sqrt{1/T}$, as expected from a variable range cotunneling model.

Additionally, we show that in the cotunneling regime a resistance modification can be amplified by several orders of magnitude. This enhancement is also expected for systems for which molecular transport properties are modified under external conditions. For example, the on/off ratio of light-sensitive switchable molecular devices may be strongly improved in this way. To utilize this effect at room temperature, networks based on smaller nanoparticles (roughly < 5 nm in diameter) should be used. All in all, nanoparticle-based molecular devices do not only have advantages in terms of robustness and reproducibility, but also in terms of enhanced susceptibility to external stimuli. The future expectation is that these nanoparticle-based molecular devices can be of valuable use to a wide variety of multifunctional molecular materials.

4.6 References

1. H. B. Akkerman, P. W. M. Blom, D. M. de Leeuw and B. de Boer, Electron Tunneling Through Alkanedithiol Self-assembled Monolayers in Large-area Molecular Junctions, *Nature*, **441**, (2006), 69-72.
2. R. P. Andres, J. D. Bielefeld, J. I. Henderson, D. B. Janes, V. R. Kolagunta, C. P. Kubiak, W. J. Mahoney and R. G. Osifchin, Self-assembly of a Two-dimensional Superlattice of Molecularly Linked Metal Clusters, *Science*, **273**, (1996), 1690-1693.
3. J. Liao, L. Bernard, M. Langer, C. Schönberger and M. Calame, Reversible Formation of Molecular Junctions in 2D Nanoparticle Arrays, *Adv. Mater.*, **18**, (2006), 2444-2447.
4. L. Bernard, Y. Kamdzhilov, M. Calame, S. J. van der Molen, J. Liao and C. Schönberger, Spectroscopy of Molecular Junction Networks Obtained by Place Exchange in 2D Nanoparticle Arrays, *J. Phys. Chem. C*, **111**, (2007), 18445-18450.

5. K. Matsuda, H. Yamaguchi, T. Sakano, M. Ikeda, N. Tanifuji and M. Irie, Conductance Photoswitching of Diarylethene-Gold Nanoparticle Network Induced by Photochromic Reaction, *J. Phys. Chem. C*, **112**, (2008), 17005-17010.
6. S. J. van der Molen, J. Liao, T. Kudernac, J. S. Agustsson, L. Bernard, M. Calame, B. J. van Wees, B. L. Feringa and C. Schönenberger, Light-controlled Conductance Switching of Ordered Metal-Molecule-Metal Devices, *Nano Lett.*, **9**, (2009), 76-80.
7. S. J. van der Molen and P. Liljeroth, Charge Transport Through Molecular Switches, *J. Phys.: Condens. Matter*, **22**, (2010), 133001(1-30).
8. I. S. Beloborodov, K. B. Efetov, A. V. Lopatin and V. M. Vinokur, Granular Electronic Systems, *Reviews of Modern Physics*, **79**, (2007), 469-518.
9. C. J. Gorter, A Possible Explanation of the Increase of the Electrical Resistance of Thin Metal Films at Low Temperatures and Small Field Strengths, *Physica*, **17**, (1951), 777-780.
10. D. V. Averin and Y. V. Nazarov, Virtual Electron Diffusion during Quantum Tunneling of the Electric Charge, *Phys. Rev. Lett.*, **65**, (1990), 2446-2449.
11. I. S. Beloborodov, A. V. Lopatin, and V. M. Vinokur, Coulomb Effects and Hopping Transport in Granular Metals, *Phys. Rev. B*, **72**, (2005), 125121(1-20).
12. M. V. Feigel'man and A. S. Ioselevich, Variable Range Cotunneling and Conductivity of a Granular Metal, *JETP Lett.*, **81**, (2005), 277-283.
13. M. Pauly, J.-F. Dayen, D. Golubev, J.-B. Beaufrand, B. P. Pichon, B. Doudin and S. Bégin-Colin, Co-tunneling Enhancement of the Electrical Response of Nanoparticle Networks, *Small*, **8**, (2012), 108-115.
14. T. B. Tran, I. S. Beloborodov, J. Hu, X. M. Lin, T. F. Rosenbaum and H. M. Jaeger, Sequential Tunneling and Inelastic Cotunneling in Nanoparticle Arrays, *Physical Review B*, **78**, (2008), 075437(1-9).
15. T. B. Tran, I. S. Beloborodov, X. M. Lin, T. P. Bigioni, V. M. Vinokur and H. M. Jaeger, Multiple Cotunneling in Large Quantum Dot Arrays, *Phys. Rev. Lett.*, **95**, (2005), 076806(1-4).
16. H. Moreira, Q. Yu, B. Nadal, B. Bresson, M. Rosticher, N. Lequeux, A. Zimmers and H. Aubin, Electron Cotunneling Transport in Gold Nanocrystal Arrays, *Phys Rev Lett.*, **107**, (2011), 176803(1-5).
17. A. Zabet-Khosousi and A.-A. Dhiran, Charge Transport in Nanoparticle Assemblies, *Chemical Reviews*, **108**, (2008), 4072-4124.
18. G.-L. Ingold and Y. V. Nazarov, *Charge Tunneling Rates in Ultrasmall Junctions*. In *Single Charge Tunneling*; H. Grabert, M. H. Devoret, Eds.; Plenum: New York, **1992**; 21-107.
19. M. Amman, R. Wilkins, E. Ben-Jacob, P. D. Maker and R. C. Jaklevic, Analytic Solution for the Current-Voltage Characteristic of Two Mesoscopic Tunnel Junctions Coupled Ion Series, *Phys. Rev. B*, **43**, (1991), 1146-1149.
20. P. D. Dresselhaus, L. Ji, S. Han, K. Lin, J. Lukens and K. K. Likharev, Single Electron Tunneling in Single Junctions and Multi-junction Systems, *Physica B: Physics of Condensed Matter*, **194**, (1994), 1335-1336.
21. M. M. A. Yajadda, K.-H. Müller and K. Ostrikov, Effect of Coulomb Blockade, Gold Resistance, and Thermal Expansion on the Electrical Resistance of Ultrathin Gold Films, *Physical Review B*, **84**, (2011), 235431(1-8).

-
22. A. A. Middleton and N. S. Wingreen, Collective Transport in Arrays of Small Metallic Dots, *Physical Review Letters*, **71**, (1993), 3198-3201.
 23. V. Santhanam and R. P. Andres, Microcontact Printing of Uniform Nanoparticle Arrays, *Nano Lett.*, **4**, (2004), 41-44.
 24. V. Santhanam, J. Liu, R. Agarwal and R. P. Andres, Self-assembly of Uniform Monolayer Arrays of Nanoparticles, *Langmuir*, **19**, (2003), 7881-7887.
 25. J.-F. Dayen, V. Faramarzi, M. Pauly, N. T. Kemp, M. Barbero, B. P. Pichon, H. Majjad, S. Begin-Colin and B. Doudin, Nanotrench for Nano and Microparticle Electrical Interconnects, *Nanotechnology*, **21**, (2010), 335303(1-7).
 26. C. M. Guédon, J. Zonneveld, H. Valkenier, J. C. Hummelen and S. J. van der Molen, Controlling the Interparticle Distance in a 2D Molecule-nanoparticle Network, *Nanotechnology*, **22**, (2011), 125205(1-5).
 27. D. V. Talapin, J-S. Lee, M. V. Kovalenko and E. V. Shevchenko, Prospects of Colloidal Nanocrystals for Electronic and Optoelectronic Applications, *Chem. Rev.*, **110**, (2010), 389-458.
 28. K. Yakushiji, S. Mitani, F. Ernult, K. Takanashi and H. Fujimori, Spin-dependent Tunneling and Coulomb Blockade in Ferromagnetic Nanoparticles, *Phys. Rep.*, **451**, (2007), 1-35.

5

The influence of molecular mobility on the properties of gold nanoparticle organic ligand networks

We prepare and investigate two-dimensional (2D) single layer arrays and multilayered networks of gold nanoparticles derivatized with conjugated hetero-aromatic molecules, i.e. S-(4-([2,6-(bipyrazol-1-yl)pyrid-4-yl]ethynyl)phenyl)thioate. This ligand molecule is used to cap the gold nanoparticles and will be referred to as S-BPP. The structures are fabricated by a combination of self-assembly and microcontact printing techniques, and are characterized by electron microscopy, UV-Vis spectroscopy and Raman spectroscopy. Selective binding of the S-BPP molecules to the gold nanoparticles via Au-S bonds is found, with no evidence for the formation of Au-N bonds between pyridine or pyrazole groups from the BPP and the gold surface. Subtle, but significant shifts with temperature of specific Raman S-BPP modes are also observed. These modes attribute to dynamic changes in the orientation and/or increased mobility of the molecules on the gold nanoparticle facets. As for their conductance, the temperature-dependence for S-BPP networks differs significantly from standard alkanethiol-capped networks, especially above 220 K. When relating the latter two observations, it appears that dynamic changes in the molecular layers effectively lower the molecular tunnel barrier for S-BPP-based arrays at higher temperatures.

5.1 Introduction to molecular ligand-nanoparticle ensembles

Inspired by nature, self-assembly is a bottom-up method to fabricate structures at all scales from nanometer-sized ingredients. In this way, new functional materials can be created with properties that are, in principle, based on the specific functionality of their building blocks [1]. An interesting approach, used for molecular conductance experiments, includes nanoparticles (~10 nm) incorporated to bridge the size gap between macroscopic electrodes (≥ 100 nm) and molecules (~1 nm) [2-8]. Typically, 2D arrays of gold nanoparticles capped by alkanethiols are created, after which dithiolated conjugated molecules are allowed to form molecular bridges between neighbouring nanoparticles [6, 8]. Although molecular insertion cannot be driven to completeness for thermodynamic reasons [9, 10], this protocol has proven successful in molecular electronics, e.g. by providing access to switchable molecular devices [11, 12]. The process can also be used for non-thiol ligands [13]. This Chapter extends the self-assembly procedure of arrays beyond alkanes, by making use of an attractive class of molecular ligands.

Molecules of the tridentate 2,6-bi(pyrazolyl)pyridine (BPP) group are well known to act as weak σ -donor/ π -acceptor ligands exhibiting octahedral coordination environment with coordination number 6 for transition metals [14]. Moreover, for the case of iron (II) ions, the S-BPP-ligands adjust the ligand field strength to access the so-called spin transition (ST) or spin crossover (SCO) regime [15], in which the physical properties depend strongly on their intrinsic low- and high-spin states (LS ($S = 0$) and HS ($S = 2$)) state. Integrated ST units may be considered as potential electronic components in the construction of switching molecular devices [16, 17], a vision for which the control of the attaching of S-BPP-units to gold nanoparticles sets the stage. Towards this goal, the synthetic introduction of substituents at the 4'-position of the pyridine moiety of BPP has been shown to be a useful strategy. In particular the introduction of highly conductive π -conjugated phenylethynyl linker moieties with acetyl protected thiol anchoring groups facilitates contact to noble and coinage metal electrodes [18].

In this study, we report on the fabrication of 2D single layer ligand-gold nanoparticle arrays (and multilayer ligand-gold nanoparticle networks) formed by gold nanoparticles covered by planar aromatic organic ligand-based S-BPP molecules. The inclusion of the thioacetate end group (see AcS-BPP molecule in Figure 5.1) [18] is

expected to steer the adsorption of the S-BPP molecule to the gold nanoparticles [19]. The results of the structural and spectroscopic characterization of the synthesized 2D ligand-gold nanoparticle arrays (in short Au-NP-S-BPP-arrays), by means of UV-Vis and electron microscopy (SEM, HR-TEM and 3D TEM) experiments, will be presented. Specifically, surface-enhanced Raman spectroscopy (SERS) provides insight into the selectivity of the bond formation. Remarkably, Raman experiments also reveal subtle shifts in some S-BPP modes related to reversible structural modification within the array induced by temperature. This observation is compared to temperature-dependent transport experiments. For this purpose, the fabricated 2D Au-NP-S-BPP arrays are electrically contacted to lithographically defined devices [5, 8, 9, 12] and the obtained conductance measurements are compared to benchmark networks formed with alkanethiols spacers.

5.2 Capping of gold nanoparticles with S-BPP molecules

To create arrays of S-BPP capped gold nanoparticles, the well-established procedure to make alkanethiol-based nanoparticles arrays [8, 9, 20] is adapted and applied. The first step is the synthesis of citrate stabilized gold nanoparticles in aqueous solvent (see paragraph 3.1.1).

This is followed by centrifuging 5 mL of monodispersed citrate stabilized gold nanoparticle suspension at 15000 RPM for 1 hour. After centrifugation, the aqueous solvent is removed from the settled gold nanoparticles, followed immediately by nanoparticles redispersion in ethanol. Through forceful shaking, the nanoparticles are redispersed quickly to yield a stable colloidal dispersion, sealed in a glass bottle and sonicated in a water bath for approximately an hour.

Functionalization of gold nanoparticles with S-BPP molecules [18] is accomplished in two steps (according to the method described earlier in paragraph 3.3.2). The process of functionalization is accelerated by sonication in a water bath. After 15 minutes, the functionalized gold nanoparticle dispersion has changed colour. As shown below, UV-Vis absorption spectroscopy reveals that this colour change can be attributed to the S-BPP molecule assembling around the gold nanoparticles. Next, the functionalized gold nanoparticles are left to settle down by gravity in a cold, dark storage environment [21, 22] for three days. The supernatant is then removed from the sediment, which is redispersed in 4 mL of chloroform and sonicated for 1 hour. Finally, a lightly purple

coloured dispersion of functionalized gold nanoparticles is used to prepare a self-assembled 2D Au-NP-S-BPP array.

5.3 The fabrication of 2D Au-NP-S-BPP arrays

The 2D single layer Au-NP-S-BPP array is prepared using a Langmuir-Schaefer (LS) method (see Figure 5.1) where a single layer array of functionalized gold nanoparticles is self-assembled at the air/water interface [8, 23, 24]. A Teflon mould, containing a hole, is filled with 300 μL of demineralised Millipore water. Then, 30 μL of S-BPP functionalized gold nanoparticles in chloroform are dispersed on the aqueous layer. The steadily evaporating chloroform leaves the nanoparticles at the air-water interface. The hydrophobically functionalized gold nanoparticles attract each other on the water surface and self-assemble into a highly ordered array. The array is then transferred on a Si wafer substrate (covered with 300 nm of SiO_2) by using a polydimethylsiloxane (PDMS) microcontact printing method [8].

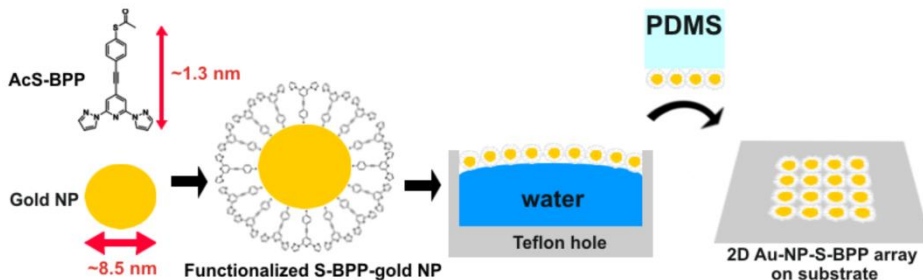


Figure 5.1: Fabrication of 2D Au-NP-S-BPP array (not to scale). The ingredients are gold nanoparticles (diameter 8.5 ± 1.5 nm) and AcS-BPP molecules (length molecule 1.3 nm without the protective acetyl (Ac) group). The arrays are fabricated through self-assembly and then placed onto a substrate of choice by PDMS microcontact printing.

Other suitable types of substrates for microcontact printing these samples are glass, quartz, several types of plastics (like polyethylene, polypropylene foils and polyimide (Kapton) films) and electron beam lithography written high-aspect-ratio (HAR) nanotrench electrodes devices (see Figure 5.2) [25]. The Au-NP-S-BPP arrays are stored in a dark and cold environment and can be kept for several months.

5.4 Imaging of Au-NP-S-BPP arrays and networks

Scanning electron microscopy (SEM) is used to image the arrays on flat (oxidized) silicon substrates and the Au-NP-S-BPP networks on nanotrench electrodes devices (see Figure 5.2).

In general the Au-NP-S-BPP networks are reasonably well ordered. However, single defects and larger voids (as seen in Figure 5.2) will be present too. Although the latter may lead to more complicated percolation paths, conductance properties are expected to be dominated by the more ordered regions. The ordering of an Au-NP-S-BPP network is similar on the SiO₂ substrate and on the Au nanotrench electrodes. The main reason for this is that the Au-NP-S-BPP arrays were self-assembled on water, before actually being transferred to a substrate. Figure 5.3(a) shows a SEM image of a nanoparticle array that was microcontact printed on a SiO₂ substrate. Typically, these Au-NP-S-BPP arrays reveal ordered structures on flat surfaces extending over several hundred nanometers, depending on the microcontact printing procedure used. The nanoparticles have not coalesced and are well separated by the capping ligands S-BPP. Scanning transmission electron microscopy (STEM) and transmission electron microscopy (HAADF-STEM, HR-TEM and 3D TEM) are also used to accurately characterize the nanoscale structuring of multilayered networks on carbon-covered TEM grids. It should be noted that, whereas regular 2D-structures are readily obtained on flat (oxidized) silicon substrates, ordered assembly on the TEM grids turned out to be more challenging, resulting in structures with local order only (see Figure 5.3(b)).

HAADF-STEM images of Au-NP-S-BPP networks (see Figure 5.3(b)) show a fairly uniform distribution of functionalized gold nanoparticles, sometimes as a single layer, but typically a few stacked layers. The latter is probably caused by repeating deposition of Au-NP-S-BPP arrays on the TEM grids by dipping the TEM grids. Microscopic analyses of the network confirm the monodispersity of the gold nanoparticles with average diameter of 8.5 ± 1.5 nm. Moreover, Fast Fourier Transforms (FFT) of the HAADF-STEM images indicate an average particle distance of 10.6 nm. The resulting average next neighbour distance is close to 2 nm, consistent with an expected value between one (1.3 nm) and two (2.6 nm) molecular lengths of S-BPP.

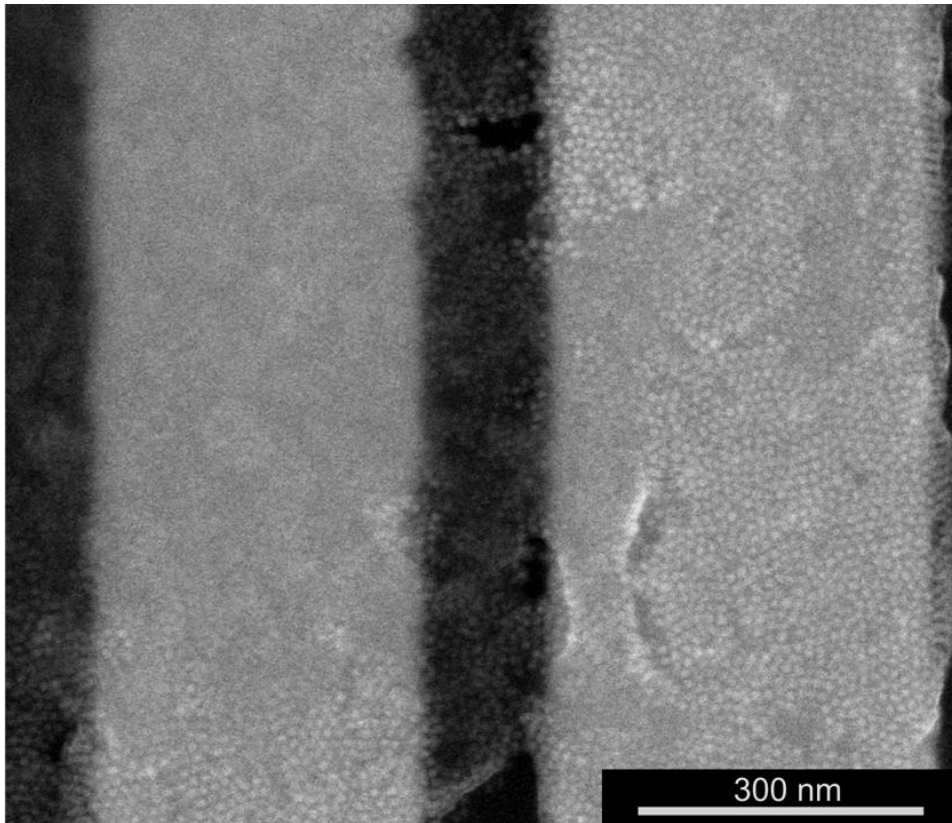


Figure 5.2: SEM image of Au-NP-S-BPP network device for conductance experiments. The two Au electrodes have been defined by electron-beam lithography. The resulting ‘nanotrenches’ of around 120 nm distance between the Au electrodes ensure a favourable aspect ratio for conductance measurements. These Au-NP-S-BPP networks have been obtained via three microcontact printing sequences of Au-NP-S-BPP arrays onto the HAR nanotrench devices.

Figure 5.3(c) shows the energy-dispersive X-ray (EDX) spectrum corresponding to the HAADF-STEM image of the thin Au-NP-S-BPP network film (see Figure 5.3(b)). In addition to Au, the expected spectra of the organic ligand elements C, N and S (partially overlapped by Au) are detected. The oxygen may originate from the presence of water when dipping the TEM grid into the self-assembled Au-NP-S-BPP array on the water.

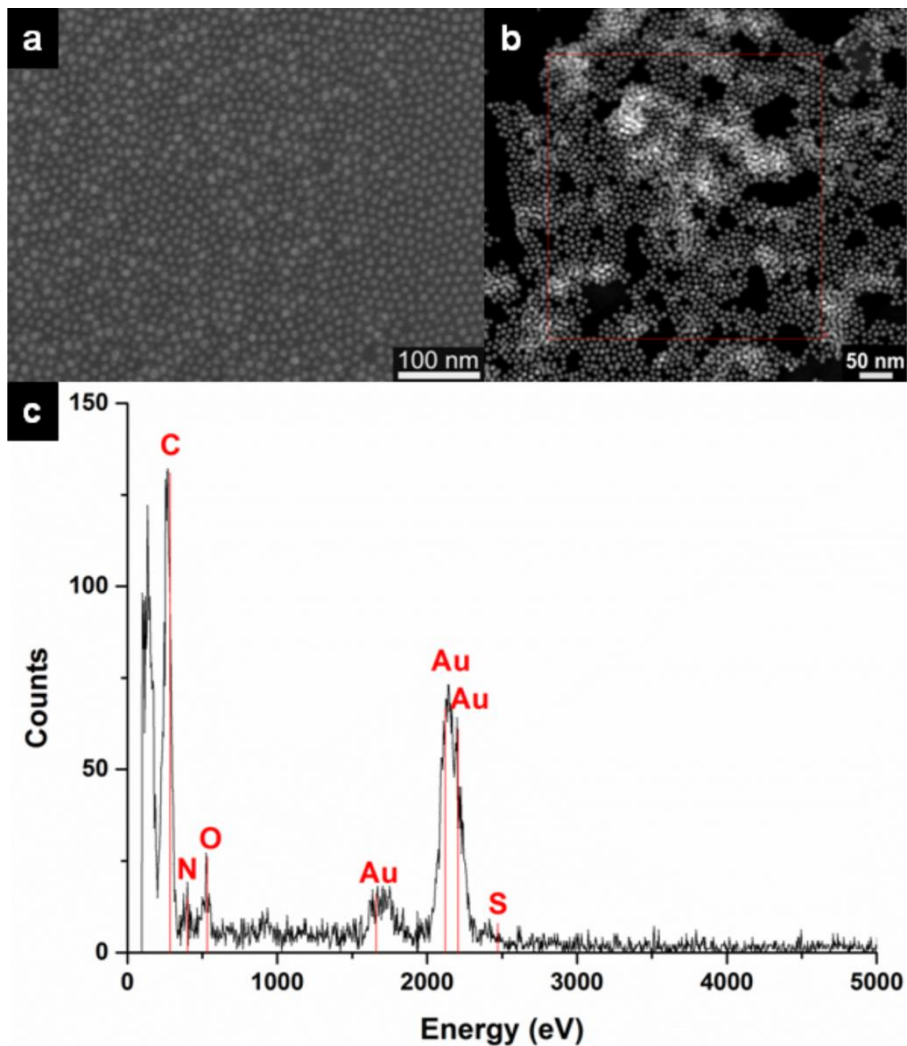


Figure 5.3: Characterization of Au-NP-S-BPP arrays and networks by electron microscopy. (a) SEM image of a 2D single layer microcontact printed Au-NP-S-BPP array on a flat Si-SiO₂ substrate. (b) STEM-reference image of a Au-NP-S-BPP network area on a TEM grid substrate. (c) local EDX analysis revealing the elemental composition.

HAADF-STEM tomography [26, 27] was used to further analyze the spatial packing of multilayered Au-NP-S-BPP networks. From 3D reconstruction of a multilayered Au-NP-S-BPP network, it is indeed observed that the S-BPP functionalized gold

nanoparticles not only form a packed array separated by organic S-BPP molecules in 2D, but also enable sterically driven ordering of gold nanoparticle layers in a partial multi-stack volume.

5.5 UV-Vis spectroscopy on 2D Au-NP-S-BPP arrays

Ultraviolet-visible (UV-Vis) spectroscopy was performed to gain insight into the optical properties of these molecule-gold nanoparticle arrays, and specifically to investigate the influence of the S-BPP molecules on the effective dielectric constant. Metal nanoparticles exhibit absorbance due to surface plasmon resonances (SPR) that occur at frequencies ω (or wavelengths λ) at which the particle's surface charges are oscillating resonantly with the electromagnetic driving field (the incoming photons, see also paragraph 3.5.1). For near-spherical particles, only one SPR mode is expected [28]. According to Mie theory in the dipolar quasi-static approximation (where the diameter d of the nanoparticle is assumed much smaller than the wavelength, i.e. $d \ll \lambda$), the position of the SPR is directly related to the permittivity of the medium surrounding the nanoparticle [29, 30]. In molecule-gold nanoparticle arrays, this permittivity will be largely influenced by the molecules separating the nanoparticles. Hence, Au-NP-S-BPP arrays are expected to have optical properties different from reference alkanethiol-gold nanoparticle arrays. A further influence on the SPR is exerted by the optical interaction of one nanoparticle with the full set of neighbouring gold nanoparticles.

A suitable way to describe the SPR in molecule-gold nanoparticle arrays is via the Maxwell-Garnett theory (again in the quasi-static approximation). This effective medium theory defines an effective dielectric constant of the medium ϵ_{eff} that takes into account both the presence of the surrounding medium and the neighbouring nanoparticles [31-33]. The resonance condition is then given by:

$$\epsilon_1(\omega_{sp})(1-f) + \epsilon_m(2+f) = 0. \quad (5.1)$$

Here, ω_{sp} denotes the frequency of the SPR and ϵ_m is the dielectric constant of the medium surrounding the nanoparticles. The so-called filling factor $f = V_{clusters}/V_{total}$ denotes the relative volume occupied by other nanoparticles around the resonating nanoparticle [9]. In this way, the surrounding nanoparticles in an array are incorporated into the theory effectively. Note that for $f = 0$ (i.e., there is no interaction between the nanoparticles) the condition is $\epsilon_1(\omega) = -2\epsilon_m$, as in standard Mie theory.

Figure 5.4 shows the absorption curves for four types of 2D molecule-gold nanoparticle arrays, with alkanethiol-protected gold nanoparticles of various lengths (C8, C10, C12) compared to the 2D Au-NP-S-BPP array. From C8 to C12, the SPR shifts to shorter wavelengths [9], as expected for a blue shift originating from a change in the spacing distance between the gold nanoparticles, i.e. a decrease in filling factor f , (see equation 5.1).

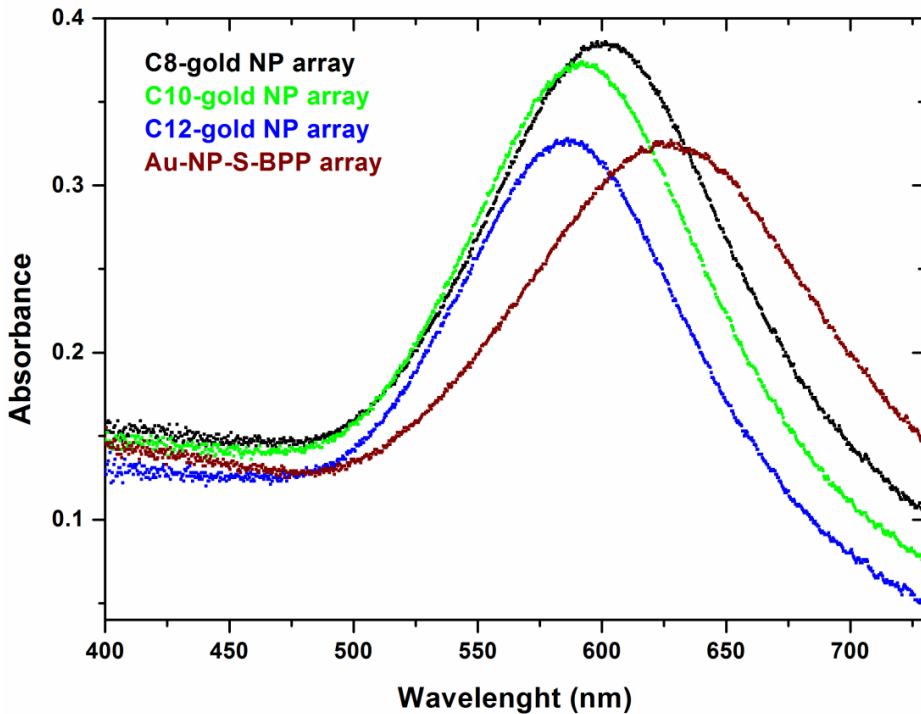


Figure 5.4: UV-Vis (ultraviolet-visible light) spectroscopy of several functionalized gold nanoparticle arrays. Gold nanoparticles are covered by C8 (black), C10 (green), C12 (blue) and S-BPP (red), respectively.

However, the situation is different for the 2D Au-NP-S-BPP array, for which a significant change in ϵ_m is expected, since S-BPP molecules are fully conjugated and hence more easily polarizable. Compared to the alkanethiols-gold nanoparticle arrays, a red shift is indeed observed in Figure 5.4. This is also confirmed experimentally via UV-Vis spectroscopy on a C8-gold nanoparticle dispersion and a S-BPP-gold

nanoparticle dispersion (both in chloroform (i.e. CHCl_3)), where effectively $f = 0$ (see Figure 5.5). Figure 5.5 shows that the SPR peak of the S-BPP-covered gold nanoparticles in CHCl_3 solvent is red-shifted by 17 nm compared to the C8-gold nanoparticle dispersion. Using Mie theory ($f = 0$), the dielectric constants is estimated for the C8-gold nanoparticle dispersion and the S-BPP-gold nanoparticle dispersion to be 2.2 ± 0.1 and 2.8 ± 0.1 , respectively. The results obtained so far can now be checked for consistency.

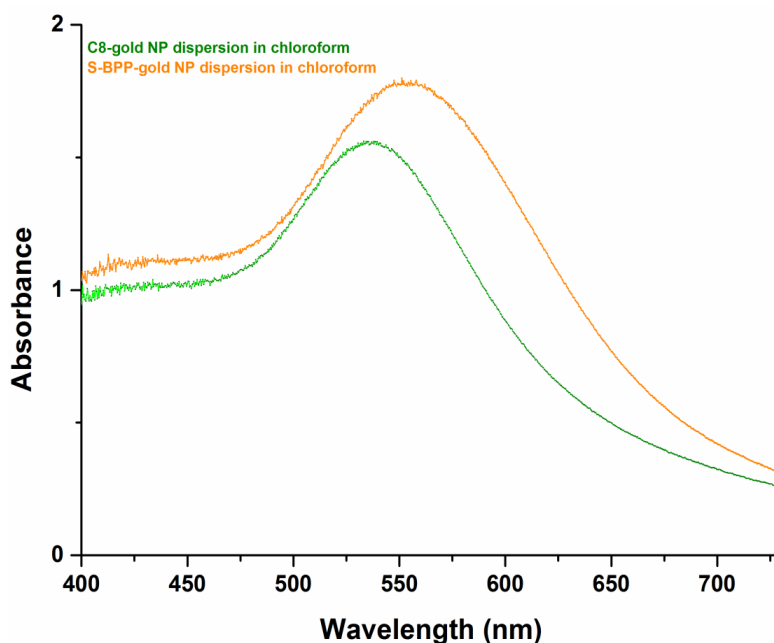


Figure 5.5: UV-Vis spectroscopy of (green) octanethiol functionalized gold nanoparticle dispersion versus (orange) S-BPP-gold nanoparticle dispersion. For both dispersions a chloroform solvent is used.

Since f can be estimated from the electron microscopy images, for both the C8-gold nanoparticle array and the Au-NP-S-BPP array, the Maxwell-Garnett theory can be applied to estimate the dielectric constant ϵ_m in these arrays. The values for ϵ_m within an array or in dispersion are approximately the same values, for both S-BPP molecules and for C8 molecules (see Table 1).

Table 1: Relative dielectric constant due to the ligands ϵ_m (octanethiols versus S-BPP) as calculated from UV-Vis spectra of both nanoparticle dispersions and nanoparticle arrays.

Type functionalized gold nanoparticles	λ_{SP} (nm)	f	Relative dielectric constant ϵ_m
C8-gold nanoparticle dispersion	535.9	0	2.2 ± 0.1
S-BPP-gold nanoparticle dispersion	553.9	0	2.8 ± 0.1
C8-gold nanoparticle array	600.2	0.35	2.4 ± 0.1
Au-NP-S-BPP array	626.0	0.36	2.8 ± 0.1

These values are consistent with values for alkanethiols-gold nanoparticle arrays and oligo(phenylene ethynylene) (OPE)-bridged gold nanoparticle arrays obtained via molecular exchange [9, 30]. For clarity the latter type of molecular exchanged arrays contain a mixture of OPE's and alkanes, unlike the Au-NP-S-BPP arrays.

5.6 Room-temperature Raman spectroscopy on 2D Au-NP-S-BPP arrays

To get more insight into the binding of the S-BPP molecules to the gold as well as to investigate the temperature-dependence of molecular ordering, surface-enhanced Raman spectroscopy on the 2D Au-NP-S-BPP array was performed. In Figure 5.6 the room-temperature Raman spectra of a bulk (powder) sample of AcS-BPP molecules (see Figure 5.6(a)) and of a 2D Au-NP-S-BPP array (see Figure 5.6(b)) are compared. In spite of the much lower concentration of the S-BPP molecule anticipated from the 2D single layer coated array (at least 3 orders of magnitude) compared to the bulk quantity, the Raman spectral intensity is comparable between the two types of samples (see Figure 5.6(a) versus Figure 5.6(b)). Moreover, the Raman spectra from the Au-NP-S-BPP array shows better signal-to-noise ratio attributed to surface enhancement of the Raman signal. The arrayed nature of the gold nanoparticles and their small

interparticle separation leads to a plasmon absorbance shown in Figure 5.4, which is resonant with the 633 nm excitation used here.

Although there are clear commonalities, the spectra of the 2D single layer array (see Figure 5.6(b)) and AcS-BPP powder spectra (see Figure 5.6(a)) exhibit notable differences. The individual spectral features are broader in the SERS spectrum, consistent with the higher heterogeneity in the microenvironment the S-BPP molecules experienced in the array compared to the powder. Furthermore, the SERS spectrum is less complex than that of the powder. This is consistent with plasmonic enhancement as the vibrational modes involving the atoms closest to the gold nanoparticle will be selectively enhanced.

Whereas the low frequency Au-S or Au-N stretch modes cannot be easily discerned from the background in the spectral region below 400 cm^{-1} , it is interesting to note that the thioacetate and acetate modes observed in the solid sample, for example a weak feature at 1698 cm^{-1} (see red arrow in Figure 5.6(a)) assigned to the acetate C=O and features between $1367\text{-}1380\text{ cm}^{-1}$, are no longer evident in the SERS spectrum of the Au-NP-S-BPP arrays. This strongly suggests that the thiol is bound to the gold after surface-mediated hydrolysis of the acetate group. The dominance of key benzenethiol modes in the SERS spectrum is also indicative of binding via thiol moiety. The most intense Raman feature in the powder spectrum of AcS-BPP is the aryl in-plane C-C stretch mode centred at 1591 cm^{-1} . This mode is shifted to 1576 cm^{-1} in the bound S-BPP molecule of the 2D arrays, which matches precisely the in-plane C-C stretch reported for SERS of benzenethiol on copper or silver and is a further indication of binding through sulphur or thioacetate [35, 36].

The second most intense feature in the SERS spectrum is a mode at 1076 cm^{-1} , which is assigned to the aromatic C-S stretch shifted from 1095 cm^{-1} in the powder sample. Both the shift and enhancement of this mode is characteristic of SAMs of benzenethiol on plasmonic metals, and is further evidence that the S-BPP is binding to the gold surface through this moiety [35, 36]. Other characteristic benzenethiol features are also enhanced, at 990, 660 (see red arrow in Figure 5.6(b)) and 406 cm^{-1} .

The alkyne $\text{C}\equiv\text{C}$ stretch mode, which is by far the most intense mode in the powder sample, is reduced in relative intensity in the 2D single layer array, but remains a dominant feature albeit shifted from 2222 to 2211 cm^{-1} on surface binding.

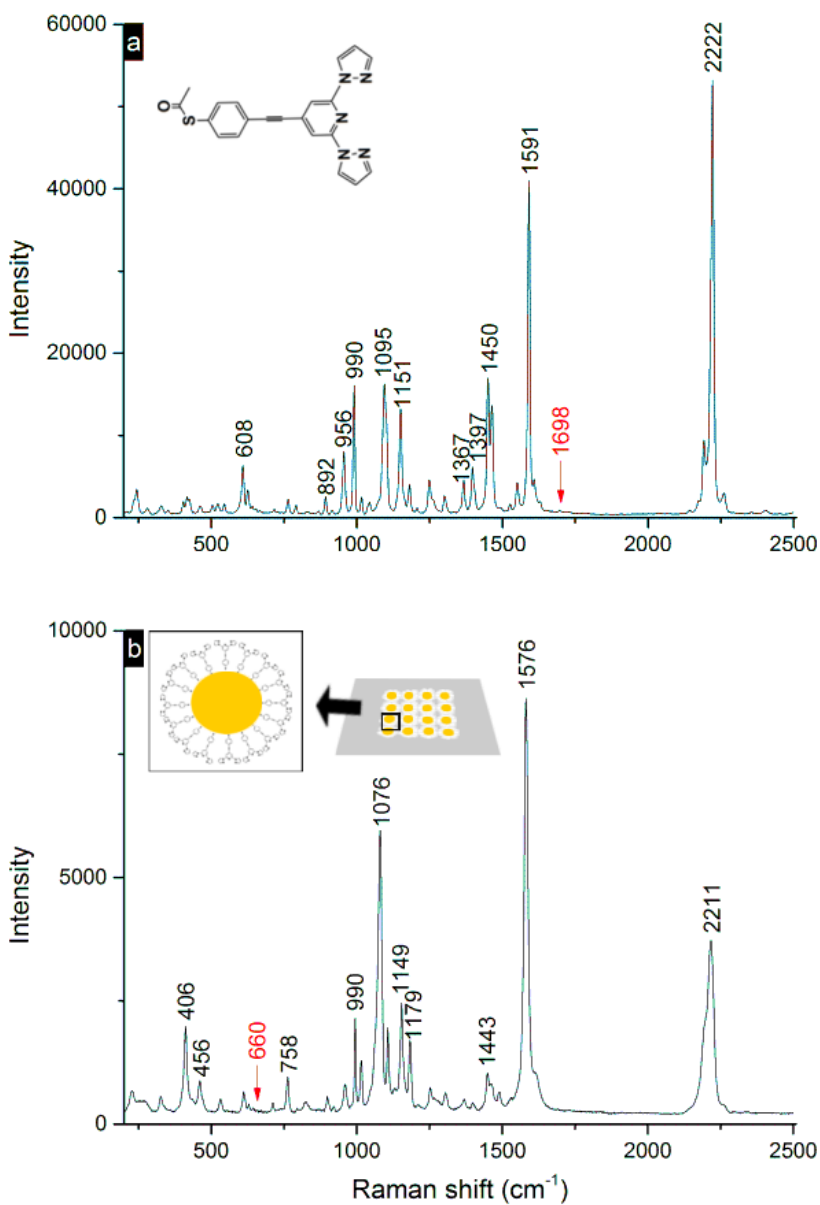


Figure 5.6: (a) Room-temperature Raman spectrum of bulk (powder) AcS-BPP molecules showing 200-2400 cm^{-1} region excited at 633 nm (1.2 mW illuminating power on the sample). (b) Room-temperature Raman spectrum of 2D (single layer) Au-NP-S-BPP array obtained by microcontact printing on a quartz substrate.

This suggests modest weakening of the C≡C bond presumably induced by binding of the thiol to the surface [37]. By comparison, the Raman modes from the S-BPP moiety are weaker than the benzenethiol moiety in the SAM spectrum. Features at 1443, 1149, 1179 and 785 cm^{-1} are attributed to the S-BPP, principally to the pyrazole moieties [38]. A weak shoulder centred at 1607 cm^{-1} is attributed to the pyridine moiety. The low relative intensity of this mode suggests it is not directly bound to the nanoparticle. Overall, the predominance of SERS signal from the benzenethiol moiety and comparatively weaker enhancement of pyrazole modes provides strong evidence that the S-BPP binds to the nanoparticles preferably via the thiol linker.

5.6.1 Temperature-dependent Raman spectroscopy on 2D Au-NP-S-BPP arrays

The 2D Au-NP-S-BPP arrays studied by Raman microscopy over the temperature range 80 to 353 K are shown in Figure 5.7. The absence of significant chemical changes with temperature is indicated by the overall similarity between the spectra under temperature variation. However, some subtle changes can be noticed. Across most of the SERS-enhanced modes, a small shift to the blue of between 2 and 4 cm^{-1} is observed with decreasing temperature. Interestingly, the unaffected modes are the weakest features in the spectrum, i.e. those that are not strongly SERS enhanced. In other words the bonds nearest the nanoparticle surface are most affected by the changing temperature. This observation suggests that temperature induces changes to bonding interactions between the nanoparticle and the S-BPP. Possible changes are conformational/orientational changes of S-BPP with respect to the nanoparticle surface, which might be expected to cause shifts in the frequencies of bonds close to the nanoparticle. Such electronic changes would also be likely to transmit to chemical moieties conjugated to the bound group [39].

Correspondingly, the most strongly affected modes are the C-C stretch associated with the benzenethiol at 1576 cm^{-1} at room temperature, which shifts to 1582 cm^{-1} at 80 K and to 1575 cm^{-1} at 353 K. The alkyne, C≡C stretch mode is also particularly strongly affected, with shifts from a 2207 cm^{-1} value at 353 K to 2211 cm^{-1} at room temperature, and to 2223 cm^{-1} at 80 K. This mode is broad at 353 K, comprising a main feature and a shoulder at room temperature, which sharpens and resolves at 80 K into a second band at 2190 cm^{-1} .

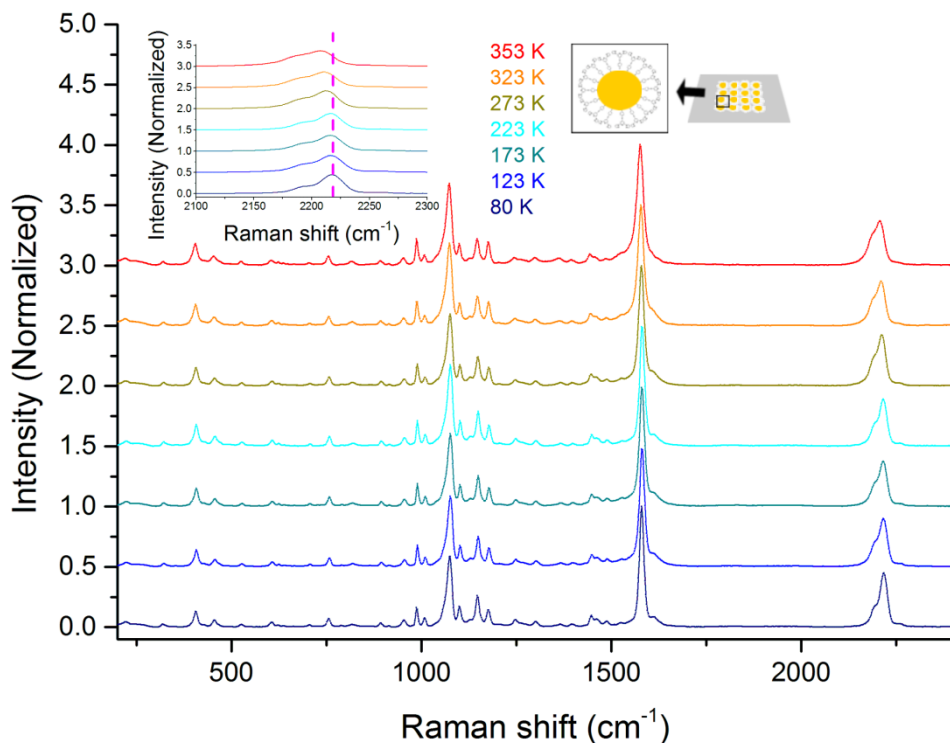


Figure 5.7: Temperature-dependent Raman spectra of 2D Au-NP-S-BPP array microcontact printed on a quartz substrate excited at 633 nm (illuminating power 1.2 mW at the sample). Inset: expansion of the alkyne stretch mode; the vertical marker shows the temperature shifts in the spectra.

As described previously, a significant shift in the $\text{C}\equiv\text{C}$ stretch mode was observed on thiol binding to the gold surface indicating the significant electronic coupling between the benzenethiol and the surface. It is noteworthy that the $\text{C}\equiv\text{C}$ stretch mode is so sensitive to temperature in this system, as also found in other reports on Raman of alkynes [37]. Their large polarizability renders them sensitive to electronic changes within their molecular vicinity, particularly in conjugated systems [40, 41]. The surface-bound benzenethiol is sensitive to temperature, but the alkyne exhibits much larger temperature-dependent spectral changes, with a 16 cm^{-1} shift between 80 and 353 K.

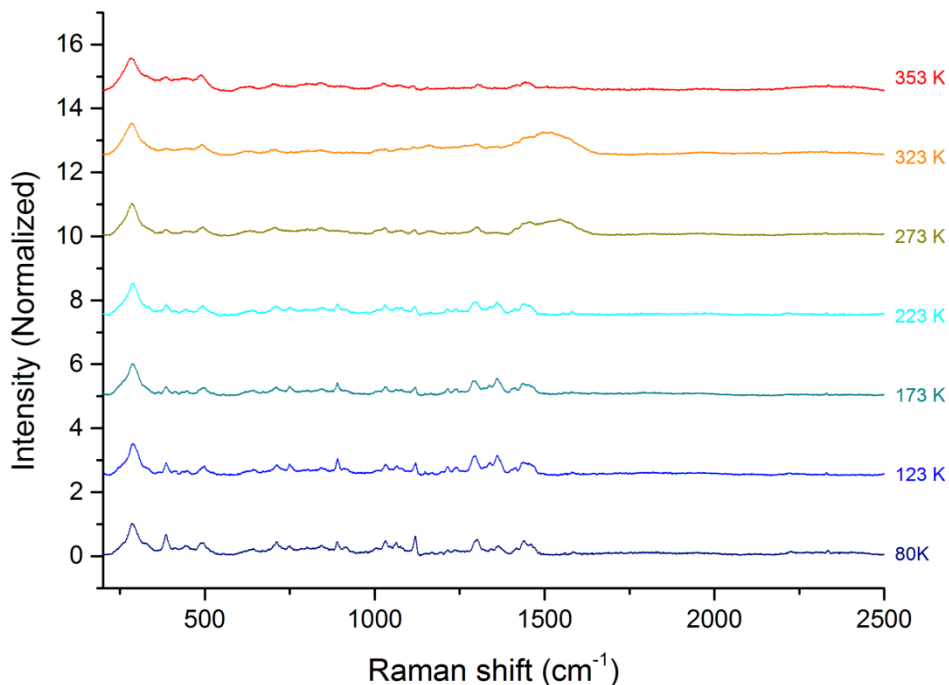


Figure 5.8: Temperature-dependent Raman spectra of octanethiol-gold nanoparticle array, microcontact printed on a quartz substrate excited at 633 nm (illuminating power 1.2 mW at the sample).

This is tentatively attributed to changes in the orientation of the molecule, possibly promoted by Au-S mobility at the surface with temperature. It is important to note that the Raman spectral changes with temperature are fully reversible, i.e. restoring the Au-NP-S-BPP arrays to room temperature following cooling to 80 K lead to recovery of the original room-temperature spectrum across all features. Comparison studies on alkanethiol-modified gold nanoparticle arrays (see Figure 5.8) reveal that temperature changes in their associated Raman spectra are much more modest than those observed for Au-NP-S-BPP arrays. Figure 5.8 shows that the largest shifts observed in individual modes does not typically exceed 2 cm^{-1} and the sharpening (improved resolution) of the vibrational bands, is the main effect of low temperature. This observation appears to validate the hypothesis that its molecular structural/orientational changes, related to the S-BPP bound to the nanoparticle, are driving the changes observed in the Raman

spectrum with temperature. Both the magnitude and the reversibility of the Raman changes observed with temperature effectively preclude the possibility that the actual binding mode to the nanoparticle is changing. The extensive lateral interactions characteristics of alkanethiol-nanoparticles arrays make them more tightly packed than S-BPP. Therefore S-BPP is more prone to random orientation and with more freedom to reorient at the nanoparticle interface promoted by temperature. The observed spatial flexibility of the thiol anchored S-BPP ligands is of interest for molecule chelation purposes, as it should facilitate the envisioned of Fe^{2+} metal ions complexation.

5.7 Conductance measurements on a multilayered Au-NP-S-BPP network

Charge transport in Au-NP-S-BPP network devices provides additional experimental insight into the question of thermal stability of the nanoparticles architecture. Here, not only the S-BPP molecules, but also the nanoparticles are expected to play a role. At low temperatures, the thermal energy $k_B T$ becomes comparable to their charging energy, $E_C = e^2/2C$, i.e. the electrostatic energy needed to add an electron onto the metallic nanoparticle (here C is the total capacitance of a nanoparticle in the array and e is the electron charge). In that case, Coulomb blockade will hamper charge transport. Earlier work on alkanethiol-gold nanoparticle networks demonstrated a wide range of charge transport behaviours within the Coulomb-blockade regime [2, 5, 9, 42]. In Chapter 4 the crossover between the sequential tunneling and cotunneling regimes have been studied for alkanethiol networks, as well as for alkanethiol networks with dithiolated OPE-3 bridges [5]. We estimated typical Coulomb blockade charging energies of around 14-17 meV, in correspondence with temperature- and voltage-dependent transport measurements. Hence, in alkanethiol and OPE-based networks Coulomb blockade dominates below 200-250 K, whereas around room temperature, the current-voltage (I - V) characteristics are linear and practically temperature-independent.

The same method as in Chapter 4 is used to investigate charge transport through Au-NP-S-BPP networks. Nanotrench devices are fabricated with a high width-to-length aspect ratio (~ 200) by electron beam lithography and metal lift-off. Through patterning Ti (3 nm)/Au (47 nm), thick electrodes of 20 μm width, separated by a gap of around 100 nm (~ 10 nanoparticles), are created on Si/SiO₂ substrates. The nanoparticle array is transferred onto these electrodes via a PDMS stamp. Samples containing 2D (single

layer) Au-NP-S-BPP arrays typically exhibited very high ($> 100 \text{ G}\Omega$) resistance values. For that reason, multilayers of Au-NP-S-BPP networks (three times an Au-NP-S-BPP array is stamped on the nanotrench device) are used. The data shown below are obtained after full stabilization of the sample, following an initial resistance decrease as a function of time at room temperature. Most likely, the latter is the result of a slow re-ordering process [43-45].

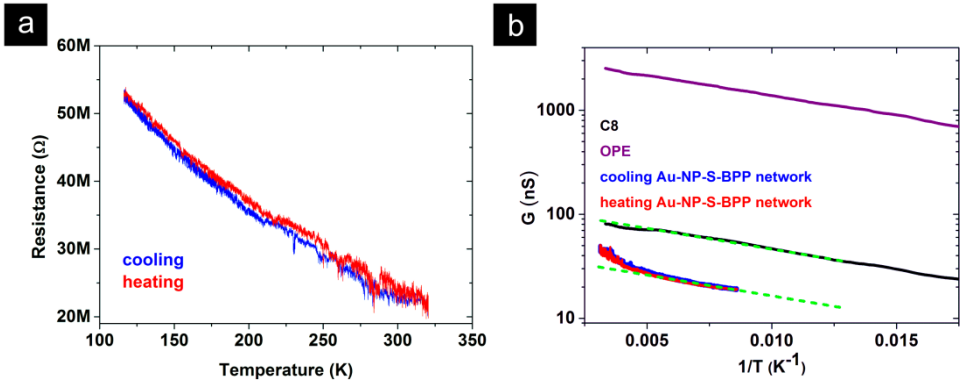


Figure 5.9: (a) Low-bias resistance of a multilayered Au-NP-S-BPP network as a function of temperature for $116 \text{ K} < T < 320 \text{ K}$. Both cooling (black) and heating (red) traces are shown. (b) Arrhenius plot (semilog plot of G versus $1/T$) of the data in Figure 5.9(a) compared to experiments on similar, i.e. three times stamped, C8 networks (black) and OPE-bridged networks (purple). The green dashed lines are parallel guides to the eye to compare the slope for various networks. (For linearly scaled R - T plots see Chapter 6: Figure 6.5(a) for the C8 and Figure 6.5(b) for the OPE case, respectively.)

Figure 5.9(a) shows the low-bias resistance versus temperature for a multilayered Au-NP-S-BPP network microcontact printed on a nanotrench device. The interparticle voltage-bias, typically a factor 10 smaller than the device voltage-bias, is of the order of 3 mV. In Figure 5.9(a), we find that the resistance is monotonically decreasing with temperature for the entire temperature range, without a clear saturation at higher temperatures. If we compare the octanethiol and OPE-based networks with the Au-NP-S-BPP network, however the latter behaves differently at higher temperatures. For example, for the first two types of samples, the low-bias resistance is basically voltage- and temperature-independent at room temperature, indicating that $k_B T_R > E_C$ (see Figures 6.5(a) and 6.5(b)) [5]. However, the I - V curves of the Au-NP-S-BPP network

are surprisingly non-linear (see Appendix B.1). Furthermore, the temperature-dependent behaviour of the low-bias conductance deviates for the Au-NP-S-BPP networks. This becomes most clear in Figure 5.9(b), which shows the data of Figure 5.9(a) in an Arrhenius plot. For comparison the Arrhenius plots for C8 and OPE networks are also displayed. The Arrhenius plots of the C8 and OPE networks point to activated behaviour between 70 K and 300 K, as indicated by the straight-line approximation in Figure 5.9. This is indeed expected for the regime of sequential tunneling (Note that for the lower-temperature cotunneling regime, Efros-Shklovskii behaviour is expected, resulting in an exponential dependence on $T^{0.5}$; see Chapter 4 and [2, 42]). For the three different types of samples, there is actually a clear similarity in the low-temperatures range. This is illustrated by the parallel lines in the semilog plot of Figure 5.9(b), indicating an activation energy of the same order for the three molecular spacers. Nevertheless the Au-NP-S-BPP network sample exhibits a very different behaviour for higher temperatures, showing a clear upturn in the Arrhenius plot (i.e. at lower $1/T$ values in Figure 5.9(b)).

A first explanation for a deviation may be that the charging energy $E_C = e^2/2C \propto C^{-1}$ is actually higher for the Au-NP-S-BPP networks than for alkanethiols networks. This were the case if the nanoparticle radius r and/or the effective dielectric constant ϵ_{eff} around the nanoparticles are considerably lower for the Au-NP-S-BPP networks than for the octanethiol networks (cf. the self-capacitance of a sphere: $C = 4\pi\epsilon_0\epsilon_r r$, see Appendix B.2). However, this is not likely. First, the nanoparticles are made in the same manner for all sets of devices (independent of the molecular species investigated). All the nanoparticles are thus observed to be of similar size. Second, UV-Vis spectroscopy indicates that ϵ_m (and also ϵ_{eff} which incorporates f) is actually higher for Au-NP-S-BPP networks than for alkanethiol networks, consistent with intuition (see Table 1). This should thus lead to a lower charging energy for S-BPP than for octanethiol networks and hence to linear I - V curves at room temperature. Additionally, it is difficult to reconcile a Coulomb-blockade picture with the continuous increase of the slope of the Arrhenius plot of Figure 5.9(b) when heating Au-NP-S-BPP networks. The latter would suggest a significant change of the activation energy, i.e. of the charging energy, as temperature increases. For these reasons, Coulomb blockade is excluded as the reason for the upturn in Figure 5.9(b).

Following the results from temperature-dependent Raman spectroscopy, the proposition can be made that the deviation from simple Arrhenius law behaviour

originates from fluctuations in the molecular interconnects. These fluctuations can result in a modification of the effective tunnel barrier. The gold nanoparticles are here separated by loosely interacting S-BPP molecules, which cannot form a close-packed structure and hence keep room for thermally-driven motions. At higher temperatures, variations in the relative orientation of S-BPP neighbours can result in fluctuations in π - π interactions, yielding changes in charge transfer probability between nanoparticles. In this situation, the effective transmission of the tunnel barrier becomes a time average of the set of all possible configurations each with their own specific transmission value, in a way somewhat similar to the recent proposal in Ref. [46]. For example, temporarily enhanced π - π interaction should lead to higher tunneling probabilities. Time-averaging of such fluctuations may thus result in enhanced transport at high temperatures, explaining the upturn in the Arrhenius plot for the S-BPP network in Figure 5.9(b). One should point out that the transport measurements *per se* do not present a conclusive evidence of disorder-enhanced conductivity of nanoparticles networks. However, the combination of Raman spectroscopy and transport measurements favours such a model, thereby proposing a new approach for understanding how disorder can impact transport properties in molecular junctions. Additional calculations will be required to extend this hypothesis of fluctuations-enhanced transport between the gold nanoparticles, taking into account the percolating character of transport in molecular interconnects arrays. Complementary future experiments may use the conducting-probe AFM or eutectic GaIn methods. In that case, monolayers of S-BPP formed at both electrodes could be gently brought into mechanical contact, after which temperature-dependent $I(V)$ measurements can be done.

5.8 Conclusions

Self-assembled gold nanoparticle arrays, stabilized by a new type of conjugated organic molecules as capping ligands, can be assembled into two-dimensional arrays, which form locally well-ordered structures on different types of substrates. Raman spectroscopy reveals that these S-BPP molecules coordinate selectively to the nanoparticles via thiol-gold bonds, leaving the pyridine and pyrazole available for further chemical binding purposes. Temperature-dependent Raman measurements exhibit frequency shifts for several key modes of the S-BPP molecules, pointing to molecular reorientational changes occurring at high temperatures. The extent of

structural dynamics is far greater than observed for simple alkanethiol modified nanoparticle arrays, and is consistent with the more limited close-packing anticipated for S-BPP. This provides also an explanation for the peculiar temperature dependence of the electrical properties of the S-BPP networks, which shows a clear deviation from Arrhenius behaviour above 220 K. This research suggests that conductance behaviour of molecule-nanoparticle arrays can be tuned as an indicator of dynamical disorder in these structures, which can be a prerequisite to create nanoparticle networks candidate for further chemical functionalization or reactivity. This sets the stage for the attractive possibility of coordinating with Fe^{2+} metal ions, thereby introducing switchable spin transition units into the network.

5.9 References

1. G. M. Whitesides and B. Grzybowski, Self-assembly at All Scales, *Science*, **295**, (2002), 2418-2421.
2. T. B. Tran, I. S. Beloborodov, X. M. Lin, T. P. Bigioni, V. M. Vinokur and H. M. Jaeger, Multiple Cotunneling in Large Quantum Dot Arrays, *Phys. Rev. Lett.*, **95**, (2005), 0768061-0768064.
3. A. Zabet-Khosousi and A.-A. Dhirani, Charge Transport in Nanoparticle Assemblies, *Chem. Rev.*, **108**, (2008), 4072-4124.
4. M. Pauly, J.-F. Dayen, D. Golubev, J.-B. Beaufrand, B. P. Pichon, B. Doudin and S. Bégin-Colin, Co-tunneling Enhancement of the Electrical Response of Nanoparticle Networks, *Small*, **8**, (2012), 108-115.
5. J.-F. Dayen, E. Devid, M. V. Kamalakar, D. Golubev, C. M. Guédon, V. Faramarzi, B. Doudin and S. J. van der Molen, Enhancing the Molecular Signature in Molecule-nanoparticle Networks via Inelastic Cotunneling, *Adv. Mater.*, **25**, (2013), 400-404.
6. R. P. Andres, J. D. Bielefeld, J. I. Henderson, D. B. Janes, V. R. Kolagunta, C. P. Kubiak, W. J. Mahoney and R. G. Osifchin, Self-assembly of a Two-dimensional Superlattice of Molecularly Linked Metal Clusters, *Science*, **273**, (1996), 1690-1693.
7. X. M. Lin, H. M. Jaeger, C. M. Sorensen and K. J. Klabunde, Formation of Long-Range-Ordered Nanocrystal Superlattices on Silicon Nitride Substrates, *J. Phys. Chem. B.*, **105**, (2001), 3353-3357.
8. J. Liao, L. Bernard, M. Langer, C. Schönenberger and M. Calame, Reversible Formation of Molecular Junctions in 2D Nanoparticle Arrays, *Adv. Mater.*, **18**, (2006), 2444-2447.
9. L. Bernard, Y. Kamdzhilov, M. Calame, S. J. van der Molen, J. Liao and C. Schönenberger, Spectroscopy of Molecular Junction Networks Obtained by Place Exchange in 2D Nanoparticle Arrays, *J. Phys. Chem. C*, **111**, (2007), 18445-18450.

10. M. J. Hostetler, A. C. Templeton and R. W. Murray, Dynamics of Place-exchange Reactions on Monolayer-protected Gold Cluster Molecules, *Langmuir*, **15**, (1999), 3782-3789.
11. J. Liao, J. S. Agustsson, S. Wu, C. Schönenberger, M. Calame, Y. Leroux, M. Mayor, O. Jeannin, Y.-F. Ran, S.-X. Liu and S. Decurtins, Cyclic Conductance Switching in Networks of Redox-active Molecular Junctions, *Nano Lett.*, **10**, (2010), 759-764.
12. S. J. van der Molen, J. Liao, T. Kudernac, J. S. Agustsson, L. Bernard, M. Calame, B. J. van Wees, B. L. Feringa and C. Schönenberger, Light-controlled Conductance Switching of Ordered Metal-Molecule-Metal Devices, *Nano Lett.*, **9**, (2009), 76-80.
13. A. Kaminska, O. Inya-Agha, R. J. Forster and T. E. Keyes, Chemically Bound Gold Nanoparticle Arrays on Silicon: Assembly, Properties and SERS Study of Protein Interactions, *Phys. Chem. Chem. Phys.*, **10**, (2008), 4172-4180.
14. M. Halcrow, The Synthesis and Coordination Chemistry of 2,6-bis(pyrazolyl)pyridines and Related Ligands - Versatile Terpyridine Analogues, *Coord. Chem. Rev.*, **249**, (2005), 2880-2908.
15. C. Rajadurai, F. Schramm, S. Brink, O. Fuhr, M. Ghafari, R. Kruk and M. Ruben, Spin Transition in a Chainlike Supramolecular Iron(II) Complex, *Inorg. Chem.*, **45**, (2006), 1019-1021.
16. M. Cavallini, I. Bergenti, S. Militta, J. C. Kengne, D. Gentili, G. Ruani, I. Šalitroš, V. Meded and M. Ruben, Thin Deposits and Patterning of Room-Temperature-Switchable One-dimensional Spin-crossover Compounds, *Langmuir*, **27**, (2011), 4076-4081.
17. V. Meded, A. Bagrets, K. Fink, R. Chandrasekar, M. Ruben, F. Evers, A. Bernard-Mantel, J. S. Seldenthuis, A. Beukman and H. S. J. van der Zant, Electrical Control over the Fe(II) Spin Crossover in a Single Molecule: Theory and Experiment, *Phys. Rev. B*, **83**, (2011), 245415(1-13).
18. R. Chandrasekar, F. Schramm, O. Fuhr and M. Ruben, An Iron(II) Spin-transition Compound with Thiol Anchoring Groups, *Eur. J. Inorg. Chem.*, **17**, (2008), 2649-2653.
19. M. Kamenetska, S. Y. Quek, A. C. Whalley, M. L. Steigerwald, H. J. Choi, S. G. Louie, C. Nuckolls, M. S. Hybertsen, J. B. Neaton and L. Venkataraman, Conductance and Geometry of Pyridine-linked Single-molecule Junctions, *J. Am. Chem. Soc.*, **132**, (2010), 6817-6821.
20. C. M. Guédon, J. Zonneveld, H. Valkenier, J. C. Hummelen and S. J. van der Molen, Controlling the Interparticle Distance in a 2D Molecule-nanoparticle Network, *Nanotechnology*, **22**, (2011), 125205(1-5).
21. R. G. Nuzzo and D. L. Allara, Adsorption of Bifunctional Organic Disulfides on Gold Surfaces, *J. Am. Chem. Soc.*, **105**, (1983), 4481-4483.
22. J. M. Tour, L. Jones II, D. L. Pearson, J. J. S. Lamba, T. P. Burgin, G. M. Whitesides, D. L. Allara, A. N. Parikh and S. Atre, Self-assembled Monolayers and Multilayers of Conjugated Thiols, .alpha.,.omega.-Dithiols, and Thioacetyl-containing Adsorbates. Understanding Attachments between Potential Molecular Wires and Gold Surfaces, *J. Am. Chem. Soc.*, **117**, (1995), 9529-9534.

-
23. S. Huang, G. Tsutsui, H. Sakaue, S. Shingubara and T. Takahagi, Experimental Conditions for a Highly Ordered Monolayer of Gold Nanoparticles Fabricated by the Langmuir-Blodgett Method, *J. Vac. Sci. Technol. B*, **19**, (2001), 2045-2049.
 24. V. Santhanam and R. P. Andres, Microcontact Printing of Uniform Nanoparticle Arrays, *Nano Lett.*, **4**, (2004), 41-44.
 25. J.-F. Dayen, V. Faramarzi, M. Pauly, N. T. Kemp, M. Barbero, B. P. Pichon, H. Majjad, S. Begin-Colin and B. Doudin, Nanotrench for Nano and Microparticle Electrical Interconnects, *Nanotechnology*, **21**, (2010), 335303(1-7).
 26. P. A. Midgley, M. Weyland, J. M. Thomas and B. F. G. Johnson, Z-contrast Tomography: a Technique in Three-dimensional Nanostructural Analysis based on Rutherfordscattering, *Chem. Commun.*, **10**, (2001), 907-908.
 27. C. Kübel, A. Voigt, R. Schoenmakers, M. Otten, D. Su, T.-C. Lee, A. Carlsson and J. Bradley, Recent Advances in Electron Tomography: TEM and HAADF-STEM Tomography for Materials Science and Semiconductor Applications, *Microsc. & Microanal.*, **11**, (2005), 378-400.
 28. J. Kumar, X. Wei, S. Barrow, A. M. Funston, K. G. Thomas and P. Mulvaney, Surface Plasmon Coupling in End-To-End Linked Gold Nanorod Dimers and Trimers, *Phys. Chem. Chem. Phys.*, **15**, (2013), 4258-4264.
 29. G. Mie, Beiträge Zur Optik Trüber Medien, Speziell Kolloidaler Metallösungen, *Ann. Phys.*, **25**, (1908), 377-445.
 30. L. Bernard, *Expanding the Horizon of Molecular Electronics via Nanoparticle Assemblies*. Ph. D. Thesis, University of Basel, Switzerland, **2006**.
 31. J. M. Garnett, Colours in Metal Glasses and in Metallic Films, *Philos. Trans. R. Soc. London*, **203**, (1904), 385-420.
 32. R. W. Cohen, G. D. Cody, M. D. Coutts and B. Abeles, Optical Properties of Granular Silver and Gold Films, *Phys. Rev. B*, **8**, (1973), 3689-3701.
 33. D. Dalascu and L. Martinu, Optical Properties of Discontinuous Gold Films: Finite-size Effects, *Journal of the Optical Society of America B: Optical Physics*, **18**, (2001), 85-92.
 34. N. Camillone III, T. Y. B. Leung, P. Schwartz, P. Eisenberger and G. Scoles, Chain Length Dependence of the Striped Phases of Alkanethiol Monolayers Self-assembled on Au(111): An Atomic Beam Diffraction Study, *Langmuir*, **12**, (1996), 2737-2746.
 35. S. K. Saikin, R. Olivares-Amaya, D. Rappoport, M. Stopa and A. Aspuru-Guzik, On the Chemical Bonding Effects in the Raman Response: Benzenethiol Adsorbed on Silver Clusters, *Phys. Chem. Chem. Phys.*, **11**, (2009), 9401-9411.
 36. K. B. Biggs, J. P. Camden, J. N. Anker and R. P. van Duyne, Surface-enhanced Raman Spectroscopy of Benzenethiol Adsorbed from the Gas Phase onto Silver Film over Nanosphere Surfaces: Determination of the Sticking Probability and Detection Limit Time, *J. Phys. Chem. A.*, **113**, (2009), 4581-4586.
 37. X. W. Kang and S. W. Chen, Electronic Conductivity of Alkyne-capped Ruthenium Nanoparticles, *Nanoscale*, **4**, (2012), 4183-4189.
 38. G. Cardini and M. Muniz-Miranda, Density Functional Study on the Adsorption of Pyrazole onto Silver Colloidal Particles, *J. Phys. Chem. B.*, **106**, (2002), 6875-6880.
 39. F. Lordan, N. Al-Attar, C. Mallon, J. Bras, G. Collet, R. J. Forster, T. E. Keyes and J. H. Rice, Temperature Dependence of a_1 and b_2 Type Modes in the Surface

- enhanced Raman from 4-Aminobenzenethiol, *Chemical Physics Letters*, **556**, (2013), 158-162.
40. H. Yan, S. I. Lim, L.-C. Zhang, S.-C. Gao, D. Mott, Y. Le, R. Loukrakpam, D.-L. An and C.-J. Zhong, Rigid, Conjugated and Shaped Arylethynes as Mediators for the Assembly of Gold Nanoparticles, *J. Mater. Chem.*, **21**, (2011), 1890-1901.
41. S. Eisler, R. McDonald, G. R. Loppnow and R. R. Tykwinski, Structural, Vibrational, and Electronic Characteristics of Enyne Macrocycles as a Function of Ring Strain, *J. Am. Chem. Soc.*, **122**, (2000), 6917-6928.
42. T. B. Tran, I. S. Beloborodov, J. Hu, X. M. Lin, T. F. Rosenbaum and H. M. Jaeger, Sequential Tunneling and Inelastic Cotunneling in Nanoparticle Arrays, *Phys. Rev. B.*, **78**, (2008), 075437-075445.
43. A. N. Shipway, E. Katz and I. Willner, Nanoparticle Arrays on Surfaces for Electronic, Optical, and Sensor Applications, *Chemphyschem*, **1**, (2000), 18-52.
44. G. Schmid, St. Peschel and Th. Sawitowski, Two-dimensional Arrangements of Gold Clusters and Gold Colloids on Various Surfaces, *Z. anorg. allg. Chem.*, **623**, (1997), 719-723.
45. T. Sato, D. Brown and B. F. G. Johnson, Nucleation and Growth of Nano-gold Colloidal Lattices, *Chem. Commun.*, **0**, (1997), 1007-1008.
46. C. George, I. Szleifer and M. Ratner, Multiple-Time-Scale Motion in Molecularly Linked Nanoparticle Arrays, *ACS Nano*, **7**, (2013), 108-116.
47. J. Slot and H. Geuze, A New Method for Preparing Gold Probes for Multiple Labeling Cytochemistry, *Eur. J. Cell Biol.*, **38**, (1985), 87-93.
48. Y. Noguchi, T. Terui, T. Katayama, M. M. Matsushita and T. Sugawara, Charge Transport in Various Dimensions of Small Networks Composed of Gold Nanoparticles and Terthiophene Wire-molecules, *Appl. Phys. Lett.*, **98**, (2011), 263114-263117.
49. M. Allen, Coulomb Blockade in Network of Nanoparticles, *Matter, Geometry, and Electromagnetics*, S-96, **4620**, (2006), 1-9.

6

Spin transition in arrays of gold nanoparticles and spin crossover molecules

We investigate if the functionality of spin crossover molecules is preserved when they are assembled into an interfacial device structure. Specifically, we prepare and investigate gold nanoparticle arrays, into which room-temperature spin crossover molecules are introduced, more precisely $[\text{Fe}(\text{AcS-BPP})_2](\text{ClO}_4)_2$, where $\text{AcS-BPP} = \text{S-(4-}\{[2,6\text{-}(\text{bipyrazol-1-yl})\text{pyrid-4-yl}]\text{ethynyl}\}\text{phenyl)ethanethioate}$ (in short $\text{Fe}(\text{S-BPP})_2$). We combine three complementary experiments to characterize the molecule-nanoparticle structure in detail. Temperature-dependent Raman measurements provide direct evidence for a (partial) spin transition in the $\text{Fe}(\text{S-BPP})_2$ -based arrays. This transition is qualitatively confirmed by magnetization measurements. Finally, charge transport measurements on the $\text{Fe}(\text{S-BPP})_2$ -gold nanoparticle devices reveal a minimum in device resistance versus temperature, $R(T)$, curves around 260-290 K. This is in contrast to similar networks containing passive molecules only, that show monotonically decreasing $R(T)$ characteristics. Backed by DFT calculations on single molecular conductance values for both spin states, we propose to relate the resistance minimum in $R(T)$ to a spin transition, under the hypothesis that 1) the molecular resistance of the high-spin state is larger than that of the low-spin state, 2) transport in the array is governed by a percolation model.

This chapter is based on the article published in ACS Nano, **9**, (2015), 4496-4507.

Spin Transition in Arrays of Gold Nanoparticles and Spin Crossover Molecules,

E. J. Devid, P. N. Martinho, M. V. Kamalakar, I. Šalitroš, Ú. Prendergast, J.-F. Dayen, V. Meded, T. Lemma, R. González-Prieto, F. Evers, T. E. Keyes, M. Ruben, B. Douidin and S. J. van der Molen.

6.1 Introduction to molecular complex-nanoparticle ensembles

One of the most exciting prospects of molecular electronics is that future nanoscopic devices may be based on molecules with a well-defined functionality. Among the most prominent examples are molecular rectifiers [1, 2] and switchable molecular devices [3-6]. Indeed, molecular switches based on a variety of mechanisms have been considered for applications. These include mechanically interlocked switches (rotaxanes, catenanes), photochromic molecules (diarylethenes, diazobenzenes), tautomerization switches and redox-active molecules. To drive switching at the device level typically requires molecular assembly at a solid interface (i.e. electrodes). *A priori*, it is difficult to judge if a switchable molecule will retain its function once it is inserted in a metal-molecule-metal device. Connecting electrodes to a molecule may affect the molecule's mechanical freedom, alter its precise density of states and/or influence the decay of the excited state initiating the switching process. Nevertheless, a growing number of proof-of-principle switchable devices, based on bistable molecules, have been presented in literature [6]. Here, we concentrate on molecules with a bistability related to the other basic property of the electron besides charge, i.e. its spin. Specifically, spin crossover (SCO) molecules are studied, with the aim of finding a signature of molecular spin transition in an interfacial device geometry.

SCO molecules generally consist of a central transition metal ion, coupled to organic ligands [4, 5, 7]. Depending on the specific geometry and the strength of the ligand field, such molecules may switch between a diamagnetic, low-spin (LS) and a paramagnetic, high-spin (HS) state as a function of temperature, illumination, pressure, magnetic or electric field [8-15]. To illustrate this principle, Figure 6.1 shows the molecular species synthesized for this study $[Fe(AcS-BPP)_2](ClO_4)_2$ (where *AcS-BPP* denotes *S*-(4-([2,6-(bipyrazol-1-yl)pyrid-4-yl]ethynyl)phenyl)ethanethioate).

Basically, a rod-like metal complex is displayed, based on an iron (II) ion and two organic ligands [16]. In bulk powder form, the formula is $[Fe(AcS-BPP)_2](ClO_4)_2$ (hereafter called molecule **1**) including thioacetate protecting groups and counter ions. After exposure to gold surfaces, deprotection of the Ac-S anchor groups occurs, leading to a formal composition of $Fe(S-BPP)_2$ under near surface conditions (hereafter called molecule **1'**).

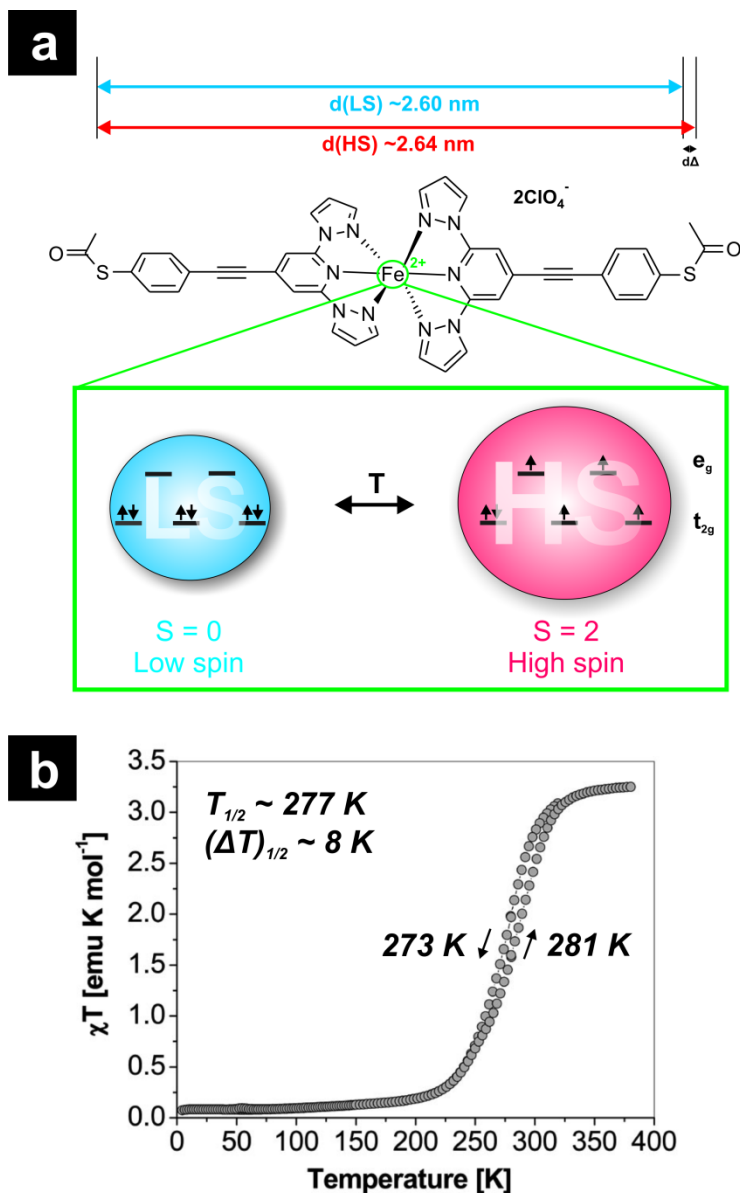


Figure 6.1: Spin crossover molecule **1**: (a) Schematic representation of molecule **1** visualizing its spin transition (governed by the occupancy of the t_{2g} and e_g states) and the corresponding tiny length change. (b) Temperature-dependent magnetic susceptibility measurement of the same bulk crystalline SCO compound. The spin transition temperature is centered at $T_{1/2} = 277 \text{ K}$ and accompanied by a thermal hysteresis loop with $\Delta T_{1/2} = 8 \text{ K}$.

The bulk sample of **1** exhibits a spin transition as illustrated by a measurement of the magnetic susceptibility χT . Plotting χT versus temperature T indicates a broad, but distinct, transition between a $S = 0$ (diamagnetic) and a $S = 2$ (paramagnetic) state, see Figure 6.1(b). Moreover, the transition is hysteretic due to intermolecular interaction ('cooperativity') in the bulk lattice [7].

While SCO compounds have been synthesized and studied in bulk since the 1930s [8, 9], the research activity in this field has intensified in recent years. On the one hand, prospective applications motivate scientists to increase the transition temperature up to ambient by synthesizing new molecules [17, 18]. On the other hand, decreasing the size of the molecular system from macroscopic (bulk) down to the nanometer scale can provide unique insight into fundamentals of spin transition properties, with applications to nanoelectronics and spintronics. The switching properties of SCO compounds may be strongly modified at the nanoscale, however. It is known that the characteristics of SCO compounds depend critically on the identity of the transition metal ion, the nature of the ligands and the exact symmetry and strength of the ligand field [19, 20]. Clearly, some of these properties may change drastically when decreasing the dimensions of ensembles of SCO molecules and their environment. Recently, scanning tunneling microscopy (STM) experiments performed on ultra-thin films at low temperatures revealed that electric field-induced switching can only occur in the second molecular layer [21] or for molecules electronically decoupled from the substrates [22]. Even though the interpretation of STM images is challenging, there are experimental indications that SCO ultra-thin films exhibit transition properties deviating significantly from the bulk, in particular by exhibiting co-existence of HS and LS states at low temperatures [23]. Molecular devices at low temperatures involving a single or a few SCO molecules were also reported by Meded *et al.*, who used a gate-controlled three-terminal molecular device to reveal possible voltage-induced switching [15]. In addition, surface spectroscopy techniques (XAS, UPS, IPES) are well-suited to characterize ultra-thin films. While these ensemble-based techniques are challenged by detection sensitivity issues, they do allow for temperature-dependent studies. M. Bernien *et al.* [24] showed that sub-monolayer films with small energy coupling with the substrate preserved the bulk properties. Furthermore, Zhang *et al.* [25] reported that the substrate ferroelectric state can constrain the stable state of SCO films of several nanometers thick and recently photothermal switching of Fe^{2+} spin crossover@silica-

gold nanocomposites was reported [26]. Finally, Warner *et al.* [27] performed X-ray absorption spectroscopy on submonolayers of iron-complexes on flat Au(111). They found evidence for both a light- and temperature-induced spin transition, but only for a fraction of the molecules. The authors argue that the precise molecular behaviour depends sensitively on the interactions with the surface and with other molecules.

Overviewing scientific literature, the question as to if and how spin transition persists in nanoscale ensembles remains open, with strong experimental indications that interactions with the substrates, or connecting electrodes, play a decisive role in the preservation or not of spin transition. Since this issue is of fundamental importance, validating the occurrence of a SCO transition is key if we want to use this type of molecule in functional devices. We propose the following two criteria for convincing experiments:

- the experimental insight should not rely on a single technique only. In other words, the electrical transport properties should be complemented by other methods, validating in particular the occurrence of a spin transition and (ideally) providing structural insight into the interaction of the SCO molecules to the substrate.
- temperature-dependent studies must be performed. Temperature is the best indicator of thermodynamic stability of a given phase, probing the cooperativity of the system, and providing a direct comparison with known bulk properties. Previous experimental approaches to SCO molecular transport provided limited insight into temperature dependence, and most published results investigate switching of SCO molecules through a stimulus (electric field) undocumented for thin films or bulk materials.

The aim of this present work is therefore to perform temperature-dependent studies of the transition behaviour of SCO molecular device structures, combining Raman spectroscopy, magnetometry, and electrical transport measurements, complemented by charge transport calculations.

We make use of two-dimensional (2D) arrays of molecular-bound Au nanoparticles, bridging the gap separating the molecular length scale and typical length scales of patterned metallic electrodes. As a basic structure, we use samples made of alkanethiol-protected gold nanoparticles. With an exchange process based on self-assembly, the molecules **1** (Figure 6.1) are inserted onto and between the nanoparticles. In this way,

an ensemble is created based on single nanoparticle-molecule-nanoparticle junctions [28-31]. The arrays thus prepared are structurally robust at room temperature, capable of withstanding temperature sweeps, and easily addressable by external stimuli. Moreover, they allow for (control) experiments to check the device properties before and after molecular insertion. These may include several varieties of optical spectroscopy, representing an important advantage over true single-molecule techniques. At a density of junctions on the order of 10^4 per μm^2 , the device architecture chosen provides direct statistical information on molecular junction properties. Still, as in most molecular device geometries, it is difficult to know the exact number of molecules involved in a single nanoparticle-molecule(s)-nanoparticle unit.

This Chapter is organized as follows. After introducing sample preparation and basic experimental methods, we describe and discuss temperature-dependent Raman spectroscopy and magnetization measurements, respectively. These give evidence for a (partial) spin transition in arrays containing SCO molecules. Next, we present conductance experiments as a function of temperature, followed by single-molecule transport calculations. Finally, we show that the experimental conductance data are consistent with the combined Raman and magnetization results and with transport calculations. For this, we employ a simple percolation model that incorporates a temperature-dependent (partial) spin transition.

6.2 Experimental method of a spin crossover-gold nanoparticle array

The method for the fabrication of molecule **1'**-gold nanoparticle arrays is described in detail in the paragraph 3.3.1. In short, spherical gold nanoparticles (8.5 ± 1.5 nm diameter) are synthesized in-house and modified with octanethiol molecules [16, 32]. Next, they are made to self-assemble in an ordered array on a water surface. Such an array can be transferred to a substrate of choice by microcontact printing. For this study, we used glass, quartz and Si-SiO₂ substrates. Furthermore, we have transferred arrays to high-aspect-ratio nanotrench devices [16, 33, 34]. The latter are made by electron-beam lithography and consist of two wide electrodes (typical widths are ≈ 20 μm) that are separated by only ~ 100 nm, so as to define a favourable aspect ratio. Figure 6.2 shows a SEM (scanning electron microscopy) micrograph and a schematic of a typical

device (see also Appendix C.1). In some cases, multiple stamping is performed to create layer-on-layer molecule-gold nanoparticle network devices. ‘Virgin’ networks of octanethiol-covered gold nanoparticles are first characterized via charge transport measurements and UV-Vis absorption spectroscopy. Subsequently, molecular exchange is performed by inserting a sample in a solution of **1** in acetonitrile (MeCN).

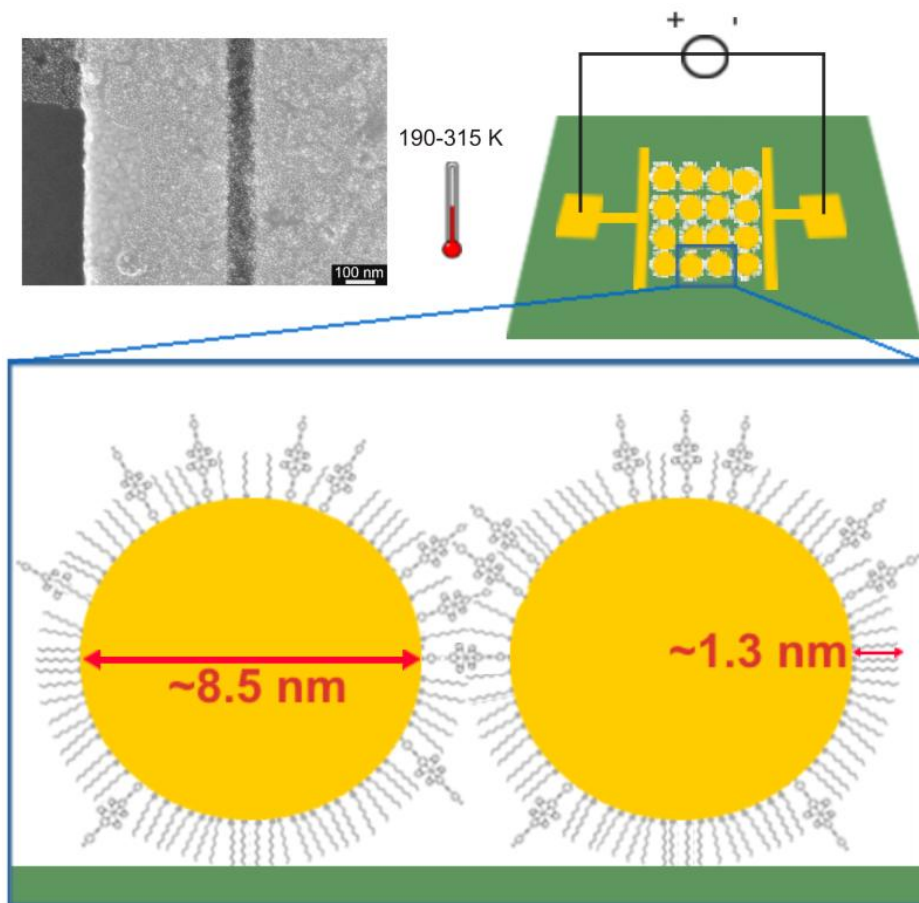


Figure 6.2: Micrograph (top left, SEM image: scale bar is 100 nm) and a schematic representation (top right) of a 2D molecule-gold nanoparticle array device (in reality, the gold nanoparticles are ordered in a triangular lattice). Bottom: schematic representation of a gold nanoparticle-molecules **1**'/C8 molecules-gold nanoparticle junction on an insulating substrate, where **1**'/C8 denotes a mixture of molecules **1**' and octanethiols.

UV-Vis spectroscopy is used to determine if the molecular exchange process was successful. In the latter case, the surface plasmon resonance (SPR) peak of the initial octanethiol-gold nanoparticle array shows a red shift after exchange, attributed to the increase in the dielectric constant experienced by the nanoparticles (see Appendix C.2). In our study, we combine charge transport experiments with Raman spectroscopy and magnetization measurements. All three sets of experiments are performed as a function of temperature. Due to practical constraints, these experiments have been performed on different samples, all prepared in an identical manner. Finally, we note that sets of reference samples have been prepared to benchmark the data on SCO molecules. The first set is based on a similar exchange procedure but with dithiolated OPE (oligo(phenylene ethynylene)) molecules instead of the deprotected SCO complex molecules **1'**. For the second set, the non-metallated ligand S-BPP (see Chapter 5, Figure 5.1) is used to coat the gold nanoparticles directly, after which array devices are created via self-assembly and microcontact printing [16].

6.3 Temperature-dependent Raman spectroscopy measurements

The arrayed nature of the gold nanoparticles and their small inter-particle separation leads to a plasmon absorbance, which is resonant with the 633 nm light used to excite the samples for Raman spectroscopy. Therefore, the Raman spectrum of the 2D molecule **1'**-gold nanoparticle array is expected to be surface enhanced (so-called surface-enhanced Raman spectroscopy (SERS)). Correspondingly, from comparison of the Raman spectra of the bulk powder of molecule **1** and the 2D molecule **1'**-gold nanoparticle array, it is evident that there are some very significant changes in the relative intensity and the vibrational frequencies of several key modes of the complex on gold nanoparticle binding. This technique, which provides a molecular fingerprint reflecting the structure of the adsorbed species, is ideally suited to detect the dominant SCO phase at a given temperature and provides insight into molecules-surface interactions.

Many of the observed changes are strongly reminiscent of our previous report on binding of the parent S-(4-{[2,6-(bipyrazol-1-yl)pyrid-4-yl]ethynyl}phenyl)thioate (S-BPP) ligand at a gold nanoparticle array [16]. For example, the mode which dominates the SERS spectrum at 1574 cm^{-1} is attributed to the aryl in-plane C-C stretch mode of the benzenethiol moiety which is observed at approximately 1590 cm^{-1} in the unbound

complex [16, 35]. In the Raman spectrum of the SCO complex, this mode is superimposed on a more intense pyridine C-C stretch mode. The frequency shift and dramatic increase in intensity of this benzenethiol mode observed on nanoparticle binding of the SCO complex are analogous to the spectral behaviour observed for the free AcS-BPP when it was bound to a gold nanoparticle array and is strong evidence that the molecule **1'** is thiol-bound to the gold. Indeed, the dramatic relative increase in intensity of the 1574 cm^{-1} mode, along with other benzenethiol modes at 1078 and 406 cm^{-1} , is consistent with the surface enhancement of these signals due to proximity of the associated moieties to the plasmonic field of the nanoparticles, which would be expected if the complex is binding to the nanoparticles through the benzenethiol unit. A new feature evident at 321 cm^{-1} is tentatively attributed to the Au-S mode. Notably, the pyrazine and pyridine modes at 1619 cm^{-1} , 1381 cm^{-1} and 1014 cm^{-1} which dominate the Raman spectra of the bulk **1** powder are considerably weaker compared with the benzenethiol features in the SERS spectrum. Therefore, the overall pattern of surface enhancement of the Raman spectral data indicates that molecule **1'** is thiol-bound and oriented largely normal to the gold nanoparticle surface, as indicated by the absence in comparable SERS enhancement in the pyrazine and pyridine modes.

The temperature-dependent Raman spectra of the bulk powder molecule **1** and the molecule **1'**-gold nanoparticle array were then compared over the temperature range 353 to 80 K , which encompasses the SCO transition in the bulk powder. The full temperature-dependent Raman spectra of the bulk SCO powder **1** are shown in Figures C-3 till C-5 in Appendix C.3. They are strongly reminiscent of Raman spectral changes accompanying spin transition of a related iron complex [17]. Indeed, similar key markers of spin transition are observed. Most notably, in going from room to low temperature, the feature at 1014 cm^{-1} disappears and is replaced by a mode at 1039 cm^{-1} . From DFT calculations, the peak at 1014 cm^{-1} is attributed to a pyridine ring breathing mode whose motion is coupled strongly to the Fe(II)-N stretch. Correspondingly, the replacement feature at 1039 cm^{-1} is attributed to the analogous normal mode in the LS state. The intensity of the feature at 1014 cm^{-1} (integrated against a relatively temperature independent mode at 1590 cm^{-1} from benzenethiol) is plotted against temperature in the inset of Figure C-4 in Appendix C.3. This plot yields a sigmoidal curve that exhibits a transition temperature in excellent agreement with the magnetization data for bulk powder (see Figure 6.1(b)). This result indicates that these Raman spectral changes can be attributed to spin transition. In addition, C-C stretch

modes for the pyridine and pyrazine ligands respectively at 1589 cm^{-1} and 1618 cm^{-1} change in relative intensity and shift to higher energy with decreasing temperature, consistent with strengthening of these bonds as the metal antibonding e_g^* levels are vacated in the LS state of the SCO complex.

The influence of changing temperature on the SERS spectrum of the spin transition molecule **1'** in the nanoparticle array (i.e. 2D molecule **1'**-gold nanoparticle array) is less dramatic. This is a result of the domination of the SERS modes of the benzenethiol which is not strongly influenced by temperature. Nonetheless, close inspection of modes associated with the iron complex show that clear spectral changes occur with temperature in **1'**-gold nanoparticle arrays, as displayed in Figure 6.3 (see also Appendix C.4, Table 1 and Figure C-6). Most tellingly, the major spectral changes occur between approximately 800 and 1200 cm^{-1} where, from DFT calculations, the majority of the coupled ligand breathing/Fe-N vibrations occur. In particular, the band at 1014 cm^{-1} , identified as a marker of spin transition in the bulk material, decreases significantly at low temperature. In parallel, a feature at 1104 cm^{-1} increases in intensity. This mode is tentatively assigned to the LS state ligand ring breathing coupled to Fe(II)-N bonds seen at 1039 cm^{-1} in the bulk SCO compound **1**, keeping in mind that unambiguous assignment of this mode is not possible without accompanying DFT calculations of the nanoparticle bound complex. We note that, in addition, a weak feature at 1125 cm^{-1} decreases with decreasing temperature with concomitant grow-in of a feature at 1151 cm^{-1} . On the basis of DFT calculations, both are attributed to in-plane ring NCH stretch modes coupled to equatorial Fe-N stretch in the LS state. Interestingly, the alkyne $\text{C}\equiv\text{C}$ stretching mode at 2207 cm^{-1} shifts to the blue by approximately 8 cm^{-1} at low temperature and sharpens significantly. Such behaviour was observed previously in experiments where S-BPP-ligand were incorporated in the nanoparticle arrays (i.e. S-BPP-gold nanoparticle array), in the absence of iron [16], and therefore this is not related to spin transition. It is important to note that some of the features observed in the molecule **1'**-gold nanoparticle array did not resolve in the bulk SCO material. This can be attributed to surface binding and SERS effect which are expected to change both the selection rules and intensities of the modes observed.

All in all, evidence from Raman spectroscopy for persistence of spin transition in the gold nanoparticle bound metal complex is compelling, but the fact that the Raman spectral features associated with the low-spin and high-spin states are not completely

lost at the most extreme temperature suggests that the transition is not as complete as was observed in the bulk.

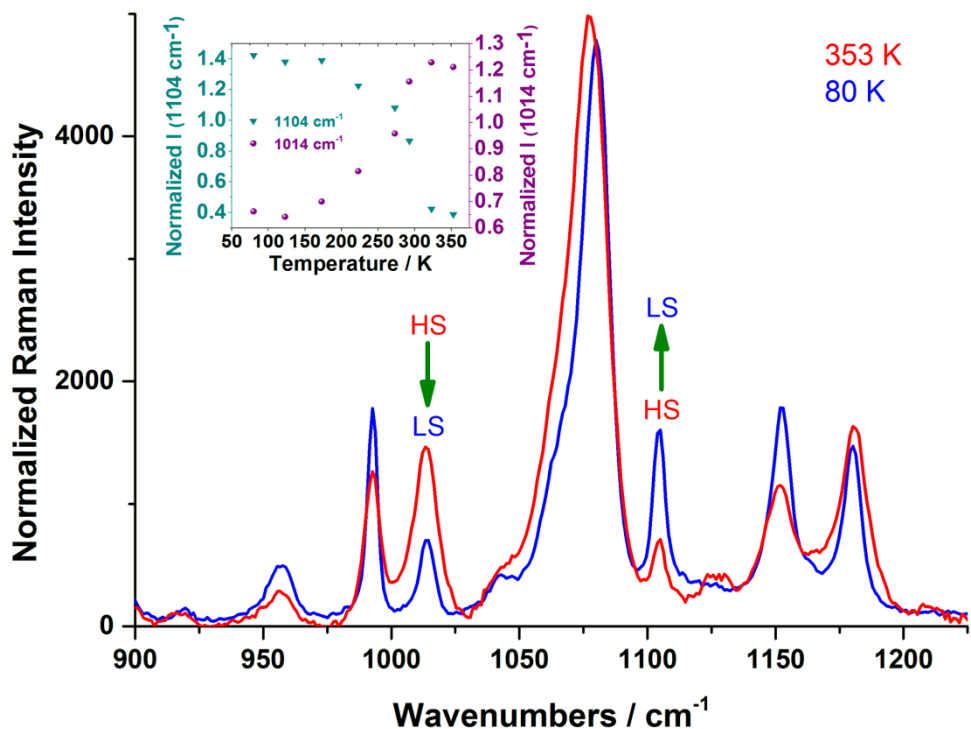


Figure 6.3: Raman spectra of a 2D molecule I'-gold nanoparticle array at 353 and 80 K, respectively, excited at 633 nm (incident power 1.2 mW at the array) on a quartz substrate. Note that the mode at 1014 cm^{-1} increases with increasing temperature, whereas the mode at 1104 cm^{-1} decreases. Inset shows more detail on the intensity of these two modes, which are sensitive to the spin transition, as a function of temperature. Both modes are normalized to the 406 cm^{-1} benzenethiol mode which showed weak temperature dependence.

To provide better quantitative insight, the intensity of both the 1014 cm^{-1} and 1104 cm^{-1} modes, which are markers of HS and LS states in the array respectively, are plotted versus temperature for the normalized spectra (see inset of Figure 6.3). Their intensity values are given relative to a benzene thiol mode, used as a phase-independent temperature marker in the bulk powder. As shown in Figure 6.3 inset, this reveals two sigmoidal curves, one growing in (the HS marker, i.e. 1014 cm^{-1} mode) and one

decreasing (the LS marker, i.e. 1104 cm^{-1} mode), with a midpoint each of around 270 K. This temperature-dependent behaviour correlates well with the magnetic data shown below and is consistently reminiscent of the behaviour of the spin transition in the bulk powder [19]. The slope of the temperature dependence, weaker in the 2D molecule **1'**-gold nanoparticle array than in the bulk powder, may be attributed to the fact that a pure HS state is not completely achieved over the temperature range explored here, as indicated by residual features from the HS state at low T and vice versa. From the relative change to the integrated area under the features at 1014 and 1104 cm^{-1} , we can estimate what fraction of the SCO molecules undergoes spin transition, however, with significant uncertainty. The percentages we find are 65% (from 1014 cm^{-1} mode) and 80% (from 1104 cm^{-1} mode), respectively. The differences in the estimated areas are attributed to residual uncorrected background in the Raman spectra which is stronger under the 1014 cm^{-1} band. We can say therefore that we obtain a minimum of 65% spin transition. It is important to note that the temperature-dependent changes to the Raman spectra of both the SCO bulk powder **1** and molecule **1'**-gold nanoparticle array were fully reversible on restoring temperature to its original value. We do not find experimental indications of hysteresis in the spin transition, i.e. the temperature sweeping direction does not matter.

We have benchmarked our findings on SCO transition by also performing temperature-dependent Raman on the reference C8-gold nanoparticle array (see Chapter 5, Figure 5.8). In contrast to the SCO spectra, little spectral change and no indication of transition are observed in the temperature-dependent data: besides broadening out of features at high temperatures with an increase of the background, no clear shifts are observed in the few bands that are attendant in Figure 5.8.

In summary, temperature-dependent Raman spectroscopy provides evidence for a spin transition in the molecule **1'**-gold nanoparticle arrays and reveals that the molecules are bound to Au with their thiol group(s). However, unlike the bulk material, the transition does not appear to be complete, with a minority of the molecules not exhibiting a crossover.

6.4 Magnetization measurements

Magnetic properties have been investigated to confirm the occurrence of a spin transition in the nanoparticle array. Three samples are prepared by layer-on-layer

deposition of C8-gold nanoparticles arrays onto quartz substrates of 10 x 6 mm size. Two of these samples are then exchanged with SCO molecules. The total magnetic moment of gold nanoparticle networks incorporating molecules **1'** (i.e. spin transition samples **B** and **C** (each sample contains different amounts of nanoparticles due to stamp size variation ect.) as well as a reference sample **A** (containing octanethiols only) have been measured on a SQUID magnetometer (see Appendix C.5) under applied magnetic field of 1 T, in the temperature range 90-400 K (see Figure 6.4).

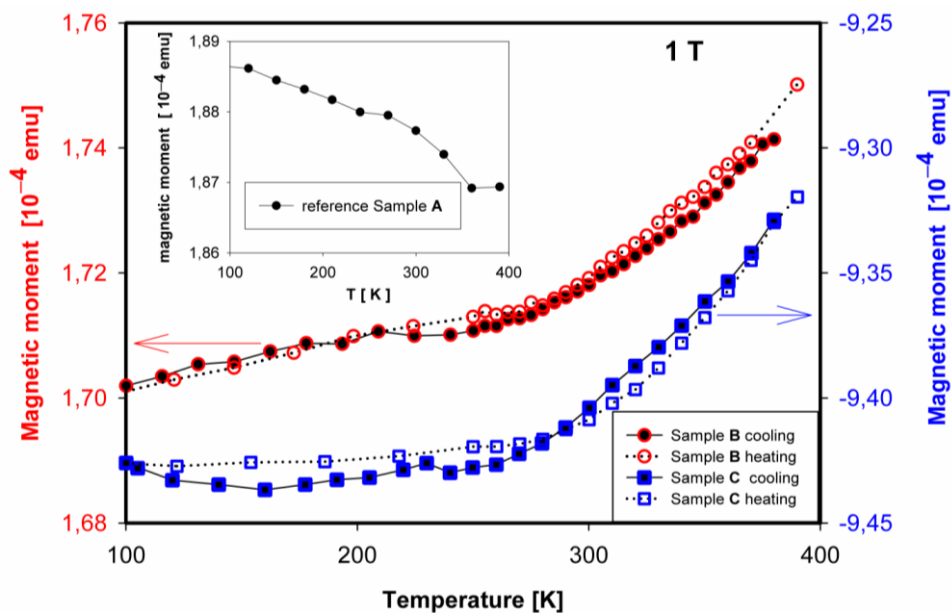


Figure 6.4: Temperature-dependent magnetization measurements on three gold nanoparticle network samples (on quartz substrates). For gold nanoparticle networks incorporating molecules **1'** (samples **B** and **C**), a clear change in magnetic moment is observed around 250 K, consistent with a partial spin transition. Inset: temperature-dependent magnetic moment of reference sample **A**, which contains a gold nanoparticle network with only octanethiol molecules. All magnetic measurements were carried out under a 1 T external magnetic field. (These experiments were performed by Dr. I. Šalitroš at the Institute of Inorganic Chemistry, Technology and Materials in Bratislava.)

All three samples contain predominantly diamagnetic material (quartz substrate, gold nanoparticle and octanethiol (C8)). A diamagnetic signal is indeed detected for sample **C**. Because the diamagnetic response of samples **A** and **B** is most probably weaker than

the signal coming from the nearby background signal environment of the sample position (tape and quartz), the signal is found to be paramagnetic for samples **A** and **B**.

In Figure 6.4, for the temperature range 100-200 K, the magnetic moment of both **B** and **C** samples remains rather constant whereas it rises with increasing temperature in the 200-400 K range. Both curves show similar temperature-dependent behaviour, indicating reproducibility. The reference sample **A** shows a different behaviour, with magnetic moment diminishing with increasing temperatures. One can therefore tentatively attribute the increase of paramagnetism with temperature for samples **B** and **C** to the occurrence of a diamagnetic-paramagnetic spin transition. Consistent with the Raman data, measurements in both cooling and heating directions confirm the temperature reversibility.

The lack of an abrupt spin transition with temperature is attributed to the diluted nature of SCO switching centers in the sample leading to diminished cooperativity and the absence of saturation at 400 K for nanoparticles samples confirms the partial nature of the spin transition [36, 37].

While care must be taken in the magnetic data interpretation due to the limited signal from the molecules of interest, the findings confirm the outcome of Raman data, with indications of a spin transition in nanoparticles arrays if molecules **1'** are present, at temperatures comparable to those found on bulk SCO powders. The persistence of a spin transition in the networks opens the possibility to create a macroscopic device providing insight into the influence of the transition at the molecular level on electrical properties.

6.5 Charge transport experiments

We have performed conductance measurements as a function of temperature on four types of samples, all made of molecular-bound nanoparticles arrays. Three are reference samples, containing 'passive' molecules only (octanethiols, OPE-dithiols and monothiolated 'S-BPP', i.e. the uncoordinated ligand AcS-BPP used in the molecule **1** in Figure 6.1(a)) [16]. For all of these, no transition is expected to occur with temperature. Hence, they provide reference temperature-dependent transport properties, to be compared to the fourth sample type, which incorporates molecule **1'**. Figure 6.5(a) shows the low-bias resistance R versus temperature T for a C8-gold nanoparticle

network (stamped three times, yielding 1-2 monolayers: see caption for details). Interestingly, for this ‘virgin’ molecular device, a monotonically decreasing curve is observed that plateaus at higher T . We note that the alkanemonthiols form a tunnel barrier between neighbouring nanoparticles. Transport through such a barrier is expected to be virtually temperature-independent. Hence, the temperature-dependence observed in Figure 6.5(a) must be related to the properties of the nanoparticles. Indeed, it is a result of Coulomb blockade: due to the small size of the gold nanoparticles, a finite energy is required to add one electron to a nanoparticle. This ‘charging energy’ E_C is connected to a nanoparticle’s capacitance C and the electron charge e via $E_C = e^2/2C$. Upon cooling the sample, the thermal energy $k_B T$ can become lower than E_C . As a result, transport is increasingly blocked (Coulomb blockaded), and the resistance increases dramatically. This effect has been well-studied in networks, by us and others [16, 29, 34, 38, 39].

Figure 6.5(b) shows R versus T for a network sample (three times stamped) into which C8 molecules have been exchanged with OPE-dithiol bridges. Clearly, the presence of the conjugated OPE rods has led to a much lower device resistance. Qualitatively, however, the $R(T)$ behaviour has not changed. Again, a monotonically decreasing curve is seen, with characteristics that are dominated by Coulomb blockade in the nanoparticles [34, 40].

For arrays and networks containing spin crossover molecules **1'**, however, the results can be very different. Figure 6.5(c) shows R versus T for such a sample (three times stamped). In contrast to Figure 6.5(a) and Figure 6.5(b), the $R(T)$ plot in Figure 6.5(c) shows an upturn. This results in a rather shallow minimum, roughly stretching between 260 and 290 K. In addition, Figure 6.5(d) shows a $R(T)$ plot for a sample on which stamping was done only once, resulting in an imperfectly ordered single nanoparticle layer. Although this yields a much higher overall resistance value, the $R(T)$ curve remains qualitatively similar to the one in Figure 6.5(c). Indeed, both Figure 6.5(c) and Figure 6.5(d) exhibit a clear minimum. This behaviour not only differs fundamentally from Figure 6.5(a) and Figure 6.5(b) but also from our third reference systems, i.e. networks containing the monothiolated S-BPP. In the latter, the Fe^{2+} ion, which is key to the spin transition, is not present. For such samples, we find that R decreases monotonically with increasing T without showing a minimum (see Chapter 5, Figure 5.9(a) and Ref. [16] for more details). Hence, the combination of all measurements suggests that the resistance minimum in Figure 6.5(c) and Figure 6.5(d) is intimately

related to the presence of SCO molecules and, specifically, to a temperature-dependent spin transition.

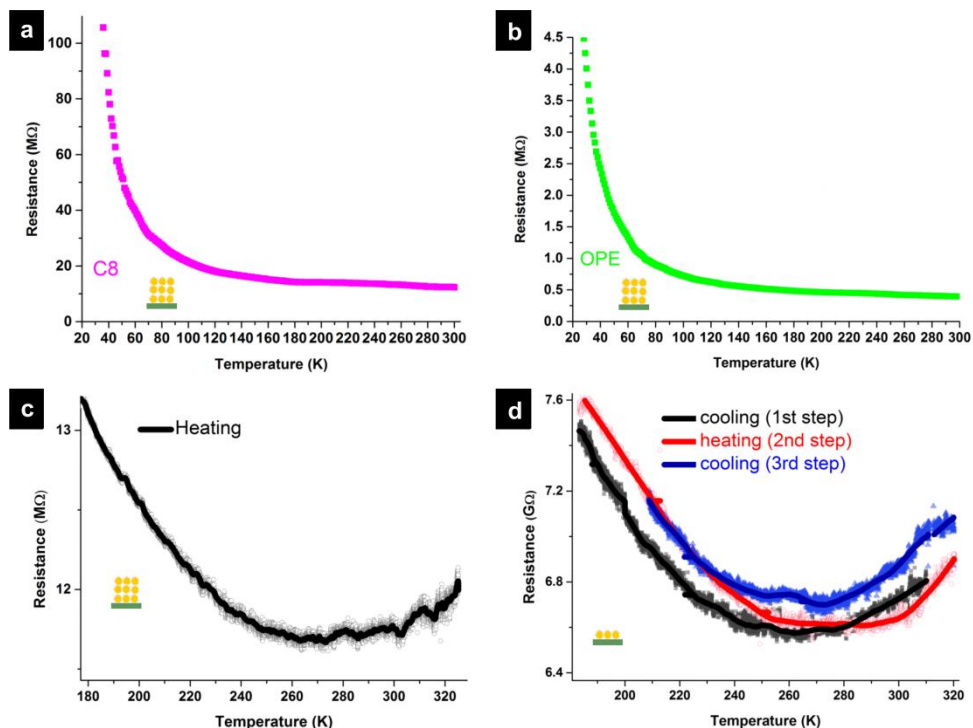


Figure 6.5: (a) Resistance versus temperature (R - T) measurement of a C8-gold nanoparticle network (stamped 3 times). (b) R - T measurement of a OPE-gold nanoparticle array (stamped 3 times). (c) R - T measurement of a molecule **1'**-gold nanoparticle network (stamped 3 times). (d) R - T measurement of a single layer molecule **1'**-gold nanoparticle array. All resistances are determined at low-bias ($V \leq 0.3$ V) on nanotrench devices [33]. In Figure 6.5(c) and Figure 6.5(d), we show both an averaged curve and (a random 10% part of the) raw data (320 data points per Kelvin). We note that while 4 out of 8 samples with spin transition molecules did exhibit a resistance minimum, also 4 did not (see Appendix C.6). We will come back to that below.

However, before accepting this hypothesis, we should consider an alternative explanation. Recently, Wang *et al.* [41] reported a variation in $R(T)$ behaviour for multilayered arrays of octanethiol-covered Au nanoparticles, dependent on thickness.

For samples containing up to four layers of 7 nm-diameter nanoparticles, they find that $R(T)$ plots shows a monotonic decrease. From five layers upwards, however, they observe a resistance minimum, an effect which they explain via a diffusive hopping model. For 13 nm particles, the latter border shifts to three layers. For this reason, it is important to emphasize that our reference samples (not only octanethiol like Wang, but also OPE and bare S-BPP arrays) do not yield a resistance minimum. This is fully consistent with the data set of Wang *et al.*, as our particles are 8.5 ± 1.5 nm in diameter, i.e. close to 7 nm [16]. In contrast, we do observe a resistance minimum for samples that contain spin transition molecules. This is the case not only for triple-stamped samples, but, importantly, also for arrays that were stamped only once (see Figure 6.5(d)).

Hence, our full set of transport experiments, in combination with our Raman and magnetometry data, indicates that a spin transition in the SCO molecules is key to the anomalous $R(T)$ plots observed. If we also assume that the HS state has a higher low-bias resistance than its LS counterpart, as we will discuss below, we have the ingredients to explain the upturn. Upon heating around the transition temperature, more and more molecules will make the transition, and the resistance will increase. Still, Coulomb blockade will play its role too, as the charging energy E_C of the gold nanoparticles in Figure 6.5(c) and Figure 6.5(d) should be similar to the values for Figure 6.5(a) and Figure 6.5(b) (the nanoparticles and samples are made according to the very same procedure). Hence, for the lower temperatures, an increase of R upon cooling is also expected. A combination of Coulomb blockade and a spin transition could thus qualitatively explain the minimum observed in Figure 6.5(c) and Figure 6.5(d).

In the following, we combine DFT calculations of the electrical properties of these molecular junctions with a simple macroscopic percolative network model to provide a better insight into the $R(T)$ findings.

6.6 Theoretical charge transport calculations

Up to now, theory is diverse on predicting how the conductance of SCO molecules would change during spin transition. Baadji *et al.* [42] found a resistance decrease when going from the LS to the HS state (i.e. $R_H < R_L$) for a SCO molecule of their choice. Meded *et al.* [15], on the other hand, predict that the resistance is lowest in the LS state (i.e. $R_H > R_L$), based on experimental findings on molecules more similar to

the ones studied here. One reason for this discrepancy is that two competing effects can play a role upon a LS to HS transition. On the one hand, the energy gap between the frontier orbitals (HOMO-LUMO gap) decreases. This is expected to increase conductance, as the distance from Fermi level to the nearest level will generally decrease as well. On the other hand, the electronic coupling between the ligands at both sides of the Fe^{2+} ion decreases when going from the LS to HS state. In first approximation, the related decrease in wave function overlap should reduce conductance. Hence, it is not *a priori* obvious if one should expect a conductance increase or decrease upon spin transition for a particular type of molecules.

For this reason, we specifically focus on calculating charge transport through molecule **1'** connected to Au leads. We perform simulations of the transmission function by utilizing our in-house developed Non-equilibrium Green's Functions (NEGF) formalism [43, 44] based on Density Function Theory (DFT) input coming from the quantum chemistry package Turbomole [45-47]. The formalism was successfully utilized earlier on a similar class of molecules [48], using BP [49, 50], a standard Generalized Gradient Approximation (GGA) exchange-correlation (XC) functional. Here, however, we use B3LYP [51, 52] as an XC functional to obtain the transmission functions for both the HS and LS state of the molecule **1'** as presented in Figure 6.6.

Upon an, admittedly, rough comparison between experimentally obtained first optical excitations and HOMO-LUMO gaps produced with a few different XC functionals, one directly observes that BP's 0.3 eV is too small (by a factor of 4) when compared to the experimental lowest optical excitation of 1.3 eV [53]. B3LYP on the other hand produces 3.2 eV, a value too high by a factor of 2. $[\text{Fe}(\text{TPY})_2]^{2+}$ (with TPY = 2,2':6',2''-terpyridine) showed very similar trends compared to molecule **1'** (only slightly smaller) on the calculations side. It is worth noting that agreement across different XC functionals is much better for the LS state where the discrepancies never exceed 50% when compared to the lowest optical excitation of LS of $[\text{Fe}(\text{TPY})_2]^{2+}$ found in experiment [54], for details see Table VI in Ref. [15]. We note that the $[\text{Fe}(\text{TPY})_2]^{2+}$ complex is not known to switch in experiment [55].

Indeed, we find that the HOMO-LUMO gap in the HS state tends to be smaller than in the LS state for the corresponding XC functional. Consequently, the HS frontier orbitals tend to be closer to resonance with the Fermi level E_F of the junction. From

this, one might expect that the HS conductance exceeds the LS conductance, as anticipated above [54]. Figure 6.6 shows the calculated transmission function versus energy, $T(E)$, for both LS and HS states. The single molecular conductance G at low-bias is related to $T(E)$ by $G = 2e^2/h T(E_F)$, where h denotes Planck's constant. Remarkably, although the transport gap in Figure 6.6 is indeed smaller for the HS state, the conductance (transmission) of the LS state is clearly the higher of the two.

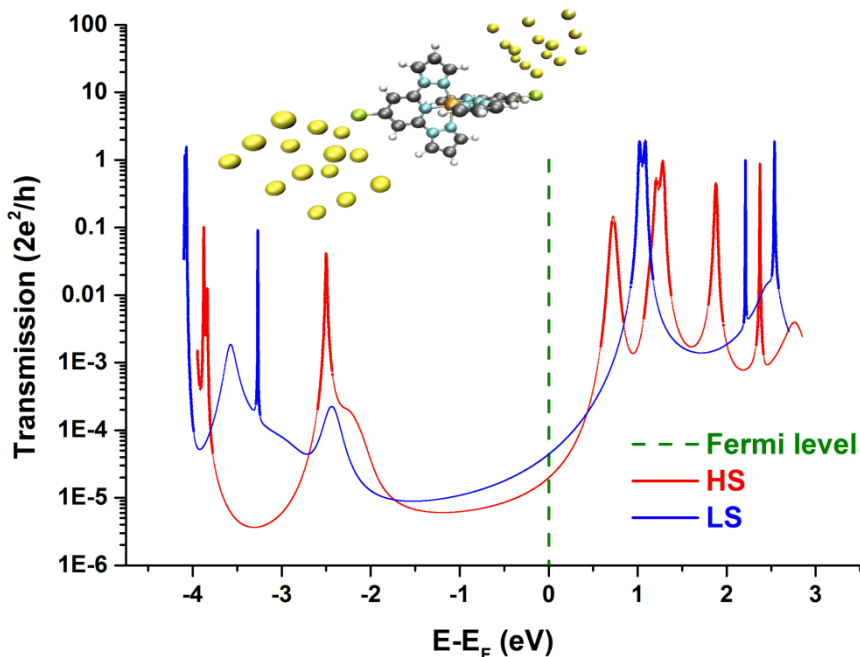


Figure 6.6: Calculated electron transmission probability as a function of energy, $T(E)$, for molecule **1'** in LS (blue curve) and HS (red curve) states. The inset shows the configuration considered (gold atoms are displayed in yellow). The conductance of the LS state is found higher than that of the HS state despite diminishing of the HOMO-LUMO gap upon LS to HS transition. Details of the calculation are described in the paragraph 6.6. (The calculations above have been done by Dr. V. Meded in collaboration with Professor Dr. F. Evers and Professor Dr. M. Ruben).

To understand this, we need to consider inter-ligand coupling as well. From Figure 6.6 we deduce that we dominantly have LUMO transport. Interestingly, the LUMO for these types of molecules is always ligand-based and additionally a ligand wave function has a better opportunity to couple to the gold leads. While spin transition does reshuffle the Fe-states, it does not influence the ligand states as much. Still, it results in

a distance increase between the left and right ligand. The latter makes inter-ligand coupling considerably weaker. In Figure 6.6, we see indeed that the HS LUMO peak (red) is much narrower than the corresponding LS peak (blue). Additionally, the HS Lorentzian peaks well below unity, indicating very asymmetric coupling for the HS state case.

Summarizing, our calculations imply a conductance decrease when going from a LS to a HS state, explained by a reduction in coupling dominating over a decrease in the HOMO-LUMO gap. Keeping in mind differences in HOMO-LUMO gaps that different XC functionals are producing, however, a definite and general answer as to which of the two spin states is better conducting from a theory point of view is still difficult to give. This in itself emphasizes the need for more experimental data.

6.7 Discussion

To relate all of the experimental evidence (Raman and magnetometry results on spin transition) as well as the transport calculations to the $R(T)$ plots in Figure 6.5(c) and Figure 6.5(d), we introduce a pragmatic model. In essence, it describes the influence of a spin transition on the device resistance R via a bond percolation model, assuming $R_H > R_L$ as in the NEGF results (Figure 6.6). Although the model captures the basic physics of our system, we note that it can at most be seen as semi-quantitative.

First, we estimate what percentage of molecules are in the LS and HS states for each temperature T . We choose to do this via a standard approach that captures the essence and allows us to vary parameters. Specifically, we take over the parameters $\Delta H = 14.3$ kJ/mol and $\Delta S = 55.4$ J/mol K, from Šalitroš *et al.* [56] who studied similar spin transition molecules in bulk. In contrast to bulk, however, we assume there is no cooperativity between the SCO molecules in the array. The normalized number of HS molecules x_H is then given by: [7]

$$x_H(T) = \frac{1}{1 + \exp\left[\frac{\Delta H}{R_B} \left(\frac{1}{T} - \frac{1}{T_{1/2}}\right)\right]}, \quad (6.1)$$

Where $R_B \equiv N_A \cdot k_B$ is the gas constant (N_A is Avogadro's number). Note that for any finite $T_{1/2}$, $x_H(T)$ does not fully reach unity for $T \rightarrow \infty$ in equation 6.1, although for our parameters it does get to 0.998.

Next, we use a percolation model to calculate the total resistance of a 2D array, taking Coulomb blockade into account as well. For this, we first make the pragmatic assumption that the resistance of a single molecule-nanoparticle junction within an array is given by $R_{H(L)} = R_{H(L)}^\infty e^{\frac{E_C}{k_B T}}$, where R_H^∞ and R_L^∞ denote the single molecule resistance for the high-spin (H) and low-spin (L) states, respectively, if there were no Coulomb blockade. We use the following normalized values: $R_H^\infty = 1 = 2 \cdot R_L^\infty$, inspired by our calculations in Figure 6.6. Furthermore, we assume that the charging energy of the nanoparticles E_C does not depend on the spin state of the molecule. (We use $E_C/k_B = 200$ K, in correspondence with typical values for octanethiol and OPE networks) [34].

To take percolation into account, we need to properly relate the device resistance R to x_H . Bond percolation displays the relation between the conductivity of the molecules (i.e. the bonds) that bridge the gold nanoparticles in an array and the path to be taken through the bonded array from the source electrode to the drain electrode. In equation 6.2, x_H represents the bridging ratio of high-spin molecules (bridging between the gold nanoparticles junction) divided by the total amount of molecular bridges. If the molecules are randomly placed in between the gold nanoparticles you can predict the probability that a pathway exists in the array related to the bridging ratio. The ratio at which the first pathway is possible (statistically) is called the percolation threshold. For a hexagonal 2D array the percolation threshold is around 35% of all possible molecular bridged junctions.

For this, we make use of a model by McLachlan, which has successfully been applied to molecule-nanoparticle arrays in literature [40]. This type of bond percolation model allows us to describe the influence of the spin crossover molecules on the resistance of the 1st-gold nanoparticle array. It yields the following implicit equation (see equation 6.2) for the array conductance $G(x_H) = 1/R(x_H)$:

$$\frac{(1-x_H)(G_L^{3/4} - G^{3/4})}{G_L^{3/4} + A_c G^{3/4}} + \frac{x_H(G_H^{3/4} - G^{3/4})}{G_H^{3/4} + A_c G^{3/4}} = 0, \quad (6.2)$$

We set $G_H = \frac{1}{R_H}$ and $G_L = \frac{1}{R_L}$ and $A_c = (1-p_c)/p_c$ where p_c denotes the percolation threshold, coming from the low conductance side. For a hexagonal network, we have p_c

$= 2 \cdot \sin(\pi/18) = 0.347$, so that $A_c = 1.88$ [57-61]. With these ingredients, we are ready to calculate $R(T) = R(x_H(T); T) = R(x_H(T)) e^{\frac{E_C}{k_B T}}$.

Figure 6.7(a) shows the result (see black curve). For a system exhibiting a nearly full (99.8%) spin transition, we find that the array's $R(T)$ plot decreases to a minimum, goes up again and slowly goes down to flatten off. The minimum has a depth of up to a few ten % and is found around 220 K.

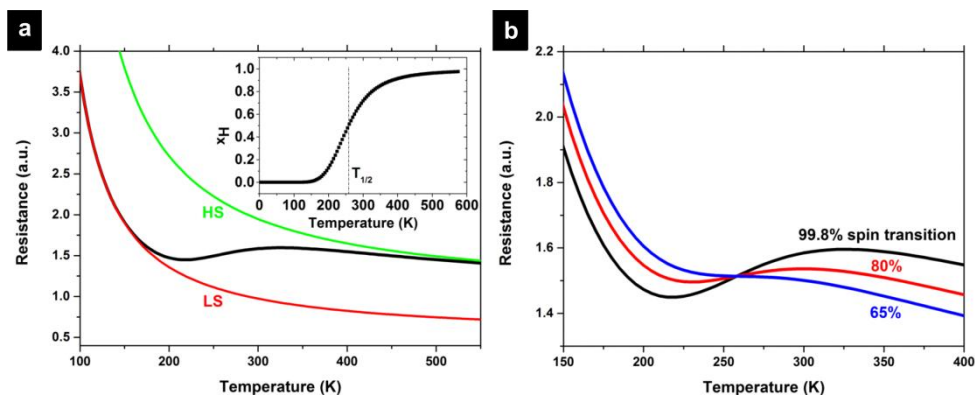


Figure 6.7: (a) General shape of R - T plot (black) calculated by a percolation network model (see paragraph 6.7). It assumes a spin transition without cooperative effects. A minimum is found for a nearly full spin transition, consistent with Figure 6.5(c) and Figure 6.5(d). The minimum can be rationalized as a transition between two $R(T)$ curves: one for the case that there were LS molecules only (red curve) and one for the case of only HS molecules (green curve). The HS molecules are assumed to have twice the resistance of the LS, consistent with DFT calculations (Figure 6.6). Inset: normalized number of molecules in the high-spin state, x_H versus T as used in the percolation model (see paragraph 6.7, parameters: $\Delta H/\Delta S = T_{1/2} = 258$ K and $\Delta H = 14.3$ kJ/mol [56], resulting in a 99.8% transition). (b) Calculated $R(T)$ curves if spin crossover is incomplete: 65% (blue curve) or 80% (red curve). The black curve is the same as for (a). The resistance minimum remains for the 80% transition, but disappears near the percolation threshold.

This is qualitatively in agreement with our $R(T)$ data in Figure 6.5(c) and Figure 6.5(d). It is instructive to compare this curve to the plot expected if there were no spin transition at all, i.e. if there were HS molecules only (described by $R_H = R_H^\infty e^{\frac{E_C}{k_B T}}$, see

green curve in Figure 6.7(a)), or LS molecules only (given by $R_L = R_L^\infty e^{\frac{E_C}{k_B T}}$, see red curve in Figure 6.7(a)), respectively. Clearly, at low temperatures the model's black curve follows the LS line, whereas it moves to the HS curve as the spin transition takes place. Since $R_H^\infty > R_L^\infty$, a minimum quite naturally appears.

The red and blue curves show R versus T for 80% and 65% spin transition, respectively, following the estimates from our Raman data. Comparing the curves, we see that a minimum is still there for the 80%-transition. For the 65%-case, which is near the percolation threshold (coming from the LS state side), the minimum has just disappeared, however. This is consistent with the fact that 4 out of 8 samples did not exhibit a resistance minimum. It shows how sensitive the presence of a resistance minimum is to the extent of the transition, i.e. details of sample preparation will clearly be crucial to observe a resistance minimum.

For instance, if molecular exchange is incomplete and/or if less than 65% of the molecular junctions are able to switch, a minimum is not anticipated.

All in all, the $R(T)$ data in Figure 6.5(c) and Figure 6.5(d) are qualitatively consistent with the Raman data, magnetometry measurements and transport calculations, assuming that the transition involves more than about 2/3 of the molecules.

6.8 Conclusions

In summary, we have experimentally studied the properties of gold nanoparticle arrays incorporating spin crossover molecules. Raman spectroscopy provides evidence for a (majority) spin transition in these arrays, as qualitatively confirmed by magnetization measurements. The Raman data indicate that molecular binding to gold occurs via benzenethiol termini. Still, it does not appear that the proximity and binding to the metal quenches the spin transition. Resistance versus temperature curves for arrays containing SCO molecules exhibit a pronounced minimum that we do not find in networks containing non-switching, passive molecules only. This resistance minimum can be explained via a percolation model that assumes a spin transition with the HS state being more resistive than the LS state. The latter is in agreement with charge transport calculations presented following the NEGF method.

Even though the electrical signature of a spin transition is not spectacular in our case, the proposed model provides a guideline to pinpoint the occurrence of a spin transition

with temperature in an electrical device. Our work thus demonstrates that proof-of-principle molecular devices based on the spin crossover phenomenon can be designed.

6.9 References

1. A. Aviram and M. A. Ratner, Molecular Rectifiers, *Chem. Phys. Lett.*, **29**, (1974), 277-283.
2. R. M. Metzger, Unimolecular Electrical Rectifiers, *Chem. Rev.*, **103**, (2003), 3803-3834.
3. B. L. Feringa, *Molecular Switches*, Eds.; Wiley-VCH.: Weinheim, June **2001**.
4. P. Gütllich and H. A. Goodwin, Spin Crossover in Transition Metal Compounds I, *Top. Curr. Chem.*, **233**, (2004).
5. M. Ruben, J. Rojo, F. J. Romero-Salguero, L. H. Uppadine and J.-M. Lehn, Grid-type Metal Ion Architectures: Functional Metallosupramolecular Arrays, *Angew. Chem. Int. Ed.*, **43**, (2004), 3644-3662.
6. S. J. van der Molen, P. Liljeroth, Charge Transport through Molecular Switches, *J. Phys.: Condens. Matter.*, **22**, (2010), 133001 (1-30).
7. O. Kahn, *Molecular Magnetism*, Eds.; Wiley-VCH.: New York, August **1993**.
8. P. Gütllich, Y. Garcia and H. A. Goodwin, Spin Crossover Phenomena in Fe(II) Complexes, *Chem. Soc. Rev.*, **29**, (2000), 419-427.
9. P. Gütllich and A. Hauser, Thermal and Light-induced Spin Crossover in Iron(II) Complexes, *Coord. Chem. Rev.*, **97**, (1990), 1-22.
10. A. Hauser, Reversibility of Light-induced Excited Spin State Trapping in the Fe(Ptz)₆(BF₄)₂ and the Zn_{1-x}Fe_x(Ptz)₆(BF₄)₂ Spin-crossover Systems, *Chem. Phys. Lett.*, **124**, (1986), 543-548.
11. M. Marchivie, P. Guionneau, J. A. K. Howard, G. Chastanet, J-F. Létard, A. E. Goeta and D. Chasseau, Structural Characterization of a Photoinduced Molecular Switch, *J. Am. Chem. Soc.*, **124**, (2002), 194-195.
12. K. Kato, M. Takata, Y. Moritomo, A. Nakamoto and N. Kojima, On-off Optical Switching of the Magnetic and Structural Properties in a Spin-crossover Complex. *Appl. Phys. Lett.*, **90**, (2007), 201902 (1-3).
13. A. Bousseksou, G. Molnár, J.-P. Tuchagues, N. Menéndez, É. Codjovi and F. Varret, Triggering the Spin-crossover of Fe(Phen)₂(NCS)₂ by a Pressure Pulse: Pressure and Magnetic Field Induced 'Mirror Effects', *C. R. Chimie.*, **6**, (2003), 329-335.
14. N. Baadji, M. Piacenza, T. Tugsuz, F. Della Sala, G. Maruccio and S. Sanvito, Electrostatic Spin Crossover Effect in Polar Magnetic Molecules, *Nature Mater.*, **8**, (2009), 813-817.
15. V. Meded, A. Bagrets, K. Fink, R. Chandrasekar, M. Ruben, F. Evers, A. Bernard-Mantel, J. S. Seldenthuis, A. Beukman and H. S. J. van der Zant, Electrical Control over the Fe(II) Spin Crossover in a Single Molecule: Theory and Experiment, *Phys. Rev. B*, **83**, (2011), 245415 (1-13).

-
16. E. J. Devid, P. N. Martinho, M. V. Kamalakar, Ú. Prendergast, C. Kübel, T. Lemma, J.-F. Dayen, T. E. Keyes, B. Doudin, M. Ruben and S. J. van der Molen, The Influence of Molecular Mobility on the Properties of Networks of Gold Nanoparticles and Organic Ligands, *Beilstein J. Nanotechnol.*, **5**, (2014), 1664-1674.
 17. M. Cavallini, I. Bergenti, S. Milita, J. C. Kengne, D. Gentili, G. Ruani, I. Šalitroš, V. Meded and M. Ruben, Thin Deposits and Patterning of Room-Temperature-Switchable One-dimensional Spin-crossover Compounds, *Langmuir*, **27**, (2011), 4076-4081.
 18. Z. Arcis-Castillo, S. Zheng, M. A. Siegler, O. Roubeau, S. Bedoui and S. Bonnet, Tuning the Transition Temperature and Cooperativity of Bapbpy-based Mononuclear Spin-crossover Compounds: Interplay between Molecular- and Crystal Engineering, *Chem. Eur. J.*, **17**, (2011), 14826-14836.
 19. R. Chandrasekar, F. Schramm, O. Fuhr and M. Ruben, An Iron(II) Spin-transition Compound with Thiol Anchoring Groups, *Eur. J. Inorg. Chem.*, **17**, (2008), 2649-2653.
 20. I. Šalitroš, O. Fuhr, A. Eichhöfer, R. Kruk, J. Pavlik, L. Dlháň, R. Boča and M. Ruben, The Interplay of Iron(II) Spin Transition and Polymorphism, *Dalton Trans.*, **41**, (2012), 5163-5171.
 21. T. G. Gopakumar, F. Matino, H. Naggert, A. Bannwarth, F. Tuczek and R. Berndt, Electron-induced Spin Crossover of Single Molecules in a Bilayer on Gold, *Angew. Chem., Int. Ed.*, **51**, (2012), 6262-6266.
 22. T. Miyamachi, M. Gruber, V. Davesne, M. Bowen, S. Boukari, L. Joly, F. Scheurer, G. Rogez, T. K. Yamada, P. Ohresser, E. Beaurepaire and W. Wulfhekel, Robust Spin Crossover and Memristance Across a Single Molecule, *Nat. Commun.*, **3**, (2012), 1-6.
 23. A. Pronschinske, R. C. Bruce, G. Lewis, Y. Chen, A. Calzolari, M. Buongiorno-Nardelli, D. A. Shultz, W. You and D. B. Dougherty, Iron(II) Spin Crossover Films on Au(111): Scanning Probe Microscopy and Photoelectron Spectroscopy, *Chem. Commun.*, **49**, (2013), 10446-10452.
 24. M. Bernien, D. Wiedemann, C. F. Hermanns, A. Krüger, D. Rolf, W. Kroener, P. Müller, A. Grohmann and W. Kuch, Spin Crossover in a Vacuum-deposited Submonolayer of a Molecular Iron(II) Complex, *J. Phys. Chem. Lett.*, **3**, (2012), 3431-3434.
 25. X. Zhang, T. Palamarciuc, J.-F. Létard, P. Rosa, E. V. Lozada, F. Torres, L. G. Rosa, B. Doudin and P. A. Dowben, The Spin State of a Molecular Adsorbate Driven by the Ferroelectric Substrate Polarization, *Chem. Commun.*, **50**, (2014), 2255-2257.
 26. I. Suleimanov, J. S. Costa, G. Molnár, L. Salmon and A. Bousseksou, The Photo-thermal Plasmonic Effect in Spin Crossover@Silica-Gold Nanocomposites, *Chem. Commun.*, **50**, (2014), 13015-13018.
 27. B. Warner, J. C. Oberg, T. G. Gill, F. El Hallak, C. F. Hirjibehedin, M. Serri, S. Heutz, M.-A. Arrio, P. Sainctavit, M. Mannini, G. Poneti, R. Sessoli and P. Rosa, Temperature- and Light-induced Spin Crossover Observed by X-ray Spectroscopy on Isolated Fe(II) Complexes on Gold, *J. Phys. Chem. Lett.*, **4**, (2013), 1546-1552.
 28. R. P. Andres, J. D. Bielefeld, J. I. Henderson, D. B. Janes, V. R. Kolagunta, C. P. Kubiak, W. J. Mahoney and R. G. Osifchin, Self-assembly of a Two-dimensional

- Superlattice of Molecularly Linked Metal Clusters, *Science*, **273**, (1996), 1690-1693.
29. T. B. Tran, I. S. Beloborodov, X. M. Lin, T. P. Bigioni, V. M. Vinokur and H. M. Jaeger, Multiple Cotunneling in Large Quantum Dot Arrays, *Phys. Rev. Lett.*, **95**, (2005), 076806 (1-4).
 30. J. Liao, L. Bernard, M. Langer, C. Schönenberger and M. Calame, Reversible Formation of Molecular Junctions in 2D Nanoparticle Arrays, *Adv. Mat.*, **18**, (2006), 2444-2447.
 31. L. Bernard, Y. Kamdzhilov, M. Calame, S. J. van der Molen, J. Liao and C. Schönenberger, Spectroscopy of Molecular Junction Networks Obtained by Place Exchange in 2D Nanoparticle Arrays, *J. Phys. Chem. C.*, **111**, (2007), 18445-18450.
 32. J. W. Slot and H. J. Geuze, A New Method of Preparing Gold Probes for Multiple Labeling Cytochemistry, *Eur. J. Cell Biol.*, **38**, (1985), 87-93.
 33. J.-F. Dayen, V. Faramarzi, M. Pauly, N. T. Kemp, M. Barbero, B. P. Pichon, H. Majjad, S. Begin-Colin and B. Doudin, Nanotrench for Nano and Microparticle Electrical Interconnects, *Nanotechnology*, **21**, (2010), 335303 (1-7).
 34. J.-F. Dayen, E. Devid, M. V. Kamalakar, D. Golubev, C. M. Guédon, V. Faramarzi, B. Doudin and S. J. van der Molen, Enhancing the Molecular Signature in Molecule-nanoparticle Networks via Inelastic Cotunneling, *Adv. Mat.*, **25**, (2013), 400-404.
 35. K. B. Biggs, J. P. Camden, J. N. Anker and R. P. van Duyne, Surface-enhanced Raman Spectroscopy of Benzenethiol Adsorbed from the Gas Phase onto Silver Film over Nanosphere Surfaces: Determination of the Sticking Probability and Detection Limit Time, *J. Phys. Chem. A*, **113**, (2009), 4581-4586.
 36. J. Larionova, L. Salmon, Y. Guari, A. Tokarev, K. Molvinger, G. Molnár and A. Bousseksou, Towards the Ultimate Size Limit of the Memory Effect in Spin-crossover Solids, *Angew. Chem. Int. Ed.*, **47**, (2008), 8236-8240.
 37. E. Coronado, J. R. Galán-Mascarós, M. Monrabal-Capilla, J. García-Martínez and P. Pardo-Ibáñez, Bistable Spin-crossover Nanoparticles Showing Magnetic Thermal Hysteresis near Room Temperature, *Adv. Mat.*, **19**, (2007), 1359-1361.
 38. T. B. Tran, I. S. Beloborodov, J. Hu, X. M. Lin, T. F. Rosenbaum and H. M. Jaeger, Sequential Tunneling and Inelastic Cotunneling in Nanoparticle Arrays, *Phys. Rev. B*, **78**, (2008), 075437(1-9).
 39. M. Pauly, J.-F. Dayen, D. Golubev, J.-B. Beaufrand, B. P. Pichon, B. Doudin and S. Bégin-Colin, Co-tunneling Enhancement of the Electrical Response of Nanoparticle Networks, *Small*, **8**, (2012), 108-115.
 40. J. Liao, S. Blok, S. J. van der Molen, S. Diefenbach, A. W. Holleitner, C. Schönenberger, A. Vladyka and M. Calame, Ordered Nanoparticle Arrays Interconnected by Molecular Linkers: Electronic and Optoelectronic Properties, *Chem. Soc. Rev.*, **44**, (2014), 999-1014.
 41. Y. Wang, C. Guan, J. Sun, L. Peng and J. Liao, Transition of Temperature Coefficient of Conductance in Weakly Coupled Gold Nanoparticle Arrays, *Appl. Phys. Lett.*, **105**, (2014), 233116 (1-5).

-
42. N. Baadji and S. Sanvito, Giant Resistance Change Across the Phase Transition in Spin-crossover Molecules, *Phys. Rev. Lett.*, **108**, (2012), 217201(1-5).
 43. F. Evers, F. Weigend and M. Köntopp, Conductance of Molecular Wires and Transport Calculations Based on Density-functional Theory, *Phys. Rev. B*, **69**, (2004), 235411(1-9).
 44. A. Arnold, F. Weigend and F. Evers, Quantum Chemistry Calculations for Molecules Coupled to Reservoirs: Formalism, Implementation, and Application to Benzenedithiol, *J. Chem. Phys.*, **126**, (2007), 174101(1-14).
 45. R. Ahlrichs, M. Bär, M. Häser, H. Horn and C. Kölmel, Electronic Structure Calculations on Workstation Computers: The Program System Turbomole, *Chem. Phys. Lett.*, **162**, (1989), 165-169.
 46. A. Schäfer, H. Horn and R. Ahlrichs, Fully Optimized Contracted Gaussian Basis Sets for Atoms Li to Kr, *J. Chem. Phys.*, **97**, (1992), 2571-2577.
 47. A. Schäfer, C. Huber and R. Ahlrichs, Fully Optimized Contracted Gaussian Basis Sets of Triple Zeta Valence Quality for Atoms Li to Kr, *J. Chem. Phys.*, **100**, (1994), 5829-5835.
 48. M. Ruben, A. Landa, E. Lörtscher, H. Riel, M. Mayor, H. Görls, H. B. Weber, A. Arnold, and F. Evers, Charge Transport Through a Cardan-joint Molecule, *Small*, **4**, (2008), 2229-2235.
 49. J. P. Perdew, Density-functional Approximation For the Correlation Energy of the Inhomogeneous Electron Gas, *Phys. Rev. B*, **33**, (1986), 8822-8824.
 50. A. D. Becke, Density-functional Exchange-energy Approximation with Correct Asymptotic Behavior, *Phys. Rev. A*, **38**, (1988), 3098-3100.
 51. C. Lee, W. Yang and R. G. Parr, Development of the Colle-Salvetti Correlation-energy Formula into a Functional of the Electron Density, *Phys. Rev. B*, **37**, (1988), 785-789.
 52. A. D. Becke, Density-functional Thermochemistry. III. The Role of Exact Exchange, *J. Chem. Phys.*, **98**, (1993), 5648-5652.
 53. J. M. Holland, J. A. McAllister, C. A. Kilner, M. Thornton-Pett, A. J. Bridgeman and M. A. Halcrow, Stereochemical Effects on the Spin-state Transition Shown by Salts of $[\text{FeL}_2]^{2+}$ [L = 2,6-di(Pyrazol-1-yl)Pyridine], *J. Chem. Soc. Dalton Trans.*, (2002), 548-554.
 54. P. S. Braterman, J.-I. Song and R. D. Peacock, Electronic Absorption Spectra of The Iron(II) Complexes of 2,2'-bipyridine, 2,2'-bipyrimidine, 1,10-phenanthroline, and 2,2':6',2''-terpyridine and Their Reduction Products, *Inorg. Chem.*, **31**, (1992), 555-559.
 55. M. Gerloch and E. C. Constable, Eds., *Transition Metal Chemistry: The Valence Shell in d-Block Chemistry; VCH.: Weinheim, June 1994*.
 56. I. Šalitrš, J. Pavlik, R. Boča, O. Fuhr, C. Rajadurai and M. Ruben, Supramolecular Lattice-solvent Control of Iron(II) Spin Transition Parameters, *CrystEngComm.*, **12**, (2010), 2361-2368.
 57. S. Kirkpatrick, Percolation and Conduction, *Rev. Mod. Phys.*, **45**, (1973), 574-588.
 58. D. S. McLachlan, M. Blaszkiewicz and R. E. Newnham, Electrical Resistivity of Composites, *J. Am. Ceram. Soc.*, **73**, (1990), 2187-2203.
 59. J. Wu and D. S. McLachlan, Percolation Exponents and Thresholds Obtained From The Nearly Ideal Continuum Percolation System Graphite-boron Nitride, *Phys. Rev. B*, **56**, (1997), 1236-1248.

60. N. I. Lebovka, S. Tarafdar and N. V. Vygornitskii, Computer Simulation of Electrical Conductivity of Colloidal Dispersions during Aggregation, *Phys. Rev. E.*, **73**, (2006), 031402 (1-6).
61. J. C. Wierman, Bond Percolation on Honeycomb and Triangular Lattices, *Adv. Appl. Probab.*, **13**, (1981), 298-313.

Appendix A.1

Additional information about cotunneling regimes

To demonstrate that equation 4.2 provides a unified description of various transport regimes observed in experiments, equation 4.2 will be elaborated for several limiting cases.

Since the dependence of the cotunneling probability on the number of junctions j is exponentially strong, one can leave only the dominating term in the sum with a good accuracy (see equation 4.2). At relatively small bias voltage, $eV_{jct} < k_B T \ln(e^2 R_T/h)$, the optimal number of junctions j_{opt} , which gives the maximum contribution to the current, is smaller than $N_{max} \approx \sqrt{E_C/eV_{jct}}$. In order to find the optimal number in this case j is treated as a continuous parameter and we solve the saddle-point equation

$$\frac{\partial}{\partial j} \left[-\frac{E_C}{jk_B T} - j \ln \frac{e^2 R_T}{h} + (j-1) \ln \frac{k_B^2 T^2 + e^2 V_{jct}^2}{E_C^2} \right] = 0.$$

The solution of this equation reads

$$j_{opt} = \sqrt{\frac{E_C}{k_B T \ln \left[\frac{e^2 R_T E_C^2}{h(e^2 V_{jct}^2 + k_B^2 T^2)} \right] - eV_{jct}}}. \quad (S4.1)$$

Thus the current may be approximated as follows

$$\begin{aligned} I &\propto V_{jct} \left(\frac{h}{e^2 R_T} \right)^{j_{opt}} \left(\frac{k_B^2 T^2 + e^2 V_{jct}^2}{E_C^2} \right)^{j_{opt}-1} \exp \left[-\frac{E_C}{j_{opt} k_B T} + j_{opt} \frac{eV_{jct}}{k_B T} \right] \\ &= \frac{E_C^2 V_{jct}}{e^2 V_{jct}^2 + k_B^2 T^2} \exp \left(-2 \sqrt{\frac{E_C}{k_B T} \left(\ln \left[\frac{e^2 R_T E_C^2}{h(e^2 V_{jct}^2 + k_B^2 T^2)} \right] \right) - \frac{eV_{jct}}{k_B T}} \right). \end{aligned} \quad (S4.2)$$

In the linear response regime $eV_{jct} < k_B T$ the current (S4.2) reduces to the form

$$I = G V_{jct}, \quad (S4.3)$$

where the zero-bias conductance follows an Efros-Shklovskii relation (in temperature):

$$G \propto \left(\frac{h}{e^2 R_T} \right)^{N_{cot}} \left(\frac{k_B T}{E_C} \right)^{2N_{cot}-2} \exp \left[-\frac{E_C}{N_{cot} k_B T} \right] = \frac{E_C^2}{k_B^2 T^2} \exp \left[-\sqrt{\frac{T^*}{T}} \right], \quad (S4.4)$$

Here the characteristic temperature $k_B T^* = 4E_C \ln(e^2 R_T E_C^2 / h k_B^2 T^2)$ is introduced, and we have defined the optimal cotunneling distance at zero bias $N_{cot} = \sqrt{\frac{E_C}{k_B T \ln(e^2 R_T E_C^2 / h k_B^2 T^2)}}$, which follows from equation S4.1 at $V_{jct} = 0$, i.e. $N_{cot} = j_{opt} |_{V_{jct}=0}$. Since in practice the ratio $E_C / k_B T$ is not extremely large, one can ignore its logarithmic contribution in the denominator and approximate N_{cot} as follows

$$N_{cot} \approx \sqrt{\frac{E_C}{k_B T \ln(e^2 R_T / h)}}. \quad (\text{S4.5})$$

The results (equations S4.3 and S4.4) apply to the region of parameters C1 defined in the main text of the article.

At higher bias voltages, $k_B T < eV_{jct} < k_B T \ln\left(\frac{e^2 R_T}{h}\right)$, the current (see equation S4.2) may be roughly approximated by a power law dependence. In order to reveal that, the combination eV_{jct} under the square root in the exponent of equation S4.2 is neglected and further is made use of the relation $\ln(1 + e^2 V_{jct}^2 / k_B^2 T^2) \ll \ln(e^2 R_T E_C^2 / h k_B^2 T^2)$, which holds in this regime.

Afterwards, the exponent in powers of $\ln(1 + e^2 V_{jct}^2 / k_B^2 T^2)$ is expanded and the following result arrives:

$$I \propto \frac{G (eV_{jct})^{2N_{cot}-1}}{e (k_B T)^{2N_{cot}-2}}. \quad (\text{S4.6})$$

Equation S4.6 describes the regime C2 introduced in the article.

At even higher bias voltages, when $eV_{jct} > k_B T \ln\left(\frac{e^2 R_T}{h}\right)$, the optimal cotunneling distance in equation S4.1 formally exceeds the maximum allowed distance N_{max} . This means that the maximum contribution to the current (S4.7) comes from the term with $j = N_{max}$. Thus, in this regime is obtained:

$$I \propto V_{jct} \left(\frac{h}{e^2 R_T}\right)^{N_{max}} \left(\frac{k_B^2 T^2 + e^2 V_{jct}^2}{E_C^2}\right)^{N_{max}-1} \approx \frac{E_C}{e} \exp\left(-\sqrt{\frac{V^*}{V_{jct}}}\right) \quad (\text{S4.7})$$

where $V^* = \frac{E_C}{e} \left(\ln \frac{e^2 R_T E_C}{h e V_{jct}}\right)^2 \approx \frac{E_C}{e} \left(\ln \frac{e^2 R_T}{h}\right)^2$ is the characteristic voltage.

Equation S4.7 corresponds to the regime C3. Interestingly, in regime C3, Efros-Shklovskii-type behaviour (in voltage) is expected.

Appendix A.2

Low-bias conductance versus temperature

Figure A-1 shows low-bias conductance versus temperature, i.e. $G(T)$, data for a quasi 2D octanethiol-gold network, plotted using different representations.

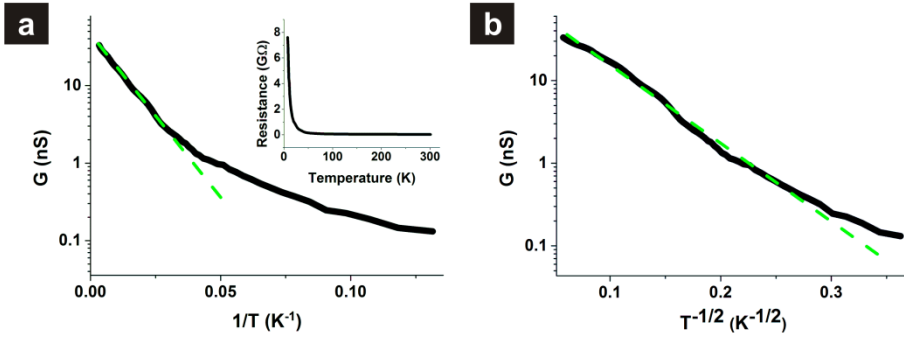


Figure A-1: (a) Arrhenius plot of conductance G versus reciprocal temperature (T^{-1}) for an octanethiol-gold nanoparticle network (see equation 4.1). The green dotted curve is a linear guide to the eye, showing the temperature range where sequential tunneling dominates. The inset shows the corresponding R versus T plot on linear axes, emphasizing the dramatic resistance increase at low temperatures (b) An Efros-Shklovskii plot of the same data as in (a). The green dotted curve is a guide to the eye (see equation 4.7). Note that at very low temperatures (< 10 K), a deviation from Efros-Shklovskii behaviour is observed.

Figure A-1(a), displays these data (see also inset) in an Arrhenius plot, based on equation 4.1. The graphs suggests that sequential tunneling dominates in the temperature range from 300 K down till roughly 50 K. At lower temperatures, however, deviations from Arrhenius behaviour are clearly observed. Figure A-1(b) shows an Efros-Shklovskii plot, based on equation 4.7. In the temperature range around 20-150 K, the data follow Efros-Shklovskii behaviour reasonably well. Hence, we find a clear indication for a crossover between sequential and cotunneling tunneling. However, the exact crossover temperature is hard to pin down as the data fit reasonably well to both types of behaviour in an extended temperature range between 50 and 150 K.

Appendix A.3

Additional data analysis

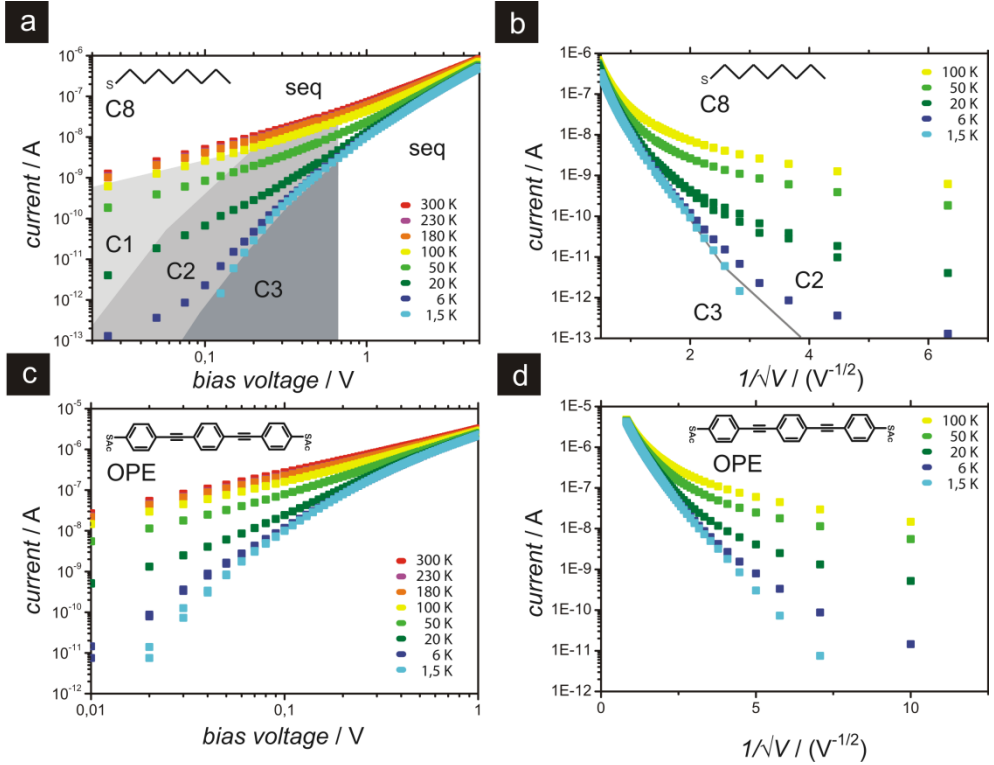


Figure A-2: I - V curves at several temperatures for the sample presented in the main text in Figure 4.4(a) and Figure 4.4(b) i.e. before (Figure A-2(a), (b)) and after exchange (Figure A-2(c), (d)). (a) Log-Log plot of the I - V curves presented in Figure 4.4(a) in the main text. In the cotunneling regime, three different signatures are observed, labelled C1 (thermally activated cotunneling), C2 (multiple inelastic cotunneling) and C3 (Efros-Shklovskii law), related to the different energy scales. In the classical and cotunneling C1 regimes, $I \propto V$ (label 1, next to the curves). In cotunneling C2 regime, $I \propto V^\alpha$ (with an exponent α between 1.8 and 6.2). (b) Same data presented in the form of Efros-Shklovskii plot. The gray line represents the limit below which Efros-Shklovskii field behaviour is expected. The I - V curves at 1.5 and 6 K are at the borderline between regimes C2 and C3. (c) Log-Log plot of the I - V curves presented in Figure 4.4(b) in the main text. (d) Same data presented in the form of Efros-Shklovskii plot.

In Figure A-2 we replotted the I - V data of C8-covered nanoparticles at different temperatures, reported in Figure 4.4(a) as well as the data after molecular exchange with OPE, presented in Figure 4.4(b) and on a Log-Log scale and in an Efros-Shklovskii plot, respectively. The results of Figure A-2 confirm the conclusions presented above in paragraph 4.5.

Appendix A.4

Methodology used to separate the different cotunneling regimes (C1, C2, C3) in the presented log-log plots.

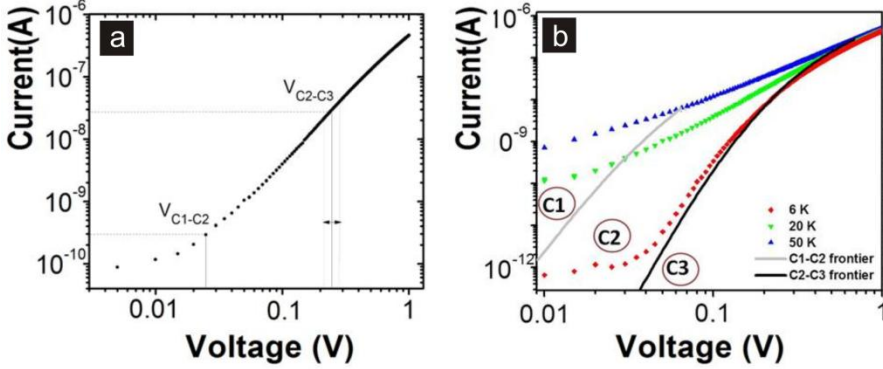


Figure A-3: (a) Example of the methodology used for estimating the current and voltage values defining the C2-C3 and C1-C2 boundaries (shown here on the I - V curve of the OPE sample, at 20 K). The error bar for the value of C2-C3, is related to the uncertainty in R_T . (b) Example of C2-C3 and C1-C2 boundaries construction from the points extracted 6 K, 20 K and 50 K curves.

Here the methodology is described to plot the delimitation line between regions C1 and C2, and between regions C2 and C3. For each I - V curve at a given temperature (see example on Figure A-3(a)) one needs to find the two points of coordinates (I_{C1-C2}, V_{C1-C2}) and (I_{C2-C3}, V_{C2-C3}) , where V_{C1-C2} and V_{C2-C3} are related to the energy range limits of regime C2 and C3 respectively as (see equations 4.4 till 4.6): $V_{C1-C2} = \frac{Nk_B T}{e}$ and $V_{C2-C3} = \frac{Nk_B T}{e} \ln\left(\frac{e^2}{h} R_T\right)$, with N is the average number of particles along an array contacting the left electrode to the right electrode ($N = 15$ for the particular sample studied here), and V the bias voltage applied between these two electrodes (with the bias of a single junction defined as $V_{jct} = V/N$). R_T is estimated from data of Figure 4.5, using the equation S4.5:

$$N_{cot} \approx \sqrt{\frac{E_C}{k_B T \ln(e^2 R_T / h)}}$$

Typical values of $R_T \sim 100 \text{ M}\Omega$ for OPE molecules and $R_T \sim 1\text{-}5 \text{ G}\Omega$ for C8 molecules are obtained. Once V_{C1-C2} and V_{C2-C3} are calculated, I_{C1-C2} and I_{C2-C3} are extracted from each I - V curves at several temperatures.

The demarcations delimiting region C1 from C2, and region C2 from C3 are obtained by joining together all (I_{C1-C2}, V_{C1-C2}) and (I_{C2-C3}, V_{C2-C3}) points (see Figure A-3(b)).

Appendix B.1

Temperature-dependent I - V 's of a multilayered Au-NP-S-BPP network

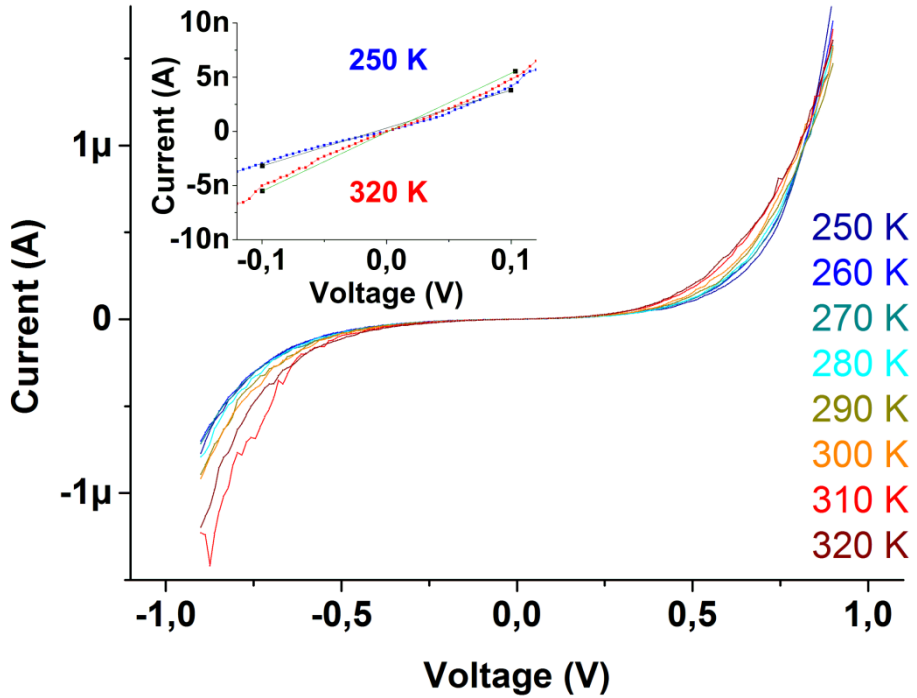


Figure B-1: Temperature-dependent I - V curves of a multilayered Au-NP-S-BPP network on a HAR nanotrench device. The data are taken between 250 K and 320 K (the inset zooms in at low-bias range for the I - V curves at 250 K and 320 K).

Appendix B.2

Modelling the charging energy of 2D Au-NP-S-BPP arrays as function of the dielectric constant

To get a feeling for the expected values of E_C for these multilayered Au-NP-S-BPP networks, the E_C is plotted in Figure B-2 as a function of the dielectric constant based on three models to approximate the E_C for a 2D Au-NP-S-BPP array.

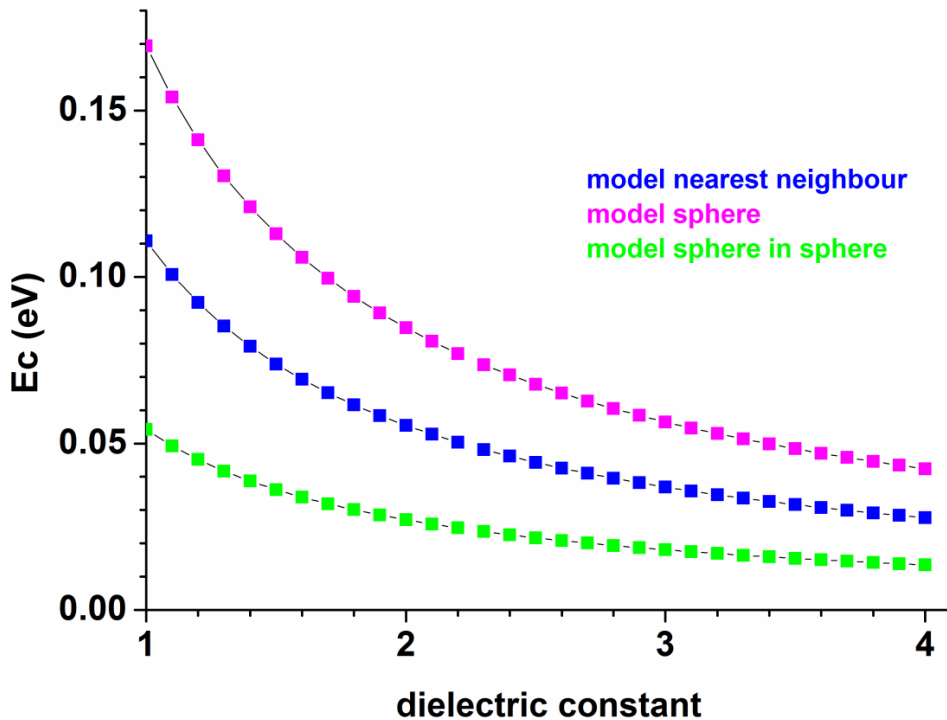


Figure B-2: E_C as function of the dielectric constant for a 2D Au-NP-S-BPP array, calculated through three different models.

The following models are used in Figure B-2 to determine the E_C of a 2D Au-NP-S-BPP array. The first model is the simple spherical model to calculate the maximum limit of E_C for a 2D Au-NP-S-BPP array (see equation S5.1)

$$E_C = \frac{e^2}{8\pi\epsilon_0\epsilon_r r}. \quad (\text{S5.1})$$

Where r is the radius of the gold nanoparticle in a 2D Au-NP-S-BPP array (earlier determined by TEM (see paragraph 5.4). The dielectric constant ϵ of a 2D Au-NP-S-BPP array (based on UV-Vis analyses, see paragraph 5.5) is set on 2.8.

The second model is called the “sphere in sphere” model which estimates a minimum limit of E_C . In the model “sphere in sphere” the total capacitance of a gold nanoparticle is calculated assuming it is fully surrounded by other gold nanoparticles. This is approximated by assuming the metallic sphere is in a second concentric metal shell [48] (see equation S5.2)

$$E_C = \frac{e^2}{\frac{8\pi\epsilon_0\epsilon_r}{\left(\frac{1}{r} - \frac{1}{r+d}\right)}}. \quad (\text{S5.2})$$

Where for d (i.e. the length of two entangled S-BPP molecules) 2 nm is used. The radius r remains set at 4.25 nm.

The third model is called the “nearest neighbour” model [49] (see equation S5.3)

$$E_C = \frac{e^2}{2\left([4\pi\epsilon_0\epsilon_r r] + \left[4\pi\epsilon_0\epsilon_r \frac{r^2}{d} \left(1 + \frac{r^2}{d^2 - 2r^2} + \frac{r^4}{d^4 - 4d^2r^2 + 3r^4}\right)\right]\right)}. \quad (\text{S5.3})$$

Based on mirror charges between two spherical nanoparticle, this model calculates an E_C intermediate value that fits between the upper and lower E_C limits of respectively equation S5.1 and S5.2. Here r is the radius of the gold NP in 2D Au-NP-S-BPP array and d is $2r + 2$ nm (i.e. the distance between two nanoparticles separated by S-BPP molecules with a dielectric constant of 2.8).

From Figure B-2 can be determined that for a 2D Au-NP-S-BPP array with a dielectric constant of 2.8, the E_C of 2D Au-NP-S-BPP array ranges 0.019-0.060 eV. Unfortunately, the models are rather crude or indicative. Note however that the experimental value of E_C is expected to be significantly larger for alkanethiol arrays than for Au-NP-S-BPP arrays, due to the lower dielectric constant in the alkanethiol arrays (see UV-Vis section in paragraph 5.5).

Appendix C.1

SEM image of 1'-gold nanoparticle network on nanotrench device

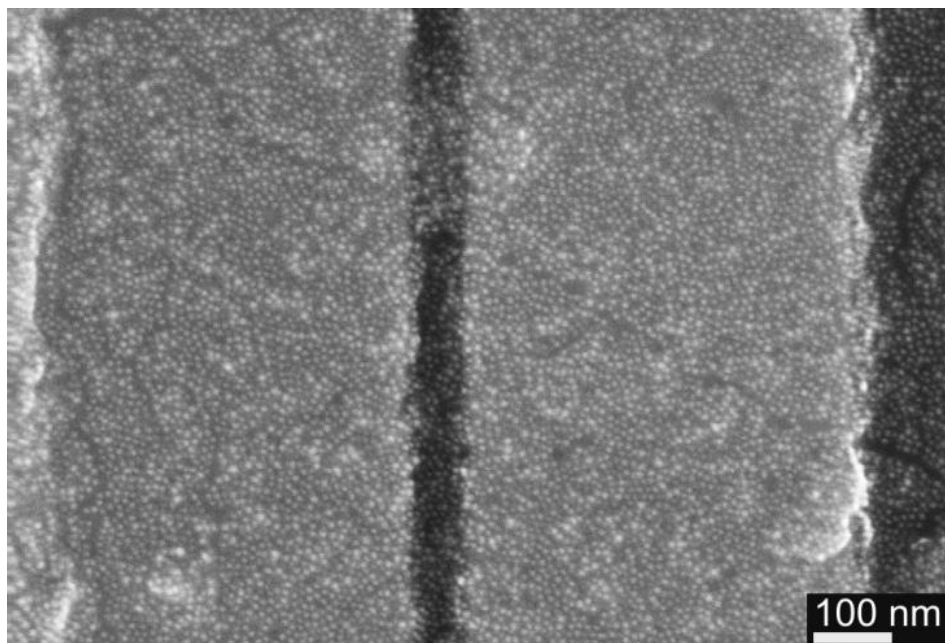


Figure C-1: SEM image of nanotrench gold electrodes device, microcontact printed with layer-on-layer C8-gold nanoparticle arrays and exchanged with 1' molecules to obtain a layered 1'-gold nanoparticle network.

Appendix C.2

UV-Vis measurement of C8-gold nanoparticle array exchanged with **1'** molecules

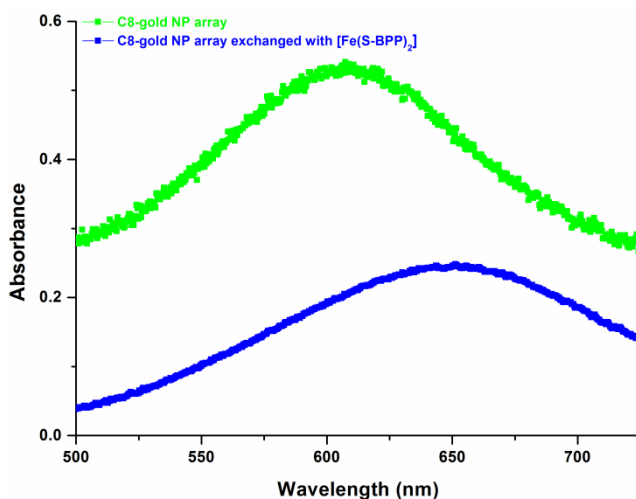


Figure C-2: UV-Vis absorption measurement of the surface plasmon resonance (SPR) peak in a single layer 2D **1'**-gold nanoparticle array on a glass substrate (see blue coloured spectra curve) compared with data from the same sample (see green coloured spectra curve) before the molecular exchange procedure.

To analyze the insertion of the conjugated **1'** molecules in the 2D C8-gold nanoparticles array by molecular exchange, ultraviolet-visible (UV-Vis) spectroscopy is used to confirm indeed that the **1'** molecules are introduced within the gold nanoparticle array. Microcontact-printed 2D alkanethiol-gold nanoparticle arrays, here stabilized by octanethiol (C8) molecules, exhibit a SPR absorption peak near 600 nm. After a molecular exchange process for four days the same sample is again analyzed by UV-Vis spectroscopy, indicating a red shift of the SPR peak (approximately ~40 nm) for a 2D **1'**-gold nanoparticles array. This confirms molecular exchange.

Appendix C.3

Temperature-dependent Raman measurements on bulk 1 SCO powder

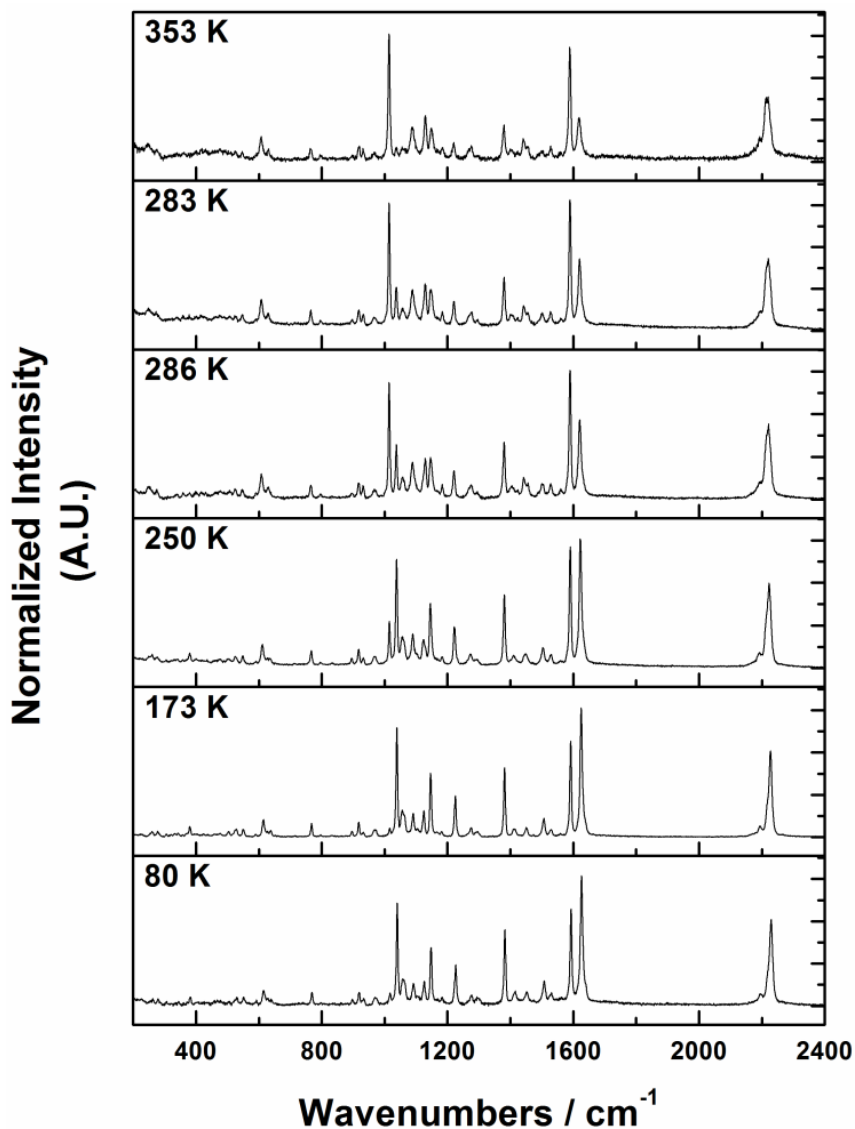


Figure C-3: Temperature-dependent Raman spectra of bulk 1 SCO powder excited at 785 nm (illuminating power 1.2 mw at the sample). The powder was kept for three hours at 80 K to ensure the SCO complex undergoes a complete spin crossover.

Temperature-dependent Raman measurements on bulk 1 SCO powder

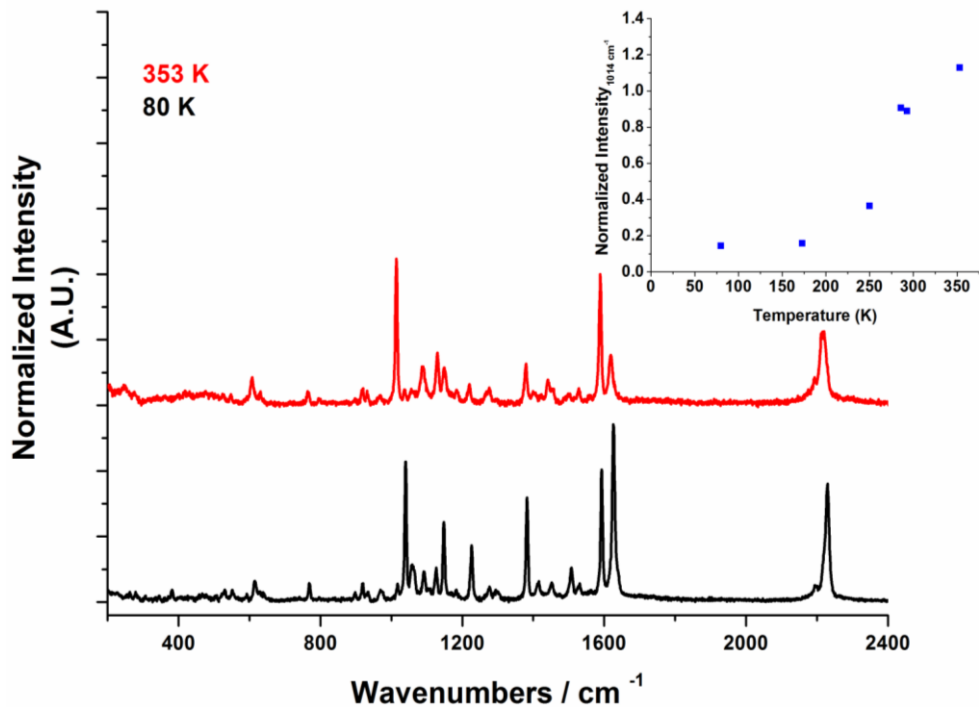


Figure C-4: Temperature-dependent Raman spectra of bulk 1 SCO powder sample at 353 K and 80 K excited at 633 nm (incident power 1.2 mW at the sample). Inset shows the intensity of mode at 1014 cm^{-1} (Pyridine ring breathing coupled Fe(II)-N str) as function of temperature normalized to 1592 cm^{-1} mode which showed weak temperature dependence. This is a qualitative indicator of the temperature-dependent spin transition taking place in the sample.

Temperature-dependent Raman measurements on bulk molecule 1 SCO powder

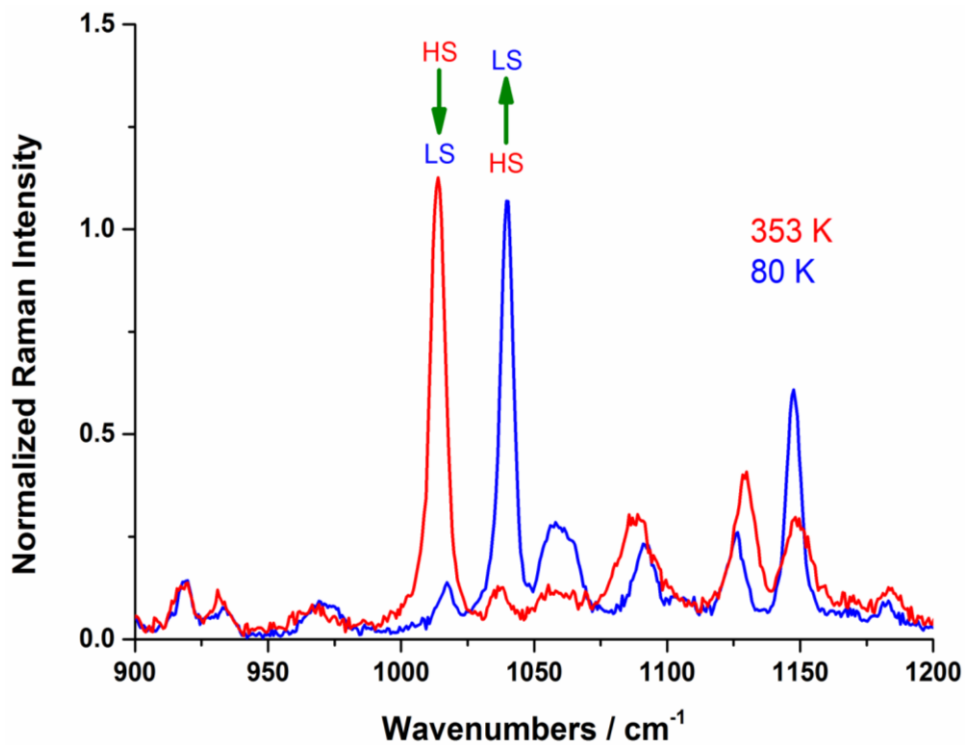


Figure C-5: Zoom in on Raman spectra of bulk molecule 1 SCO powder sample at 353 K and 80 K excited at 633 nm (incident power 1.2 mW at the sample). The intensity is normalized to 1592 cm⁻¹ mode, which showed weak temperature dependence.

Appendix C.4

Temperature-dependent Raman measurements on 2D molecule **1**'-gold nanoparticle array

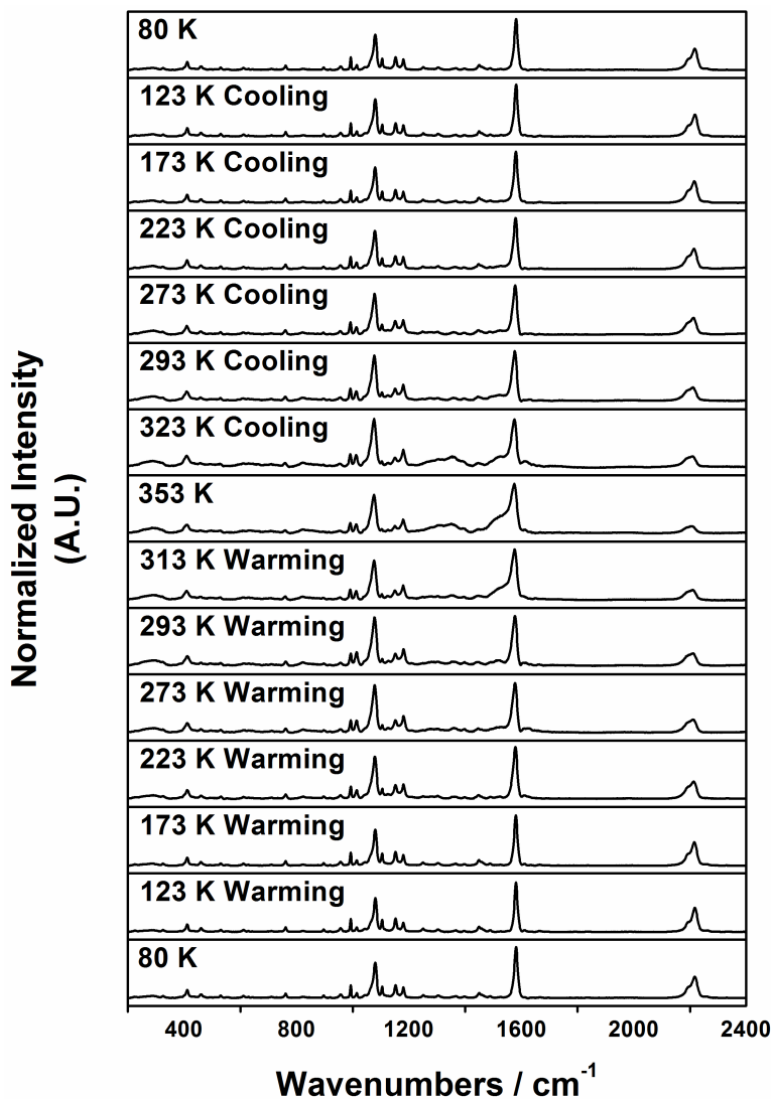


Figure C-6: Temperature-dependent Raman spectra of 2D molecule **1**'-gold nanoparticle array, excited at 633 nm (illuminating power 1.2 mW at the sample) on a quartz substrate.

Table 1: Selected key Raman peak assignments in high- and low-spin states

Raman Shift 1-Complex (cm ⁻¹) HS	Raman Shift 1-Complex (cm ⁻¹) LS	Raman Shift 1'- NP array (cm ⁻¹) HS	Raman Shift 1'- NP array (cm ⁻¹) LS	Assignment
-		321		Au-S mode
-		409 (s)	409 (s)	C-S str AT
990		990 (s)	990 (s)	AT in-plane ring-breathing mode,
1014	1039	1014	1035, 1014 (w)	Pyridine ring breathing coupled Fe(II)-N str
-	-	1076 (vs)	1080 (vs)	AT in-plane ring-breathing coupled to C-S stretch mode
1129	1125	1105	1125	in plane ring NCH str coupled to equatorial Fe-N str
1576 (w)	1576 (w)	1576 (s)	1580 (s)	AT in-plane C-C stretch
1589	1592	-	-	C=C str pyridine
1619	1626	1610 (w)	1633 (w)	C=C str pyrazine
2220 (s)	2229 (s)	2210 (s)	2216 (s)	alkyne C≡C stretch

- where AT is arylthiol moiety; ((v)s) is (very) sharp; str is stretch; (w) is wide

Where a Raman mode appears in SERS spectrum but not in the complex spectrum, it is because that feature is either obscured or exceedingly weak in the SERS spectrum.

Appendix C.5

Experimental part SQUID

The magnetic measurements were performed on a SQUID magnetometer (MPMS-XL-7 Quantum Design) at the Institute of Inorganic Chemistry, Technology and Materials in Bratislava. A multilayered (>3 layers) octanethiol-gold nanoparticles network without **1'** molecules (reference sample A) as well as two multilayered (>3 layers) gold nanoparticle networks with **1'** molecules (via molecular exchange) (Samples B and C) were each deposited on both sides of the quartz substrate (10 x 6 mm). Each sample was inserted into a plastic straw and fixed with tape to seal and to protect the samples (size microcontact printed array: ~ 5 x 5 mm on front side and also ~ 5 x 5 mm on backside of quartz substrate) from the surrounding environment. All herein reported magnetic measurements were carried out at 1 T external magnetic field in the temperature range 90-400 K. The temperature sweeping rate was 1 K min⁻¹ and it was the same for cooling and heating modes. Magnetic data are represented as temperature dependence of magnetic moment.

Appendix C.6

A sample of a **1'**-gold nanoparticle network that did not exhibit a resistance minimum

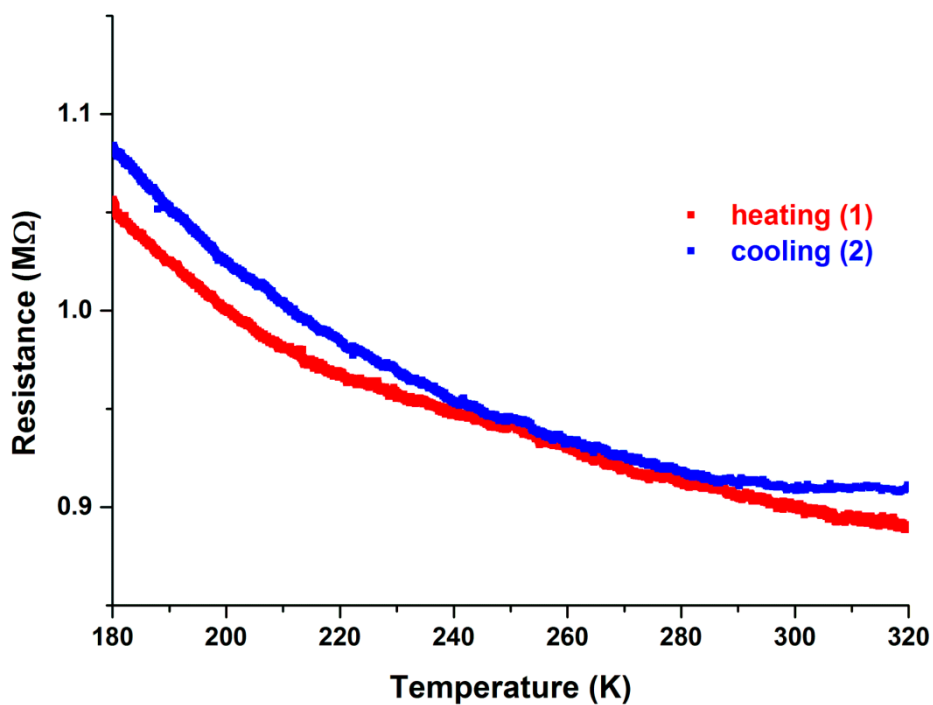


Figure C-7: *R-T* measurement of a molecule **1'**-gold nanoparticle network (stamped 3 times) where no minimum is exhibited. The first cycle is heating and the second cycle is cooling.

Summary

For more than 65 years, scientists have been fascinated by the idea to miniaturize electrical circuits toward the smallest length scales. One particular way is inspired by nature itself, specifically to assemble electrical components and switches from atoms and molecules. After all, it is through such building blocks that life itself is possible. In particular the functionality of our brain is based on organic molecules. The scientific research area that represents the study of electrical currents through molecules is called "molecular charge transport" or "molecular electronics". This research field is strongly stimulated by the developments in organic chemistry to design and synthesize molecules that contain different functionalities. For instance there are relatively well-conducting (conjugated) types of molecules, badly conducting (non-conjugated) type of molecules and even switchable molecules. The molecules typically used have dimensions of the scale of a few nanometers (1 nanometer = 0,000000001 meter). Hence the field of molecular charge transport is part of the larger area of nanoscience and nanotechnology.

To make a working molecular circuit based on a single molecule or a few molecules is challenging. There is a large gap in the length scales of molecules and macroscopic electrodes. Also a so-called "molecular device" needs to be stable enough to function at room temperatures and atmospheric pressures. In this thesis, I have performed fundamental research on charge transport through various molecules. Specifically, I have investigated a special type of molecule that has the ability to change its spin state. To test these functional molecules, I have used a more robust type of molecular device that enables me to bridge the size gap mentioned above.

The concept behind these molecular devices is as follows. First, alkanethiol organic molecules are used to functionalize a gold nanoparticle (~8.5 nm in diameter), forming a molecular monolayer on the gold surface via a Au-S bond. Second, these functionalized gold nanoparticles are self-assembled into a two-dimensional (2D) molecule-gold nanoparticle ensemble. During this process, the functionalized nanoparticles order themselves into an array that can be printed on different types of substrates via a transfer method called microcontact printing. A 2D molecule-gold nanoparticle array can thus be transferred to a device with pre-patterned gold electrodes. The gold electrodes are made via a series of lithographic techniques and they are typically separated by a trench of nanoscopic dimensions. Using the resulting device, the charge transport properties of a molecular-gold nanoparticle network can be measured and analyzed (see Figure 1).

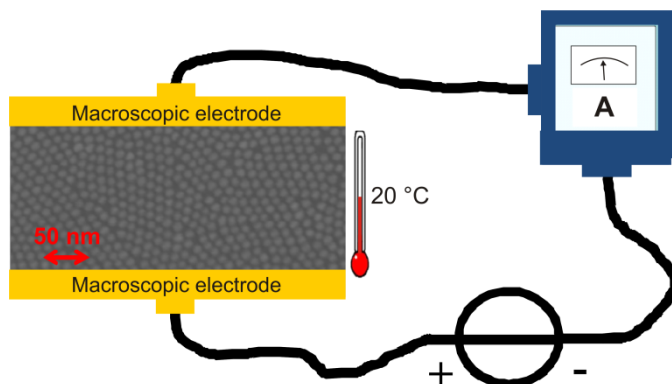


Figure 1: Schematic representation of an electrical circuit based on a 2D molecular-gold nanoparticle array (in this drawing the image of a real molecule-gold nanoparticle array made via a scanning electron microscope is inserted, with a scale bar of 50 nm). This array is contacted to the macroscopic electrodes to measure the charge transport properties of the molecules.

Basically, a molecule-gold nanoparticle array is a collective of multiple gold nanoparticle-molecules-gold nanoparticle junctions. Near room temperature, the conductance of this array is dominated by the molecules, because under these conditions the gold nanoparticles will behave like tiny electrodes with a low electrical resistance. In that case, the electrical resistance of a molecular-gold nanoparticle array is a spatial average of all the gold nanoparticle-molecules-gold nanoparticle junctions. Another advantage of this molecular device is the possibility to perform additional (optical) control experiments on the chemical and physical properties of all the molecules. For a single molecular device these additional analyses are not possible or at least very challenging. The open structure of molecular-gold nanoparticle ensembles makes it also easy to influence the properties of both the molecule and the nanoparticle via external stimuli (i.e. temperature, light).

This thesis comprises six chapters. In Chapter 1, I elaborate on the motivation and history of molecular charge transport. Also I will explain the role of organic molecules in molecular junctions and introduce the experimental techniques used nowadays to study the charge transport through single or multiple metal-molecule(s)-metal junction(s). Here, I motivate my choice to use 2D molecular-nanoparticle ensembles as an experimental technique. In addition, I introduce a special category of compounds, called the spin crossover molecules. This intriguing type of complex molecules possesses the ability to reversibly undergo a spin transition (i.e. a change of spin state under the influence of external stimuli (temperature, light, pressure, magnetic fields)). The measurements of molecular devices containing spin crossover molecules are further described in Chapter 6.

Chapter 2 describes the fact that the electrical conductance through molecules on a nanoscopic scale behaves differently compared with bulk matter on the macroscopic

scale. The conduction of current in macroscopic matter behaves according to the classical laws of Ohm and Drude. On a nanoscopic scale, conduction of current is dominated by quantum mechanics. Chapter 2 also describes how the conductance of a molecular device changes as the chemical/physical conditions change, or “switches”.

Chapter 3 describes the techniques used to synthesize 2D molecular-gold nanoparticle arrays via self-assembly processes and to microcontact print these arrays on macroscopic electrodes devices. Also other (optical) techniques are explained that are used to determine the properties of my molecules and gold nanoparticles in a 2D molecular-gold nanoparticle array.

Chapter 4 explains my research on the charge transport mechanisms in molecular-gold nanoparticle ensembles as a function of temperature. At low temperatures, the gold nanoparticles demonstrate a special behaviour. Each gold nanoparticle possesses a small electrical capacitance. This capacitance causes the need for an additional energy (also called the charging energy) to allow an electron to hop onto a gold nanoparticle. Hence, when the thermal energy is lower than the charging energy, the gold nanoparticles in the molecular-gold nanoparticle ensemble will not behave as perfectly conducting electrodes anymore. The consequence of this is that the electrical resistance of the molecular-gold nanoparticle ensemble increases dramatically with decreasing temperature. This phenomenon is called Coulomb blockade. Still, limited conduction is possible in the Coulomb-blockade regime. This form of conduction is driven by a charge transport mechanism called multiple inelastic cotunneling, which actually follows from the uncertainty principles of Heisenberg. Simply put, during a multiple inelastic cotunneling event, electrons can be simultaneously transported over multiple gold nanoparticle-molecules-gold nanoparticle junctions.

Here, we first study the charge transport regimes for octanethiol (C8)-gold nanoparticle networks. Through a process called molecular exchange we subsequently insert better-conducting (conjugated) molecules in the same molecular-gold nanoparticle network and study transport behaviour again. We show that the resistance ratio between a conductive network and a non-conductive network increases enormously at low temperatures. This ratio grows with an exponent that is directly related to the number of simultaneous cotunneling events. The fascinating consequence of this is that the on/off ratio of a switchable molecular-gold nanoparticle network could be dramatically enhanced by entering the multiple cotunneling regime. The results of Chapter 4 thus introduce a totally new concept to artificially enhance the properties of switchable molecular devices.

In Chapter 5, I describe my research toward a new type of molecular-gold nanoparticle ensembles. Here, a special type of conjugated molecule is used, called a ligand. A ligand is a molecule that can bond in a distinctive way with (metal)ion(s) to form a “complex” molecule. These new ligand-gold nanoparticle ensembles are also synthesized via a self-assembly process. By using multiple analysis techniques on these ligand-gold nanoparticle ensembles (e.g. electron microscopy) we have studied its structure and chemical configuration. (Surface-enhanced) Raman spectroscopy allows us to study molecular vibrations in these networks. We find that the ligands and the gold nanoparticles are connected via Au-S bonds. In addition we have determined that increasing the temperature in these ligand-gold nanoparticle ensembles causes a

significant change in the conformation and orientation of the ligands on the gold nanoparticles. These effects in the junctions of a ligand-gold nanoparticle ensemble appear to be related to another effect encountered during temperature-dependent conductance measurements of a ligand-gold nanoparticle network. Here, the conduction continues to increase when increasing the temperature beyond room temperature. Such an effect is not found in C8-gold nanoparticle networks. The surprising conductive properties of a ligand-gold nanoparticle network could be caused by the increased interactions and fluctuations in gold nanoparticle-ligands-gold nanoparticle junctions when increasing the temperature.

Finally Chapter 6 presents my research on the properties of gold nanoparticle ensembles containing spin crossover molecules. These spin crossover molecules are an exceptional type of complex compounds that can reversibly change spin state via temperature and other stimuli. This phenomenon is called spin transition and it mostly occurs in Fe^{2+} -ion-based complex compounds. Complex compounds originate from coordination chemistry where (transition) metal ion(s) can interact with the functional groups of ligands. During spin transition, two electrons in the d orbitals of the metal ion are transferred from a lower energy state toward a higher energy state or vice versa. Simultaneously, the dimensions of a spin crossover molecule will change a little. For this research we have used a spin crossover molecule that consists of one Fe^{2+} ion and two ligand molecules, similar to the ligands used in Chapter 5. These spin crossover molecules are inserted in C8-gold nanoparticle ensembles via a modified molecular exchange process.

Surface-enhanced Raman spectroscopy is used to determine if at room temperature the spin crossover molecules functionalize the gold nanoparticles via Au-S bonds. Interestingly, temperature-dependent Raman spectroscopy on the arrays shows that significant changes occur in the molecular vibrations of the spin crossover molecules. Analyzing these data, we derive that the majority of the spin crossover molecules in the arrays change from a low-spin state ($S = 0$) to a high-spin state ($S = 2$) when increasing the temperature from low to high. The spin transition phenomenon takes place reversibly, close to room temperature. Also magnetization measurements on these spin crossover molecule-gold nanoparticle ensembles have been performed. These results give indications of a (incomplete) spin transition, as a transition takes place from diamagnetic behaviour to paramagnetic behaviour (and vice versa) around temperatures consistent with the Raman measurements.

At last we have studied the conductance properties of spin crossover molecule-gold nanoparticle networks as a function of the temperature. In reference types of networks (see Chapters 4 and 5), the electrical resistance decreases monotonically with increasing temperature. The spin crossover molecule-gold nanoparticle network, however, shows a clear minimum in the resistance versus temperature curves. This minimum appears to be related to the spin transition, also because theoretical calculations show that the resistance of the spin crossover molecule in the high-spin state should be higher than in the low-spin state. The minimum in the temperature-dependent resistance curves can hence be explained via a simple model based on percolation theory. Percolation theory describes the formation of conduction pathways in a network in which more and more points (here: nanoparticles) are connected (here:

conducting molecules). In a way, this theory can be compared with how water tries to find the easiest way to flow through a medium, for example through coffee in an espresso machine (sometimes called a percolator).

To summarize, this thesis has led to two important new insights. First, the properties of a switchable molecular device can be strongly enhanced artificially by making use of a charge transport mechanism called multiple inelastic cotunneling (see Chapter 4). Second, we show that the spin transition phenomenon can take place in a molecular-nanoparticle ensemble (see Chapter 6).

Samenvatting

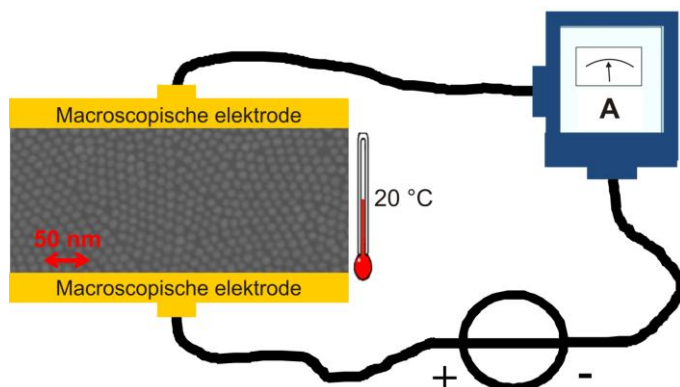
Al meer dan 65 jaar zijn wetenschappers gefascineerd door het idee om elektrische schakelingen te miniaturiseren tot de kleinst mogelijke afmetingen. Eén manier is geïnspireerd door de natuur zelf, namelijk om elektrische componenten en schakelaars op te bouwen vanuit enkele atomen en moleculen. Al het leven op onze planeet en in het bijzonder de werking van onze hersenen zijn tenslotte gebaseerd op organische moleculen. Het vakgebied dat geleiding door moleculen bestudeert heet ‘moleculair ladingstransport’ of soms ‘moleculaire elektronica’. Het maakt gebruik van ontwikkelingen in de organische chemie, waar moleculen met zeer verschillende eigenschappen kunnen worden gesynthetiseerd. Denk daarbij aan goed geleidende (‘geconjugeerde’) en minder goed geleidende moleculen, maar ook aan moleculaire schakelaars. De gebruikte moleculen hebben afmetingen op de schaal van enkele nanometers (1 nanometer = 0,000000001 meter). Daarmee valt dit geheel gebied onder de zogenaamde ‘nanowetenschappen’.

Het maken van een werkende elektrische schakeling die bestaat uit slechts één of een paar moleculen is lastig. Er is namelijk een grote kloof tussen de kleine moleculen enerzijds en de veel grotere elektroden anderzijds. Daarnaast dient een zogeheten ‘moleculair device’ stabiel te functioneren bij kamertemperatuur en atmosferische druk. In dit proefschrift heb ik fundamenteel onderzoek gedaan aan elektrisch transport door verschillende types moleculen. In het bijzonder heb ik gewerkt aan een type molecuul dat kan schakelen tussen twee magnetische (spin) toestanden. Daarvoor heb ik gebruik gemaakt van een robuust type moleculaire devices, die op natuurlijke wijze de genoemde kloof in dimensies (groottes) kan overbruggen. Mede hierdoor blijven ze goed functioneren bij kamertemperatuur en atmosferische druk.

Het concept werkt als volgt. Eerst worden organische alkaanmoleculen (octaanthiolen) via een goud-zwavel binding gekoppeld aan goud nanodeeltjes (diameter: ~8,5 nm). Vervolgens laten we die deeltjes samen een twee-dimensionaal (2D) netwerk vormen. Dit gebeurt via een zelfassemblage proces: de deeltjes ordenen zichzelf. Het zo verkregen netwerk kan via een stempeltechniek afgedrukt worden op een dragermateriaal (substraat) naar keuze. Op dit materiaal zijn van tevoren kleine elektrodes aangebracht, met lithografische technieken, en daardoor kan het netwerk nu elektrisch worden doorgemeten. Zie Figuur 1 voor een schematische weergave.

Het moleculaire netwerk bestaat feitelijk uit een collectief aan goud-moleculen-goud juncties. De geleidingseigenschappen bij kamertemperatuur worden bepaald door de moleculen. Dit komt doordat de nanodeeltjes zich bij die temperatuur als kleine elektrodes gedragen, met een zeer kleine weerstand. De weerstand van het device is daardoor een ruimtelijk gemiddelde van de weerstand van alle goud-molecuul-goud contacten. We hebben tevens het voordeel dat we via optische metingen chemische en fysische eigenschappen van de hele verzameling moleculen kunnen bepalen. Dit is niet

mogelijk voor een device met slechts één molecuul. Door de open structuur van de netwerken is het ook relatief eenvoudig om de eigenschappen van zowel het molecuul als het nanodeeltje te beïnvloeden, bijvoorbeeld door te belichten of door de temperatuur te veranderen.



Figuur 1: Een schematische afbeelding van een elektrisch circuit op basis van een 2D molecuulair-goud nanodeeltjes netwerk (in deze afbeelding een beeld van een echt netwerk, gemaakt met een elektronenmicroscop, met een maat voor de schaal). Het netwerk is gekoppeld aan macroscopische elektrodes die het mogelijk maken de geleidingseigenschappen van de moleculen te bepalen.

Dit proefschrift bestaat uit zes hoofdstukken. In hoofdstuk 1 geef ik een toelichting op de motivatie voor en geschiedenis van moleculair ladingtransport. Vervolgens licht ik de rol van organische moleculen in moleculaire juncties toe. Dit wordt gevolgd door een introductie over de hedendaags gebruikte experimentele technieken om ladingtransport door metaal-molecule(n)-metaal juncties te bestuderen. Hierbij motiveer ik mijn gebruik van een 2D molecuulair-nanodeeltjes netwerk als experimentele techniek. Verder leg ik de essentie uit van een speciale categorie verbindingen, namelijk spin-overgangs moleculen. Dit speciaal type complexmoleculen kan van magnetische spintoestand veranderen bij een verandering in temperatuur of bij bijvoorbeeld belichting. Metingen aan devices gebaseerd op spin-overgangsmoleculen beschrijf ik verder in hoofdstuk 6.

In hoofdstuk 2 ga ik dieper in op het feit dat de elektrische geleiding door moleculen op nanoscopische schaal zich anders gedraagt dan voor bulkmaterie op macroscopische schaal. De geleiding van macroscopische materie gedraagt zich volgens de klassieke wetten van Ohm en Drude. Op de nanoscopische schaal gedraagt de geleiding zich volgens de kwantummechanica. In hoofdstuk 2 bespreek ik ook hoe de geleiding van een moleculair device verandert als het molecuul van chemische toestand verandert, of beter gezegd “schakelt”.

Hoofdstuk 3 behandelt de technieken die zijn gebruikt om via een zelfassemblage proces verschillende types 2D molecuulair-goud nanodeeltjes netwerken te maken en deze vervolgens in contact te brengen met de macroscopische elektroden. Daarnaast ga

ik in op de (optische) technieken die zijn gebruikt om de eigenschappen van zowel de moleculen als de nanodeeltjes in een 2D netwerk te meten.

In hoofdstuk 4 onderzoeken we de ladingtransportmechanismes in moleculaire netwerken als functie van temperatuur. Interessant is daarbij dat bij lagere temperaturen ook de goud nanodeeltjes een bijzondere rol gaan vervullen. Dat komt doordat elk nanodeeltje een kleine elektrische capaciteit vertegenwoordigt. Daarom kost het een beetje energie om een elektron op een nanodeeltje te laten springen, de zogenaamde oplaadenergie. Wanneer de thermische energie lager is dan de oplaadenergie, zullen de goud nanodeeltjes zich niet langer gedragen als perfecte elektrodes. Dit heeft als gevolg dat de elektrische weerstand van het netwerk enorm toeneemt wanneer de temperatuur omlaag gaat. Dit verschijnsel heet Coulomb-blokkade. Toch is er ook in dat regime nog een beetje geleiding mogelijk. Dit ladingtransportmechanisme heet inelastisch meervoudig cotunnellen; het is mogelijk dankzij het onzekerheidsprincipe van Heisenberg. Tijdens inelastisch meervoudig cotunnellen worden elektronen ‘simultaan’ getransporteerd over meerdere goud-octaanthiol moleculen-goud juncties. We bestuderen dit transportregime eerst in octaan(mono)thiol (C8) netwerken. Daarna brengen we beter geleidende (geconjugeerde) moleculen in hetzelfde netwerk aan en bestuderen opnieuw het cotunnelgedrag. We laten zien dat de verhouding van de geleiding tussen een netwerk met en een netwerk zonder geconjugeerde moleculen enorm toeneemt bij lagere temperaturen. Om precies te zijn schaal het met een macht, die wordt bepaald door het aantal ‘simultane’ cotunnelstappen. Dit heeft een interessante consequentie: de aan/uit ratio voor een schakelbaar molecuul in een moleculair-goud nanodeeltjes netwerk kan dramatisch vergroot worden in het cotunnelregime. Daarmee introduceert hoofdstuk 4 een totaal nieuw concept om schakelbare moleculaire devices te optimaliseren.

Hoofdstuk 5 beschrijft het onderzoek aan een nieuw soort netwerk. Het type molecuul dat hierbij wordt gebruikt is een geconjugerd ligand. Een ligand is een speciaal molecuul dat een binding aan kan gaan met (metaal)ionen en zo een groter, ‘complex’ molecuul kan vormen. Ook de nieuwe ‘ligand’ netwerken blijken te kunnen worden gesynthetiseerd via zelfassemblage. Via diverse technieken, waaronder elektronenmicroscopie, hebben we de configuratie en structuur van zulke netwerken bestudeerd. Raman-spectroscopiemetingen laten zien dat de liganden aan de goud nanodeeltjes koppelen via goud-zwavelbindingen. Bovendien zien we dat als een dergelijk netwerk wordt verwarmd, de conformatie en oriëntatie van de liganden op de goud nanodeeltjes significant veranderen. We vergelijken dit effect met een andere opmerkelijke waarneming: de geleiding van dit type netwerk blijft toenemen bij verwarmen, ook bij temperaturen hoger dan kamertemperatuur. Dit is niet het geval bij bijvoorbeeld octaanthiol netwerken. De verrassende geleidingseigenschappen van een liganden-goud nanodeeltjes netwerk kunnen dus het gevolg zijn van de toenemende interacties en fluctuaties in de goud-liganden-goud juncties bij toenemende temperaturen.

In hoofdstuk 6 beschrijf ik het onderzoek naar de eigenschappen van netwerken met spin-overgangsmoleculen. Dit zijn moleculen die reversibel van (magnetische) spintoestand kunnen veranderen als functie van temperatuur en andere externe stimuli. Dit bijzonder fenomeen komt voor in bepaalde complexverbindingen.

Complexverbindingen zijn moleculen die voortkomen uit de zogenaamde coördinatiechemie waarin een metaalion interacties aan kan gaan met de functionele groepen afkomstig van liganden. Tijdens de spinovergang gaan twee d-elektronen van een lage energietoestand naar een hoge energietoestand en daarbij wijzigt de spintoestand. Meestal verandert ook de afmeting van een spin-overgangsmolecuul daarbij enigszins. Voor dit onderzoek maken we gebruik van een spin-overgangsmolecuul dat is opgebouwd uit een Fe^{2+} ion dat complexbindingen aan gaat met twee liganden van het type gebruikt in hoofdstuk 5. Deze spin-overgangsmoleculen worden ingebracht in een octaan(mono)thiol moleculen-goud nanodeeltjes netwerk via een aangepast moleculair uitwisselingsproces.

Via Raman spectroscopie bij kamertemperatuur kunnen we vaststellen dat de spin-overgangsmoleculen een goud-zwavel binding aangaan met de goud nanodeeltjes in het netwerk. Bovendien kunnen we via Raman spectroscopie de veranderingen van bepaalde moleculaire trillingen analyseren als functie van temperatuur. Uit deze metingen kunnen we afleiden dat een meerderheid van de moleculen in het netwerk van een lage-spin ($S = 0$) toestand naar een hoge-spin ($S = 2$) toestand verandert, als we het netwerk van koud naar warm opwarmen. De overgang vindt vlak onder kamertemperatuur plaats. Aanvullend op deze bevindingen hebben we ook magnetisatie-metingen uitgevoerd. Hierbij vinden we een (incomplete) overgang van diamagnetisch naar paramagnetisch gedrag. Dit is kwalitatief consistent met de Raman metingen.

Ten slotte hebben we de geleiding van dit type netwerk gemeten, als functie van de temperatuur. Waar onze referentienetwerken (besproken in hoofdstukken 4 en 5) een monotoon afnemende elektrische weerstand R tonen bij stijgende temperaturen T , laten de ‘spin-overgangs netwerken’ een duidelijk minimum zien in $R(T)$ plots. We relateren dit minimum aan een spin-overgang, mede omdat theoretische berekeningen een hogere weerstand toekennen aan de hoge-spin toestand van het molecuul. Het minimum in $R(T)$ kan dan via een simpel fysisch model verklaard worden. We maken daarvoor gebruik van percolatietheorie. Dit is een theorie die rekening houdt met de makkelijkste geleidingspaden door het netwerk (vergelijk hoe water de makkelijkste weg kiest door een laag koffie in een espressomaker, of ‘percolator’).

Samenvattend leidt dit proefschrift tot twee belangrijke nieuwe inzichten. Ten eerste dat we de eigenschappen van schakelbare moleculaire devices sterk kunnen verbeteren door bewust gebruik te maken van meervoudig inelastisch cotunnelen (hoofdstuk 4). Ten tweede dat een spinovergang kan plaatsvinden in een netwerkgeometrie en dat deze overgang tot een duidelijk meetbaar weerstandseffect kan leiden (hoofdstuk 6).

List of publications

- **Enhancing the Molecular Signature in Molecule-Nanoparticle Networks via Inelastic Cotunneling**, J.-F. Dayen, E. J. Devid, M. V. Kamalakar, D. Golubev, C. M. Guédon, V. Faramarzi, B. Doudin and S. J. van der Molen, *Adv. Mater.*, **25**, (2013), 400-404.
- **The Influence of Molecular Mobility on the Properties of Gold Nanoparticle Organic Ligand Networks**, E. J. Devid, P. N. Martinho, M. V. Kamalakar, Ú. Prendergast, C. Kübel, T. Lemma, J.-F. Dayen, T. E. Keyes, B. Doudin, M. Ruben and S. J. van der Molen, *Beilstein J. Nanotechnol.*, **5**, (2014), 1664-1674.
- **Spin Transition in Arrays of Gold Nanoparticles and Spin Crossover Molecules**, E. J. Devid, P. N. Martinho, M. V. Kamalakar, I. Šalitraš, Ú. Prendergast, J.-F. Dayen, V. Meded, T. Lemma, R. González-Prieto, F. Evers, T. E. Keyes, M. Ruben, B. Doudin and S. J. van der Molen, *ACS Nano*, **9**, (2015), 4496-4507.

Other publication

- **Formation of Nematic Liquid Crystals of Sterically Stabilized Layered Double Hydroxide Platelets**, M. C. D. Mourad, E. J. Devid, M. M. van Schooneveld, C. Vonk and H. N. W. Lekkerkerker, *J. Phys. Chem. B*, **112**, (2008), 10142-10152.

Curriculum Vitae

Edwin Johan Devid, born March 18, 1979 in Amsterdam, The Netherlands

Previous education

- 1992 - 1996 **Lower business school** (secondary school) at ‘Bernard Nieuwentijt college’ (location IJdoorn, Amsterdam).
- 1996 - 1997 First year of **Pre-Laboratory College** completed at Amsterdam Techniek and promoted to Laboratory College.
- 1997 - 2001 **Laboratory College** (Amsterdam Techniek).
- 2001 - 2005 **B.Eng. Chemical Technology** (Hogeschool van Utrecht).
- 2005 - 2007 **M.Sc. Chemistry and Physics** (Utrecht University).

Employment history

- 2008 - 2009 **Research scientist** at Unilever Research & Development laboratory
- 2010 - 2014 **Ph. D. thesis** (Leiden University)
In the group of dr. ir. S. J. van der Molen regarding project INTERNET.

Acknowledgements

Allereerst wil ik Sense Jan van der Molen bedanken voor zijn begeleiding en de mogelijkheid om te werken aan project INTERNET aan de Universiteit Leiden. Ik bedank de Stichting FOM voor het faciliteren van mijn promotie en voor de memorabele ervaring. Tevens wil ik Jan van Ruitenbeek en Jan Aarts bedanken voor alle gesprekken en deelname aan de gezamenlijke werkoverleggen van de respectievelijke onderzoeksgroepen.

I also want to thank everybody for being present during my promotion and defense.

I especially want to express my gratitude to my project INTERNET colleagues abroad. I am thankful to Bernard Doudin, Vina, Venkata, Jean-François, Fabien, Celine, Silvia and many others at IPCMS for all the effort, enjoyable cooperation and support.

Also I want to thank very much Mario Ruben, Paulo, Ivan, Rodrigo, Senthil, Frank, Coral, Andrea and all the others at KIT for all the conversations, enjoyable support and their constructive efforts. I gratefully thank Tia Keyes and Úna Prendergast for their kind collegial support and valuable efforts to contribute to the success of project INTERNET. Also I like to acknowledge Stefano Sanvito, Nadjib Baadji and all others for their fruitful discussions and conversations. I wish you all the best and I am glad to have worked with you all.

My thanks go to all the previous and current Ph.D. researchers, postdoctoral researchers and other colleagues in the Huygens building (especially the 7th and 6th floors) for the great time. I want to thank Sipeng and Sylvestre for the inspiring, pleasant discussions regarding complex molecules.

Mijn dank gaat uit naar Anouk, Koen en Jeroen voor de fijne samenwerking en hun verrichte werkzaamheden gedurende hun bachelor en master onderzoeksprojecten.

Ik wil Fred Robbers, Peter Gast en Henk Buisman bedanken voor de goede contacten en de samenwerking tijdens mijn onderwijswerkzaamheden en de practica voor VWO scholieren. Graag wil ik de ELD, in het bijzonder Bert Crama en Peter van Veldhuizen, en FMD, in het bijzonder de Quickservice en Ruud van Egmond, bedanken voor hun elektronische/technische advies. Ik bedank Ruud van Kuyvenhoven voor de aangename gesprekken en voor hulp bij ICT kwesties. Tot slot bedank ik de mensen bij het secretariaat, in het bijzonder Charlotte Laurens-Griffioen en Daniëlle Duijn-ter Veer, voor de gezellige gesprekken en hun hulp bij administratieve kwesties.

Ik bedank graag alle overige mensen die ik heb ontmoet de afgelopen 4 jaar en met wie ik heb samengewerkt.

Bovenal wil ik mijn familie bedanken voor hun onmetelijke steun gedurende mijn lange weg richting de werelden van innovatie, wetenschap en technologie.

